3D Printing Biopolymer: A Comprehensively Experimental Study of Interfacial Bonding Performance

By

Yuxuan Wang

A Thesis Submitted in Partial Fulfilment of the Requirements for the Degree of Doctor of Philosophy

Department of Civil and Environmental Engineering

College of Engineering, Design and Physical Sciences

Brunel University London

February 2022

Declaration

The work in this thesis is based upon the research carried out at the Department of Civil and Environmental Engineering, Brunel University London. Except where specific reference has been made to the work of others, this thesis is the result of my own work. No part of this thesis has been submitted elsewhere for any other degree or qualification.

Candidate: (Yuxuan Wang)

Acknowledgements

Table of Contents

Abbreviations

Acronym	*Meaning*
AM	Additive manufacturing
ABS	Acrylonitrile butadiene styrene
ANOVA	Analysis of Variance
ASA	Acrylonitrile styrene acrylate
BT	Bed temperature
CAD	Computer-aided design
CF	Carbon fibre
CFRP	Carbon fibre reinforced polymer
CM	Cast moulding
CLIP	Continuous liquid interface production
CNF	Cellulose nanofibrils
CNT	Carbon nanotubes
DMA	Dynamic mechanical analysis
DTG	Derivative thermogravimetry
DSC	Differential scanning calorimetry
DSF	Dynamic sheet forming
FDM	Fused deposition modelling
FM	Flexural modulus
FS	Flexural strength
GF	Glass fibre
GNP	Graphene nanoplatelets

GO	Graphene oxide
GRA	Gray relational analysis
HDPE	High density polyethylene
KF	Kelvar fibre
LDPE	Low density polyethylene
LENS	Laser engineered net shaping
LOM	Laminated object manufacturing
LT	Layer thickness
MCC	Microcrystalline cellulose
MMT	Montmorillonite
MWCNT	Multi-wall carbon nanotubes
NCC	Nanocrystalline cellulose
ND	Nozzle diameter
NFC	Natural fibre composites
NT	Nozzle temperature
PA	Polyamides
PBS	Polybutylene Succinate
PBSA	Poly(butylene succinate-co-butylene adipate)
PC	polycarbonate
PCL	Polyecaprolactone
PEG	Polyethylene glycol
PEEK	Poly-ether-ether-ketone
PET	Polyethylene terephthalate

PGA	Polyglycolic acid
PHA	Polyhydroxyalkanoates
PHB	Poly(b-hydroxybutyrate)
PHBV	Poly(3-hydroxybutyrate-co-3-hydroxyvalerate)
PLA	Polylactide or polylactic acid
PP	Polypropylene
PS	Printing speed
TPF	Treated palm fibre
SEM	Scanning electron microscope
SLA	Stereolithography
SLM	selective laser melting
SLS	Selective laser sintering
SS	Shear strength
SPM	Scanning probe microscopy
TGA	Thermogravimetric analysis
TM	Tensile modulus
TMA	Thermomechanical analysis
TS	Tensile strength
UTS	Ultimate Tensile Strength
UV	Ultraviolet
VDP	Vertical density profile
3DP	Three dimensional printing

List of Figures

xiii

List of Tables

Abstract

Additive manufacturing (AM) technologies have experienced a substantial growth in recent decades. AM technologies are able to fabricate and build complicated customised geometry composites without extra tools and execute multi-materials manufacturing that conventional manufacturing methods cannot offer. Polymeric material applied in AM has become the mainstream, but industrialisation still faces many challenges. Currently, bio-based polymers have also been highly demanded due to the sustainability requirements. The combination of AM and bio-based polymeric material shows significant potential in a wide range of applications.

This study has presented a comprehensive investigation programme focusing on the interface formulation, structure, bonding and performance of 3D printed biopolymeric materials. The experimental analysis firstly investigated the interfacial bonding performance of various bio-based polymeric materials in detail, then several material combinations and modifications have been investigated in order to enhance the printability and performance of AM biopolymeric materials. The formation mechanisms, failure modes and micromechanical performance of interlaminar bonding were comprehensively studied throughout the work programme. The printing performance was determined by the density profile, mechanical properties testing and micromechanical properties across the thickness and over cross-section area for all the materials studied. Thermal properties have also been carried out in order to determine the miscibility of the copolymers.

The optimised printing parameters and the effect of postprocess of Polylactide (PLA) polymer have been generated following this programme, up to 24% higher in tensile strength when the printing temperature is 220 ˚C compared to the 200 ˚C. Impressive mechanical strength obtained but severe anisotropy property and brittleness have also existed. The reduction of tensile strain in y-axis specimens compared to the x-axis has improved from 62% to 22% and competitive mechanical properties have also been achieved by the addition of PHBV biopolymer into the PLA, up to 86% increase in tensile strain has been achieved. Lastly, innovatively bio-based printing materials, such as Polylactide (PLA)/Polybutylene Succinate (PBS) and Polylactide (PLA)/Polybutylene Succinate (PBS)/Polyethylene glycol (PEG), have been investigated and up to 80% increase in ductility has been achieved in PLA/PBS/PEG blends. While the limited improvement has been achieved in the PHBV modifications and some challenges emerged and remained for further development, such as the anisotropy,

brittleness, processability and geometric accuracy, a promising path is provided by this study to extend further research and commercial applications of bio-based polymers for additive manufacturing.

1. Introduction

1.1 Background of research

Additive manufacturing (AM), a.k.a. 3D printing is a growing incredibly fast manufacturing process, and it can be predicted that a large share of production line will be fabricated via AM method in the near future, especially for customized products. However, a new environmental issue is followed by the emerging AM process, which is the great amount of wastes disposal. Even though the AM has brought higher efficiency of material usage, higher rejection rate, the need of support structure and prototype making cannot be ignored in the AM process. Thus, the material sustainability has come along with the importance of the AM.

In the last decade, the application of AM has two distinct tendencies. Firstly, highly customisable parts can be produced in a number of materials by industrial high-end 3D printer. Due to the 'net-shape' properties and almost no complexity and geometry constraints of the product, there are several major applications, when the AM is particularly outstanding compared with conventional manufacturing processes, like injection moulding. Mass customization production like human implants, temporary alternative parts and part which is almost impossible to fabricate apart from AM [1,2]. Secondly a tremendous community, which is formed by 3D printing enthusiasts, offers an open-source approach to share the resource and knowledge of AM. This community has significantly lowered the entry threshold of AM to the world and also benefits the professional level, such as industry, education and research [2].

Biobased polymers are the polymers that can be degraded into constituent monomers with the production of gases or liquid, like CO_2, CH_4 or water, without generating toxic material. Compared with the conventional petroleum-based polymers, these polymers have significantly lower carbon footprint with low greenhouse gases emission. With the development of bio-based polymers, more modifications have emerged to create a large range of applications, such as food packaging, biomedical engineering and other industrial manufacturing. Therefore, the combination of AM and bio-based polymers has shown great promising for further development of applications [3,4].

Polymeric materials in the AM have become a major research stream and many challenges remain, and one of the most critical parameters, which could be crucial for the industrialisation, property and application of the 3D printed products, is the interfacial bonding among printed

filaments. Therefore, this research programme is specifically established to better understand the interface formulation, structure, bonding and performance, especially focusing on bio-based polymers, e.g. PLA and its hybrid systems, which have been widely employed in the AM.

1.2 Aims and objectives of research

This study aims to understand and optimise the 3D printing performance of existing PLA polymer by experimental design, production and performance assessment. The project then develops novel biobased polymeric products through 3D printing. To deeply study the interfacial bonding of 3D printed parts, experimental procedures like Vertical Density Profile (VDP) and nanoindentation are firstly introduced and investigated in 3D printing throughout the study to provide a comprehensive evaluation. The mechanical performance of the 3D printed materials and interfaces are tested and characterised by tension testing and nanoindentation. The interfacial bonding area is examined through by nanoindentation to reveal the specific bonding strength between printed layers and the origin of anisotropy property of 3D printed parts.

With the addition of biobased polymer, the 3D printed copolymer of PLA and PHBV is fabricated and analysed. Various modifications are compounded and manufactured by introducing the copolymer/additives material, such as Polybutylene Succinate (PBS), Polyecaprolactone (PCL) and Polyethylene glycol (PEG), to improve the printability, anisotropy properties and brittleness of the printed composite products.

The specific objectives of the project include:

1) Establish 3D printing processing technologies for biobased polymers with PLA and its hybrid systems;

2) Comprehensively investigate the interfacial bonding properties of 3D printed biobased polymers from nano to macro dimension;

3) Understand the forming mechanisms of interface structure and establish its relationship with the properties of 3D printed products;

4) Introduce novel biobased printing material to the Fused Deposition Modelling (FDM) 3D printing process;

5) Analyse the effects of copolymer and additives to the mechanical and thermal properties of biobased polymers in AM;

6) Improve the ductility and anisotropy properties of biobased material in the AM through modifications with novel bio-copolymers and additives.

1.3 Significance of research

Numerous researches have been carried out for various biopolymers for their application in the AM, however, the emphases of these studies are mainly placed in some specific material properties or applications, and the experimental testing and analysis procedures are also limited in several common methods. Evaluation processes like VDP and nanoindentation have been firstly implemented in this study and a comprehensive study about the 3D printing biopolymer from the nano-size to the macro-size has been innovatively established, which shall provide a database to the researchers who are developing novel polymeric or composite materials with the AM.

Different bio-based polymers have been introduced to the AM for the last decades, but there are limited studies regarding the interfacial bonding performance of biopolymer in 3D printing [5,6], since the bottlenecks in mechanical performance, anisotropy property and processability remain. This study is introducing novel biobased polymers into FDM 3D printing process. To improve the processability, anisotropy and brittleness properties, various modifications have been employed and tested, such the abovementioned concerns can be adequately improved. The overall mechanical performance of 3D printed specimens is impressive and competitive over other synthetic polymers in FDM 3D printing. The tensile strain of the PLA is enhanced 86% to by the addition of PBS copolymer and PEG additive, and the anisotropy of the printed specimen is reduced by 64% in tensile strain when the PHBV copolymer is added.

Current studies have focused little on the experimental analysis of 3D printed part, and the performance of interfacial bonding at the neck growth area needs to be investigated as little related previous research is available. The general density distribution profile of entire printed part, which is implemented by VDP process, is also critical to the 3D printed database due to the absence of experimental data.

1.4 Scope of research

In this research, to investigate the interfacial boundary and introduce novel biobased polymers in 3D printing manufacturing, a comprehensive evaluation procedure is established, which contains VDP, mechanical properties testing, microstructure analysis, nanoindentation testing and thermal properties evaluation. To achieve a better understanding of the interfacial bonding of 3D printing products, the forming and failure mechanisms, tensile and interlayer mechanical performance, and fracture and cross-section morphology are experimentally studied. Meanwhile, the copolymerization of PLA with other newly available biobased polymers and modifications with additives are investigated to achieve a superior mechanical performance to neat PLA polymer in 3D printing. More details for the scope of this study is given in Fig. 1.
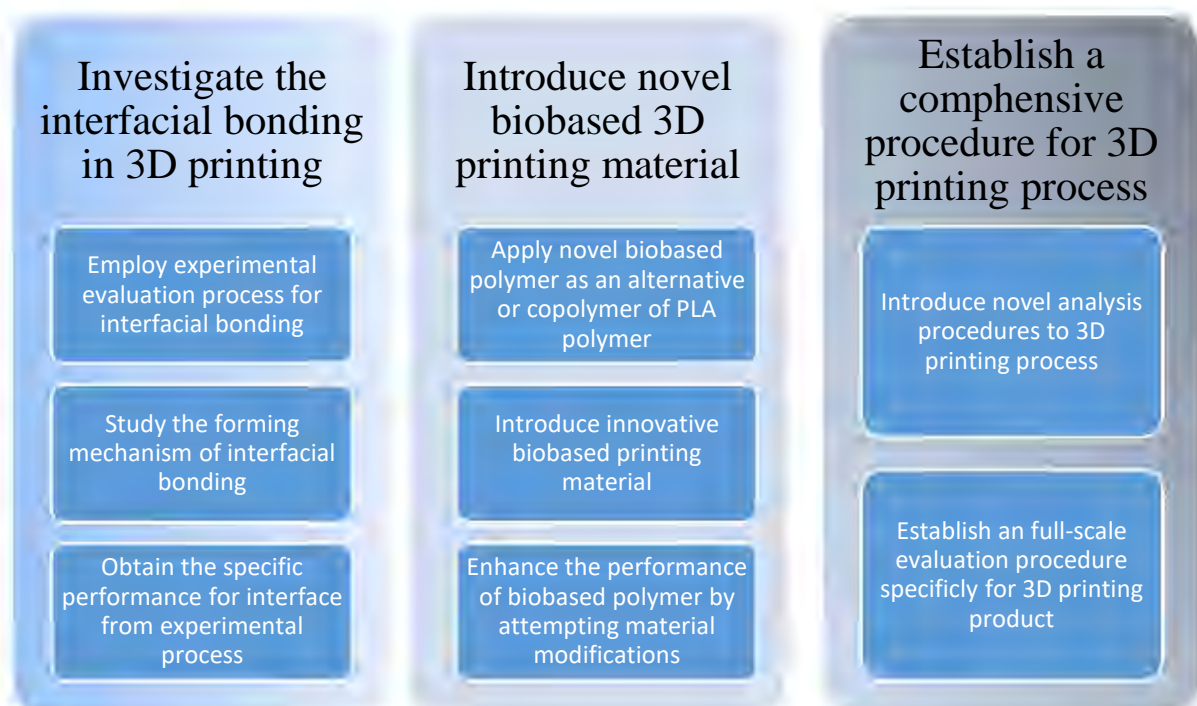
Fig. 1 Scope of research in this study

1.5 Thesis Structure
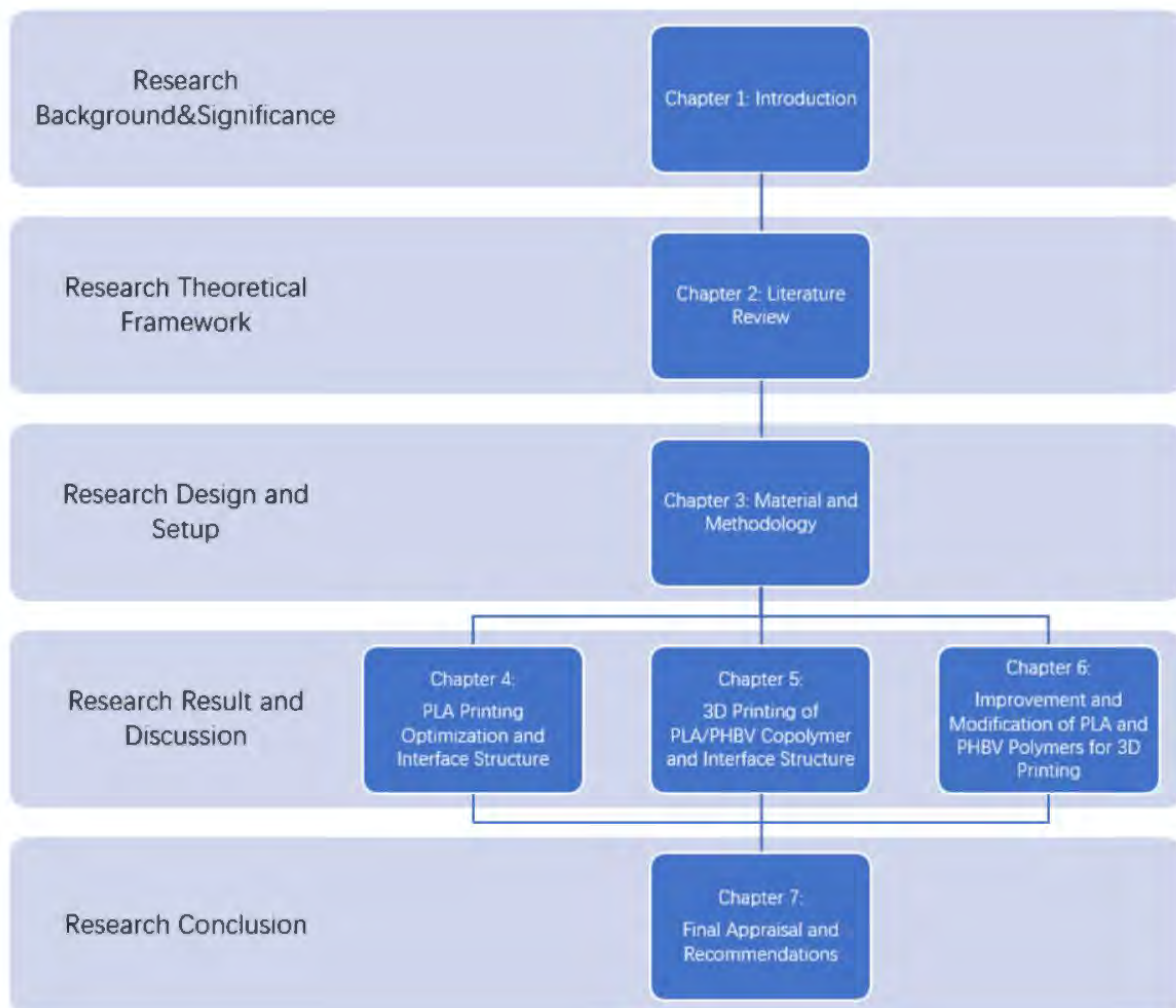
Fig. 2 Structure of the thesis

2. Literature Review

2.1 Introduction of additive manufacturing (AM)

In 1980s, physical objects or parts were firstly fabricated through computer-aided design (CAD) data by a group of techniques called rapid prototyping, which directly offers the realization for the design without applying a mould or other machining preparation. Since then, this technology has been developed exponentially and various types of technology were invented and developed in conjunction with different implementing materials. The additive manufacturing (AM) as the building process normally used in rapid prototyping, has been implemented for years and various technologies are available, even though there are limitations of this process, admittedly, and brings a new era of manufacturing to the world. Unlike the traditional manufacturing methods, AM process is to stack the blocks layer by layer. By using CAD software to create 3D model, which is then transferred to slicing process format and incorporating whole tool path for the AM printer, the AM printer then starts a printing process to obtain the final designed object (Fig. 2).

3D CAD Model	⇒	Slicing Software	⇒	Generation of Path	⇒	3D Printing	⇒	3D Part

Fig. 3 Systemic process of AM

AM process is mainly applied in customized products, medical models and conceptual models. In engineering fields, AM has also been employed in many industrial sectors, such as aerospace, automobile, civil, biomedical engineering. In recent decades, with the increased competition from competitors and requirements from customers, one of the most critical challenges to the designers and engineers is how to quickly produce the new product from designing models to qualified products. AM technology provides a highly efficient process to build a product with almost all geometry complexity without any new tooling device. It will considerably shorten the design-to-production cycle and relatively low cost [7-9].

Nevertheless, numerous publications reported AM techniques, materials available and possible applications for many industrial sectors still require a deeper understanding. Hence this review intends to lay out the principle of these technologies, their working mechanisms, advantages and possible operational limitations. The corresponding material selections and

their possible applications are also investigated. The review should provide a foundation database for understanding the potentials and further research and commercial development of various AM technologies, and for AM materials innovation and manufacturing.

2.2 Overview of current AM technologies

Since the implemented materials of AM vary considerably, different technologies are developed to fulfil the printing requirements. Different subdivisions of AM technologies are available and usually categorized based on the base materials. This review discusses AM technologies by dividing into liquid based, solid based and powder based productions, and the merits and demerits of each process are described and assessed to identify the knowledge and research gaps. To optimize the AM processes, several main quality factors are proposed to enhance AM production, which are divided into products (surface roughness, dimensional accuracy, material behaviour and building time) and processes (heat transfer, material deposition/ melt pool and phase change). Each factor should be considered when manufacturers intend to employ an AM technology into product production [10-12].

2.2.1 Liquid based AM technologies

2.2.1.1 Fused deposition modelling (FDM)

Fused deposition modelling (FDM), a.k.a. Fused Filament Fabrication (FFF) is to apply the melted thermoplastic polymer through an extrusion into layer-by-layer filaments. The thermoplastic polymer is heated at the orifice of nozzle and the melted filaments are extruded on a platform, which is also heated for an easier fusion process, and fused together to form a layer of the printed thermoplastic polymer. The following extruded filaments stack on the previous layers/materials and solidify into final objects. Material selection range of FDM is extremely broad which covers most of thermoplastic polymers, powder/fibre composites and even metals. Common thermoplastic polymers used are ABS, PLA and nylon, especially ABS and PLA are widely used in a commercial printer due to their reasonable price and printing quality. Polymer composite materials like carbon fibre reinforced composite can also be fabricated by FDM technique. Even through, the inherent anisotropy property in this process is still existed, the weak interlayer performance cannot be completely compensated by composite printing. Recently, metal materials are innovatively employed in the conventional FDM printer through metal filaments. The metal/polymer composite filament can be commonly printed and the polymer will be chemically dissolved by the solvent, then sintering

of metal powder is requested to bond powder to final metal part [13]. A commercial printable 316L austenitic stainless steel filament was developed by BASF with a decent mechanical performance. This solution induced a lowering of admittance of metal in additive manufacturing, but the shrinkage of final part after sintering limits the geometric accuracy of this process [13].

FDM process provides a series of advantages comparing with other additive manufacturing processes, the lowest cost is no doubt the leading one. Most of FDM requires no post process for solidification or geometric accuracy [10]. FDM process can also be extended into multi-nozzle to achieve various material printing. However, this technique has several fatal drawbacks; the resolution of printing is limited by the diameter of filaments, the representative resolution is 0.2 mm [14], therefore, it is difficult to achieve a highly smooth surface on the printed objects without post process. The printing speed is also limited by heating and extrusion process, and such the rheological properties of the printed material has to be high. This means that there is a limitation on the materials available for this technique. Anisotropy and inter-layer interface bonding properties in FDM printed parts is inherent and severe. The anisotropy of FDM has been reported at around 50% which is the severest among all AM technologies [15].

Many researches have devoted to optimize FDM process through various approaches: Nancharaiah, et al. [16] applied Taguchi method and ANOVA technique to analyse the impact of several main factors to surface roughness and dimensional accuracy when applying ABS as the deposited material. It showed that the surface roughness and part accuracy could be considerably influenced by layer thickness and air gap, and a smaller filament thickness and air gap has been found to produce a better surface quality. Chung, et al. [17] also studied the surface roughness and dimensional accuracy in FDM process by using a statistical optimization method which combined the Taguchi method and Gray relational analysis (GRA). This approach analysed various configurations of deposition, supports and other parameters, such as layer thickness and deposition orientations. The conclusion of this study was that applying optimum settings could make a 66% improvement in surface roughness and different directions of deposition could result in a variation in accuracy. The FDM built parts had also much higher tensile strength when the loading direction is parallel to the deposition path than the loading perpendicular to building path. The distribution of stress and distortion of patterns were evaluated in various deposition situations by Zhang and Chou [18]. The result of this research

was that an increase in the layer thickness and width of path during printing could lead to a higher distortion of objects and residual stresses.

Post process also plays a significant role in FDM process since some abovementioned inherent issues like surface finish and anisotropy property can be enhanced by different post process. To approach better surface finish, chemical and mechanical processes are primarily adopted. The theory of chemical process is to apply the solvent of the printing material to smooth the surface of the printed objects. Galantucci et al. [19,20] introduced an acetone bath to improve the printed ABS part, it resulted in a considerable enhancement in surface roughness and also surprisingly found that the flexural strength and elongation at break were reinforced after the acetone bath process. The microscopic image (Fig. 3) shows that the enhanced contact area inter-filament may lead to this remarkable result. Few other works also achieve similar enhancement [21-23]. Jin et al. [24]created a thin film on printed PLA parts by using dichloromethane vapour treatment process to improve the surface roughness, the tensile properties reported decreased dramatically by 63%. On the contrary to the additive manufacturing, a subtractive manufacturing method was also introduced to improve the surface finishing of FDM part. Pandey et al. [25] successfully introduced a hot cutter machining to improve surface finishing, however the process complexity and time-consuming limit its application. Similarly, Boschetto et al. [26] applied CNC machining to smooth the surface morphology of printed ABS after the printing process, the average roughness dropped significantly from 20 µm to 2 µm. An annealing treatment was studied by Torres et al. [27], the PLA specimens were annealed at 100 °C for 20 mins. 35% improvement on shear strength was achieved but the strain loses significantly. Compared with the chemical surface treatments, mechanical methods require a more complex process like path designing, and longer processing cycle, but the chemical treatments may modify the mechanical performance of printed parts. Table 1 summarises the FDM post-processes from different works of other researchers.

Table 1 FDM Post-processes studies and results

	Study	Printing Material	Treatment	Process	Variable parameters	Properties
Chemical method	Galantucci et al. [19,20]	ABS	Dimethylketone (acetone)	Bath	90% dimethylketone and 10% water, 300s immersion time	Roughness reduced more than 50%, small decrease in tensile strength but better ductility and flexural strength.
	Percoco [21]	ABS	Dimethylketone (acetone)	Bath	90% dimethylketone and 10% water, 300s immersion time	Roughness reduced up to 90% and slightly higher compressive strength.
	Garg et al. [23]	ABS	Dimethylketone (acetone)	Cold vapour	acetone, 99% concentration, 18-20 °C for 30s and 40 min of exposure time	Possible low surface roughness up to 0.02 μm with minimum dimensional deviation.
	Jin et al. [24]	PLA	Dichloromethane	Vapour	30 ml of dichloromethane 99% pure	Decrease in roughness, 50% improvement in ductility but 63% deduction in tensile strength.
Mechanical method	Pandey et al. [25]	ABS	Hot cutter machine	Edge cutting	Various cutting speed, rake angle and cutting angle	Roughness drop up to 0.3 μm
	Boschetto et al. [26]	ABS	CNC machine	Edge cutting	Various cutting depth	The optimized average roughness is 0.97 μm when the cutting depth is 0.15mm
	Torres et al. [27]	PLA	Annealing treatment	Heating	Annealing at 100 °C for 5 and 20 mins, print with various layer thickness and infill density	Increase in shear strength but fracture strain dropped largely
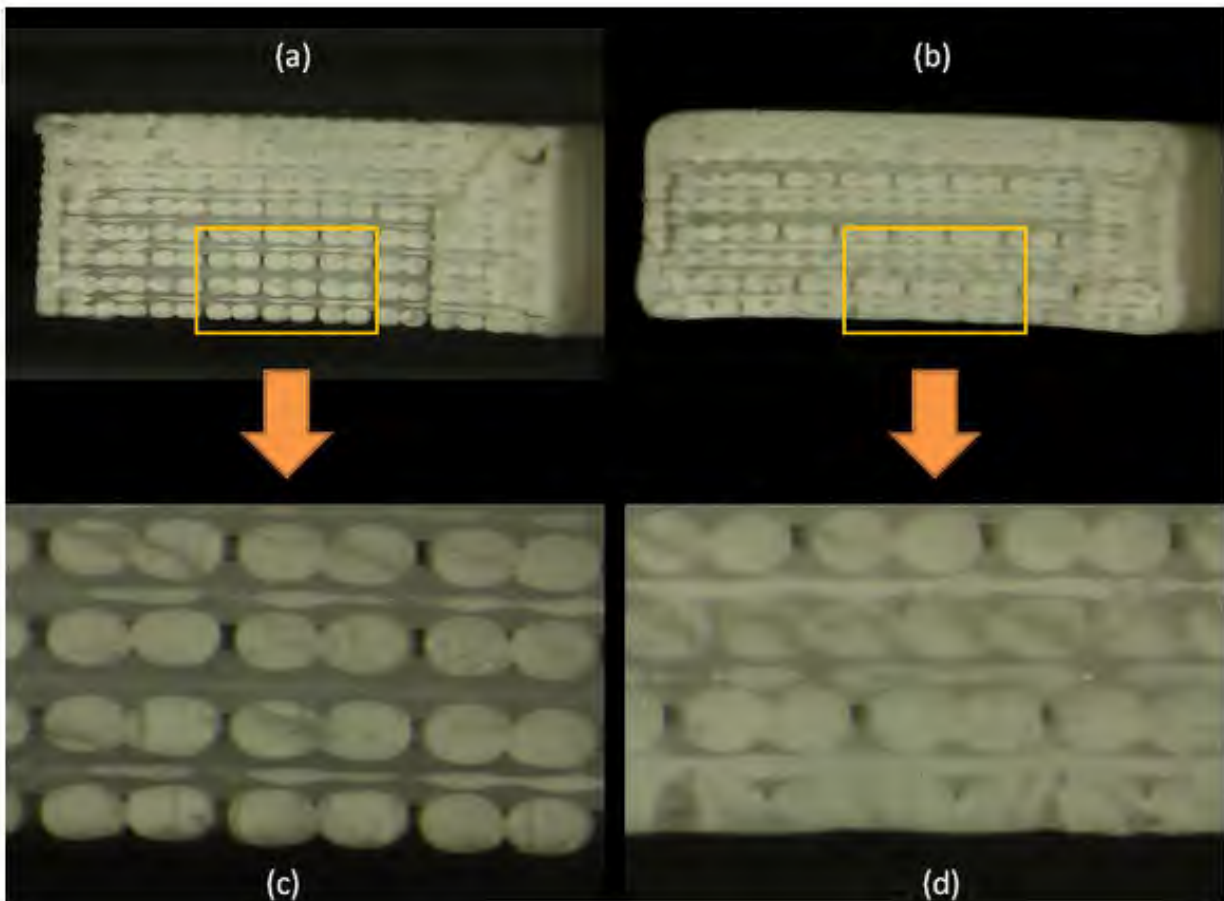
Fig. 4 Microscopic image of cross section of printed parts before and after acetone bath process ((a) and (c): before the process, (b) and (d): after the process) [19]

2.2.1.2 Stereolithography (SLA)

Stereolithography was patented in 1986 by Hull [28] and the first commercially employed AM technique. Since then other techniques have been invented. The process to print a 3D part by applying SLA technique is by using the controlled ultraviolet (UV) light projector to polymerize the liquid resin in the storage tank (Fig. 4), which results in a patterned layer of polymerized resin. The resins used are normally photoesthetic polymer, such as acrylic and epoxy resins [29]. After the first layer is built on the platform, the platform is moved down, and roller moved over to prepare the second layer. Compared to the FDM process, the main advantages of SLA are higher printing resolution and no nozzle obstruction. The sub-micron resolution of SLA technique has in fact been developed in the laboratory research [30].
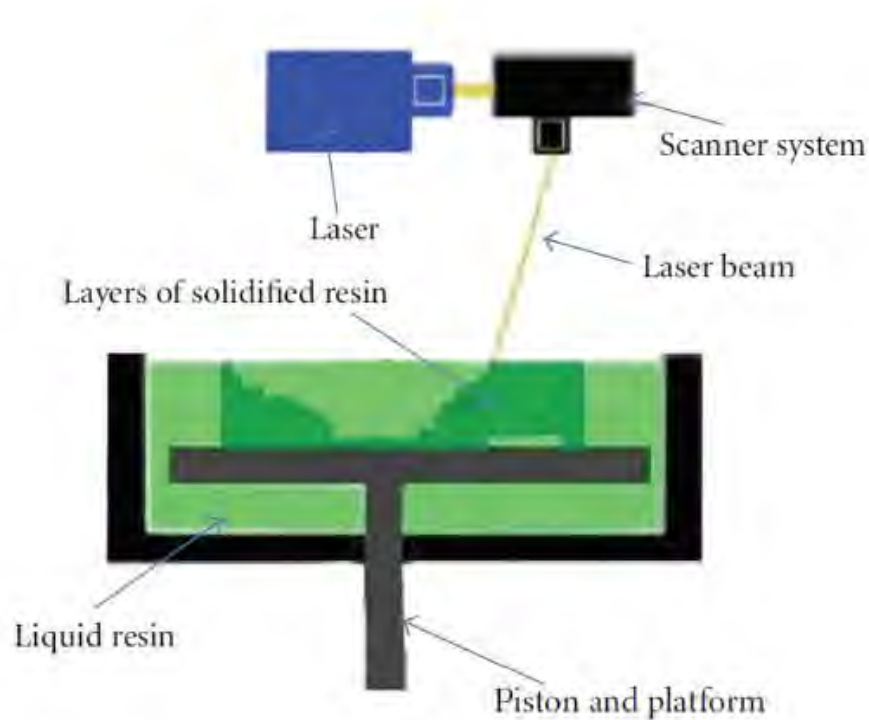
Fig. 5 Schematic diagram of SLA [14]

However, the main issue of this process is its high cost, incomplete material polymerization and limited material employed in SLA process. The thickness of each pattern is the most important parameter of this technique and could be related to many factors, namely, the resolution of printing, power of UV light, printing speed and curing time (exposure time) of photopolymer [31]. The polymerisation process (initiation – propagation - termination) is complicated even though it can be described and analysed mathematically. Moreover, the trend of photopolymers employed currently is multi-monomer, such the polymerisation of different monomers may vary, resulting in further complicated transition [32]. Another limitation of SLA technology is its single resin processing at one time. Several studies tried to break through the bottleneck, but the result has not been optimistic. In short, the SLA process was too complicated, and more procedures were added in printing each individual layer [33,34]. The technical bottleneck of multiple polymers printing is difficult to replace polymer reservoirs by automated procedures. Continuous liquid interface production (CLIP) was invented as a next generation of SLA technology, the production time of CLIP can be up to 100 times faster than the SLA [35]. The continuous printing is achieved by an oxygen permeable membrane placed between optical window and liquid resin, the polymerization is inhibited by the oxygen penetrated through the membrane layer. Moreover, the continuous printed photopolymer also

eliminates the existence of 'layers' in other additive manufacturing processes: staircase effect and anisotropy property [36].

The application of SLA currently mainly remains in biomedical fields due to the highest printing resolution and versatile, but the clinical application is also limited as the biocompatibility, the presence of photoinitiators which act as a cross-linker of resin polymerization. The excessed photoinitiator will lead to a cytotoxicity [37], the versatility of SLA process also leads to popular studies of ceramic reinforced composites. Along with an increase in the content of ceramic particles (e.g. hydroxyapatite or alumina), which has been reported up to 53 wt% [38,39], the viscosity of such composite in the storage tank is a major research subject. Naturally the diameter of ceramic particles should be smaller than the thickness of printing layer, a post process is needed to remove the polymeric phase in high temperature curing and ceramic structures should be sintered (1550°C for 3 hrs for example). It must be noted that the grind of final products may also be required to reduce the surface roughness, and this process may also correct a deformation and remove appearance of voids or even cracking [40,41].

Numerous studies have been published for further improvement of the resolution. For instance, Moon and Yang [42] applied two or even more light sources to build a multi-interference pattern. Various light intensities are achieved by light wave superposition. This approach provides faster and more accurate polymerisation which can be widely employed in nanostructure printing. However, one disadvantage of this process is limited amount of patterns. Another possible technique in SLA is called two-photon polymerisation; two photons with relatively low intensity are simultaneously applied to produce just enough energy to break the labile bonding and generate photo-polymerisation procedures. Compared with other single photon SLA process, a non-linear optical process is provided by two-photon polymerisation process other than linear polymerisation, which can result in a superior precise polymerisation and higher process resolution. A study reported that a 200 nm resolution SLA process can be achieved [43]. It is apparent that SLA process is more suitable for application where is less sensitive to cost control, relatively small size and high resolution and surface quality.

Polymerization of SLA process is partly incomplete and will cause a weak mechanical performance without any further processing. Zguris [44] suggested that a UV post cure chamber for SLA printed parts, the curing should take at least 30 mins under an elevated temperature (60°C). The result shows that when the wavelength was 405 nm, an optimizing

improvement in mechanical performance was achieved. The anisotropy of SLA parts can also be reduced by similar post process reported by Salmoria et al. [45] which is due to the enhanced cross-linking of resins introduced to a more homogeneous stress distribution. However the layer interface area is still normally the inducement of stress concentration.

2.2.1.3 Polyjet

Polyjet is an AM which seems to combine the FDM and SLA process, the droplet-size liquid photopolymer resin is dispensed by multi-nozzle of a printer to form a thin layer of pattern and the UV light cures the resin afterward. The platform will then move down to print second layer of material. The resolution of this technique could reach 16μm [46] and due to multi-nozzle applied, various colours of objects can be fabricated. The mechanical properties of parts built by this process are normally lower than other techniques, such as stereolithography and selective laser sintering [14]. Unlike other AM processes having poor accuracy in Z-axis, Polyjet gives super Z-resolution [47], which is better than X-Y printing resolution (600 dpi). The multi-materials application of Polyjet also enables designers to setup an actuated mechanism without post processes or assembly [48].

2.2.2 Solid based AM in composites

2.2.2.1 Laminated object manufacturing (LOM)

Laminated object manufacturing (LOM) was developed in 1988 by Feygin and Pak [49]. LOM is a technique which feeds the adhesive-coated thin film material and integrates cutting and laminating processes to build the objects. The adhesive-coated film bonded together between layers and a laser beam employed to cut the film to the designed pattern. The film sequentially covers the previous layer, then the second cross section pattern is cut and laminated. Due to the film sheet is applied as a raw material in LOM process, a wide range of materials can be employed, such as polymers, metals, composites and papers. Unlike the SLA process which the material is limited to photopolymers, LOM process is non-toxic and cost of this process is relatively low. Whereas due to the application of laser beam to cut the sheet material, it is difficult to control the cutting depth in Z-axis. It may cause the unsmooth surface and internal cavity of objects. More importantly, due to the cutting process, waste material is generated during this process [50,51].

Kechagias [52] investigated the surface roughness of LOM fabricated parts, it was found that many parameters, such as heater temperature, layer thickness and laser speed, may affect the surface roughness, although the pressure and heater speed were observed less influenced to the

14

surface roughness. Several attempts have been made to fabricate LiO2–ZrO2–SiO2–Al2O3 (LZSA) glass-ceramics by employing LOM process; e.g. Gomes et al. [53]exhibited a LZSA sample with high flexural strength which is comparable to LZSA bodies fabricated by injection moulding, extrusion or roll pressing [54]. When comparing LOM with these conventional processes mentioned above, LOM offers adequate mechanical performance of the fabricated parts and possibility to produce parts with relatively complicated 3D geometry [53,55].

2.2.3 Powder based AM in composites

2.2.3.1 Selective laser sintering (SLS)

Following the release of LOM technique, another free-forming technique, called SLS, was patented. It is a similar process with SLA, but liquid photopolymer is replaced by powder raw materials. Instead of using laser beam to polymerize the photopolymer to bind materials together, a high-power laser is employed to fuse the powder. During the process, the powder is heated to the temperature just below its melting point to minimize the deviation during the sintering. The piston-controlled platform moves downward and then the second layer is patterned subsequently on the powder bed. This process does not need any support structure as the powder bed is able to maintain the structure of the printing part during printing process. This technique is also suitable for a wide range of materials, including composite, metal, polymer and hybrid materials, moreover, the part manufactured by this process shows almost the same mechanical properties as mould casting parts [54]. Nevertheless, the surface finishing of this process is not as good as SLA process and the material switch in the process is difficult [34,56].

Two main factors, which affect the density and flowability of powder bed, are morphology and powder granulometry [57]. Therefore, a specific range of powder size should be defined for SLS and spherical particles should be applied in this process. Commercially, the size distribution of around 60μm is suitable for SLS process and a very limited scope is available for fine particles with a diameter below 10μm [58]. An agent such as silica which offers higher powder flowability can also be added [56,59].

One principle of the materials applied in SLS process is that the process temperature should be lower than the melting temperature of the particles. Shrinkage and curling may happen if the particle melting occurs prior to binding. The increase in temperature of surrounding powder close to the particles should be minimized [56]. It is apparent that the desirable processing temperature of SLS should range between particle crystallization and melting temperature. It

must be noted that in SLS process, the laser sinters the surface of particles and partially melts the material, which may cause an insufficient crystallization of particle and induce various mechanisms [56,60]. From the above, the temperature control in powder bed is a critical factor in SLS process. To minimize the oxidation of the printed objects, a vacuum chamber which is filled with nitrogen or argon is applied. [61,62].

Significant development of SLS process has taken place in recent years. For instance, an advanced technology called selective laser melting (SLM) is developed. Unlike the partial melting of particle in SLS process, a highly controlled laser power is applied to complete melting particles for SLM technology [63]. Fusion of metal powder by using laser beam is the principle of this technology. Amorphous polymers like polycarbonate (PC) are also suitable for SLM process due to no shrinkage issue encountered [64]. The resolution of SLM technology is significantly high, but the layer thickness is limited to 20µm due to a higher porosity observed when further increase of layer thickness is taken [56]. The SLS/SLM technology currently has various commercial providers in biomedical field and been proven to facilitate the quality of surgical procedures. Further potential applications should be developed, and the cost, material and process time can be further optimized.

Like the FDM process, the surface finishing of the parts built by SLS also have staircase effect. The polymer parts like Nylon can be improved by commercial media tumblers or vibro machine [65], a smooth surface can be achieved with a relatively high efficiency production rate. But some detailed feature or geometries could be damaged by this post process. Other surface post processes for SLS fabricated parts like spray painting and can also be applied to compensate the poor surface finishing [65]. Heating post process of SLS Nylon parts was studied by Zarringhalam and Hopkinson [66], the impact and tensile properties had the best improvement when the post-sintering temperature is close to the melt temperature of polymer. But the few disadvantages like geometry distortion and loss of ductility.

2.2.3.2 Laser engineered net shaping (LENS)

LENS is an AM technology, which allows to fabricate a wide range of metal composites/alloys, including stainless steel, nickel-based alloys, titanium alloys, aluminium alloys, tooling steel, copper alloys. Similar to FDM process, LENS applies laser beam which has strong power to melt metal powder, then the molten metal is jet to a designed location. This technology is widely employed to repair parts like wind turbine blade or other repair work which other

technologies are difficult to finish. Uneven melting and cooling may happen during this process, which could result in a residual stress [14].

2.2.4 Hybrid of powder-liquid AM in composites

2.2.4.1 Three dimensional printing (3DP)

3DP is an AM process combining the liquid binder with powder base. The liquid binder is selectively dropped on a powder bed to form a solid pattern for one lamination. Similar with SLS process, a large variety of suitable materials applied in this technique (polymer, metal, ceramic and composite) and further combinations of powder-binder are potentially possible.

The combination of powder and binder is the key in 3DP technology and its post-process [67]. Deposit-ability is critical in powder properties and depends on the size and shape of the particles. The effects of particle size can be summarised in Table 2. Compared with the effect of particle size, the shape of the particle has less impact on the process. Nevertheless, spherical powders are preferable due to better fluidity and low friction among particles [68,69]. Due to the liquid binder and post processes needed, the porosity of parts is normally higher than the other techniques [67], but multi-size powder can provide the benefits from both small and large size powders, which means that the dry state process and small particles can fill the pores generated by large particles, leading to a higher density of powder tank, for example, an increase from 59% to 73% when 31% volume of fine copper particle added into coarse bronze powder tank [70].

Table 2 Impact of particle size on 3DP process

Particle Size	Advantages	Disadvantages	References
>20 µm	Dry state deposition, large pores among powder, tend to fluidity	Poor surface finish and layer thickness	[71,72]
<5 µm	Higher surface quality and smaller thickness of layers, better sintering quality	Trend to clustering by van der Waal's and moisture, more impact from droplet, slurry deposition may be required	[73,74]

A number of binding methodologies are reported applicable to 3DP and each has different traits, which has been reviewed and summarised in Table 3. It can be seen that organic liquid binder approach is a commonly used methodology, such as polymeric resins and various polyvinyl [72]. However, the liquid may dry in the printing orifice, causing clogging, although this can

be avoided by modifying the rheological properties of liquids [75]. In-bed adhesive binding method, like maltodextrin and sucrose, is another commonly used approach in lieu of its advantages [76,77]. Similar with organic binders, the material applied in the adhesive binding is not specific and this binding is thermally degradable to leave little residual stress. Unlike organic liquid binder, in-bed adhesives have normally a low viscosity, which could lead to a better filling to the pores among particles and a higher bonding strength. Low hygroscopicity of in-bed adhesive binder offers a low moisture absorption from surroundings [76]. Nevertheless, the available particles applied in this binding approach is limited from 10 to 40µm [78].

Hydration-based system is another binding methodology, which is able to bind bulk materials in wet condition. This approach is relatively inexpensive but catalyst may be needed to modify setting processes [78]. Acid-based system binding is relied on the interaction between two components and the binding process can either be initiated by depositing one component as liquid binder into the powder bed, which containing other component, or print a binder as the solvent into the powder bed, which has both components. Similar to organic liquid binding and in-bed adhesive binding, this binding has large scope for material selection and produces little residual stress during thermal effects [79]. In addition, acid-based system is also available applied as a co-binding process [78].

Inorganic binders are normally silicate based like colloidal silica due to easy application [69]. Due to silica solutions are normally acidic, a neutralization reaction occurs when depositing silica solutions to the colloid gels bed, the pH drops and CO_2 produced [80]. Colloidal silica can also contribute to final strength after deposition process [69].

Solvent deposition binding is suitable for polymer powder such as chloroform can be employed to bond bio-based polymers like polyurethanes [81]. A stronger binding can also be achieved by applying multi-solvents and warping risk can be decreased by adding vapour pressure solvents [68]. Moreover, due to solvent evaporate after deposition process, the purity of final part is significantly high and also can leave little residual stress.

Phase-changing binding is an approach which is a low melting binder deposited to a heated powder bed, the melted binder can penetrate into powder and the powder solidifies after printing and cooling to room temperature. It can be applied with most of powders, but they also limit the potential high-temperature post process of printed parts [73]. The last binding approach is to control sintering by different materials deposition, such as applying a sintering inhibitor,

the heat-reflective materials or chemical oxidizers is selectively deposited into a heated powder bed, leading to selective inhibition [82]. A drawback of this approach is that the sintering inhibitor may result in excess powder sintering and hence even the whole powder bed may be contaminated.

The flexibility of material combinations can significantly enhance the potential of 3DP technology. The improvement of part performance and new materials can be obtained by studying the refinement of material combinations.

Table 3 Advantages and disadvantages of various binding approaches

Binding approach name	Advantages	Disadvantages	References
Organic liquid binder	Not material specific; Can be thermally decomposed and little residue produced	Clogging may be occurred; May fail under high temperature	[67,72,75]
In-bed adhesive binder	Highly soluble and low viscosity; Low hygroscopicity; High bonding strength; Not material specific; Can be thermally decomposed and little residue produced	Difficult to be applied in small particle bed	[76-78]
Hydration-based system binding	High printing reliability; Easy to apply; Inexpensive price	Catalyst needed; limited material employed	[67,78]
Acid-based binder	Strong bonding approach; Can be combined with other binding approaches;		[78,79]
Inorganic binder	Heat the bed after printing	Cannot bind the powder quickly	[69,80]
Solvent binding	Multi-solvent binder result a strong binding; High purity of final parts; Leave little residue		[68,81]
Phase-changing binding	Not material specific; Suitable for secondary bonding	Limit the post-processing temperature	[69]
Sintering control binding	Benefit of only part boundaries deposition is required	Excess powder may be sintered or contaminated during printing	[82]

Since the 3DP technology has similar powder bed system, which is similar with the SLS process, post-sintering is the most common process to improve the performance of printed parts. Effects of post-sintering are also similar, Butscher et al. [83] pointed out the voids are

eliminated after the post-sintering. Geometry distortion during the process is inevitable. Another solution to remove the voids is to generate a second material phase by infiltrate another material into the printed parts. The infiltrant can be melt and penetrate to fill the voids without affecting the bulk material, but the heterogeneity of combined part may also happen [84]. However, compared with the sintering, an accurate and controllable geometry finish can be achieved and when applying an infiltrant with decent mechanical performance like epoxy, the mechanical performance of overall part will be improved [85].
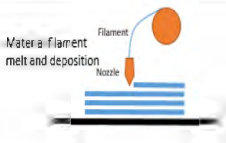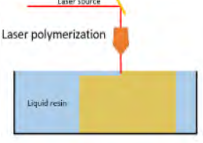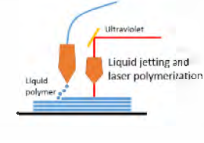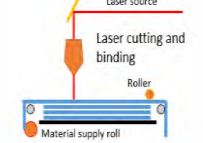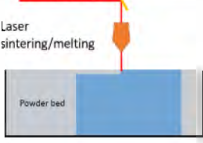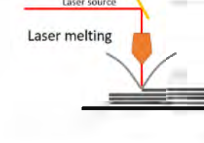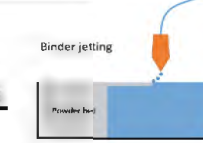
2.2.4.2 Prometal

Prometal is a three-dimensional printing process to build injection tools and dies. This is a powder-based process similar with 3DP process in which stainless steel can be applied. The printing process occurs when a liquid binder is spurt out from multi-jets to steel powder. The powder is located in a powder bed that lowers the bed when each layer is finished. A feed piston supplies the material for each layer. After finishing, the residual powder must be removed. When building a mould no post-processing is required [28,51]. If a functional part is being built, the sintering, infiltration and finishing processes may be required. In the sintering process, the part is heated to 350°F for 24hrs, hardening and fusing the binder with the steel in a 60% porous specimen. In the infiltration process, the piece is infused with bronze powder when they are heated together to more than 2000°F in an alloy of 60% stainless steel and 40% bronze [14]. Prometal offers production printer which has significantly bigger printing volume (3.696L) than other techniques and also integrate powder mixer and multiple printing area which can implement two operations simultaneously [86,87].

Research and innovation of AM technologies continue, the new technologies are developed in responding to more requirements from different directions, such as new materials, higher surface roughness, better mechanical performance and higher geometrical complexity. Table 4 summarizes main factors and properties of the technologies discussed above for an ease of future references. The brief schematic for individual technologies is also given and the main physical effects during process and power source applied are presented. It can be concluded that the FDM process currently is most widely applied AM technology due to its lowest cost and simple machine setup, but the dimensional accuracy and anisotropic properties limit its wide applications where require isotropic mechanical properties and intricate geometry. The printing resolution can be enhanced by using smaller nozzle like 0.25mm (commonly 0.4mm) [88], but that will result in a less deposited material then longer building time. SLA process is limited employed in such as visual prototype fabrication due to the ultra-high resolution and

surface finish. Specific material and relatively poor mechanical performance also confine this technology to non-functional application. For the technologies using the powder or liquid bed as printing materials, multi-colour or multi-material printing is normally difficult to realize. When applying metals as the printing materials, binder jetting technologies, such as Prometal, can considerably reduce the energy consumption compared to laser processes [89]. Composite is more popular in AM to compensate the downside of the process, almost all technologies can realize powder reinforced composite printing. SLS and 3DP can be applied to fabricate short fibre composite, but the fibre length is exceedingly limited to one layer thickness. Only FDM and LOM process can print long fibre composite although the fibre orientation is fixed horizontal.

Table 4 Comparison of AM technologies [8,11,12,14,43,46,47,86,90-94]

Liquid based			*Solid based*	*Powder based*		*Hybrid of powder-liquid*	
Process schematic							
Technology							
Fused Deposition Modelling (FDM)	Stereolithography (SLA)	Polyjet	Laminated Object Manufacturing (LOM)	Selective Laser Sintering (SLS), Selective Laser Melting (SLM)	Laser engineered net shaping (LENS)	Three dimensional printing (3DP)	Prometal
Principal mechanism							
Melting	Photo-polymerization	Photo-polymerization, liquid deposition	Adhesive binding	Sintering	Melting	Adhesive binding	Adhesive binding and sintering
Power source							
Thermal energy	Ultraviolet laser	Ultraviolet laser, thermal energy	Laser beam	Laser beam	Laser beam	Thermal energy	Thermal energy
Highest resolution							
50 µm	200 nm	16 µm	112 µm	25 µm (SLM)	30 µm	50 µm	100 µm
Reinforcement							
Powder, short fibre, long fibre	Powder	Unknown	Powder, short fibre, long fibre	Powder, short fibre	Powder	Powder, short fibre	Powder
Strengths							

Inexpensive, multi-material printing, no post-process.	High resolution and surface finish, no nozzle clogging, high printing speed, no support structure.	High printing speed, high resolution multi-material printing.	Wide material selections, available to print long fibre composite.	Wide material selections, high mechanical performance, no need support structure	In-site application, suitable for repair damaged part.	Wide material selections, no support structure, multi-binding combinations.	Multi-binding combinations, no support structure.

Drawbacks

Limited surface finish, low printing resolution, Clogging issue.	Limited material applied, poor mechanical performance, cost high	Limited material applied, poor mechanical performance, post-process may need. High cost	Low resolution, material waste.	Insufficient sintering (melting), shrinkage or curling.	Post-process required, uneven melting	High porosity, post-process required.	High porosity, post-process required.

2.3 Polymeric materials selection in AM

Research in polymeric materials for AM is enormous, including synthetic and bio-based polymers. The difference between synthetic and bio-based polymers is defined by analysing their polymerisation process, the former is fabricated through chemical polymerisation and the latter is made by biological processes [95]. Both categories of polymers consist of thermoplastic and thermosetting materials respectively. There are also two types of thermoplastics called amorphous and semi-crystalline thermoplastics. Amorphous thermoplastics have no certain molecular orders after cooled, the molecular structures are randomly distributed. Semi-crystalline thermoplastics have a certain molecular structure after solidified, which means there is a certain glass transition temperature in semi-crystalline thermoplastics. The difference of thermoplastics and thermosets is mainly in molecules. Some of the large molecules in thermoplastics are not crosslinked with each other, then the molecules are freely moveable relatively to neighbours. In contrast, the molecules of thermosets are crosslinked or connected with others. This difference decides the preference of the polymers for AM application, as the heating process may make the molecules in thermoplastics moving freely, but those in thermoset broken chemically. Even though the physical properties of thermosetting materials due to the crosslinking are commonly high in stiffness, its difficult manufacturing process limits the applications in AM.

2.3.1 Synthetic polymeric materials in AM

The synthetic polymeric materials have been employed in various AM technologies as both commercial and research levels for decades. The features, mechanical performance and other properties of commonly used synthetic polymers have been reviewed as follows and a comparison of printing properties of each applied synthetic polymeric materials in AM can be summarised in Table 5.

Table 5 Printing parameters and properties of synthetic polymers in AM [88,96-101]

Properties	Unit	ABS	PA (Nylon)	PP	PC	PET	PEEK
Printing temperature	°C	230-250	250	165	270-310	200-240	370-410
Print bed temperature	°C	80-110	70-100	Room temperature	90-110	50-75	120-150
Density	g/m3	1.04	1.1 – 1.4	0.9 – 1.06	1.15	1.36	1.32
Tensile strength	MPa	38	60-100	20 – 40	65	75	60-80
Tensile modulus	GPa	2.2	2.5	3.5 – 6.0	2.8	3	
Elongation at break	%	8	60-300	150	100	70	
Printing technology		FDM, SLA, 3DP	FDM, SLS	FDM, SLS	FDM, SLS	FDM	FDM, SLS

2.3.1.1 Acrylonitrile-butadiene-styrene (ABS)

ABS is a petroleum-based polymer and has been widely used as an engineering plastic in many industries and recently for AM. ABS is a polymer which is polymerized by styrene and acrylonitrile in the presence of polybutadiene. The proportion of styrene and acrylonitrile can be varied which result in different properties. The impact resistance and toughness are two main mechanical properties of ABS, and an increase in polybutadiene proportion can lead to an improvement in impact resistance. Compared to similar nylon and acetal, the lower cost of ABS is a significantly advantage, but some chlorinated solvents, such as esters, ketones, acids and alkalis may corrode ABS [102].

ABS has a superior thermo-resistance and mechanical performance, these make it attractive as printing filaments material for AM and various AM technologies can be employed to fabricate ABS polymer, such as FDM, SLA and 3DP [102-104]. The printing temperature of ABS in FDM process is advised from 220 to 250°C and a heated platform (50 to 100°C) is also required to minimize the bending and warping of printed ABS filaments [105]. AM printed ABS products are in general with high quality; the surface of FDM printed ABS part is glossy and ABS can

be easily dyed, making ABS popular as a commercial 3D printing material. However, toxic substance, such as butadiene, acrylonitrile and styrene may be produced if overheated (around 400°C) due to the decomposition taking place [96]. Therefore, a ventilation is needed due to unpleasant fumes released during printing and a long-term outdoor application of ABS parts should be avoid due to relatively poor UV resistance of ABS [97].

Acrylonitrile styrene acrylate (ASA) was developed by BASF in the 1970's as an alternative to ABS with several advantages, recently associated with AM. ASA is similar to ABS structurally, instead of polybutadiene rubber, poly (alkyl acrylate) is grafted with poly (styrene-acrylonitrile) [98]. Compared with double bonds of polybutadiene, which is prone to oxidation and ultraviolet (UV), the poly (alkyl acrylate) is considerably superior in the heat, weathering, chemical and ultraviolet radiation resistance [98,99]. In addition, due to the lower glass transition temperature of ASA (-65°C), low-temperature applications can be developed [98].

The production of ASA is relatively low due to limited manufacturers, so the cost of ASA is remaining high. Copolymers which combine ASA and other polymers such as ABS or PVC can be co-extruded to reduce the cost. When apply ASA in FDM process, the nozzle temperature is almost same as ABS, but the viscosity of melt ASA filaments is higher than that of ABS and the printing clogging may happen during printing. ASA shows a minimised shrinkage in FDM process, so an impressive geometric complexity can be achieved in 3D printed ASA parts [105].

2.3.1.2 Polyamides (Nylon) (PA)

PA is considered suitable for AM production. PA is a series of synthetic polymeric materials which were in early date applied to replace the natural silks. PA has very high tensile strength which earns it a reputation as engineering plastics, several properties of PA are superior to light metal alloys [102]. PA has been used as engineering plastics, such as, small gears and bearings with good mechanical performance and chemical, UV resistance. Fibre reinforced PA composites are also widely applied to further enhance the mechanical performance. Similar with ABS and PLA, PA also absorbs moisture from atmosphere, resulting in an increase in volume. In FDM process, the printing temperature of PA filaments is very high, around 250°C, and the heated printing bed is also required to facilitate the adhesion of deposited PA filaments [105]. The shrinkage and warping of FDM printed PA often takes place. Li et al. [106] found that the FDM PA12 parts have significantly higher interface bonding performance than ABS benchmarks and also when the printing orientation was +45°/-45°, the FDM printed parts have

almost same UTS (Ultimate Tensile Strength) compared with specimens made by injection molding. Lederle et al. [107] employed nitrogen atmosphere as an inert printing environment to improve the printing results, the Nylon specimens achieved 30% improvement compare with common printing chamber, but further works like shrinkage measurements and water/oxygen contents analysis need to be implemented. Rahim [108] suggested a slower cooling rate during the PA and its composite printing process since less residual stress can be reached. This found matched with the inert gas printing atmosphere as a low cooling rate of the printed filament and this method also has potential application in other polymer and composite printing progress.

2.3.1.3 Polypropylene (PP)

PP is another potential polymer for AM. PP is produced by the polymerization of propylene and a semi-crystalline thermoplastic polymer with relatively low density (0.9-1.06g/m3). The application of PP is continuously expanding due to more grades of PP being developed by applying new catalysts, modified molecular or copolymers. The development of PP creates an opportunity to replace the polymers with higher cost such as PS, PC or TPE [95].

A remarkable property of PP is that the available range of molecular weight, crystallinity, spherulite structure is significantly wide, therefore, the property of different PP varies considerably. Nonetheless, the glass transition temperature of PP is 0°C and the shrinkage coefficient of PP homopolymer is relatively high, that limits the impact resistance at sub-zero temperatures, although this limitation can be surmounted by using copolymerization process (such as copolymerize with ethylene) or applying as fibre reinforcement composites (such as glass fibres reinforced PP composites) [100].

A wide range of properties available leads to massive applications for PP, such as packaging, adhesives, automobile insulation materials, furniture and household appliances. PP is still an emerging polymer in AM. Due to the relatively low melting temperature, the AM printing temperature of PP is around 165°C and heated printing bed is not necessary in FDM process [100]. The electrical insulating property of PP also limits the solubility during the dyeing process of filaments and static charges may be generated during printing, which can attract dust from the surrounding environment to the printed surface [105].

2.3.1.4 Polycarbonate (PC)

PC is also an ideal polymer for FDM process due to the high performance and AM PC is able to compensate the mechanical properties loss in the printing process. PC is an amorphous thermoplastic material, and the appearance of pure PC is crystal clear with high surface gloss.

It is also available for dyeing to any colours. In addition to the outstanding mechanical performance, the range of working temperature of PC is extremely wide, ranging from -150°C to 135°C. PC also offers the resistance of high-energy radiation [95].

Therefore, the nozzle temperature can be relatively high (270-310°C) and the printing bed temperature is also high (90-110°C) for the prevention of warping [105]. In AM, PC-ABS blend is more often applied as this blend integrates the advantages from both PC and ABS, producing superior performance of combining high heat resistance, impact strength and tensile properties of PC with good flexural strength and various surface appeal of ABS [102]. Meanwhile, the biocompatibility of PC can be achieved by modification process, for instance, PC ISO (ISO-1099-3 compliant) is biocompatible and an alternative for biomedical, pharmaceutical and food packaging fields with higher mechanical performance than AM printed ABS, i.e. being 33% and 59% higher in tensile and flexural strength respectively comparing the former with the latter [97,102].

PC is widely applied in many industrial sectors, where relatively thermal performance is required, such as insulation layer in the automobile hoods, hot water containers and housing of various lights due to its high working temperature. Helmets, automobile window glazing, and window panels can also be made by PC due to its high mechanical performance. Moreover, due to the optical clarity property, PC is being tried to take advantages in lighting projects or like screens. There are several disadvantages of PC, such as the chemical resistance is restricted by alkaline solutions and hydrocarbon solvents, susceptible to the stress cracking and high penetrability of CO_2 [87,94].

2.3.1.5 Polyethylene terephthalate (PET)

Polyethylene terephthalate (PET) currently is one of the most applied thermoplastic polymer in the world with numerous applications, such as water bottles, clothing fibres and even engineering glass fibre reinforced PET composites. PET can be synthesized into amorphous or semi-crystalline polymer depending on the polymerization processes. The amorphous PET is transparent and semi-crystalline polymer may appear opaque or white depending on the degree of polymerization. The semi-crystalline PET has slightly higher hardness, stiffness and heat resistance than amorphous one [95]. The overall properties of PET are outstanding, the tensile strength is around 75 MPa which is significantly high in thermoplastic, other mechanical properties, such as hardness, stiffness, surface quality, chemical resistance and dimensional stabilities are also relatively high [99,102], except net resistant to alkalis, esters, oxidizing acids

and chlorinated hydrocarbons [95]. The range of serving temperature is from -40 to 100°C, which is suitable for various applications.

The application of PET in AM is recently commercially available. The printing parameters and properties of PET are in the middle of PLA and ABS filaments; the printing temperature is slightly lower than ABS (200-240°C) and normally higher than PLA deposition (180-220°C) [88,101]. The heated printing platform is needed with mild temperature (50-75°C) [88]. Compared with printed PLA filaments, PET has better mechanical performance and durability (Table 3), PET is also easier to deposit than ABS filaments due to lower temperature needed and better viscosity in melt state (0.60-1.00 dl/g) [102]. Based on the viscosity property, the adhesion, shrinkage and warping of PET filaments are minimal. Nevertheless, during PET printing process, the temperature control is a critical procedure due to unstable printing temperature may result in different surface appearance of final parts and overheating of PET can also lead to brittleness. There is derivative polymer of PET called PETG, which is modified by glycol, popular in AM recently. There are several advantages of PETG than conventional PET; the PETG can remain its properties in high temperature without brittleness and the appearance of PETG is clearer than that of PET. However, the ultraviolet resistance of PETG is relatively poor [104,105].

In summary, the AM printing temperature is lowest for PP and highest for PA and ABS, so is the required bed temperature (Table 5). Although the tensile strength of the AM products seems to follow the trend of their density, which is the lowest for PP and highest for PET, the tensile modules behave differently (Table 5). Elongation is another interesting property, which is highest for PP products, but lowest for AM ABS.

2.3.1.6 Poly-ether-ether-ketone (PEEK)

As one of the most outstanding end-use semicrystalline engineering polymers, PEEK in additive manufacturing is one of the most popular sub-topic in AM industry. The magnificent properties like mechanical performance, lightweight, high temperature and chemical resistance of PEEK attract engineers and researchers from automobile, aerospace and biomedical industries. In 2007, AM fabricated PEEK was announced by Schmidt et al. [109] by the SLS process and then EOS released a commercial PEEK SLS printer [110]. But the application of SLS printed PEEK is widely limited since the cost of SLS producer. With the development of AM technologies, FDM process with higher processing temperature is applied to print PEEK filament become a solution to the AM fabricated PEEK. However, there are still plenty of

challenges for PEEK printing due to its high processing temperature, extrusion swelling and semicrystalline properties [111,112].

The current common printing nozzle temperature of PEEK is 370 to 410 °C and a high temperature heated bed is necessary (120-150 °C) in FDM process [113]. Yang et al. [114] studied the effects of various processing parameters to the crystallinity and mechanical performance of printed PEEK, the crystallinity of printed PEEK is increased from 17% to 31% with the ambient temperature grows from 25-200°C, however the effect to mechanical performance is still unknown. The post-process of PEEK printing is also evaluated and the furnace cooling and annealing process could result in a higher crystallinity (36% and 38% respectively) [114]. From recent study, Wang et al. [115] give an optimizing printing parameter for PEEK, a 440 °C nozzle temperature, 20 mm/s printing speed and 0.1 mm layer thickness were suggested. A greater heat unit to ensure a proper melt of PEEK filament is also employed, but the printing chamber temperature which is supposed to act as an important role in PEEK printing hasn't been disclosed. Another work from Deng et al. [116] applied lower printing temperature and higher speed (370°C and 60 mm/s), the results showed an unsatisfactory maximum tensile strength of 40 MPa when the infill rate was 40%. Plenty further studies are highly required in PEEK printing and optimize detailed printing features and mechanical performance to enhance the application range of 3D printed PEEK.

2.3.2 Bio-based polymeric materials in AM

In common with the popularity of bio-based polymers over traditional polymers, AM in the production of bio-based polymers becomes more and more attractive in both research community and commercial industrial sectors. The bio-based polymers can be classified either by the degradation methods or the basic origins. Based on the degradation method, the bio-based polymers can be divided into hydrolytically degradable polymers and enzymatically degradable polymers [117]. A number of biopolymers currently employed in AM are discussed in the following sections.

2.3.2.1 Polylactide or polylactic acid (PLA)

PLA was firstly introduced in 1932 [118], but its application is restricted in medical industry due to limited production. The breakthrough of production in the late 1980s dwindled the cost and extended the applications of PLA, and currently wide commercial market and mass production earn itself as the substitution of petro-chemical polymers with a few of modifications [119]. The PLA and ABS (Acrylonitrile Butadiene Styrene) are currently two

materials used in commercial FDM 3-D printing technology [88]. PLA is typically used in medical field, food packaging and film or sheet appliance, it can be employed individually or as a copolymer with other synthetic or biopolymer [101]. When applying PLA in FDM process, PLA is easily malleable when heated, which is suitable for the extrusion process of filaments. Compared with ABS, PLA printing is commercially favourable due to its low printing conditions; Tm and print temperature for PLA AM are 150-200°C and 180-220°C respectively, while the print temperature for ABS is 210-250°C and, due to the amorphous structure, there is no specific melting temperature of ABS [88,101]. Apart from that, the heated platform in FDM process is not compulsory for AM PLA filaments and no fume is needed during heating and printing process for the commercial AM printing of PLA. However, PLA is suffered from occasionally clog or jam in orifice during printing process due to expansion of heated PLA. The storage of PLA should also be concerned due to hygroscopic properties. In medical industry, PLA has been employed as sutures, drug delivery, orthopedic implants from 1970s [101]. It is applied in AM to blend and copolymerise other biodegradable or non-degradable materials in tissue engineering field [120,121].

2.3.2.2 Polyhydroxyalkanoates (PHAs)

PHAs are a series of bio-based polymers which are synthesized by conventional poly-condensation reactions like microbial fermentation [118,122]. Poly(b-hydroxybutyrate) (PHB) is one of the polyesters in this series, which is an attractive and potential bio-based thermoplastic polymer. It's a more environmentally friendly material which can be easily degraded by bacteria in water and CO_2 condition [123]. Two main drawbacks of PHA and PHB is their brittleness and poor thermal stability (degradation under 250°C) [118,124,125]. Poly(3-hydroxybutyrate-co-3-hydroxyvalerate) (PHBV), which is the copolymer of hydroxyalkanoate (HA) and 3-hydroxybutyrate (3HB) units, is synthesized by Monsanto as the commercial name Biopol [123]. The PHB and PHBV are applied in automobile oil tank, paper painting materials, packaging materials and films for decades [126,127]. PHAs have also been concerned by researchers in AM, especially in biomedical fields due to its biodegradability and biocompatibility [128-130]. Unlike other materials, PHB can be applied in AM process without blending with other additives. In SLS process, PHB powder is chemical stable after a 32.5-hour process [129,130]. The PHBV has also been formulated with calcium phosphate (Ca-P) to fabricate nanocomposite scaffolds by using SLS process [131]. In addition to the medical applications, AM PHAs for other applications is implemented. For instance, Wu et al. [132] fabricated a green composite which combined PHA with treated palm fibre (TPF) by using

commercial FDM AM printer. Maleic anhydride (MA) was added to increase the adhesion between matrix PHA and TPF. The PHA-g-MA/TPF composite has been proven to have better mechanical properties than pure PHA. Commercial AM PHA composites have also emerged, Adafruit [133] used PLA/PHA copolymers to combine with various materials, such as the recycled bamboo, bronze particle and bronze particle, but the main purpose of these composites is for a better composite appearance.

2.3.2.3 Polyecaprolactone (PCL)

PCL, like PLA, is applicable for AM production. PCL is a partially crystalline biodegradable polymer which is produced by ring-opening polymerization process of crude oil. The physical properties of PCL include good resistance to water, solvent and oil, low melting point (60°C), and low viscosity [118,122]. The mechanical properties of PCL in room temperature are moderate, which is between those of LDPE (low density polyethylene) and HDPE (high density polyethylene) [122]. Conventionally, PCL can be applied to mix with starch to fabricate trash bags. PCL in combination with fibre, such as cellulose or nonwovens, is also applied to make incontinence products, scrub-suits or bandage [118]. PCL, like other biodegradable polymers, has been certified to be a solution in tissue engineering for decade, it is usually employed by copolymers of such as PCL/PLA blend scaffolds, PCL/hydroxyapatite (HA) and PCL/alginate hydrogel [134-137].

2.3.2.4 Polyglycolic acid (PGA)

PGA, like PLA, is another poly(α-hydroxy esters) for possible AM production. PGA has one of the highest melting point in biodegradable polyesters and relative high mechanical properties [101,138]. It has been applied in medical industry as PGA/PLA copolymers since 1970s [139]. However, PGA is less hydrophobic compared with PLA due to PLA has the -CH3 side groups intercalation and poor hydrolysis resistance. These drawbacks lead PGA to copolymer applications [102].

2.4 Reinforced composites in AM

2.4.1 Particle reinforced composites in AM

Currently, one popularity in the development of AM technologies is reinforced composite printing as AM printed pure polymers have in general lower mechanical properties than the products fabricated by cast moulding (CM). The application of AM particle reinforced composite is more popular than that of AM fibre reinforced composites, as the former is easily

to be mixed, has less void, better interfacial binding and low cost. The combination of particles and matrix materials is extensive and current main combinations can be summarised in Table. 6. Reinforced particles are employed depending on the required properties of end products, for example, applying glass beads and iron powders as reinforcement to improve tensile strength and modulus [140,141], the aluminium or aluminium oxide (Al2O3) to enhance the wear resistance property [142], the alumina, ceramics or tungsten particles to boost dielectric permittivity of materials [143-145]. Various AM processes have been employed to fabricate the composites, such as FDM, SLS, SLA and 3DP.

Table 6 Combination of particle reinforced composites

Particle-matrix	AM technology	Targeted property reinforcement	Ref.
Nylon-11/glass beads	SLS	Enhanced tensile strength and modulus	[140]
ABS/Iron, ABS/copper	FDM	enhanced tensile modulus, thermal conductivity	[141,146]
Nylon-6/Al/Al$_2$O$_3$	FDM	Higher wear resistance, lower coefficient of friction	[142]
UV-cured-resin/Alumina	SLA	Enhanced dielectric permittivity	[143]
Acrylate resins/micro-diamond	SLA	Improved heat transfer	[147]
ABS/BaTiO$_3$, ABS/Ba$_{0.64}$Sr$_{0.36}$TiO$_3$, PP/CaTiO$_3$	FDM	Enhanced dielectric permittivity and more controllable resonance frequency	[144]
ABS/BaTiO$_3$	FDM	Enhanced dielectric permittivity and adjustable effective permittivity	[148]
PC/tungsten	FDM	Enhanced dielectric permittivity, Increased storage modulus and impact resistance	[145]
ABS/TiO$_2$	FDM	Increased tensile properties but brittleness	[149]
ABS/TPE	FDM	Decreased anisotropy in different printing orientation samples	[150]

The study on the microstructure of the composites manufactured by AM is crucial to the overall performance of the composite. Khatri et al. [151] developed magnetic functional composite which was the ABS polymer matrix filled by stainless steel powder, the filler content in the composite was up to 40 vol.% and turned out that the composite had improved magnetic

functions but more brittle than pure ABS polymer. Fig. 5 reveals the cross-section microscopic photos of the composites with different filler contents, the distribution of particle powder is appreciably homogeneous but partial uniformities are still inevitable. This could result in porosity and stress concentrations which are also proven by afterward tensile tests, nevertheless, the variations of tensile strength and Young's modulus are not constantly descending which need further study to demonstrate that whether these are system errors. Similarly, Nikzad et al. [141] applied copper and iron powders reinforced ABS binder composites in FDM process which the uniformed powder distribution and decrease of tensile stresses are also reported in iron powder composites. Fig. 6 indicated the iron/ABS composite SEM image, further studies in microstructures are needed regarding the mechanism of incremental composite thermal conductivity. Good homogeneous distributions of particles, good interface of particle-matrix, boundary among printed filaments should be further investigated.

Kokkinis et al. [152] applied low magnetic fields in a multi-nozzle FDM platform which can control the filler particle orientations, the magnetized alumina platelets used as reinforcement and the purpose of this study is to achieve enhanced properties in specific directions. Shemelya et al. [145] fabricated tungsten reinforced polycarbonate composite specimens by FDM technology for x-ray shielding purpose, the filler contents were fabricated incrementally which filling 1wt%, 3wt% and 5wt% (0.1vt%, 0.2vt% and 0.3vt%) of tungsten powder compared with pure PC polymer. Fig. 7 [145] shows the scanning electron microscopy figure of tungsten particles in crack hackle region (a) and craze cracking area (b). The highlights indicate that the fractures tend to propagate around the tungsten particles, but this situation is more like a defect point than a cracking origin due to no shows of characteristic mirror and mist zones in the figure, this implied that the tungsten particles are acted as defects in fracture morphology. The result of composite samples is aggressive with a 10% increment in x-ray shielding (0.3vt% tungsten content) and unharmed electromagnetic properties, mechanical properties of composite are also positive with an increased storage modulus [145].
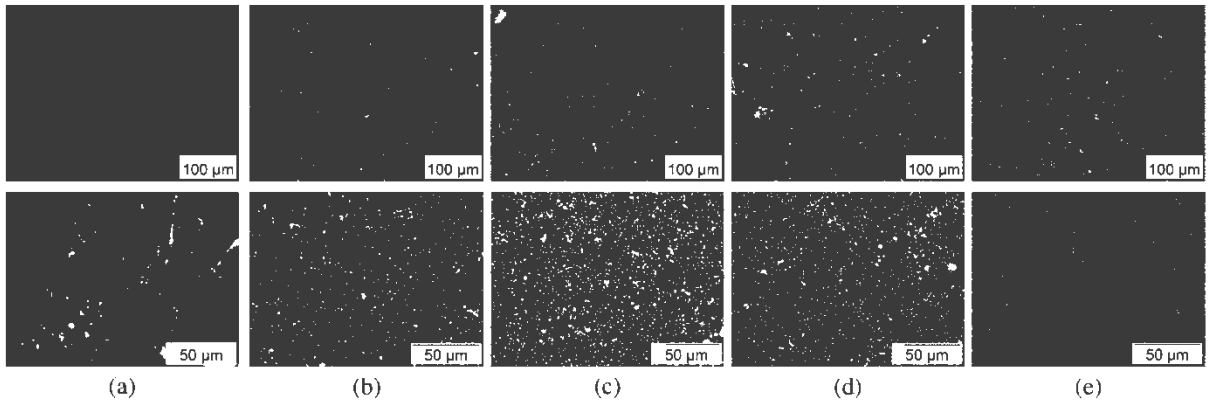
Fig. 6 Cross-section microscopic photos of stainless steel powder reinforced composites ((a) Pure ABS, (b) 10 vol. %, (c) 20 vol. %, (d) 30 vol. %; and (e) 40 vol. %.)
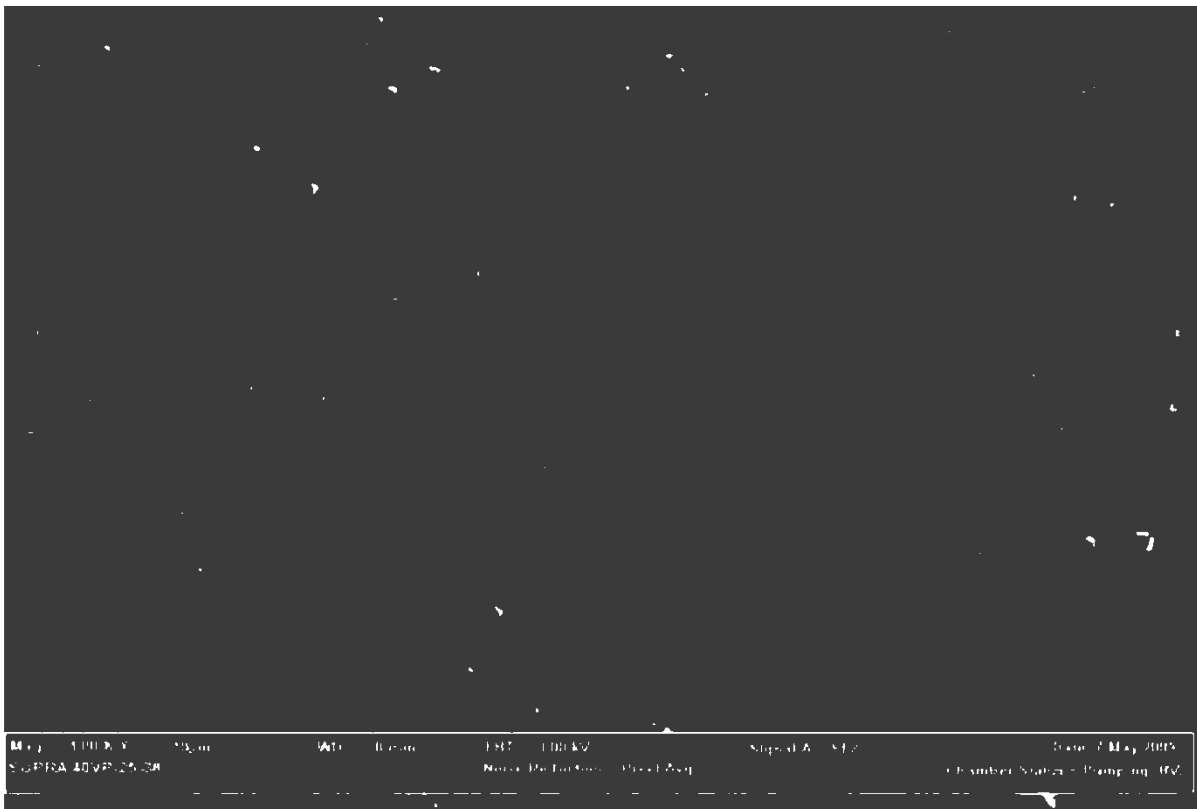
Fig. 7 Microstructure of Iron powder reinforced ABS composite
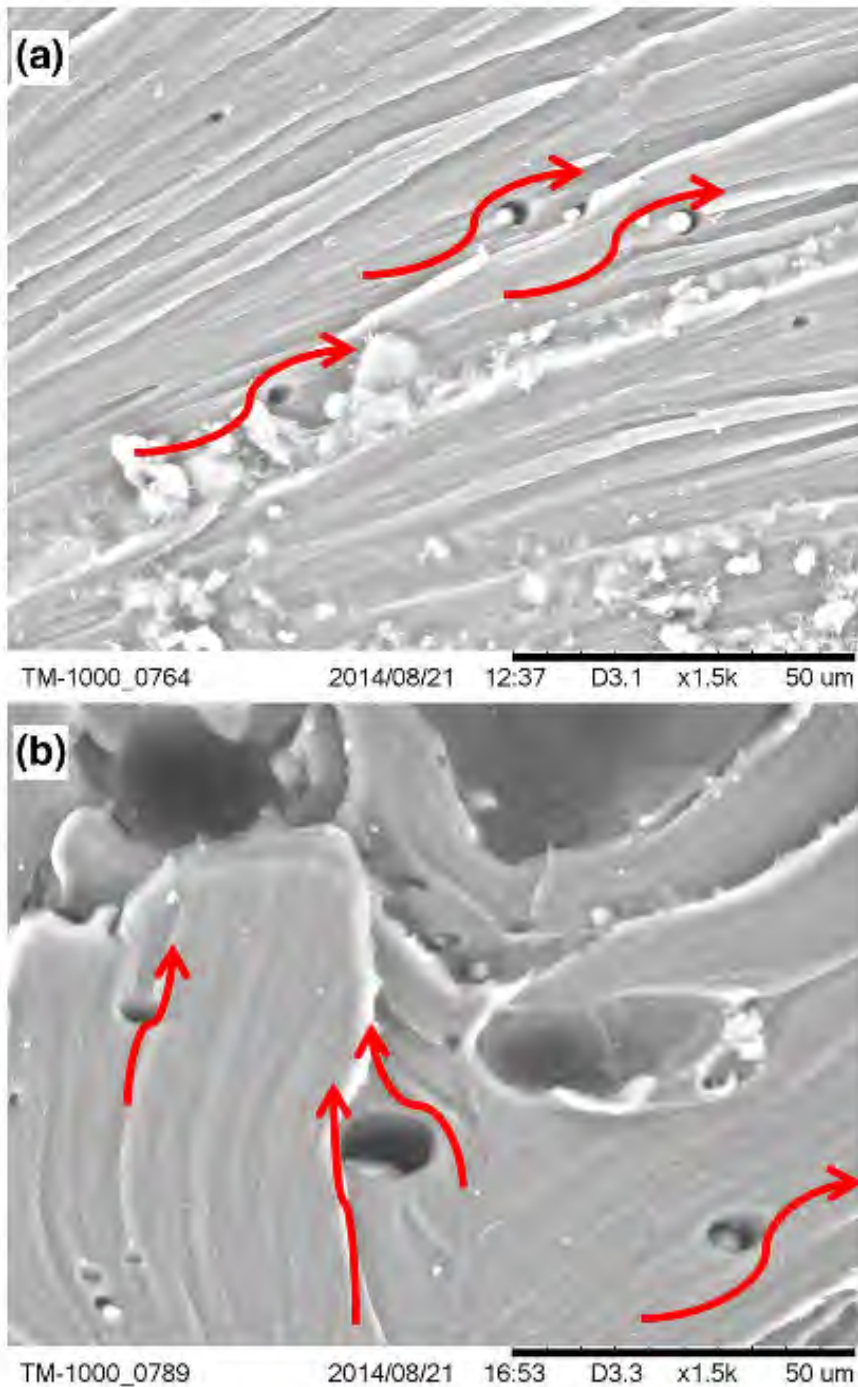
Fig. 8 High magnification of tungsten particles in a crack hackle region (a) and a region of high craze cracking (b) show that crack propagation passes around the tungsten particles

Polymer composites which contain a minority content of inorganic powders have also been developed diffusely due to versatile functional and mechanical properties, in contrast of iron powder filled polymer composites, inorganic powder fillers like ceramics can also provide tailored dielectricity via AM technologies. In the work of Chung and Das [140], SLS (selective laser sintering) technology was employed to build glass bead reinforced Nylon-11 composite

by stepwise composition gradients of glass bead (10% increments). The glass bead particle was sieved to a majority 45-63 µm size range and homogeneously distributed by applying a rotary tumbler. The test result of mechanical properties significantly shows growth in mean tensile and compressive modulus. SEM microscopic shown in Fig. 8, the black spots which highlighted for example are voids in the composite. The 20% glass beads composite sample seems has minimized voids observationally. There are also interesting alignments (marked red dotted lines) of the voids in 10% and 30% glass beads content, the reason is not mentioned but the voids may be easier generated at the interlayer bonding area, higher magnification ratio should be applied to further study the relationship between particle fraction and porosity of composite. Isakov et al. [144] investigated the interfacial boundary of two printed filaments (ABS/PP copolymer matrix and ABS/$Ba_{0.64}Sr_{0.36}TiO_3$ composite) which is fabricated by FDM process, shown in Fig. 9. The filler content is 30 vol.%, micro-voids were found in both side and the distribution of $Ba_{0.64}Sr_{0.36}TiO_3$ particles is reasonably homogeneous.
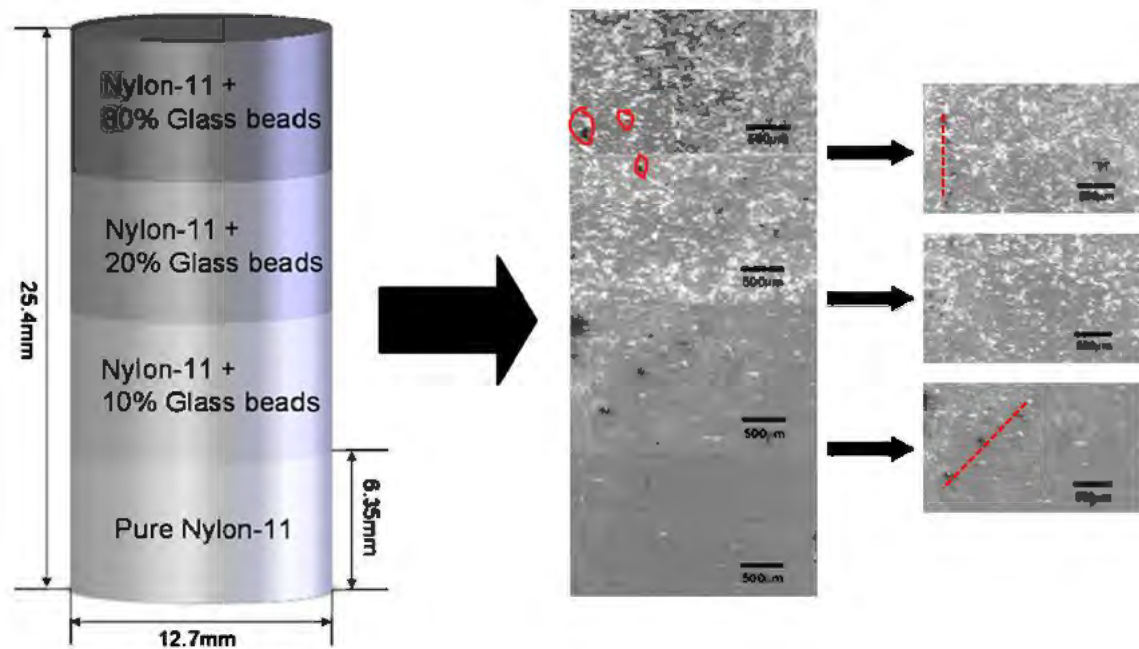
Fig. 9 SEM micrographs of each composition in the fabricated Nylon-11/Glass beads specimen by SLS process, and SEM micrographs of composition of interfaces in the fabricated specimen
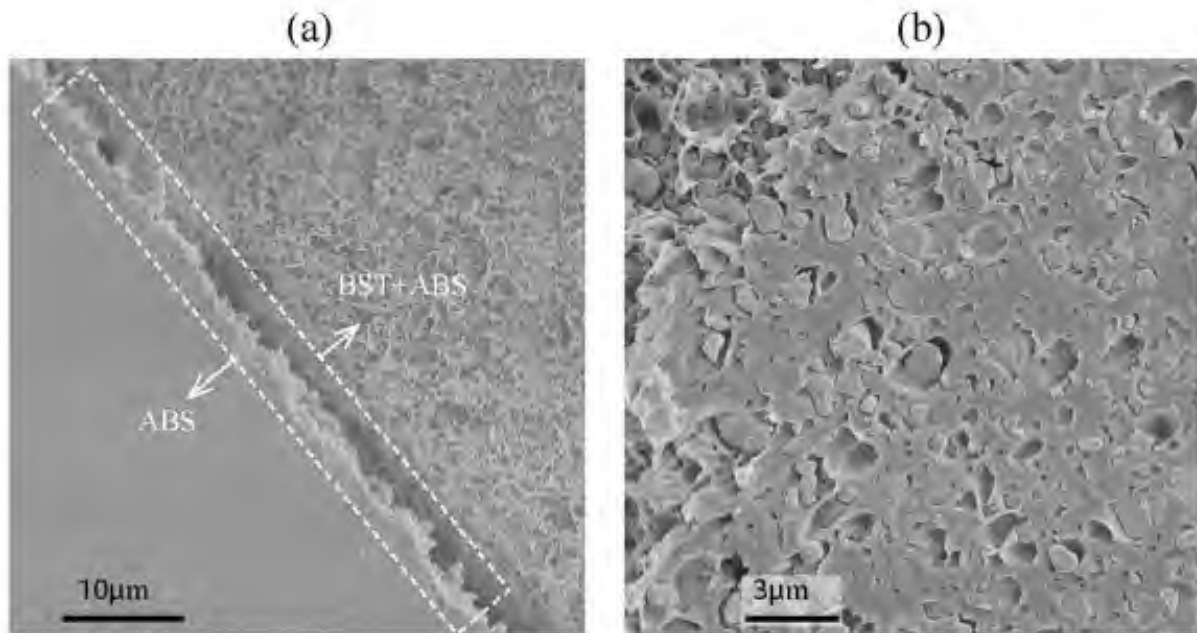
Fig. 10 SEM images of printed ABS + 30 vol.% filled $Ba_{0.64}Sr_{0.36}TiO_3$, a: boundary between ABS and ABS/ $Ba_{0.64}Sr_{0.36}TiO_3$ composite; b: distribution of the $Ba_{0.64}Sr_{0.36}TiO_3$ particles in composite

Kalsoom et al. [147] applied SLA technology to fabricate a composite which consists of acrylate resins as matrix and micro-diamond (2-4 µm) as reinforcement to achieve an outstanding heat transfer rate, the micro-diamond particle reinforcement concentration is limited to 30% (w/v) for minimum resin adhesion. The SEM images given shows that the distribution of micro-diamond particle is hardly agglomerated, the less contact among the particle lead to a poor heat transfer in a relatively low micro-diamond content (less than 25 % w/v) but there is a dramatic improvement of heat transfer efficiency in 30% (w/v) particle concentration due to considerably more connected particles.

Despite the metal and nonmetal powder employed as filler, more tailored, functional and potential composites could be developed by AM processes, other composites which contain both metal and ceramic powder were also studied due to some merits like high temperature service ability, high strength, high wear and corrosion resistance. Boparai et al. [142] proposed a low-cost composite which has better wear resistance than pure polymers. The composite applied Al and Al2O3 as reinforcements in Nylon 6 matrix which the Al has self-lubricated function and Al2O3 is more applied in grinding tools as abrasive. The composite sample were investigated compare with pure ABS polymer, Fig. 10 [142] shows the microstructures of samples after stand wear test, the composite samples show fewer abrasive grooves especially continuous grooves due to the present of Al2O3 (large particles), voids are also present but

mostly due to the rupture of filler particles. Further morphology of the surface of tested specimens may need to be investigated by higher magnification. The result of wear test was affirmative that the composite samples have higher wear resistance than ABS polymer, but more comparative studies may be needed to optimize composition of filler content and other polymer materials may also be added into reference material.
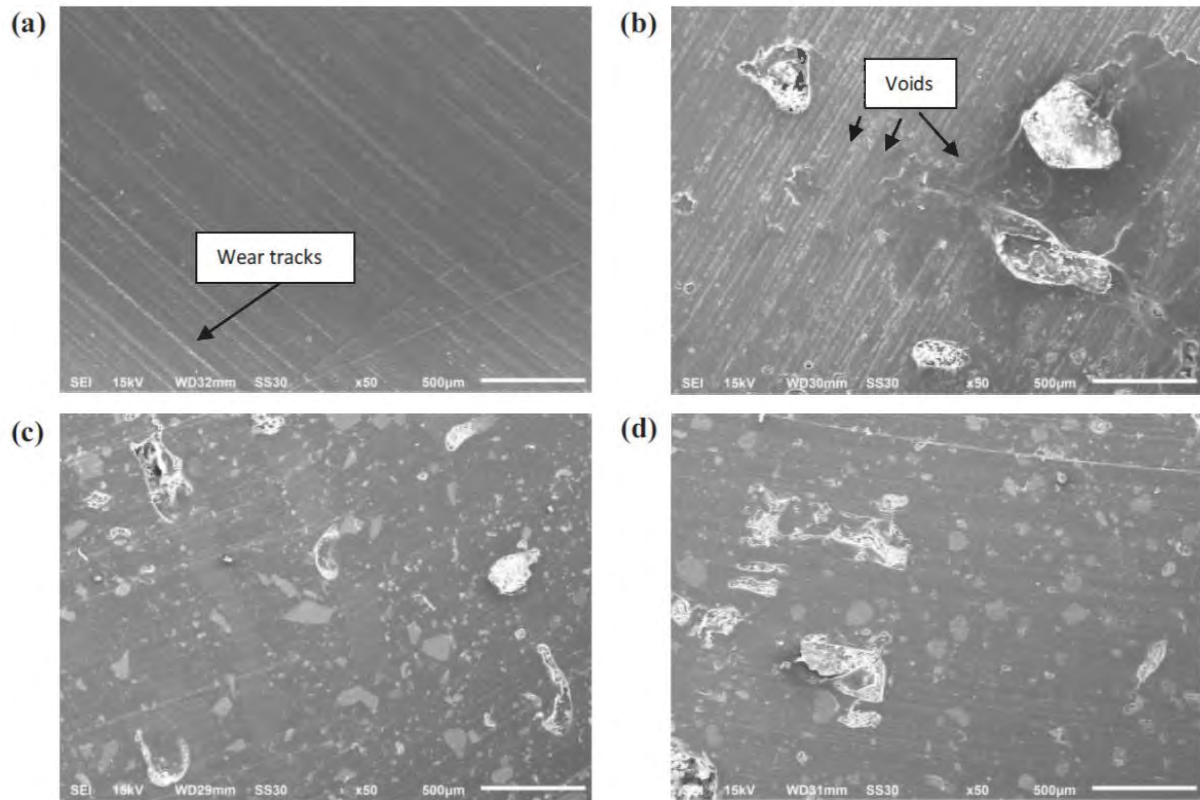
Fig. 11 SEM images of Al/Al2O3/Nylon 6 composites compare with ABS polymer after wear test ((a), ABS polymer, (b) composition 1, (c) composition 2, (d) composition 3)

2.4.2 Nanofiller composite in AM

The development of nanofillers applied on AM fabrication process growing fast recently. Nanofiller polylmer composite can provide decent improvement in specific properties like mechanical performance, electrical conductivity, thermal and dimensional stability [153]. Graphene oxide, carbon nanotubes, nanoclay and nanocellulose etc. act as nanofiller reinforced composite are investigated by researchers in recent years.

Graphene known as a carbon allotrope, has been a popular research subject since the properties enhancement it provided, which including mechanical [154-157], thermal [158-161], electrical, thermal and optical properties. The AM graphene polymer composite can be fabricated by

different AM processes like SLS and FDM, limited studies on SLA since the UV light during fabrication may be blocked by graphene particle and deteriorate the polymerization [162]. To maintain the dimension and performance of printed parts, the graphene content is suggested under 5wt% [163]. Lin et al. [164] successfully fabricated graphene oxide (GO) composite by SLA process and improved tensile properties was shown when the GO content is only 0.2 wt%, the tensile strength and elongation increased 62% and 13% respectively. More studies investigated graphene and GO polymer composite via FDM process since an enhanced aligned orientation of reinforcement is offered. Gao et al. [165] mixed graphene nanoplatelets (GNP) and PLA polymer and fabricated via a multilayer coextrusion technique, the result shows a significant improvement in tensile modulus (120%) when the GNP content was 1 wt%. Zhu et al. [166] composited GNP with PA12 and achieved similar outcome that >50% maximum increase in elastic modulus but the elongation at break dropped substantially. Soft polymer like PU can also be composited with graphene, a respectively 14% and 28% increase in flexural modulus and fracture toughness was achieved when the addition of graphene was 0.5 wt% [167].

As one of the strongest materials in the world, carbon nanotubes (CNT) are a derivative from 2D graphene sheet with considerable aspect ratio and carbon-carbon covalent bond, offers high potential to high-end industries which required remarkable mechanical, conductive performance. Past research investigated CNT polymer composite via various AM processes like FDM, SLA and SLS. Research regarding the mechanical performance of AM CNT and reinforced polymer composite are summarized and shown in Table 7. Bai et al. [168] printed and analysed CNT/PA12 nanocomposite via a commercial SLS printer and the result of testing shows a dramatically enhance in Young's modulus, a decent dispersion of CNT was also observed due to the shear thinning effect. Similar in FDM process CNT printing, printed samples can be improved in mechanical properties by a small addition of CNT filler, but the ductility of CNT composite is ambiguous from different studies. The reason may be due to the different preparation processes applied, then the dispersion and distribution of CNT in the composite raw material are unpredictable. An excessive wear in the brass nozzle orifice of FDM printer was found and it may lead to an inhomogeneous CNT distribution (shown in Fig. 11), an alternative stainless steel nozzle should be applied and investigated [169].

Table 7 Studies on nanofiller reinforced composite in AM

AM Technique	Matrix material	Nanofiller content	Mechanical characteristic	Testing	Ref
SLS	PA12	0.1 wt% and 0.2 wt% of CNT	16.9% (0.1 wt%) and 20% (0.2 wt%) enhancement in elastic modulus	Dynamic mechanical analysis (DMA)	[168]
SLS	PA12	0.5 wt% CNT	UTS: 86 MPa to 94 MPa (10% improvement); Elongation: 11% to 9%; 12% increase in storage modulus	Tensile testing and DMA	[170]
FDM	PLA	0.1 wt%, 0.2 wt%, 0.5 wt% of graphene and MWCNT	47% increase in UTS and 17% in Young's modulus when 0.2 wt% of graphene; 41% increase in UTS and 26% in Young's modulus when 0.1 wt% of MWCNT; Elongation decrease in both graphene and MWCNT samples.	Tensile testing, Izod impact testing, differential scanning calorimetry (DSC)	[171]
FDM	PLA	0.1 wt%, 0.3 wt%, 0.5 wt% and 1 wt% CNT	Different printing parameters like layer thickness, infill content, infill pattern/orientation were studied, only shown 1 wt% reinforcement lead to an improved tensile strength, increased Young's modulus shown in all CNT contents; Honeycomb infill pattern shows larger increase in thermal stability and mechanical properties.	Tensile testing, DSC, thermomechanical analysis (TMA)	[172]
FDM	ABS	Mixing 15% MWCNT and 5 wt%, Proprietary Dispersion Additive; Coated with 5 wt% of MWCNT	51% tensile strength increase in coated MWCNT, 25.6% increase in mixing sample; Elongation increased observed (4.1% to coated 4.5% and mixing 5.65%); 30% increase in flexural strength in coated MWCNT, 17% increase in mixing sample.	Tensile and flexural testing	[173]
FDM	ABS	1 wt% of MWCNT, SiO_2, MMT (montmorillonite) and $CaCO_3$	All printed samples had increased mechanical performance than pure printed ABS. Maximum increase happened in nano-MMT/ABS which the tensile strength improved 25.8% and 17.1% increase in flexural strength.	Tensile and flexural testing, Vicat softening temperature measurement,	[174]
FDM	PBT	0.49 wt% of CNT and 5.2 wt% graphene	PBT/CNT is 28% higher in storage modulus than PBT/graphene, PBT/graphene has higher crystallinity	DSC, DMA, X-ray scattering, Electrical conductivity analysis, Morphological analysis, thermogravimetric analysis (TGA)	[169]
FDM	TPU	4 wt% of CNT	0.55% increase in maximum resistance, 0.65% decrease after 1000 cycles.	Single beam type sensor testing	[175]
Liquid deposition modeling (LDM)	PLA	1 wt% of MWCNT, 25/30/35 wt% of PLA in dichloromethane solution.	The optimized printing window is given when the printing speed is 0.1mm/s and shear rate is 10 s-1, by applying 30 wt% concentration PLA.	Rheometer	[176]
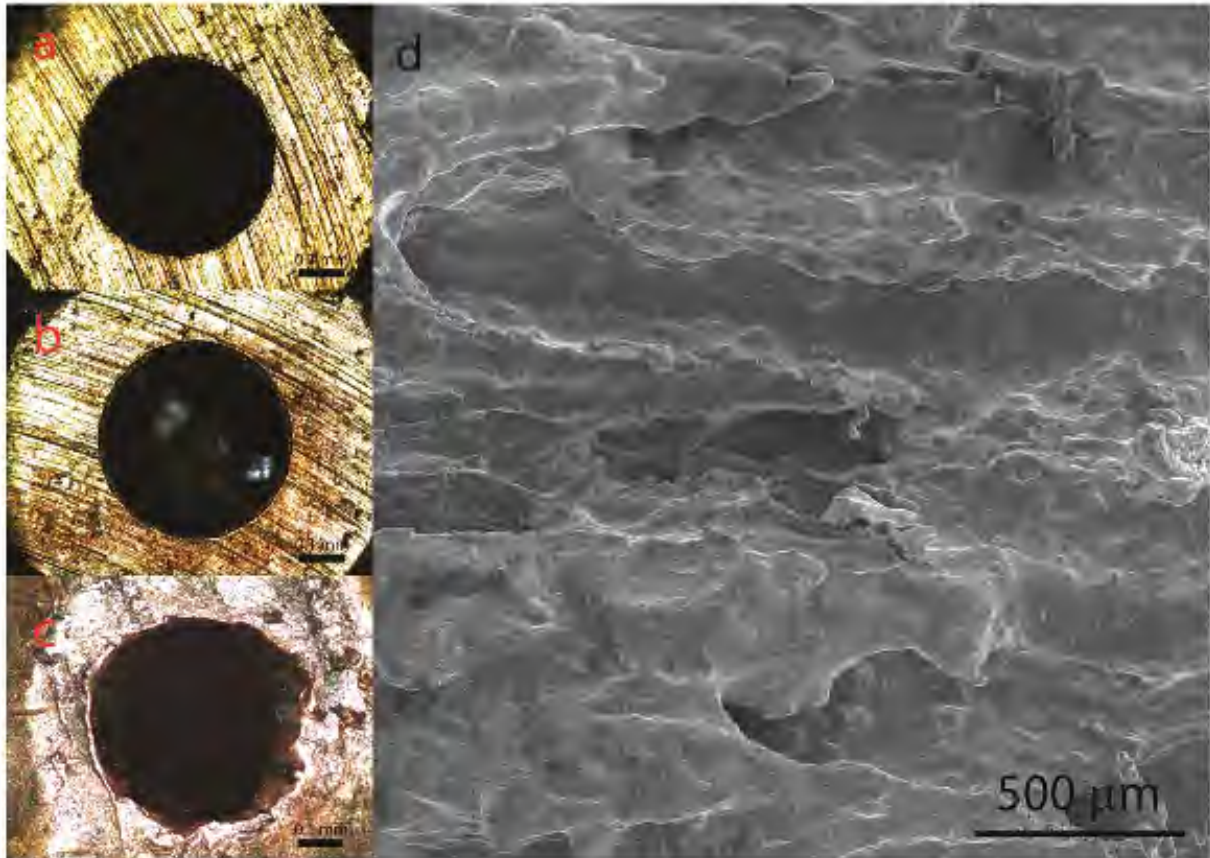
Fig. 12 Comparison of brass nozzle orifice graphs given by optical microscope and SEM image of part printed by worn nozzle. (a) unused nozzle. (b) nozzle when print around 10cm of filament. (c) ~1.5 m filament printed. (d) SEM image of PBTG composite printed with an abraded nozzle.

Substantial nanofillers polymer composite have been fabricated and investigated for versatile potential applications. Smectite family nanocomposite like nanoclay is derived from montmorillonite (MMT) which also has high aspect ratio (>50) [177] like CNTs but the natural-based and considerably low cost. Specific features can be offered by nanoclay like improved permittivity [178] and mechanical performance [174,179]. Francis and Jain [180] found that there is an optimized 94.9% decrease in surface roughness when 1 wt% of nanoclay reinforced with ABS polymer. The 5wt% addition of nano SiO2 filler increased the sterolithography resin by 20.6% and 65.1% in tensile strength and modulus repectively in SLA process [181]. Nanofillers composite can also be employed into shape memory material which are available in various responsive actuation sources like light, humidity, magnetic field and electric [182,183].

2.4.3 Fibre reinforced composites in AM

2.4.3.1 Inorganic fibres reinforced composites in AM

FDM process is one of the few available printing processes which are able to fabricate both short and continuous fibre reinforced composites [29]. Commonly, the fibres applied in composites are glass and carbon fibres to improve mechanical performance. In fibre reinforced composite, fibre orientation, interfacial bonding and voids significantly influence the properties of final AM composites. Almost all studies show that the interfacial bonding and [184] voids of AM printed composites are poor compared to CM composites [185]. Table 8 summarized the diversity of recent works on fibre reinforced composite in AM-FDM process.

Table 8 Summary of recent fibre reinforced composite research in AM-FDM

Matrix	Fibre	Printing Parameters	Fibre Content	Printing Orientation	Testing Standard	Mechanical Properties	Result Highlights	Remark	Ref
PLA	Chopped short carbon fibre (~60μm)	NT: 190°C; BT: 70°C;LT: 0.3 mm, PS: 50 mm/s	15%	0°, 90°, ±45°	ASTM D638-10, Tensile ASTMD3518-13, Shear	TS: 53.4 MPa, TM: 7541 MPa (0°); TS: 35.4 MPa, TM: 3920 MPa (90°) SS: 18.9 MPa, SM: 1268 MPa (±45°);	TM increased approximately 2.2 times than PLA, Reduced TS in both 0° and 90°	Voids happened when NT was 220°C	[185]
ABS	Chopped short carbon fibre (3.2 mm length, up to 0.4 mm after premix)	NT: 205°C; BT: 85°C;ND: 0.5 mm LT: 0.2 mm	10%, 20%, 30%, 40%	0°	ASTM D638 Type V	TS and TM increased with fibre contents; FDM ABS has higher TS than CM ABS; Voids increased with fibre content and poor bonding between fibre and matrix	High orientation with printing direction and severe porosity in FDM samples; The nozzle orifice clogging was also found when fibre content was 40%	Triangular gap between printed thread decreased in FDM ABS-CF samples as enhanced thermal conductivity and less die-swell.	[186]
ABS	Short carbon fibre, carbon nanotube (CNT)	BT: 110°C; LT: 0.18, 0.24, 0.3 mm; PS: 60, 80, 100 mm/s	8%, 15%	0°, 90°, ±45°	ASTM D3518/D3518M−13, in-plane shear; D3039/D3039M-14, tensile; ASTM D3846-08, double notch shear	TS: 27.69, 29.64, 39.05 MPa (0°); 23.95, 29.20, 29.23 MPa (±45°); 22.31, 21.46, 13.74 MPa (90°); TM: 2445, 2522, 5899 MPa (0°); 2061, 2196, 2830 MPa (±45°); 1952, 2017, 2193 MPa (90°); Double notch shear strengh decrease with increase of PS and LT;	Porosity of FDM ABS, CNT/ABS and CF/ABS: 0°: 0.82%, 0.85%, 4.18%; ±45°: 0.49, 2.39, 8.54%; 90°: 1.87, 1.39, 6.93%; less voids at the bottom;	Main failure mode is poor fibre-matrix bonding; Triangular gap increased with the presence of CF.	[187]
ABS	Short carbon fibre (150 µm and 100 µm)	NT: 230 °C, ND: 0.35 mm, LT: 0.2 mm, PS: 20 mm/s to 25 mm/s,	3, 5, 7.5 10, 15 wt%	±45°	ASTM D638-10, Tensile ASTM D790-10, Flexural	Maximum TS is 42 MPa when 5% of fibre, almost no increase in 10% and 15%; Greater increase in TM when 5% and 7.5% than other fibre contents; Ductility reduced 33.8% when fibre content is 10%; Longer fibre result in higher TS and TM; Minor increase in flexural properties.	The greatest porosity was 9.04% when the fibre content is 10%, and it dropped to 3.27% when increased to 15% of fibre;	Significant larger improvement in tensile and flexural modulus than increase in strength.	[188]
PP	Short carbon fibre (250 µm average)	NT: 230 °C, BT: 70 °C, CT: 55 °C, ND: 0.6 mm, LT: 0.25 mm, PS: 28.3 mm/s (first layer) and 56.6 mm/s,	10, 15,20 vt%	0°, 90°, 0°/90° and ±45°	EN ISO 178, flexural EN ISO 179-1, impact ISO 22007-2, thermal conductivity	FS: 74.2 Mpa (0°), 36.5 Mpa (90°), 51.4 Mpa (0°/90°) and 44.5 Mpa (±45°); FM: 5.60 Gpa (0°), 1.65 GPa (90°), 3.39 GPa (0°/90°) and 1.92 GPa (±45°); TS and TM of 10%CF/PP increased more than 100% and 400% repectively than neat PP speciments, the strain at yield reduced 50%; 90°, 0°/90° neat PP speciments have dramatically lower impact energy than 0° and ±45°, the CF/PP specimens have reduced impact energy than all PP samples.	CF/PP specimens tended to less in wraping and oozing than neat PP since the highly orientated CF distribution; Maleic anhydride modification proved to improve matrix-fibre interface Thermal conductivity of composite can be altered by various printing orientations.	A fabrication of PP/CF composite extrusion and printing with ease may bring wider application to AM fibre composites.	[189]
PLA	Continuous carbon fibre (1000 fibres bundle)	NT: 180-240 °C, LT: 0.3-0.8 mm, PS: 100-600mm/min,	Maximum 27% (varied with different	0°	ISO 14125:1998	Flexural strength increased with PT, and decreased dramatically with LT and hatch spacing. PS has an insignificant impact to the flexural properties.	The parameters like LT were suggested to 0.4 mm - 0.6 mm and hatch spacing was ~0.6 mm recommended, optimized fibre content of	Voids within the fibre bundles and poor interfacial bonding between fibre and PLA polymer.	[190]

	Hatch Spacing: 0.4-1.8 mm	printing parameters)					27% can leat to a 335 MPa of flexural strength and 30GPa of flexural modulus.		
PLA	Continuous carbon/jute fibre	NT: 210 °C,BT: 80 °C,LT: ~1 mm,PT: 60 mm/s,ND: 1.4 mm	CF: 6.6 vt%,JF: 6.1 vt%	0°	JIS K 7162	CF/PLA: TS: 185.2 Mpa, TM: 19.5 Gpa; tensile strain-to-failure: 0.95%, FS: 133 Mpa, FM: 5.93 Gpa, flexural strain-to-failure: 4.09%JF/PLA: TS: 57.1 Mpa, TM: 5.11 Gpa.	Insufficient bonding between fibre and matrix polymer in both carbon and jute composite; Voids were reported among printed filaments;	Higher fibre content up to approximately 40-50 vt% was propoesd to improve the performance.	[191]
PLA	Continuous aramid fibre	NT: 180 °C, PS: 1 mm/s, LT: 0.15 mm (0.2 mm in first layer), ND: 1 mm,	8.6 vt% (9.5 wt%)	0°, 90°	Not mentioned	TS: 203 Mpa, TM: 9.34 Gpa and 1.54 Gpa (0° and 90° repectively), SM: 1.54 Gpa, ultimate tensile strain: 3.3%.	499% and 186% increase in TS and TM repectively compared with PLA specimens; The estimated TM when fibre orientation is 90°, was significantly higher than experimental result since the poor interlaminar bonding strength.	The co-feeding of polymer filament and fibre bundle can lead to a decent deposition but the feed and movement rate are severely limited.	[192]
Nylon	Continuous carbon/glass/Kevlar fibre	NT: 263 °C, BT: RT, LT: 0.1 mm (0.125 mm in CF)	CF: 11 vt%, KF: 8 and 10 vt% GF: 8 and 10 vt%	Concentric and Isotropic pattern	ASTM D3039, tensile ASTM 790, flexural	CF: TS: 216 Mpa, TM: 7.73 Gpa, Elongation at break: 4.22 %, FS: 250.23 Mpa, FM: 13.02 Gpa; KF: 164 Mpa, TM: 4.37 Gpa, Elongation at break: 4.98 %, FS: 125.80 Mpa, FM: 6.65 Gpa; GF: 206 Mpa, TM: 3.75 Gpa, Elongation at break: 8.42 %, FS: 125.80 Mpa, FM: 6.65 Gpa;	Delamination failure in some specimens; Concentric pattern has slightly lower performance than Isotropic (6 and 9% lower TS and 20 and 21% lower TM in GF and KF repectively); Porosity increased with the content of fibre and limit the increase in mechanical performance of final parts;	Compare with conventional way, AM fibre reinforced composite have significant higher porosity since the absence of vacuum environment.	[193]
Nylon	Continuous carbon/glass/Kevlar fibre	NT: 273 °C (232 °C in fibre layers), BT: RT, LT: 0.1 mm (0.125 mm in CF)	~27.2 vt% (Type A) and ~73.2 vt% (Type B)	Isotropic	ISO 14130, shear	SS: CF: 22.19 Mpa (Type A), 31.94 Mpa (Type B); KF: 13.65 MPa (Type A), 14.28 Mpa (Type B); GF: 13.87 Mpa (Type A), 20.99 Mpa (Type B). Nylon: 10.19 Mpa (0.1 mm layer), 9.79 Mpa (0.125 mm layer), 9.33 Mpa (0.2 mm layer).	KF specimens shows greatest delamination and the SS of all the printed composite still dramatically lower than conventional pre-preg composite;	The improvement in SS of continuously fibre is significantly lower than the increase in TS and FS.	[194]
Nylon	Continuous carbon fibre	ND: 0.4 mm, LT: 0.15 mm, Hatch Spacing: 0.8-1.0 mm	33 vt%	4 pattern designs with 0° shell and five 0°/90° bottom layers	JIS K 7017: 1999, flexural, JIS K 7165: 2008, tensile	Rhombus and rectangle pattern had superior mechanical performance than honeycomb pattern; Bending result shows significantly lower than carculated maximum load due to poor interface bonding performance; Tensile failure happened at the interface between bottom and designed pattern layers.	The surface roughness of printed CF reinforced composite was dramatically lower than neat PLA polymer; Poor interface adhesions facilitate the low experimental result when compared with theoretical calculations.	The machanical performance of specimens were mainly dependent on the bottom solid layers rather than the designed infill patterns.	[195]
Nylon	Continuous and short carbon fibre (~0.1 mm)	NT: 260 °C BT: RT, LT: 0.125 mm (0.2 mm in short fibre), ND: 0.4 mm, PS: 6.90 cm3/hr (Nylon), 2.39 cm3/hr (Fibre)	27 vt% (continuous), 6 wt% (short)	0° (Concentric and Isotropic), ±45°	ASTM D638, tensile, ASTM D7264, flexural, ASTM D3518, shear	Short CF fibre: TS: 33.5 Mpa, TM: 1.85 Gpa, FS: 55.3 Mpa, FM: 3 Gpa, SS: 19 Mpa, SM: 0.31 Gpa; Continuous CF fibre: TS: 726 Mpa, TM: 46.9 Gpa, FS: 363.8 Mpa, FM: 31.2 Gpa, SS: 23.4 Mpa, SM: 1.7 Gpa.	Short fibre has lower porosity (1.1%)than continuous CF (9%).	Desired printing properties were suggested for 3D printing fibre reinforced composite filament.	[184]

| Nylon | Continuous carbon fibre | NT: 250 °C, BT: 120 °C, LT: 0.2 mm, ND: 0.4 mm, | 2, 4, 6, 8 and 10wt% | 0°, 90° | ASTM D638–10, tensile ISO 14125: 1998, flexural ISO 180–2000, shear | TS improved from 46.4 Mpa to 93.8 Mpa with the increase of fibre content and TM also enhanced significantly (from 0.98 Gpa to 3.58GPa), elongation at break dropped from 192.1% to 8.1%; FS improved from 35.6 Mpa to 124.9 Mpa with the increase of fibre content and FM also enhanced significantly (from 1.18 Gpa to 5.26 GPa). Impact strength reduced in lower fibre contents (2,4,6 and 8 wt%) compared with neat Nylon specimen but slightly improved when content of fibre was 10 wt%. | The printing orientation design can lead to a significant discrepancy in thermal conductivity (up to 277.8% of increase). | A self-fabricated continuous CF composite shown greatly improvement in mechanical performance and thermal conductivity. | [196] |
| Thermoplastic polymide (TPI) | Short and continuous carbon fibre | NT: 395 °C, LT: 0.9 mm, ND: 1.0 mm, PS: 5 mm/s. | Short: 5 wt% | 0° | ISO527-2:1993, tensile, ISO14125:1998, flexural | TS: Short fibre TPI: 23.8 MPa, pure TPI: 31.8 MPa, continuous and short fibre TPI: 214% of pure TPI; FS: Short fibre TPI: 36.6 MPa, pure TPI: 47.4 MPa, continuous and short fibre TPI: 83.4 MPa. | Increased drying time of filament helped to reduce the porosity; Printed TPI specimen has considerably poorer mechanical performance than injection moulded parts; Higher porosity in short fibre TPI and result in lower strength than pure TPI specimens. | Novel separated (both short and continuous fibres) reinforced FDM printing was introduced and the novel applied matrix of TPI polymer. | [197] |

Both the short and continuous fibre reinforced composite have shown the common enhancement in mechanical performance especially continuous carbon fibres. Other properties like thermal conductivity and energy absorption capacity also have substantial improvement from some research [189,190,196]. The geometric accuracy also be improved in short fibre composites since the presence of orientated fibre facilitate the elimination of warpage [189]. However, several drawbacks raised like high porosity, anisotropy and poor inter-laminar adhesion. The length of chopped fibre is also limited due to the printing orifice diameter which is commonly 0.4 mm to 0.8 mm, the maximum length of short reported is 0.4 mm printed by a 0.5 mm nozzle which the nozzle clogging happened when fibre content reached 40% [186]. The restricted aspect ratio of fibre limits the improvement in mechanical performance but a decent processability reported may lead short fibre reinforced composite printing to wide range of applications [189].

Continuous fibre reinforced composites drew more attention by researchers recently due to remarkable improvement in mechanical performance. The printer layout shown in Fig. 12 [185], highly aligned fibre distribution offers superior tensile performance than 6061-T6 Aluminium [198]. Part of research studied mechanical properties based on commercial MarkForged continuous fibre composite printer or filaments [184,193-195] which generally obtained greater mechanical performance. The tensile and flexural properties have been enhanced exponentially, but the impact and shear strength reported minor or reduced in continuous fibre composite [192,194,196]. Different reinforcement design was investigated such as sandwich structures (combination with polymer layers) [193,194] and various infill pattern designs [184,193,195]. Similar with short fibre composite printing, poor interlaminar adhesion, high porosity and anisotropy have been reported as a common limitation in continuous fibre composite printing. Some acute angel printing is inherently limited to print in continuous fibres [192]. The modification of fibre surface was also reported to contribute to the development of interfacial bonding [186]. It is apparent that the modified fibre surface and matrix bonding ability are two of the most parameters for optimizing the performance of both short and continuous fibre reinforced composite fabricated by FDM process.
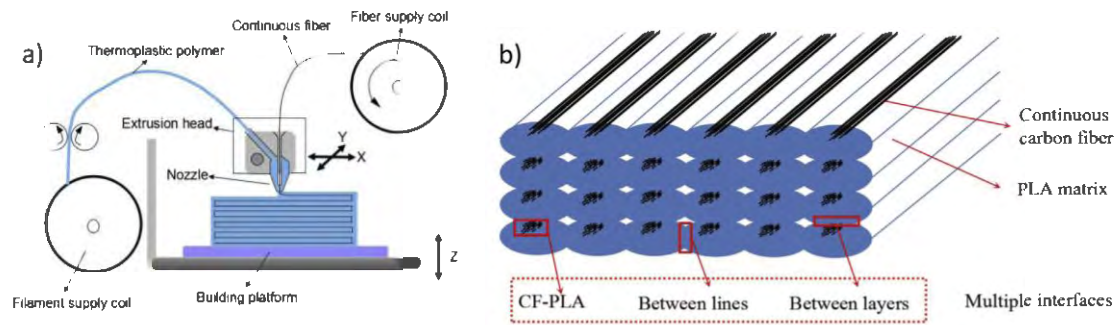
Fig. 13 Continuous CFRP printing and fibre distributions

2.4.3.1.1 Fibre-matrix interfacial bonding in 3D printing composite

Zhang et al. [187] and Ferreira et al. [185] observed the microscopic cross-sectional pictures of the short CF-ABS and CF-PLA filaments and indicated the voids in the commercial filament existed before printing process but there are no specific explanations that how this type of porosity is generated. It is also reported that the pores in the printing filament are more concentrated in the central areas of the filament, shown in Fig. 13 [199]. Tekinalp et al. [186] refined and explained this porosity in his work, the generation of these voids is due to the rheology properties of two phases of composite (ABS and short CF) are different, it will possibly lead to a void formed at the fibre-matrix interface and then an inadequate overall interfacial bonding. The heterogeneous fibre distributions and unsteady fusion process also increase the voids content in the final printed specimens [188]. To improve the compatibility of fibre-matrix phases may help to decrease this inner filament porosity. Zhang et al. [187] suggested to apply elevated printing bed temperature to reduce the voids content as the refined fusion of printed threads, but the microscopy image of this method need further investigation and only lower layers which are close to the heated bed can be attributed in this condition. Surface treatment of reinforced fibres can also contribute a lower voids content and better fibre-matrix interfacial bonding.
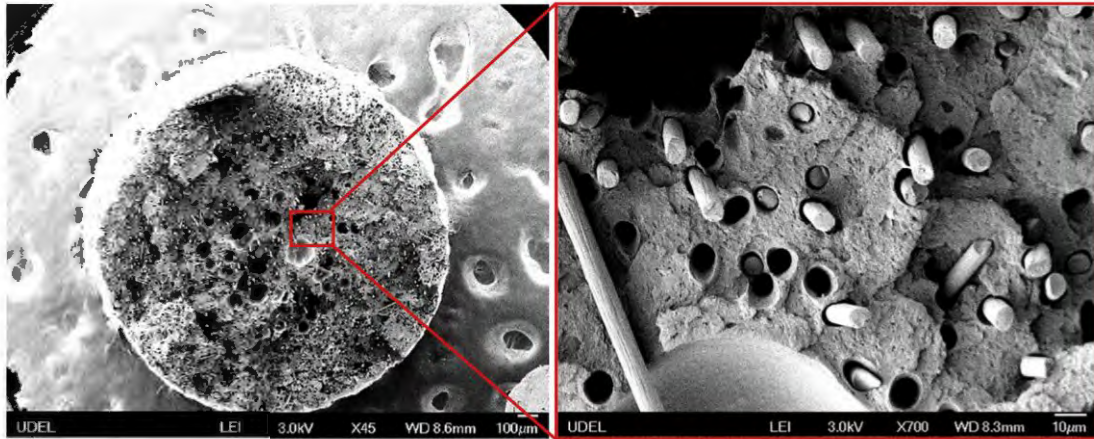
Fig. 14 SEM image of CF/ABS filament cross-sections

2.4.3.1.2 Fused filament beads interfacial bonding in 3D printing composite

The voids content of CF-ABS printed samples have also been evaluated from 4.18% - 8.54% based on different printing raster orientations. As mentioned above, Heated printing bed (110 °C) is recommended achieve a better fusion and less porosity, Fig. 14 compared the microstructural cross-section images of FDM samples fabricated by ABS, CNT (carbon nanotubes)/ABS and CF/ABS filaments [187]. The poor printed cables interfacial adhesion can be easily observed in CF/ABS specimens in all printing orientations and the tensile properties are also deteriorated considerably when the tensile force is perpendicular to the printing orientation. On the contrary, there is an opposite result obtained by which the cross-sectional microstructure is shown below in Fig. 15 [186]. The specimens printed have triangular pores among the deposited filaments in printed neat ABS specimens, whereas there is fewer presence of these triangular pores in the short carbon fibre (3.2 mm fibre length) reinforced ABS composite. The occurrence of these opposite results is highly dependent on the printing parameters, such as the filament deposition speed and length of hatch space. The different material properties also affect the result but there is lack of detailed information like chopped fibre length.
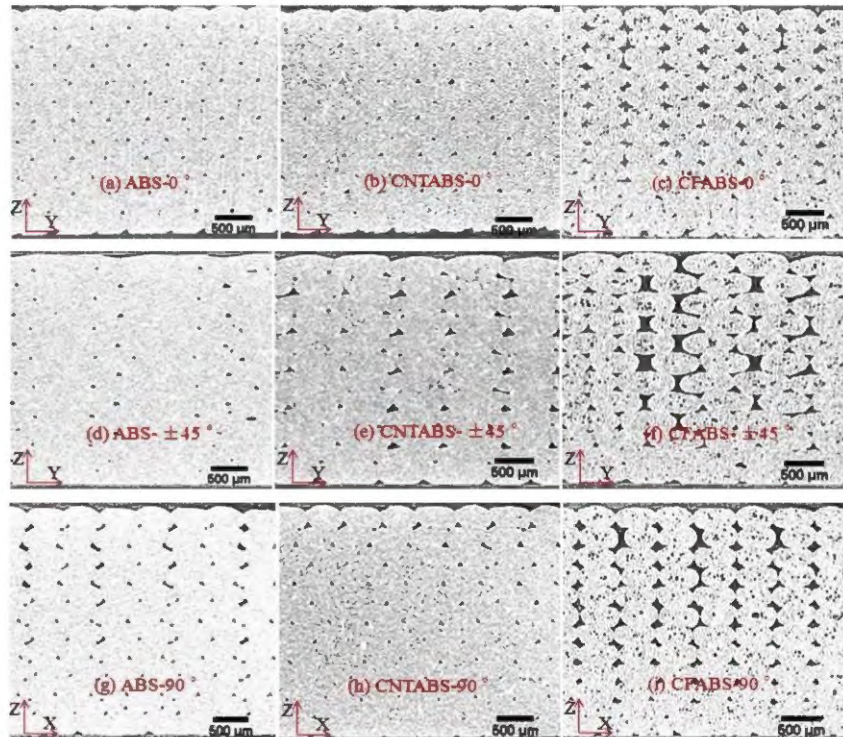
Fig. 15 Cross-section microstructure and void distribution of FDM specimens (a) ABS-0°, (b) CNTABS-0°, (c) CFABS-0°, (d) ABS-±45°, (e) CNTABS-±45°, (f) CNTABS-90°, (g) ABS-90°, (h) CFABS-±45°, (i) CFABS-90°
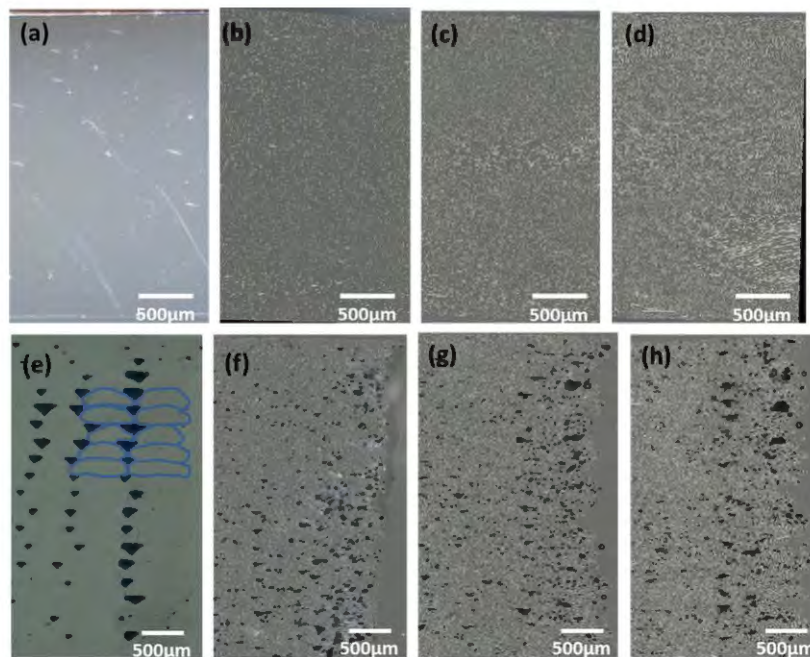
Fig. 16 Micrographs of polished surfaces of dog-bone slices (a) CM neat-ABS, (b) CM10%CF, (c) CM20%CF, (d) CM30%CF, (e) FDM neat-ABS, (f) FDM10%CF, (g) FDM20%CF, and (h) FDM30%CF

Based on the mentioned research works, the improvement of mechanical performance is limited in the additive manufactured fibre reinforced composite in both short and continuous fibres composite. The mechanical performance of printed sample is directly dependent on the interface quality of fibre and matrix materials, therefore the microstructure of multiple interfaces circumstances with various process parameters ought to be investigated to optimize 3D printing fibre reinforced composite.

In the work from Tekinalp et al. [186] , the specimens printed have triangular channels among the deposited filaments in printed neat ABS specimens, whereas there is no presence of these triangular channels in the short carbon fibre (3.2 mm fibre length) reinforced ABS composite as shown in Fig. 16. This elimination is contributed by the presence of fibre which can lead to minimise the die-swell and enhance thermal conductivity, even 10 wt% of fibre addition can dramatically eliminate die-swell which lead to smaller filaments deposited and increased thermal conductivity contribute to have a better contact interface among depositing layer and previous one. However, the interfacial bonding between printed filaments is still poor and porosity is much severe than cast moulding (CM) fabricated specimens (Fig. 16a and 16b). When applying short fibre in the additive manufacturing, risen fibre content led to better packing of printed filaments but also more void generated when increased fibre ends during printing process [200]. Pores generated mostly be observed around the fibres in FDM sample due to during deposition process, polymer matrix are melted and cause different flowability with fibre phases. Pre-process like surface treatment of fibres can be employed to reduce the porosity [186]. Unlike CM process, there is no outer pressure to eliminate the pores which generated during the melting and setting of matrix polymers in deposition process, the continuous fibre which this issue hasn't been found may be more employed in further study and industry application.

The relationship between the printing temperature and interfacial bonding quality has been investigated by Tian et al. [190], higher temperature is tested that can improve the bonding and even mechanical performance. The microstructures and fracture patterns comparison between the specimens fabricated by 180 °C and 240 is shown in Fig. 17. When the printing temperature is 180 °C, delamination happens as shown in Fig. 17b, the impregnation and interfacial bonding quality is poor when apply 180 °C as nozzle temperature. However, when the temperature is increased to 240 °C, as shown in Fig. 17d, 17e and 17f, the matrix can be observed that the carbon fibre bundles are

impregnated by the matrix PLA polymer. The test of specimens also verifies that the specimen fabricated by 240 °C nozzle temperature has dramatically higher flexural strength (155 MPa in average) than the specimen made by 180 °C nozzle (110 MPa in average).
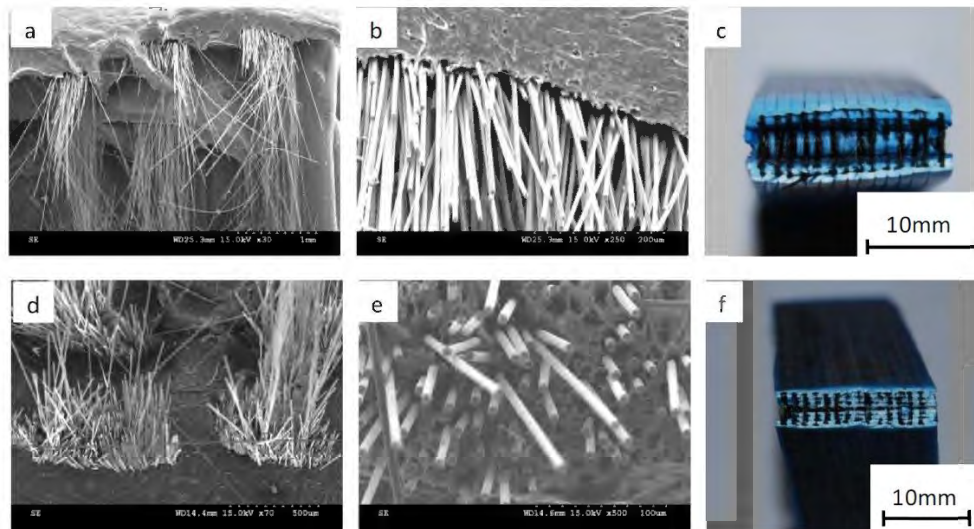
Fig. 17 The microstructures and fracture patterns comparison between the specimens fabricated by the temperature 180 °C (a, b, c) and 240 °C (d, e, f)

The layer thickness of patterns in FDM process is also critical to the final specimen performance, Ning et al. [188] analysed the properties of continuous carbon fibre reinforced ABS composite via FDM process, the best tensile strength of specimens tested is 42 MPa when the printing temperature is 230 °C, layer thickness is 0.2 mm and fibre content is 5 wt%. Best Young's modulus value is found around 2.5 GPa when the fibre content is 7.5 wt%. Tian et al. [190] also investigated the influence of layer thickness to specimen properties, the results shows that the flexural strength is considerably decreased when the layer thickness is enlarged (240 MPa of flexural strength when layer thickness is 0.3 mm, only 100 MPa when layer thickness is 0.8 mm). The fracture cross section microstructure figure also further proved this result, Fig. 18 demonstrates the microstructure of fracture cross section of the specimen with layer thickness 0.5 mm (a, b, c) and 0.7 mm (d, e, f) respectively. Delamination and impregnation are much worse in Fig. 18e, shear fracture and fibre pull-out are severe in Fig. 18f. They mentioned that smaller layer thickness may cause an increased in contact pressure among filaments and nozzle.
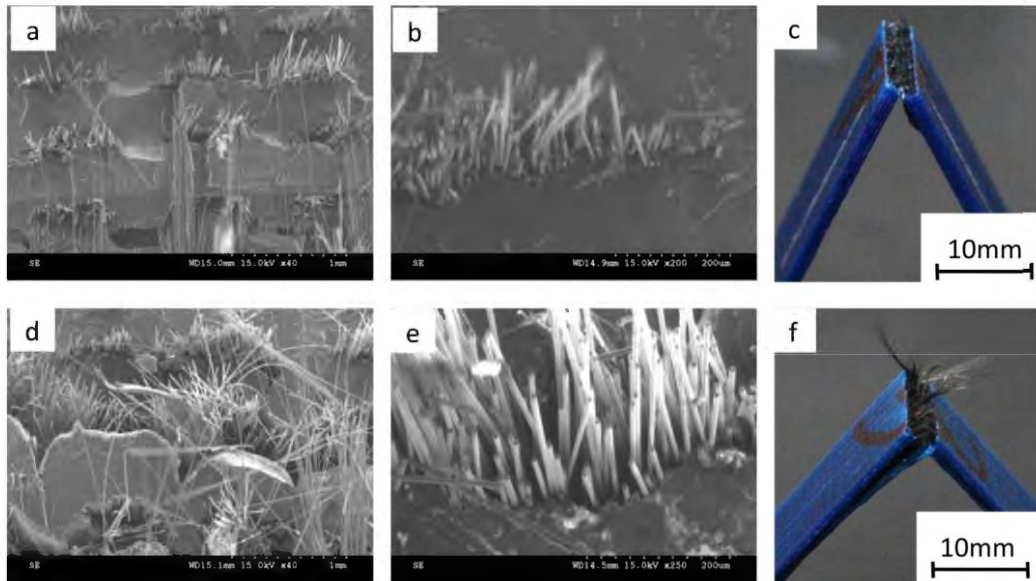
Fig. 18 The microstructures and fracture patterns comparison between the specimens fabricated by the layer thickness of 0.5 mm (a, b, c) and 0.7 mm (d, e, f)

2.4.3.2 Natural fibres reinforced composites in AM

2.4.3.2.1 Overview

Natural fibres which are commonly lignocellulosic in nature are another recyclable and renewable material, which could be applied as reinforcement for polymers to AM composites. The categories of natural fibres are based on their origins, divided into plant, animal and mineral fibres. Although there is less report of AM on natural fibre reinforced synthetic polymer composites, natural fibres may be a substitution for synthetic fibres, such as glass or carbon fibres in AM. Unlike biopolymers, these natural fibres are relatively low cost, recyclable, bio-degradable, and fair strength, elongation and elastic modulus. Natural fibres are proven to have better thermal resistance due to specific cellular structure [201-203]. However, cautions must be taken when replacing synthetic with natural fibres for AM, as some characteristics of natural fibres can be significantly lower than those synthetic e-glass and carbon fibre (Table. 9), although specific elastic modulus can be competitive and particular tensile strength of some natural fibres is also favourable compared with some glass fibres. The properties of fibres can also be different due to season, soil, sunshine or environment conditions [201,204,205]. The nature fibre reinforced composite also has some physical properties which may cause difficulty to AM, such as poor thermal resistance and ductility. Further surface modification of polymer-fibre interface should be studied to improve

the performance. Table 9 compared the mechanical performance of natural and common synthetic fibres.

Table 9 Comparison of mechanical properties of natural with synthetic fibres

Name of fibre	Density(g/cm3)	Elongation (%)	Tensile strength (MPa)	Young's modulus (GPa)	Ref
Wood	1.4	-	90-180	10-70	[203]
Bamboo	0.6-1.1	4.0-10	140-230	11-17	[203,206,207]
Bagasse	0.89	5.8	350	22	[208]
Sisal	1.5	2-2.5	511-635	9.0-22	[209]
Abaca	1.5	3.0-10	400	12	[208,210]
Pineapple	1.44	14.5	413-1627	26.5	[211]
Palm	0.7-1.55	7.0-17	64-111	0.5-1.1	[209,212]
Flax	1.4-1.5	2.7-3.2	345-1035	27.6	[206,209]
Hemp	1.4-1.6	1.6	690	30-70	[206,209]
Jute	1.3-1.5	1.5-1.8	393-773	20-55	[206,209]
Kenaf	1.4-1.5	1.5	930	53	[203]
Cotton	1.5-1.6	7.0-8.0	287-597	5.5-12.6	[205]
Coir	1.2	30.0	175	4.0-6.0	[205]
Wool	1.39	25-35	120-174	2.3-3.4	[213]
Silk	1.3-1.4	15-60	100-1500	5-25	[214]
Basalt	2.7	3.15	4840	89	[214,215]
E-glass	2.5	2.5	2000-3500	70	[205]
Carbon	1.4	1.4-1.8	4000	230-240	[209]

Like synthetic fibres, the strength and stiffness of natural fibres are higher than those of matrix materials, therefore the fibre content in AM composite may affect the composite performance significantly. An injection moulding process of natural fibre composites with thermoplastic matrix was reported to give rise to the peak fibre content of 40-55% and a decreased mechanical performance was observed when the fibre

content increased further, this may be due to a poor fibre-matrix interface and resulted high porosity [216].

Elongation at break of AM composites should also be determined by the reinforced fibre because of higher strain of matrix compared to fibres. In the composite material, a parameter called critical volume fraction (V_{crit}) indicates that the strength of a composite will deteriorate when fibre volume fraction is higher than V_{crit}. The matrix material could deal with the load if the fibre failed when fibre volume fraction is lower than V_{crit}. The jute and flax polyester composites have been studied and the V_{crit} was found ranging from 8.1% to 9.3%, which is remarkably higher than synthetic fibre composites [217]. Stoof and Pickering [218] studied Harakeke and hemp fibre reinforced PP composites processed by FDM process, various fibre contents have been tested and the greatest enhance of mechanical performance was found at 30wt% harakeke fibre content, with the tensile strength and modulus increasing by 52% and 147% respectively compared with the pure recycled PP polymer. It was also found that the increase in mechanical properties is relatively low, 2.5 MPa and 430 MPa in tensile strength and modulus respectively, when the fibre content increased from 20% to 30%, due possibly to poor wetting and hence interface bonding of fibre-matrix. Perez et al. [150] printed a jute-ABS composite by FDM process. The composite filaments were pre-extruded and the test fibre content was 5 wt%; different printing orientations specimens were fabricated and tested. The ultimate tensile strength of 5% jute fibre composite was lower than pure ABS polymer and 5% TiO2 particle reinforced composite, 26, 29 and 32MPa for 5% jute, pure ABS and 5% TiO2 reinforced composites respectively. It is apparent that the compatibility and hence interface between particle and ABS could be an important parameter for future development.

The length of fibre and aspect ratio are also important to the mechanical properties of AM composites. When applying a tensile load to short fibre composite, another parameter called critical length (L_c) is established. A fibre length should be longer than critical length in a composite, such the fibre can be broken before matrix during a tensile load [219]. Theoretically, the L_c can be applied to modify the fibre and matrix content in a composite. Increasing the fibre length is commonly believed to improve the strength of composite, but too long fibres may be disorderly distributed in the matrix and result in a poor performance [220].

Compared to the aforementioned natural fibre synthetic polymer composite, more radical approach has been taken, i.e. all natural based materials. Along with its more environmental-friendly fabricating process, AM of fully bio-based composites is becoming attractive to researchers and relevant authorities. By using FDM process, Le Duigou el al. [221] fabricated wood biopolymer composite with various fibre contents, by applying recycled wood fibre or coconut fibre composite with PLA/PHA blend matrix. The mechanical properties are tested and evaluated. A PP or PLA/wood flour composite has also been studied with various fibre contents by FDM process [222]. A comparison of injection moulding (IM) and AM full biocomposites and synthetic fibre reinforced AM composites can be summarised in Table 10 It can be seen that overall, the composites made by IM was able to produce higher tensile strength and Young's modulus compared to AM whether for PLA or PP matrix, while the influence of fibre content on the properties of composites seems similar across the processing technologies.

Table 10 AM biocomposites with injection moulding (IM) and Additive manufacturing (AM)

Fibre material	Matrix material	Manufacturing process	Fibre content	Tensile strength (MPa)	Flexural strength (MPa)	Young's modulus (GPa)	Ref
Wood (aligned)	PLA/PHA	FDM	40wt%	21	-	2.2	[221]
Wood (aligned)	PLA/PHA	IM	40wt%	31		3.9	[221]
Wood	PLA	FDM	20wt%	17	20	1.3	[222]
Wood	PLA	IM	20wt%	44	70	3.4	[222]
Hemp (aligned)	PLA	IM	30wt%	77	101	10	[223]
Hemp (random)	PLA	IM	47wt%	55	113	9	[219]
Wood	PP	IM	40wt%	50	78	3	[224]
Jute	ABS	FDM	5wt%	25.9	23.6	1.5	[150]
Continuous Jute	PLA	FDM	6.1vt%	55 (approximately)	-	5 (approximately)	[191]
Harakeke	PP	FDM	30wt%	38.5	-	2.8	[218]
Basalt	PLA/PCL	FDM	15wt%	44.5-80.5	-	3.0-5.3	[225]
Continuous Carbon fibre	Nylon	FDM	11vol%	216	250	7.7	[193]

The mechanical properties of natural fibre composites (NFC) fabricated by FDM process is mostly lower than those of composites manufactured by conventional IM. The FDM process, unlike IM, does not have compressive effect during AM production, the contact between fibres and polymer may not be fully developed, resulting in poor interface structure and hence bonding strength. High hygroscopic sensitivity and high swelling of FDM produced NFCs has also been reported [221]. Nevertheless, the thermal degradation of FDM produced NFCs was similar to that of IM and the shrinkage of printed NFCs (0.34%) was considerably lower than the printed pure polymer (2.13%) [150,218]. In short, AM of NFCs shows significant potentials to many industrial sectors and the interface bonding characteristics should be further examined and enhanced in near future.

2.4.3.2.2 Natural fibre reinforced composite interfacial bonding

Interfacial bonding of natural fibre composite is significantly crucial to mechanical performance, as mentioned before, load transferred from matrix to fibres through the interface, good bonding interface leads to a desirable reinforcement. The plant-based fibre composite has normally poor in interfacial bonding and moisture resistance due to the hydrophilic properties of fibres and commonly hydrophobic polymer matrix. Wetting of fibre leads to stress concentrations caused by interfacial bonding defects and wettability of fibre has been proven to deteriorate the toughness, tensile and flexural strength of composite [226,227]. There are several circumstances of interfacial bonding, mechanical interlocking, electrostatic bonding, chemical bonding and inter-diffusion bonding [228]. Good mechanical bonding occurs that the surface of fibre is coarse, which improve the interfacial shear strength between fibre surface and matrix. Electrostatic bonding has more effects for metallic interfaces. By applying coupling agent can help to achieve a chemical reaction between fibre surface and matrix, which can result in a good bonding and interfacial strength. Inter-diffusion bonding which is the interaction between the atoms and molecules in fibre and matrix [214].

The interfacial bonding can be enhanced through various methods, which are divided into physical and chemical approaches. Commonly chemical methods include alkali, acetyl, enzyme, silane and acrylonitrile treatments and also maleated anhydride can be employed as coupling agent [229,230]. When apply enzyme treatment on abaca/PP

composite, the tensile and flexural strength increase respectively 45% and 35% [231]. Beside the mechanical performance, enzyme treatment also offers benefit to environmental friendliness [230]. Alkali fibres treatment is commonly applied to wipe the hemicellulose, lignin, fat and wax of fibre, the cellulose is exposed and the surface roughness area improved by this process to enhance interfacial bonding. The structure of cellulose can be improved and increased fibre strength also been proven by alkali treatment process [232,233]. Physical treatment methods commonly include corona, plasma, ultraviolet, heat treatments, electron radiation and fibre beating [230]. UV treatment showed 30% improvement of flexural strength in jute/epoxy composite [234]. Besides, the interlaminar shear and flexural strength of plasma treatment process can be improved 47% and 45% respectively [235]. Heat treatment also provide an increase in 37% to sisal fibre strength, but heat treatment could result in a heterogeneous increase to the mechanical properties of composite [230,236]. Electron radiation can provide an increase (from 21% to 53%) of interfacial bonding performance due to the free radicals produced during process may cause a crosslinking between fibre and matrix [237]. Fibre beating has been seen to enhance 10% in strength to kraft/PP composite [238].

In short fibre composite, the dispersion of fibre is another important factor to affect the properties of composites. Good performance of composite such as good interfacial bonding, less voids and wetting resistance can be achieved by a desirable fibre dispersion [230]. Several parameters link to the dispersion of fibre which include process temperature, pressure and additives. Proper mixing process of composite also possess better fibre dispersion, twin-screw extruder has better performance than single-screw extruder in mixing quality [239].

Another important factor to the performance of composite is the alignment of fibre. When the fibre is aligned parallel to the direction of load, the mechanical properties of the composite can be significantly higher compared to the anisotropic composites where the applied load is not in line with the direction of fibres [240,241]. In natural fibre composites, it is difficult to achieve alignment of fibre due to the orientation applied short natural fibre is hardly to control. In synthetic fibre composite, a continuous fibre can be employed to realize fibre alignment. Nevertheless, several procedures are developed to implement fibre alignment in natural fibre composite. The traditional textile processing of fibre can help as a pre-process to produce a continuous yarn by warp spinning the fibre [242]. Continuous fibre can also be produced by using

pectin as an adhesive under a water mist, then dry during stretching condition [243]. Besides, a recently employed process called dynamic sheet forming (DSF), DSF is a process which suspend short fibre on water then sprayed out through nozzle on a rotating drum which covered with wire mesh, during rotating of drum, water is spin-dried and fibre is aligned in rotation direction. Recently a short hemp and harakeke fibre is developed which has over 100 MPa in strength [230].

Porosity commonly severe in NFCs due to poor wettability of fibres, hollow parts in fibre and rough surface of fibre [244]. Commonly the porosity of NFCs increases with the content of fibre, dependent on the length of fibre, fibre type, orientation and treatments. Flax/PP composite has been studied that increase the content of fibre from 56 to 72 m%, porosity of composite raising from 4 to 8 v% [245].

2.4.3.2.3 Natural based nano filler reinforced composite in AM

As another natural based reinforcement, cellulose, as one of the most abundant bio-fibre on the earth. With decades of researches and developments, micro or even nano sized cellulose with customizable properties has emerged, such as microcrystalline cellulose (MCC), nanocrystalline cellulose (NCC) and cellulose nanofibrils (CNF) [246,247]. Issues of AM lignocellulose and micro/nano-sized cellulose fillers are the insufficient interfacial bonding between hydrophilic fibre and hydrophobic matrix polymer, poor thermal stability and the distribution and dispersion of fillers when composite with polymers. These are essential heterogeneity among the composition of composites [248]. Various solutions were studied to overcome these issues like chemical modification, diameter control and optimized filament processing. Wang et al. [249] printed the MCC/PLA up to 30 wt% and efficiently modified the compatibility and adhesion of two material by employing silane coupling agent named KH-550 and PEG polymer as plasticizer. It results in enhanced printability by higher melt flow rate and increased mechanical properties (59.7 MPa of tensile strength and 50.7 MPa of flexural strength). The ductility has also been improved by added PEG, up to 12% in elongation at break. Dong et al. [250] introduced a printable L-lactide grafted CNF reinforced with PLA polymer and an annealing post-extrusion process. The ring-opening polymerization graft process successfully improved the dispersion of CNF in PLA in organic solvent and the annealing of filament treatment led to an enhanced tensile performance by 63 and 28% in tensile strength and modulus respectively.

2.5 Interim conclusions

There have reported a number of AM techniques, corresponding materials and proposed possible applications of AM technologies in various industrial sectors. Nevertheless, there are various limitations in both AM technologies and existing materials, which require further research and innovations, but the application of AM process and product shows continuous growth rapidly. AM could support the decentralized production to implement relatively small scale production and help simplify the manufacturing processes which can result in better cost controlling and tailor products to the requirements of customers.

Current AM technologies cover liquid, solid, powder and hybrid of liquid-powder printings. AM is now employed in prototype fabrication, hobby levels and small scale production. Several factors limit the further applications like production rate, long-running fabrication, limited product size and difficulties of maintaining product quality when fabricating. Overall, the FDM process currently has been most widely applied AM technology due to its lowest cost and simple machine setup, but the dimensional accuracy and anisotropic properties limit the wide applications of FDM. SLA process is limited employed in such as visual prototype fabrication due to the ultra-high resolution and surface finish. When applying metals as the printing materials, binder jetting technologies, such as Prometal, can considerably reduce the energy consumption compared to laser processes. SLS and 3DP can be applied to fabricate short fibre composite and only FDM and LOM process can print long fibre composite.

Various materials are available for AM processing including both synthetic and bio-based polymer and their composites, however, the printable polymers are still limited in thermoplastic polymers with reasonable viscosity. Reinforced composites offer the compensation of several insufficient properties in pure polymers, but major challenges remain, such as inferior mechanical performance due to poor compatibility and interface of fibre and matrix, although continuous fibre reinforced composite shows potential superior mechanical performance. Full bio-composite (natural fibre composite with biopolymer) becomes most attractive in AM with promising properties needing further studies.

Massive potentials of AM and the corresponding materials have emerged, but further development is highly required. The 'traditional' AM could be evolved to all spectrum

of printing scalability (nano to mega), ultra-high resolution printing, fast printing, high performance composite printing, hybrid AM technology and 4D printing etc.

3. Materials and Methodology

3.1 Materials

3.1.1 Polylactic acid (PLA)

PLA has been implemented in the AM industry for years and now become the most applied 3D printing filament due to several certain advantages which mentioned in the previous chapter. In this study, the PLA was applied as both a standalone printing polymer and polymer blends, which was coordinated with another biopolymer. The trade name of neat PLA was Areoblend 2640[®], supplied by TECNARO GmbH. The density of the PLA applied in the research is between 1.24-1.26 g/cm^3.

3.1.2 Polyhydroxybutyrate-co-valerate (PHBV)

Polyhydroxybutyrate-co-valerate (PHBV) is gaining increasing attention in the bio-based polymer market due to its promising properties, such as high biodegradability in different environments, not just in composting plants and processing versatility. Indeed, among biopolymers, these biogenic polyesters represent a potential sustainable replacement for fossil fuel-based thermoplastics. Most commercially available PHBV is obtained with pure microbial cultures grown on renewable feedstocks (i.e. glucose) under sterile conditions, but recent research studies focus on the use of wastes as growth media. PHBV can be extracted from the bacteria cell and then formulated and processed by extrusion for production of rigid and flexible plastic suitable not just for the most assessed medical applications, but also considered for applications including packaging, moulded goods, paper coatings, non-woven fabrics, adhesives, films and performance additives [251]. The PHBV applied in the research is in fine powder, supplied by Tianan ENMAT^{TM} Y1000P. The density is 1.25 g/cm^3, melting temperature is 170 °C, tensile strength is 39 MPa.

3.1.3 Copolymers and additives

3.1.3.1 Polycaprolactone (PCL)

Polycaprolactone (PCL), is another bio-based polymer which can be employed in the AM. PCL is a partially crystalline bio-based polymer, which is produced by a ring-opening polymerization process of crude oil. The low melting temperature of PCL

(around 60 °C) lead to lower printing temperature and also a potential superior processibility since the low viscosity of PCL [252]. The mechanical properties of PCL are moderate, and the ductility is impressive which can be applied as a copolymer in this research. PCL polymers are currently applied in the tissue engineering and similar biomedical applications since the biocompatible and relatively high cost [253]. The PCL polymer applied in this study is sourced from Sigma-Aldrich, the average molecular weight M_n is 80,000, the melting temperature is around 60 °C and density at 25 °C is 1.145 g/mL.

3.1.3.2 Polybutylene succinate (PBS)

Polybutylene Succinate (PBS) is employed as a copolymer in this research. It's a biopolymer from the condensation of succinic acid, 1-4 butanediol (BDO) and most of cases, a third monomer organic di-acid. It offers an attractive performance to the plastic industry. PBS is bio-degradable and compostable and also a crystalline polymer with relatively high processing temperature (Tm is higher than 100 °C and up to 200 °C dependent on the conversion procedure), which allows a broad range of application. Although a long exposure time in a high temperature can lead to a reduction of mechanical properties, due to chain scissions, the degradation of polymer and risen rheological properties may also happen. PBSA is a common engineering biopolymer in the industry, and it is PBS with an additive called adipate acid [254]. The mechanical performance of PBS and PBSA are provided below in Table 11. When comparing the PBS to the petroleum-based polymer, PBS has a similar mechanical performance to LDPE [255]. The PBS pellets in this research is supplied from Sigma-Aldrich, the T_m is 120 °C and density is 1.3 g/mL at 25 °C.

Table 11 Exemplary physical properties of PBS compared to other(biobased) polymers

Polymer	PBS	PBSA	PLA	HDPE	LDPE	PP
Glass transition temp (°C)	-32	-45	55	-120	-120 to -40	-5
Melting temperature (°C)	120	96	140 to 180	129	110	163
Tensile strength (MPa)	34	19	66	28	10	33
Elongtation at brake (%)	560	807	4	700	300	415
Degree of crystallinity (%)	34 to 45	20 to 30	0 to 40	69	49	56

3.1.3.3 Polyethylene glycol (PEG)

Poly(ethylene glycol) (PEG) is commonly used as a plasticizer in PLA biopolymer, the efforts of PEG are to improve the crystallinity and enhance biodegradability of PLA polymer [256]. Plasticizers with relatively higher M_w are recommended for better miscible and compatible [257,258]. The PEGs are employed as one of the most competent additives to reduce the T_g of PLA polymer and it is reported that they have more than 20% efficiency than other plasticizers. Other blends present a limitation of miscibility and the T_g touches a plateau value [259]. When investigating the PHBV/PEG copolymer using XRD, the crystallinity degree is relatively high when the values ranging from 60% to 90% based on the percentage of the PEG due to the high crystallinity of PEG. The PHBV used has a mol weight of $M_w = 206000$ g mol^{-1} and the PEG has $M_w = 1350$ to 1650 g mol^{-1}. The PEG plasticizer also lead to a reduction of the melting temperature of PHBV polymer. The PHBV/PEG copolymers are uniform from the SEM analysis result, but the PHBV/PEG: 50%/50% composition is presented too heterogeneous [260]. The PEG which is applied in this work, a white powder, has average mol weight 8,000 from Sigma-Aldrich.

3.2 Methodology

3.2.1 Filament processing

Raw polymers (granulates and powders) were weighted and mixed by a stirrer if needed, then dried the polymer in the preheated 40 ˚C oven for 24 hours. The compounding was carried out by the Barbender, W 50 EHT measuring mixer. The mixing type was roller blades, and the bowl volume was approximately 55 cm^3. The maximum torque and operating temperature were 200 Nm and 500 °C respectively. To determine the sample weight as follows:

$$m = V(cm^3) \cdot \rho_M(g/cm^3) \cdot K$$

With:

$m = mass\ of\ the\ sample\ material$

$V = mixer\ volume: 55\ cm^3 with\ roller\ blades$

$\rho_M = density\ of\ the\ sample\ material\ at\ ambient\ temperature$

$K = constant\ 0.7 - 0.8$

The mass of each material compounding was between 47.3 g to 55.4 g, each sample material composition had three separated compounding sessions, therefore, the weight of each sample material was in the range of 142 g to 166 g.

After the compounder was preheated to around 180 ˚C (compounder temperature was varied dependent on the polymer composition) and roller blades speed was 50 rpm, the mixed polymer sample was poured into the feeder, then compacted and sealed the feed inlet. After mixing for around 3 mins until the internal pressure dropped to a constant level, the chamber was opened, and mixed melt polymer was removed by using a copper scraper. The shredder was applied to downsize the compounded bulk polymer into granulates for further filament extrusion. The sieve was setup to 2 mm and shredded for 30 seconds, 3 times due to overheat prevention.

The single screw measuring extruder in this study was supplied by Brabender. The sample material was plastified under practice-oriented conditions and extruded through

the die head. All measuring values such as torque, melt temperature, melt pressure (if requested, screw backforce, too) were recorded continuously and presented in the form of tables and diagrams parallel to the running test. The diameter of the screw was 19 mm and length was 25D. Maximum torque and operating temperature were 150 Nm and 450 ˚C respectively. The die heads were shown below in Fig. 19, heated electrically and form separated control zones triggered by the temperature control unit. The required dimension of the printing filament was approximately $1.75 \ mm \pm 0.07mm$, therefore the round strand die head with 2mm die insert nozzle was applied on the extruder.
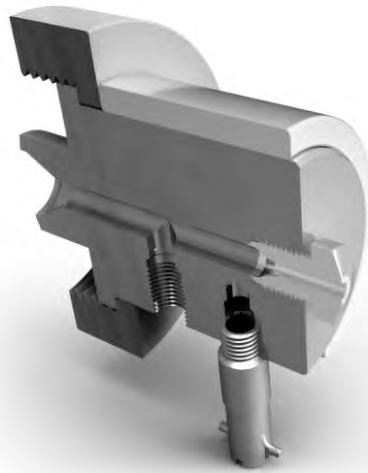
Fig. 19 The structure of the round die head without the die insert nozzle

A follow-up conveyor belt was applied to adjust the diameter of extruded filament, the belt speed could be controlled to achieve optimized diameter and the extruded material then stayed air cooled on the conveyor belt. The diameter was consistently measured by vernier calliper at the end of conveyor belt for further printing process. Therefore, the diameter deviation of filament might not match with the commercial filament which was fabricated by laser diameter controlling system ($1.75 \ mm \pm 0.03mm$).

3.2.2 3D printing

The 3D printing process in this research was fused deposition modelling (FDM), which was currently the most common additive manufacturing process. Abovementioned the

detail and properties of this process have been discussed in the last chapter. The printer used in the study was Prusa i3 MK3 printer, which was an open sourced FDM printer. In this research. The setup of the printer is shown in the Table 12 below.

Table 12 General printing parameters of the Prusa i3 MK3 printer

	Parameters
Nozzle diameter	100-600 µm
Printing temperature	Up to 350 ˚C dependent on the material
Platform temperature	Ambient temp to 120 ˚C
Printing speed	Up to 200 mm/s
Layer thickness	50-200 µm
Infill	Up to 100%

The process of the 3D printing is shown below in Fig. 20. The sample was created in 3D model by the Solidworks by importing the 3D drawing model in the slicing software (Simplify3D) to output the printing parameters and procedures (G-code). The last step was to transfer the controlled G-code to 3D printer and then the fabrication of sample.
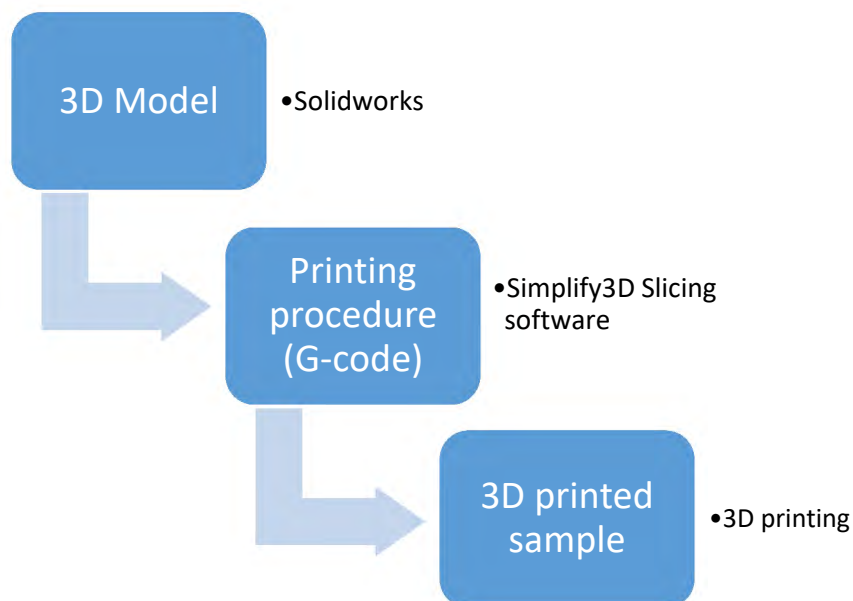
Fig. 20 The process of the FDM 3D printing

The UI (User interface) of the Simplify3D slicing software is given below in the Fig. 21 and the general setting of the printed sample is also summarised below in Table 13. The setting and sample parameters are variable dependent on different material and testing and all setting and parameters will be described in the following chapter.
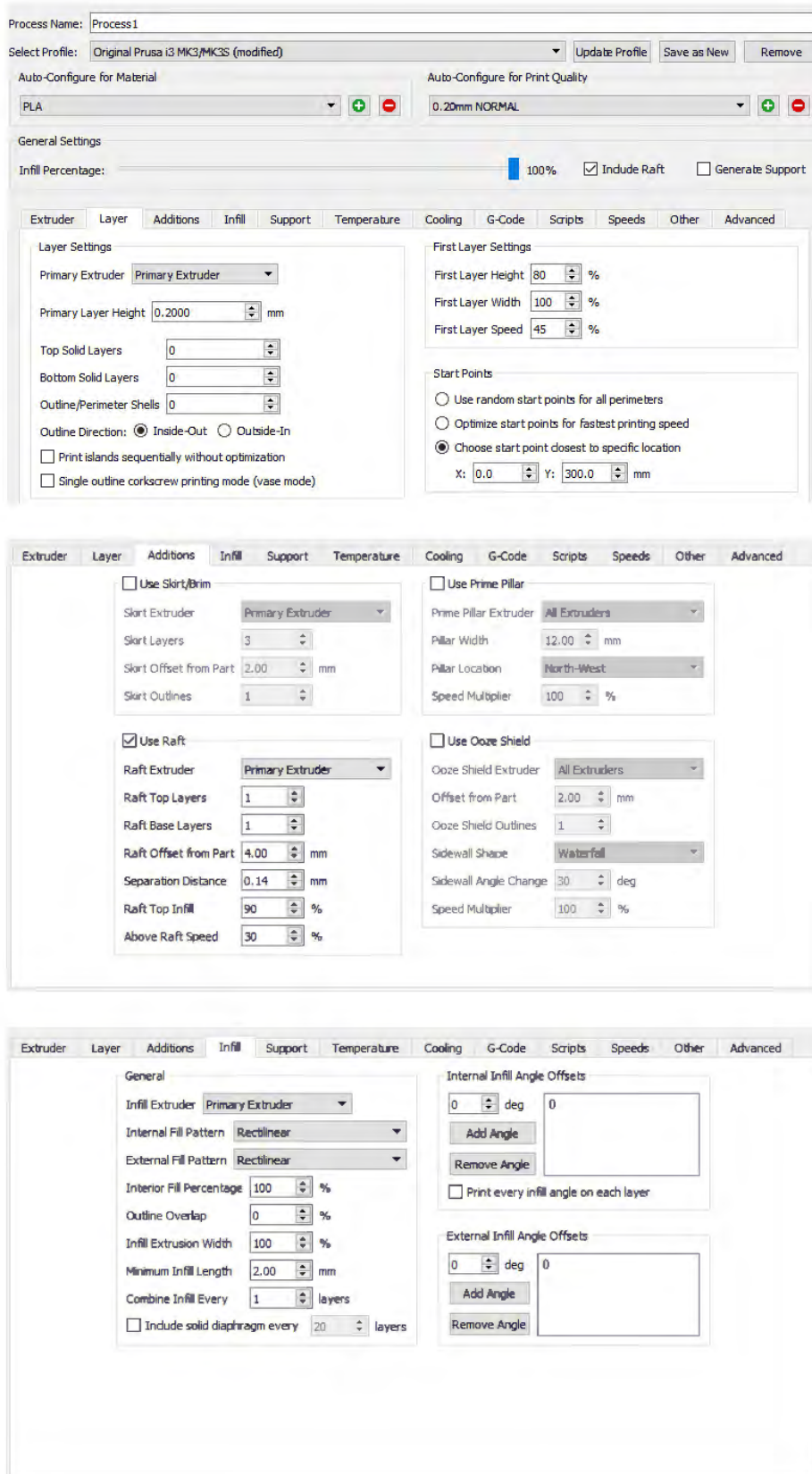
Fig. 21 Detail of printing parameter settings and the UI of Simplify3D slicer software

Table 13 Slicing setting and sample parameters

	Parameters
Sample diameter (Length*width*thickness)	$50 \times 10 \times 3\ mm$
Printing temperature	170-230 ˚C dependent on the material
Platform temperature	50-60 ˚C
Printing speed	50mm/s
Layer thickness	0.2mm
Infill	100%

The printing samples were designed into x and y printing orientations, printing path of two designs are shown below in Fig. 22. To investigate the interface of printed filaments from outside of the part, there was no outer 'wall' designed in the samples. And the infill was setup to 100% to investigate the maximum capacity and to achieve the minimum porosity of 3D printing part. Due to warping happened in some of the sample printing and the adhesion of printed material and platform had failed. To bring into correspondence with all printed parts, a pre-printed 'raft platform' was designed embedded into the printing programme before the sample start to be fabricated. The setting has been provided in Fig. 22 and the printed material raft platform designed and the fabrication process of 3D printing part (x axis specimen) has been provided. The printed specimens then put into drying in the ambient temperature and humidity for 24 hrs for the further testing and characterization.
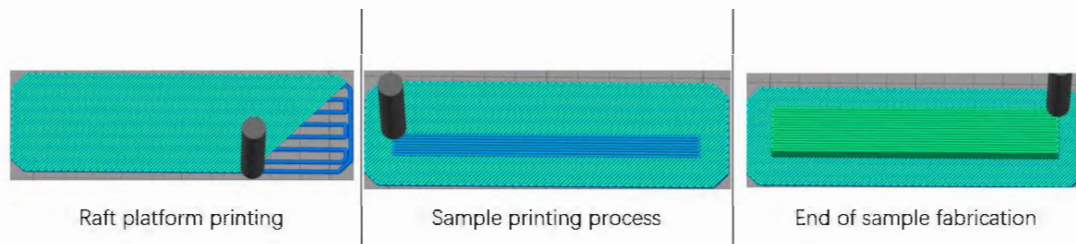
Fig. 22 Printed 'raft platform' and specimen 3D printing fabrication

The weight ratio of PHBV was ascending by 20% each composition from 90:10wt%, but the 10:90 wt% and neat PHBV specimens were difficult to build due to severe wrappage and nozzle clogging were occurred on our printer. The x-axis neat PHBV specimen was fabricated by another industrial printer (INTAMSYS Funmat HT) as a reference but only x-axis due to the difficulty of printing and inconsistency of the filament diameter. With the ascending PHBV ratio, the warpage occurred more often due to the thermal properties of PHBV, which will be discussed in the following sections. To prevent the wrappage during printing process, the printing specimens were taped after the raft was printed for extra adhesion, before the actual sample was manufactured for the PLA/PHBV 50:50 wt% and PLA/PHBV 30:70 wt% specimens.

In Chapter 5, four different material proportions were employed in this study, which increased with the ascending of PHBV ratio, and the printing parameters are shown in the Table 14. Due to the different thermal properties like thermogravimetric and thermorheologic properties, the printing temperature was decreased with the increasing proportion of PHBV.

Table 14 Printing parameters of PLA/PHBV copolymers

	Printing temperature	Platform temperature	Printing speed	Extra adhesion	Infill	Printing Orientation
PLA/PHBV 90:10 wt%	215 ˚C	60 ˚C				x & y axis
PLA/PHBV 70:30 wt%	210 ˚C	60 ˚C		✗		x & y axis
PLA/PHBV 50:50 wt%	205 ˚C	55 ˚C	50 mm/s		100%	x & y axis
PLA/PHBV 30:70 wt%	200 ˚C	50 ˚C		✓		x & y axis
PHBV	190 ˚C	50 ˚C				x axis

Samples printed in both x-axis and y-axis orientations were prepared with few exceptions which the printing process could not be completely finished due to various reasons like the sever warpage occurred.

In Chapter 6, due to the different processing temperature of copolymers, they were separately employed in the modification. Due to there was difficult to print neat PHBV employing current printer, to evaluate the improvement of the printability of PHBV and other effects of modification, the PCL and PBS were separately applied to the PHBV polymer. Then the PCL was added as a copolymer to modify the brittleness of the PLA/PHBV blends. The PBS copolymer and further PEG which acted as an additive were added into PLA polymer to investigate the variation of ductility and anisotropy property.

Table 15 summarised the samples studied in this chapter and their processing parameters. The printing temperatures were determined in proportion to the added weight ratio of copolymers and additives and their thermal properties were based on the supplier's specifications.

Table 15 Printing parameters of modified materials

		Printing temperature	Platform temperature	Printing speed	Extra adhesion	Infill	Printing Orientation
PLA based	PLA/PBS 80:20 wt%	210 ˚C	50 ˚C				x & y axis
	PLA/PBS 80:20 with 2% PEG	210 ˚C	50 ˚C		✗		x & y axis
	PHBV/PCL 90:10 wt%	200 ˚C	50 ˚C				x & y axis
PHBV based	PHBV/PCL 80:20	190 ˚C	55 ˚C				x axis
	PHBV/PBS 80:20 wt%	190 ˚C	55 ˚C	50 mm/s		100%	x axis
	PHBV/PLA/PCL 75:20:5 wt%	190 ˚C	55 ˚C		✓		x axis
	PHBV/PLA/PCL 70:20:10 wt%	190 ˚C	55 ˚C				x axis

3.2.3 Vertical density profile (VDP)

Vertical density profile (VDP) was an important parameter that relates to both mechanical and physical properties of composites. VDP showed the density variation through the thickness direction, which was started to develop when the top and bottom hot-press platens contact the surface of the wet mat [261,262]. To evaluate the mechanical and physical properties of the sample like particleboard or other polymer boards, the vertical density profile (VDP) was a beneficial method.

The theory of VDP testing was based on the principle of radioactive radiation and reception, a non-contact measurement was carried out by employing the absorption of the ray. When the ray irradiated the material, it was attenuated due to the partial absorption by the material. By detecting the change in the attenuation count rate, which

was caused by the ray penetration into the unit section of the specimen (per unit time), the indirect measurement of the unit section density of the specimen was achieved. The process was shown below in Fig. 23.
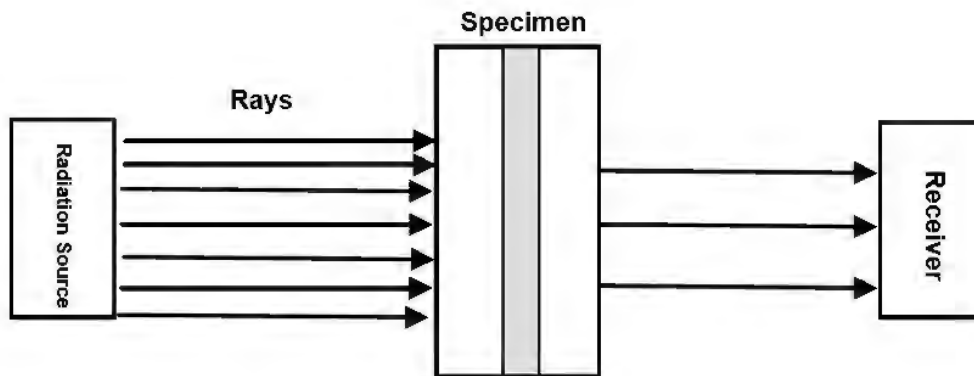
Fig. 23 The principle of radioactive radiation and receiving.

The ray scans along the thickness direction of the specimen and the radiation intensity after passing through the specimen was calculated below:

$$I = I_0 e^{-\mu \rho t}$$

$I = Radiation\ intensity\ after\ absorption$

$I_0 = Radiation\ intensity\ before\ absorption$

$\mu = Mass\ absorption\ coefficient$

$\rho = Density\ of\ the\ specimen\ (g/cm^3)$

$t = Thickness\ of\ the\ specimen\ (cm)$

In this study, X-ray profile densimeter (DENSE-LAB, EWS, Germany) was applied. Before implementing the sample in the instrument, dimensions and weight of the sample were measured, and then the bulk density was calculated to calibrate the VDP instrument. The density of the sample was tested at intervals of 0.04 mm through the thickness direction of printed samples. All printed specimens have been tested to investigate the internal printing quality.

The geometry design of the neat PLA sample is blocked with a square side: $length \times width \times thickness = 50 \times 50 \times 20\ mm$. The following PLA/PHBV and

modification specimens applied in the VDP were using the size of $length \times width \times thickness = 50 \times 10 \times 3\ mm$ due to limited filament produced.

Layering thickness is 200 μm and printing speed is 50 mm/s. The printing temperature was set in an ascending order from 200 to 230 ˚C at intervals of 10 ˚C and the printing flatform temperature was 60 ˚C for all PLA specimens. 10 specimens were built in each printing temperature. The density of the sample was tested at intervals of 0.02 mm, profiling across the thickness direction of printed samples.

3.2.4 Mechanical performance

The mechanical performance in this research was tested in a static tensile test on an Instron 5900 series universal testing machine, under conditions in compliance with BS ISO 527 standard. The shape of the specimen is rectangular and the size is $length \times width \times thickness = 50 \times 10 \times 3\ mm$. Due to the limited printed specimens of PLA/PHBV and following modifications, there were not enough sample capacity for other mechanical evaluations, hence only tensile properties were tested. Before setting up the sample on the Instron machine (Fig. 24), due to the geometry inconsistency of the 3D printed specimens was inevitable in this study (due to different material properties and large tolerance of filament diameter), the actual widths and thicknesses of the samples were measured by vernier calliper after drying process. A continuous and constant load was applied until the material fails. The Young's modulus could be calculated by employing the equation shown below when the sample material was working against the load applied:

$$E_{max} = \frac{k_{average} l_{average}^3}{4 w_{average} t_{average}^3}$$

$E_{max} = Maximum\ of\ Modulus\ of\ Elasticity$

$k_{average} = Average\ gradient\ of\ linear\ part\ of\ force\ deflection\ graph$

$l_{average} = Average\ distance\ between\ supports$

$w_{average} = Average\ width\ of\ sample$

$t_{average} = Average\ thickness\ of\ sample$

A set of axes were designed to study the bonding mechanism of 3D printing objects. All the samples with different printing orientations ought to be tested on the Instron machine. The printed samples with X axis printing orientation had main axis aligned with the tensile force and the sample with Y axis orientation as an antithesis, the tensile load was perpendicular with the transversely bonded printed filament. Fig. 25 shows the relationship of tensile load and printing orientations. The testing speed was fixed to 2 mm/min and the tensile strength of the sample can be calculated by the output of the testing from the 'Bluhill' software. The force (F) and extension length (Δl) as the output of tensile testing could lead to the ultimate tensile stress (σ_{UTS}). The engineering strain (ε) was given by applying the following equations:

$$\sigma_{UTS} = \frac{F_{Max}}{A} = \frac{F_{Max}}{t \times w}$$

$\sigma_{UTS} = Ultimate\ tensile\ stress$ (MPa)

$F_{Max} = Maximum\ force\ expressed\ in\ Nowton\ (N)$

$A = Average\ cross\ section\ in\ mm^2$

$t = thickness\ in\ mm$

$w = width\ in\ mm$

And

$$\varepsilon = \frac{\Delta l}{l_0}$$

$\varepsilon = Engineering\ strain\ (mm/mm)$

$\Delta l = Extension\ length\ in\ mm$

$l = The\ orginal\ gauge\ length\ before\ load\ applied\ (mm)$

Fig. 24 The setup of tensile properties testing on the Instron machine

Fig. 25 The relationship of load applied and printing orientations

3.2.5 Microstructure characterization

The morphology of the printed samples was inspected, and the images were captured by LEO 1455VP scanning electron microscope (SEM). Both cross-section and fracture surface after tensile property testing were examined in the research. For the observation of cross-section image, the fracture surface was taken in the middle of the sample at the length direction. The cut surface was wiped and then gold-plate coated. The fracture surface was cleaned with a soft brush and coated directly.

Gold coating was processed by using the sputter coater. The coating voltage was set to 1.5kV, plasma current was 15 mA and manual operation was selected. Then the coating

process was started and held under an argon atmosphere. Ventilation step was necessary when the coating process is finished before removing the sample out. SEM images were taken by a LEO high-resolution SEM with a probe moulded. SEM was carried out from 1 to 10 kV on the LEO 1455VP. Spot size, aperture settings and working distance were chosen to maximise focal working depth. Each image needed to be acquired with the sample correctly centred to ensure that enough overlap with adjacent images can be identified by the reconstruction software. The macros written to control the stage require that sample height, centre of rotation and tilt centre be correctly calibrated. The image acquisition macros were used to acquire the following image series:

- The electron gun moving vertically up or down.
- The sample holder moving horizontally left or right for the position of the electron gun to be focused on the samples.

3.2.6 Nanoindentation

Nanoindentation has been proven a powerful quantitative testing technique for acquiring mechanical performance from a very limited material volume like the interface of composites, thin film or coating [263]. The mechanical properties like elastic modulus, hardness, fracture toughness and yield stress can be determined by this process. This process offers an amount of penetration of nano-indenter tip into the tested material and the measurement of this process is normally applying a constant loading rate or a constant displacement rate. The contact areas and penetration depth can also be inspected during the process [263,264]. The purpose of applying nanoindentation in this research is to evaluate the interphase properties between the printed filament material, a better understanding of the interphase of the printed part can help to reduce the inherit anisotropy properties of 3D printing part and understand its effect on the performance of the printed products.

During the nanoindentation process, a three-sided pyramidal Berkovich indenter tip approached the surface of the specimen. Fig. 26 indicates the contact indention of the specimen in microscope as an example. After the specimen was tipped, the load increased linearly and the surface of the material was indented. Then a dwell time was given at the maximum force and then the sample was released. The stiffness of the sample was measured when the unloading process was about to start. The mechanical performance such as Young's modulus and hardness of the specimen then exported

from the machine with the calibrations of the data of load and tip displacement along with the close loop area.

The prerequisite for calculating the hardness and elastic modulus of the sample is to accurately measure the elastic contact stiffness (S) and the contact area (A). Oliver-Pharr method is currently one of the most widely applied methods for determining S and A, the principle and process are as follows:

To establish the relationship between load and unloading depth, fit the unloading part of the load-indentation depth curve,

$$P = \alpha(h - h_f)^m$$

P is the applied load, α and m are the fitting parameters. The elastic contact stiffness can be acquired by differentiating equation (4-5),

$$S = (\frac{dP}{dh})_{h=h_{max}} = \alpha m(h_{max} - h_f)^{m-1}$$

The maximum indentation depth h_{max} is greater than the contact depth h_c for the elastic contact. The contact depth h_c can be calculated by the theory of elastic contact,

$$h_c = h_{max} - \varepsilon \frac{P_{max}}{S}$$

In the equation, ε is a constant, which is dependent on the type of the indenter; for the unloading behaviour of the three-sided pyramidal Berkovich indenter, ε=0.75. The contact area is determined by the area function $A = f(hc)$. For Berkovich indenter, $A = 24.56h_c^2$, but the actual area function should be different from the ideal area function in the area which the indentation is relatively superficial, and it needs to be corrected as following equation on the basis of the ideal area function.

$$A = 24.56h_c^2 + \sum_{i=0}^{7} C_i h_c^{\frac{1}{2^i}}$$

C_i is depended by the type of indenter and can be determined by experiments. The harness which is the measurement of load bearing capacity of the sample, can be acquired as following equation,

$$H = \frac{P_{max}}{A}$$

And the reduced modulus is defined as,

$$E_r = \frac{\sqrt{\pi}}{2\beta} \frac{S}{\sqrt{A}}$$

β is a constant which is based on the type of the indenter, for Berkovich indenter, β=1.034. The indentation modulus (E_i) of the sample material can be obtained from the following equation,

$$\frac{1}{E_r} = \frac{1 - \gamma^2}{E} + \frac{1 - \gamma_i^2}{E_i}$$

$E = Modulus\ of\ the\ specimen$

$\gamma = Poisson's\ ratio\ of\ the\ specimen$

$E_i = 1141\ GPa, which\ is\ the\ Modulus\ of\ the\ indenter$
$\gamma_i = 0.07, which\ is\ the\ Poisson's\ ratio\ of\ the\ indenter$

The nanoindentation process were carried out in a TI 950 Triboindenter supplied by Hysitron, USA. The in-situ scanning probe microscopy (SPM) was also offered by this nanomechanical testing instrument. The driving, load and displacement measurement were integrated and fixed on a piezoelectric scanner to achieve three-dimensional high-precision indenter positioning and in-situ imaging, the schematic diagram of piezo scanner was shown in Fig. 27.
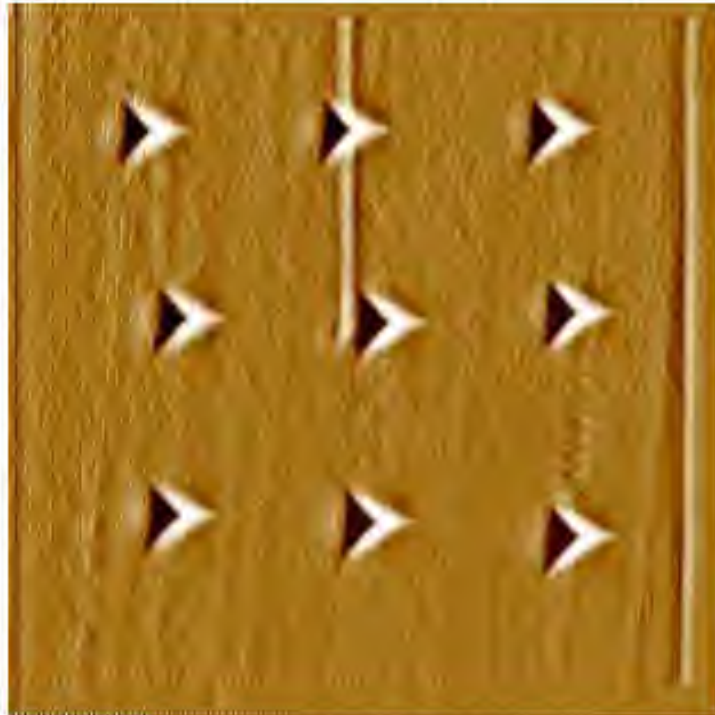
Fig. 26 The contact indention of the PLA specimen under the optical microscope
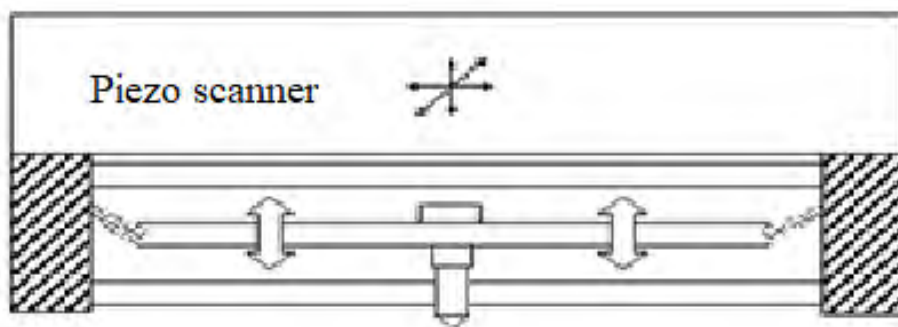
Fig. 27 The schematic diagram of Piezo scanner

3.2.7 TGA analysis

Thermogravimetry analysis (TGA) was applied in the study to evaluate the thermal characterization of the bio-copolymers, both crystalline and amorphous polymer could be examined. TGA measured the degradation of biopolymers with an enthalpy change observed and the various thermal transitions such as milting of the polymer [265,266]. By using TGA, the components of a sample can be measured, including the moisture and volatile content. A highly sensitive scale measures weight changes, and a programmable furnace controls the temperature of the sample. Above the furnace, the

balance is thermally isolated from the heat and hangs down in the furnace with a high-precision wire. For maximum sensitivity, accuracy, and precision of weighing, the sample pan should be at the end of the hang-down wire and isolated from thermal effects (e.g., employing a thermostatic chamber). TGA can also identify and analyse gases generated from degradation of the sample with the addition of an infrared spectrometer [267]. The derivative thermogravimetry (DTG) curve can also be introduced to indicate the weight loss rate of the material.

The Simultaneous DTA-TG apparatus (DTG-60, Shimadzu, Japan) and Differential scanning calorimeter (DSC-60, Shimadzu, Japan) was employed in this work. The TGA Investigations were processed by heating the samples from 25 to 550°C at the rate of 10°C/min in the air atmosphere. The mass of the specimens varied from 4.3 mg to 7.2 mg and simultaneous recording of TGA signals were applied.

4. PLA Printing Optimization and Interface Structure

4.1 Introduction

Pioneers have studied [268-270] the heat transfer model in the FDM process and made conclusions based on three assumptions as follows:

1) The cross-sectional area of the filament bead has homogeneous temperature distribution.

2) The filament is considered semi-infinite.

3) Coefficient of heat convention is assumed consistent.

Although different models have been established, most of the models have to neglect some features like heat transfer between the filament and printing platform. It is difficult to take all the variates into one model. However, mutual conclusions from different models have been established. In the early stage of the filament cooling after being printed, most of the neck growth is formed when the filament temperature is above the glass transition temperature. Most of material bonding occurs at a very short period of time after the filament is extruded.

It is apparent that all the established models led to a conclusion that 3D printing process is extremely temperature sensitive. Therefore, four different printing temperatures have been studied in this chapter to investigate the outcome of interfacial bonding of 3D printing PLA polymer by using VDP analysis. The further mechanical properties and microstructure have also been studied. The boundary quality of printed filament beads is also tested by nanoindentation process.

4.2 Boundary theory and mechanism of 3D printing polymer

The filament bonding in the 3D printing is critical to the final quality of the part. The anisotropy performance is highly determined by the bonding quality of adjacent filament. It is one of the inherent properties in additive manufacturing industry due to different boundary performance. On a molecular level, chemical bonding among the polymer chains strongly determines the mechanical properties of the printed part.

During the printing process, a neck is formed due to the heat distribution of the melt printed bead start to contact the previously printed bead till the absorptive equilibrium is achieved. Polymer chains diffusion is occurred, and an interfacial zone is formed due to the molecule's diffusion across two beads. The flow of viscous polymer is limited during the neck formation process and randomization can be reached when substantial interdiffusion of chain segments under the boundary conditions. The viscosity of the material rises on materials cooling and the quality of the printed object is critically affected by the viscosity variation tendency. This includes the thermal conductivity and capacity of the printing material, and the external features which affects the cooling rate of the material like printing temperature, printing platform temperature and the temperature of printing environment. A better material flow when melt can normally lead to an improved polymer bonding process. A higher thermal conductivity of the material will also result in an increase in the chemical bonding of filament beads. However, there is a limitation of printing temperature due to degradation may occur and the geometrical accuracy can be deteriorated due to excessed material flow during printing process. Fig. 28 shows the bonding process of the adjacent printed bead which is established by Bellehumeur et al [268].

1) surface contact 2) neck formation

3) diffusion and neck growth 4) randomization
Fig. 28 Filament bonding process
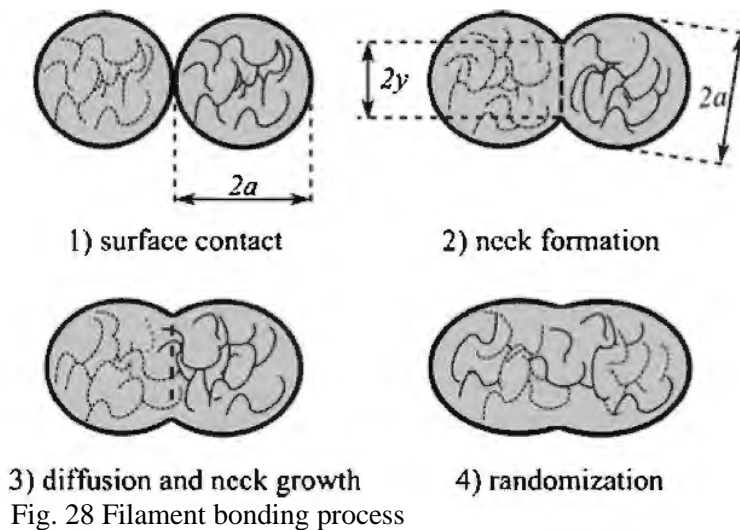
4.3 Effect of printing temperature and postprocess on the density profile of PLA polymer

To evaluate the effect of printing temperature on the printed parts, the density profile of PLA samples is firstly plotted (Fig. 29). It can be seen that while all four printing temperatures result in similar density profile/tendency across the thickness of the specimen, there are several interesting features after the scrutiny of the profile diagram.

It is evident that the average density result of PLA specimens printed at 200 °C has the greatest amplitude between the highest and lowest density, and lowest average density along the printed sample thickness, especially for the layers approaches the bottom and top surfaces. The lower density at the bottom layers is mainly because low temperature of printing bed leads to lower neck formation and less homogeneous structures. The average density of the printed parts at 200 °C printing temperature is 1.144 kg/m3, which is 2.1%, 3.3% and 3% lower than that printed with a temperature of 210 °C, 220 °C and 230 °C respectively. However, specimens printed in other three temperatures have lower wave amplitude (Fig. 29).

The density of the printed part with the temperature of 210 °C is higher than that with the temperature of 200 °C, is low in the bottom surface and seems to decrease slightly from one surface to the other surface. The density also increased considerably in the top section of the sample (Fig. 30). This may be due to that the temperature of the printed beads is low, the heat from the printer platform cannot be transferred through the printed material. Therefore, the 'platform temperature' of this area will be closed to ambient temperature, which is room temperature. This may lead to higher voids between layers. The 220 °C and 230 °C have similar waves and the zoomed diagram has been provided for further discussion in Fig. 30.

It is interesting that the composites printed with a temperature of 220 °C have the highest average density, especially higher density in the bottom and mid-section of the sample compared with that printed at 230 °C temperature. It seems that the printed part at 230 °C temperature have a more uniform density distribution across the thickness, which may be due to less influence from the heat printing platform, as the printed PLA filament has the highest thermo-rheologic properties compared with other samples. However, it must be noted that the high temperature could also disorder the dimension

of the final part. As the printed part for the density profile testing is bulk, the printed material has sufficient cooling time before the next layer covers the previous layer, therefore, the dimension disorder is not visible in this analysis process.

It is apparent that the fluctuation from the average curve in the diagram may indicate the voids between the printed layers. The magnitude of the density fluctuation can be calculated as a percentage of porosity between two layers. Fig. 31. Shows that the raw diagram of VDP testing result, the voids among layers are generally reflected on the chart. The frequency of the wave is roughly 0.2 mm which is the layer thickness setup. The porosity of the sample is varied in the chart mainly due to the intervals along the thickness may skip the point which has the greatest pores, or it can also be caused by printing inconsistency. It will be further discussed in the following sections.
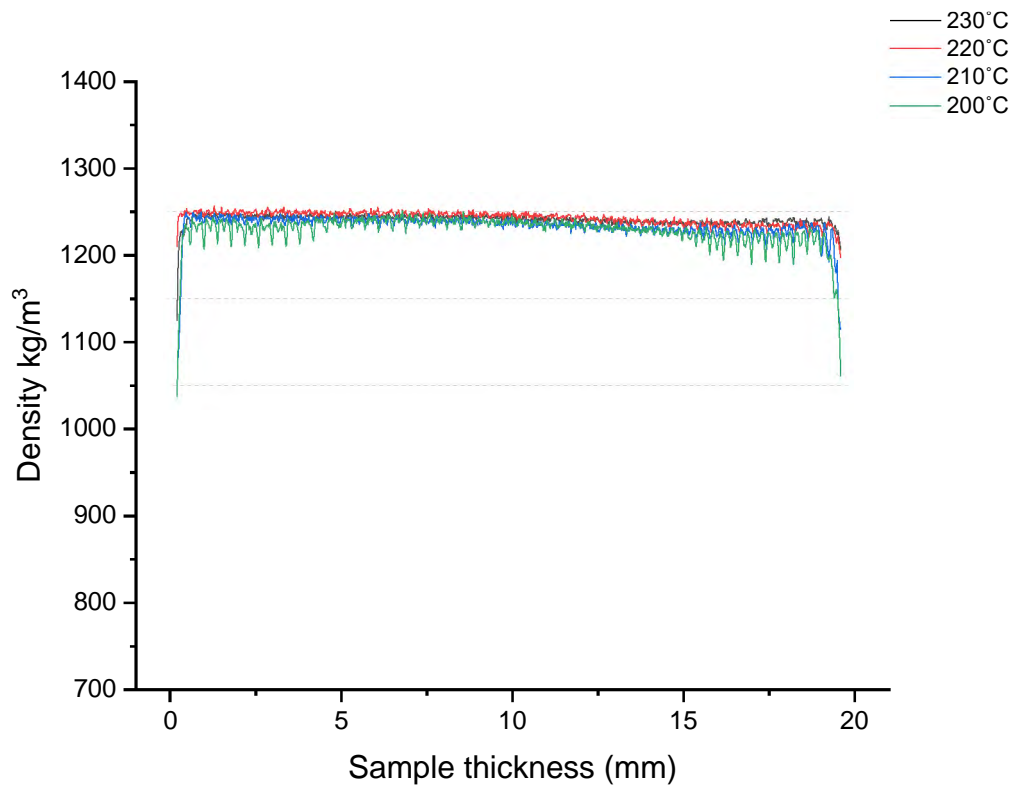
Fig. 29 Average density profile of PLA specimens printed at different printing temperatures
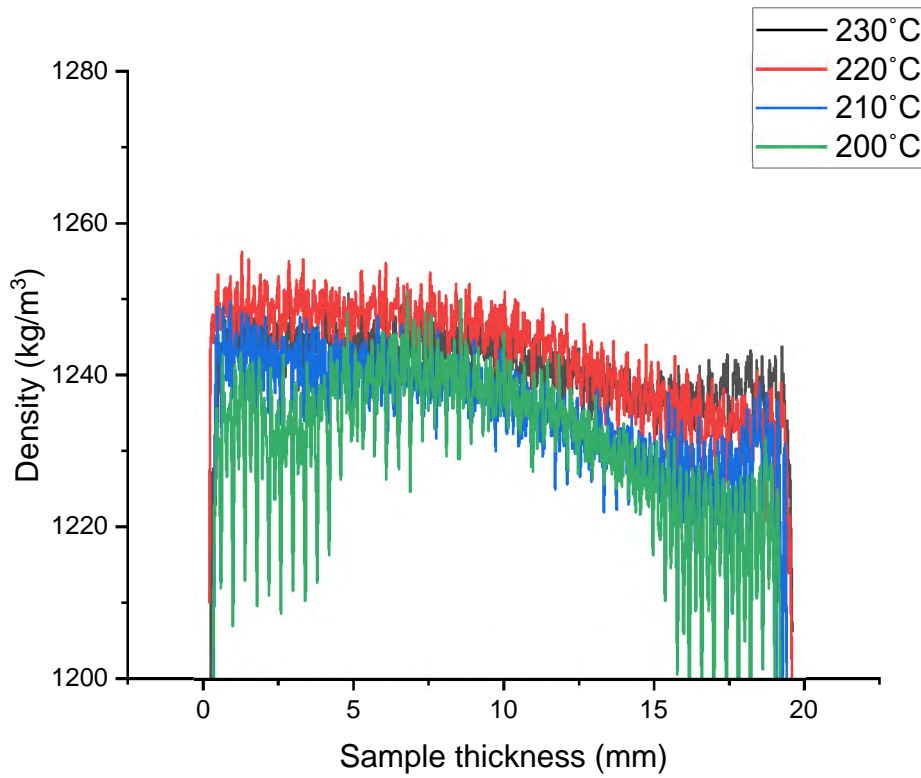
Fig. 30 'Zoom-in' density profile diagram of PLA
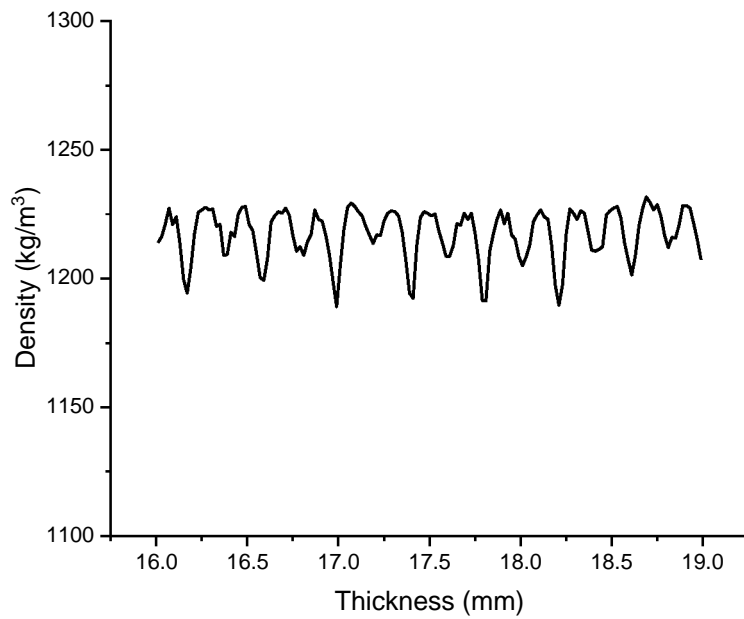
Fig. 31 Raw data of density profile of 220 ˚C

Table 16 Shows the density of samples of four different printing temperatures. The sample at 200 ˚C printing temperature has the lowest average density, which is 1.2%, 1.7% and 1.6% lower than the samples at the other three printing temperatures respectively. This may indicate that the average porosity between the layers is slightly larger than that of the samples printed with other printing temperatures. Meanwhile, comparing the density of the PLA raw material master batch (1.24-1.26g/m3), The specimens printed at the temperature 230 ˚C has the nearest density. After removing the bottom and top edge density data of the sample, the porosity of the sample can be obtained.

Table 16 Average density of PLA specimen printed in four printing temperature

	200 ˚C	210 ˚C	220 ˚C	230 ˚C
Density (kg/m^3)	1228.7	1233.5	1242.7	1240.7

Since the fluctuation of density profile distribution is inconspicuous (the range of fluctuation is subtle) compared to the density of the material, in order to analyse the trend of density aligned with thickness, a 'smooth' process has been carried out to the density profiles to investigate the trend of the density profile at each printing temperature intuitively. The 'smooth' data is obtained from averaging 50 density profiles and the density profile distribution after 'smooth' process are given in Fig. 32. The individual density profile is included in Appendix A. It clearly shows that the average density profile at the printing temperature of 200 ˚C and 210 ˚C is lower than that at the printing temperature of 220 ˚C and 230 ˚C. As the thickness increases, the sample density has a slight declination for all four printing temperatures. In the printing temperature of 230 ˚C, this declination is minimum compared with the specimens at other printing temperatures.

The density in near the bottom and top of the printed parts is significantly lower at lower printing temperatures, especially at the printing temperature 200 ˚C, although all printed parts have lower density near the bottom and top surfaces compared to the centre. It is also observed that in the bottom of the specimen, which is also the early stage of the printing process, there is a slight inconsistency, when the first layer of the PLA filament is printed on the pre-set 60 ˚C printing platform. Moreover, the deviation of the printing nozzle can also lead to the inconsistency in the early stage of printing

programme (±5℃ based on reading from the temperature sensor). This phenomenon occurs in the printing process for all printing temperatures and all different materials. This issue is especially severe at the printing temperature of 200 ˚C among all PLA specimens. It is considered that a quicker solidification during the deposition may result in a lower heat flow, which hence may deteriorate the printing process. Although this issue can be eased by the calibration of the printer and printing programme, the higher heat flow is recommended to achieve the higher density profile and further mechanical performance. A higher platform temperature may also lead to a lower geometry accuracy at the bottom layers due to the temperature of platform is higher than the glass transition temperature of PLA polymer.

Another low density profile also happened in the final stage of the PLA specimen printing, it is mainly due to the increase of pores, as the top layers of the printed materials may have lower pressure from self-weight compared to those layers printed previously. The deposited material has also been cooled down to ambient temperature rather than the printing platform temperature of 60 ˚C, which also increase the temperature gap and lead to a faster cooling down. Inconsistent geometry may also cause this reduction of density. The thickness deviation may also be significant for the specimen printed in a lower temperature.

As aforementioned, the melt PLA deposition previous layers on the ambient temperature can contribute the declination of the density, as the greater pores are created during printing. In addition, at a printing temperature of 230 ˚C, there is a lower density in the initial stage of printing compared to that at a printing temperature of 220 ˚C due to the warpage occurring under high-temperature printing. The warpage occurs in the middle or final stages of the printing process, the residual stress has been generated during the printing when the printing temperature is either too high or too low. The deviation among the nozzle tip and previous deposited material and the temperature fluctuation on printing nozzle can also lead to the declination of density and increased pores.

The declination in the specimen printed at 230 ˚C is more severe than that printed at 220 ˚C. This is also probably due to the excessive heat flow of PLA filament when the nozzle is heated to 230 ˚C, which will lead to a thinner thickness lay than setting parameter. The sensor may not adaptively adjust the distance among material and

nozzle tip either, as it is negligible in one layer, but this issue would have accumulated along with the increasing thickness. Finally, a greater porosity is occurred at the late stage of the printing process.

After comparing density profile of PLA polymer at incremental printing temperatures, it can be concluded that the printing temperature of 220 ˚C has the least warpage happened, the most homogeneous density profile distribution and the highest geometric accuracy. The optimized PLA printing temperature would also be referenced for the further study in the following chapters when applying other biopolymers.
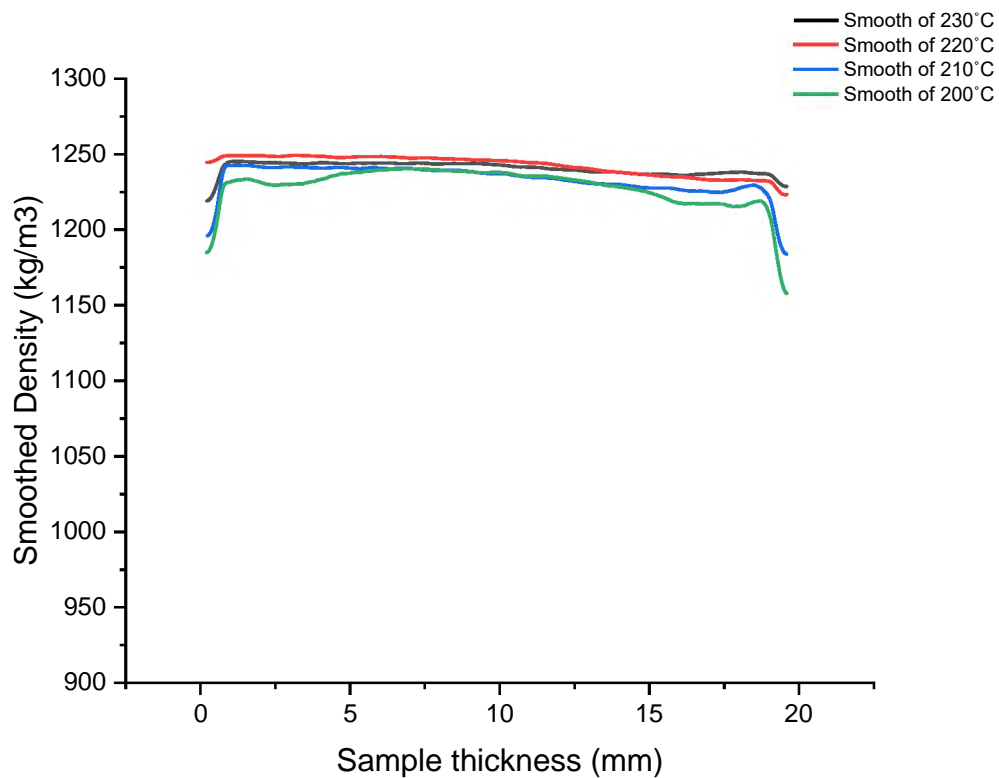
Fig. 32 Density profile of PLA specimens after the smooth process

4.4 Mechanical performance of 3D printed PLA polymer

4.4.1 Tensile properties of 3D printed PLA at different printing temperatures

The tensile testing of 3D printed PLA specimens in ascending printing temperatures is implemented to compare the final mechanical performance. The testing is carried out in accordance with BS EN ISO-527 standard. The 3D printed specimen is rectangular and the gauge length in testing is 15 mm.

Primarily, all the mechanical testing of printed PLA polymer indicates a monotonically increasing stress-strain curve, which shows brittle fracture for the printed products. Due to the anisotropy property of the printed products, it is expected that the properties in the y-axis are lower than those in the x-axis direction. The property of the PLA products printed at ascending printing temperature is evaluated and discussed in the following sections.

The strength-strain comparison shows that the printed PLA specimens have a different performance between x-axis and y-axis, and among different printing temperatures (Fig. 33). In x-axis direction, the products printed at 230 ˚C have the highest strength but the variation between the printing temperatures is insignificant (Fig. 33a). The PLA specimens printed at 230 ˚C have 7% higher strength than the specimens printed in 200 ˚C. The elongation at break of the 3D printed specimens shows very similar result (Fig. 33b), four printing temperatures have resulted in almost the same average strain and it seems that there is no correlation with the printing homogeneity and density profile. Overall, the tensile performance of the parts printed in x-axis orientation have generally subtle difference among various printing temperature, this may be due to the printing orientation which is aligned with tensile load in the x-axis direction and that there are no printed interfacial boundaries in this printing orientation. However, there may present an abnormal outcome when printed at a low temperature, for instance, the strain of 200 ˚C specimens varied abruptly from 2% to 3.7% in this study (Fig. 33b), and the minimum stress (51.4 MPa) is occurred when the elongation at break is 2%. The performance of printed objects may be deteriorated by weak printing homogeneity when the printing temperature is low.

By contrast, in the y-axis direction, due to the existence of the interfacial boundaries, as the printing orientation is perpendicular to the load direction, the tensile properties are significantly affected by the interlaminar bonding performance (Fig. 33c). The average tensile strength of the y-axis PLA specimens reached 22.0 MPa in both of the 220 ˚C and 230 ˚C printing temperatures, which are 24% higher than the specimens printed in 200 ˚C (average 15.3 MPa). The 210 ˚C specimens have a moderate 19.1 MPa, which indicated that a stepped improvement in tensile properties with the increase of printing temperature. The elongation at break is also different for different printing temperatures (Fig. 33d). It can be seen that the elongation for the printed products at 200 ˚C is higher than other three printing temperatures. It seems that the printing temperature of 230 ˚C resulted in lowest elongation in the y-axis direction. It is still unclear why this has happened, but it is suspected that a high temperature may resulted in a deterioration for some early printed layers.

It is evident that the anisotropy property is very significant for the PLA printed products. At 200 ˚C printing temperature, the tensile strength and strain in the y-axis specimen are up to 71% and 61% lower than those in the x-axis specimen respectively. Quick brittle fracture is expected in the following section of fracture surface due to the brittleness of the testing specimens.
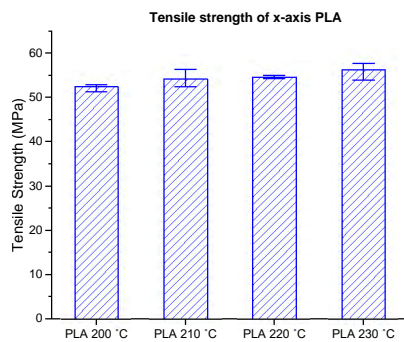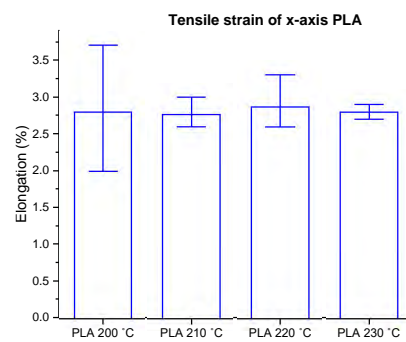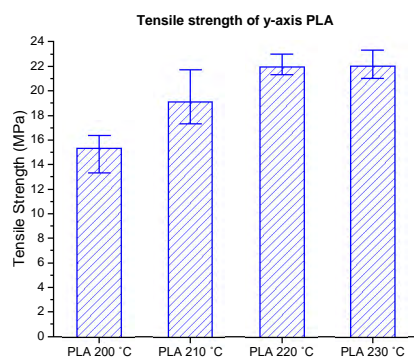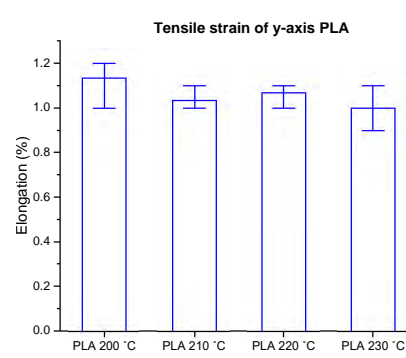
Fig. 33 Comparison of the tensile strength and strain of PLA printed in the ascending temperature

4.4.2 Tensile properties of post-processed PLA specimen

The samples which have been post-processed by the oven curing procedure have also been tested and analysed. The difference and comparison are given in Fig. 34, It can be seen that the tensile strength significantly improved compared with the uncured PLA specimens. The tensile strength has an average 19% increase compared with the PLA printed at 220 ˚C. The increase of mechanical properties may be due to the improved crystallization of PLA polymer. Unlike other studies that the strain has also an improvement along with the crystallinity [271,272], the strain has in fact decreased by 42% compared with that of the uncured PLA. The comparison of strength/strain curves have also provided in Fig. 35, the curve of cured PLA has significantly greater slope than the uncured specimen, which also indicate an enhanced crystallization degree after

the post-process. The reduction is due to that the printed specimen is cured in a vented oven rather than cured as an unprinted filament, the residual stress may increase during the postprocess. The wrapping of the specimen is observed after the curing. The failure mechanism will be further discussed and analysed in the following section.
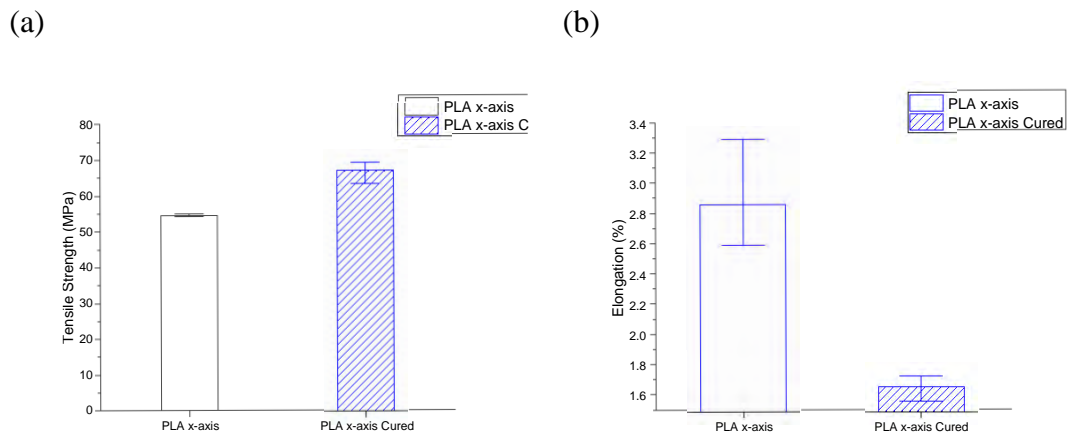
Fig. 34 Comparison of PLA and cured PLA printed in x-axis orientation
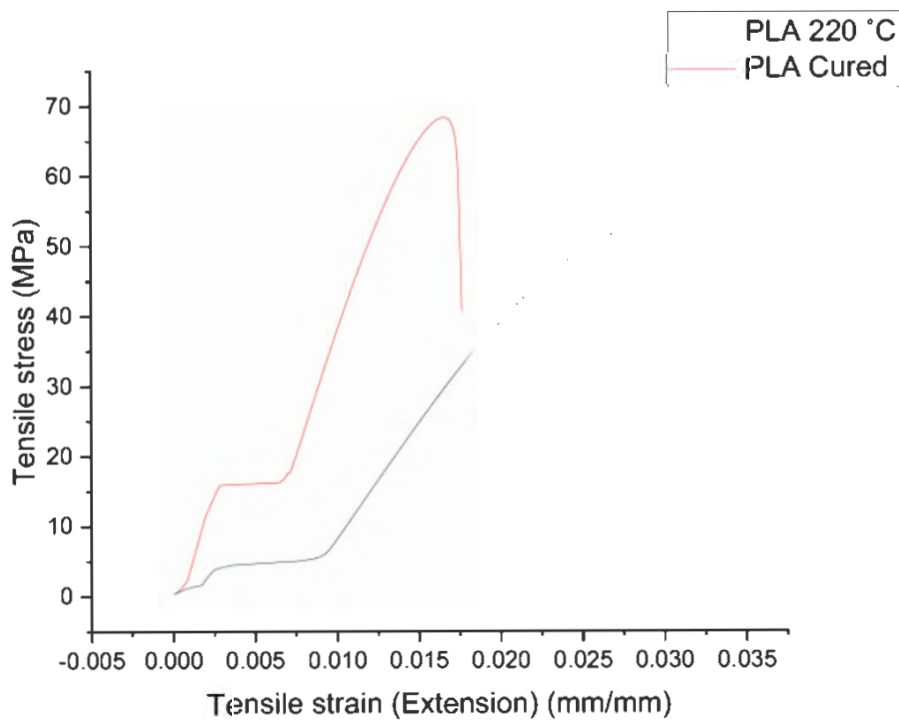
Fig. 35 Comparison of the strength/stain curve of uncured and cured PLA

4.4.3 Tensile properties of PLA polymer in x and y orientation

As aforementioned, inherent anisotropy properties in the 3D printed objects are significant. To further understand their difference, overall average tensile properties of the PLA printed with various temperatures in two printing orientations are compared and plotted in Fig. 36. It can be seen that the printed PLA products show considerable anisotropy, 59.8% and 62.8% reduction in tensile strength and elongation respectively.

The x-axis specimens have average tensile strength of 54.6 MPa but only 21.9 MPa of the specimens printed in y-axis direction. The strain of the specimens has a similar reduction, have 2.9% and 1.1% in x and y axis respectively. The tensile properties of transverse direction (y-axis) are considerably deteriorated by the anisotropy properties of 3D printed specimens, compared to that aligned in the x-axis direction. The performance of interfacial bonding among printed filament layers could be crucial to the 3D printing anisotropy property. This may also be confirmed in the examination of microstructure and micro-mechanical performance which are discussed in the next sections.
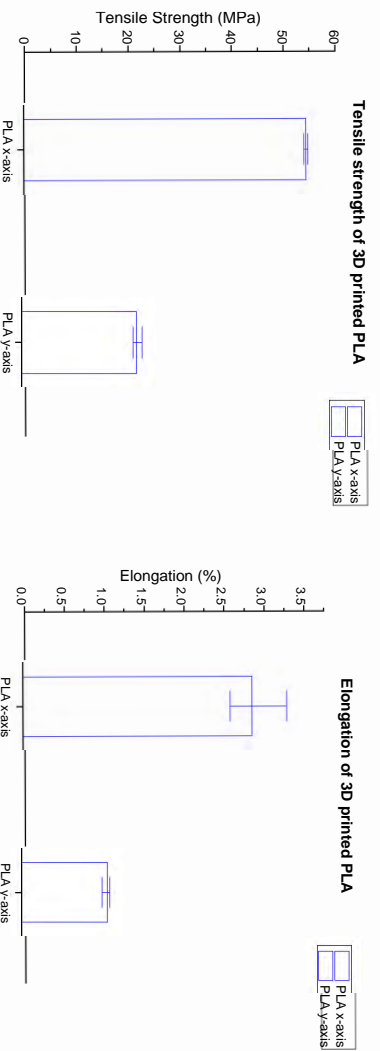
Fig. 36 The tensile properties comparison of 3D printed PLA printed in two orientations (x and y axis)

4.5 Microstructure analysis

4.5.1 Failure mechanism of printed PLA in x and y axis orientation

To further investigate the failure mechanisms of 3D printed PLA specimens, scanning electronic microscope (SEM) images are implemented. The fracture surfaces of 3D printed tension testing specimens are shown in the Fig. 37. It was found that there is little fracture observed on the surfaces, but limited ductile areas occurred before the crack propagation, e.g. the mid-layers in Fig. 37a. The inherently filamentous structure and a combination of smooth and rough fracture surfaces is clearly shown in both fracture surfaces. However, the fracture surface in x-axis has smoother than that in the y-axis due to significantly less delamination. Amorphous structure has shown in most

of both fracture images. An integral sample failure mode can be determined rather than independent failure of printed filament beads.

Fracture surface of x-axis has two rough surface areas in bottom and middle of the image, and a smooth fracture surface in the rest of the sample (Fig. 37a and 37c). These two damages occurred progressively, shown in Fig. 37a. Two potential crack initiation have been observed from the image. Delamination occurred in the left bottom of the image among the adjacent filaments, but the effect of these delamination is negligible due to no loading applied on this direction. For the left-middle of the cross-section, the ledges could also be considered one of the initiations of crack. Both of these two cracks propagate horizontally along with the width of the specimen and then caused the overload for the adjoining area, marked on the Fig. 37a. Finally, a clean brittle fracture surface is created proceeded to the break of the specimen. The filament beads in the bottom of the specimen have pores and impurities, shown in Fig. 37c, which indicates insufficient strength and initiation of crack. Additionally, weak bonding is observed in the other crack initiation in the middle of the sample upon close inspection. Overload may occur on the filament beads which have less or even no interlaminar boundary with the transversely adjacent filaments.

A mixture of facture surface is shown in Fig. 37b, but a large surface has insufficient bonding mechanism between adjacent printed layers. On the other hand, the bonding is dramatically differed from the middle of sample at both ends of the fracture morphology. Overstocked material is deposited at the end of the y-axis printing path where the nozzle is making a U-turn. It leads to a sufficient and symmetrical bonding areas at both ends of sample between adjacent filament beads.

Due to this strong inhomogeneity properties of the specimen, it is indicative that the failure mechanism is not stochastic, and the damage is initiated when the adjacent filament beads have the minimum bonding. The fracture occurred by progressive damage in the boundary of delamination and packed material near the edge of the sample. The following crack propagation and proceeding also have the trend which aligns with the interfacial boundaries of printed layer thickness, shown in Fig. 37d. The outer geometry of y-axis specimen is trapezoidal-like rather than the programmed rectangular, caused by excessively layer-stacked material at the turning points. It can

be counted that an improved mechanical performance could be achieved by increasing the bonding area in the middle of the y-axis specimen.

(a) PLA x-axis
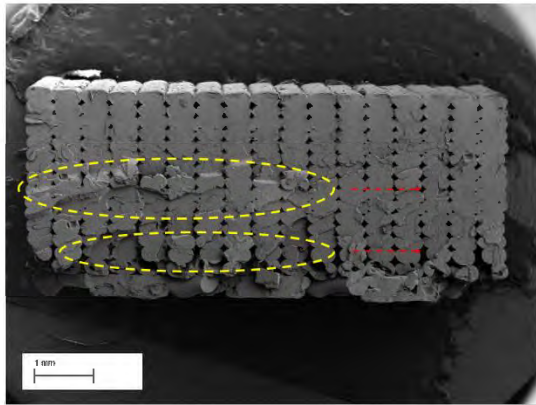
(b) PLA y-axis
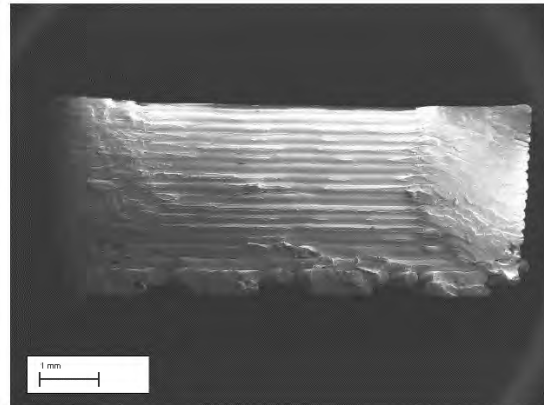
(c) PLA x-axis
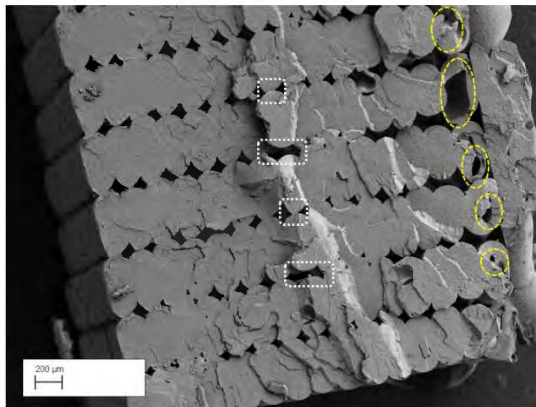
(d) PLA y-axis
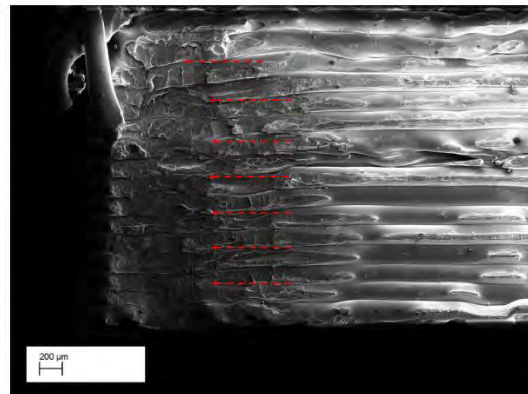
Fig. 37 The fracture surface of 3D printed PLA printed in two orientations (x and y axis)

4.5.2 Failure mechanism of printed PLA in ascending printing temperature

The mechanical performance of the PLA printed in ascending printing temperature is tested and analysed in the previous section, and the microstructure of the fracture surface is acquired afterwards. Corresponding fracture morphology is characterized (Fig. 38). It can be seen that there is a very similar fracture morphology for the printed products at 200℃ compared to 220℃ (Fig. 38a and 38b) and a progressive damage is observed which combined with a rough and smooth fracture surface. However, a larger ledge area is observed for the printed products at 220℃ (Fig. 38b), which is considered a crack initiation of sample. There is less delamination of filament beads occurred in the fracture surface of 220 ˚C specimen. This seems to reflect the tested mechanical property that a higher final ultimate tensile stress is achieved due to these two differences in the failure morphology.

On the other hand, due to the tensile load is directly applied on the interlaminar bonding among filament beads in the y-axis specimens, the mechanical properties of the specimen are highly dependent on the bonding performance. As aforementioned, stronger tensile strength of the PLA specimens can be achieved when the printing temperature is relatively higher. Fig. 38c and 38d compare the difference of fracture surfaces when printed under different temperatures. Both failures are initiated from the middle area of the sample due to lack of bonding and attachment among printed beads. Nevertheless, the printing layers are clearly shown in the Fig. 38c when the printing temperature is low due to insufficient material deposition and neck growth, while there were no obvious layers shown in Fig. 38d. It can be assumed that the crack in the lower printing temperature specimen would be propagated along with the grooves built parallel to the printed layers and caused an orientation effect. It may lead to a lower strength to the final object. The crack propagation is similar in Fig. 38d, but there are less orientated due to lack of the physical grooves.
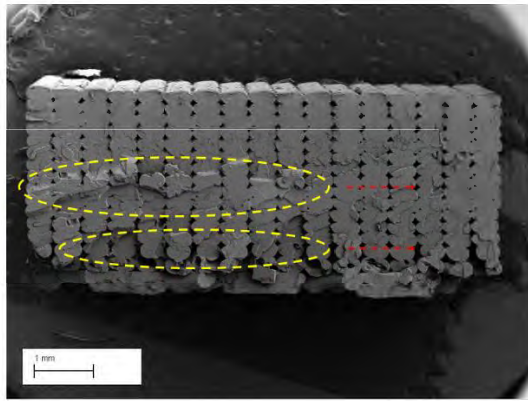
(a) 200 °C PLA x-axis   (b) 220 °C PLA x-axis
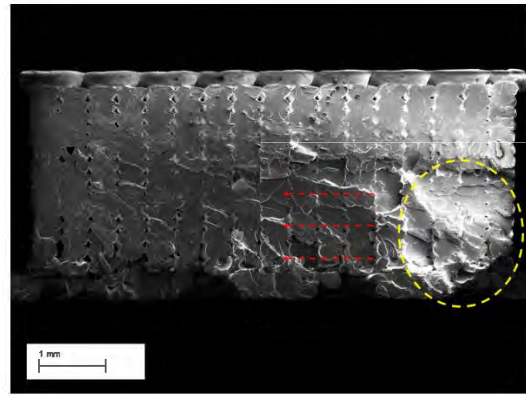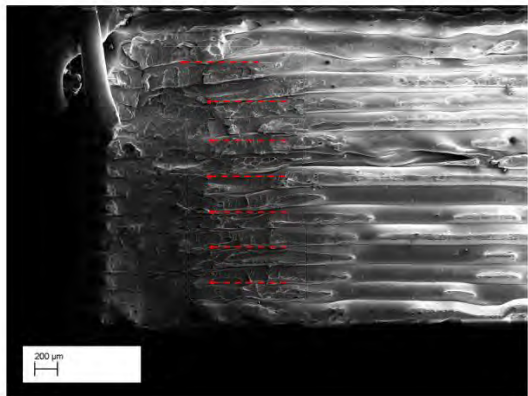
(c) 200 °C PLA y-axis   (d) 220 °C PLA y-axis
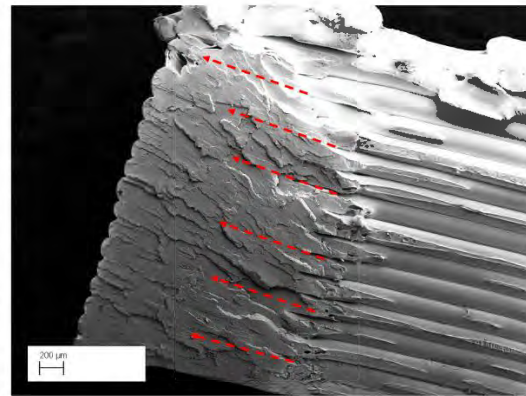
Fig. 38 Comparison of the fracture surfaces when printed in different temperatures

4.5.3 Failure mechanism of post-processed PLA specimen

The fracture surface of postprocessed (oven curing) PLA specimen is much rougher compared to the uncured specimens, as the increased degree of crystallinity is expected from previous studies, although both fracture surfaces have amorphous character (Fig. 39a and 39b). Shorter route of crack propagation among spherulites or crystalline lamella occurs with the increase of crystallinity (Fig. 39a), which may lead to a decrease in the crack propagation resistance of the material structure. Finally, the brittleness of the postprocessed parts is aggravated. The interfacial bonding strength is slightly improved in the y-axis specimen by the superior contact through wetting and reptation. However, the curing effect is limited due to the healing benefits of interfacial boundaries from annealing process is suppressed by the semi-crystalline structure.

Overall, the interfacial bonding of the postprocessed parts has inadequate increase to interlaminar mechanical properties.

(a) (b)

(c) (d)
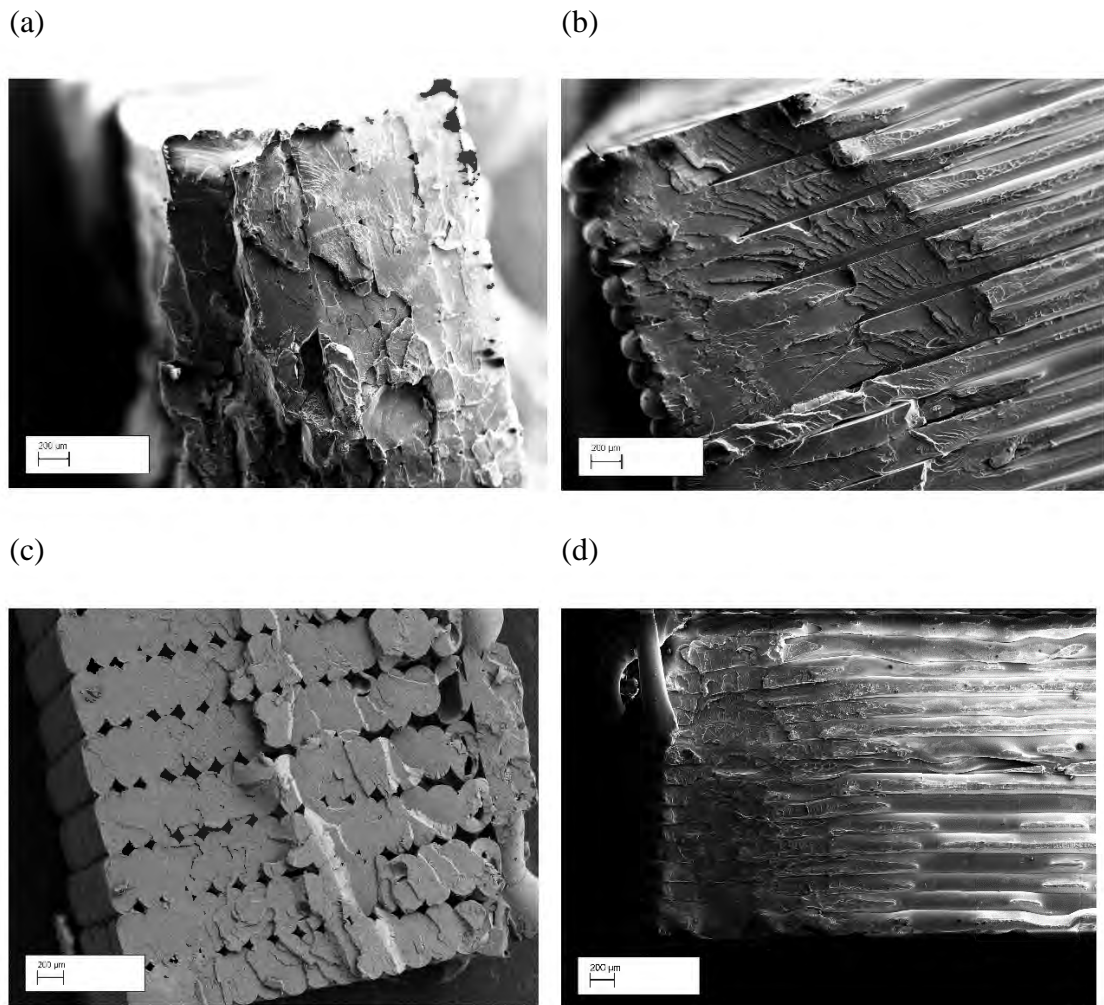
Fig. 39 The fracture surface of postprocessed 3D printed PLA printed in two orientations (a: cured PLA printed x-axis, b: cured PLA printed x-axis, c: uncured PLA printed in x-axis, d: uncured PLA printed in y-axis)

4.5.4 Cross-section morphology of 3D printed PLA specimen

To further investigate the characteristics of interfacial bonding and the distribution of voids, the cross-section cut has been implemented on 3D printed PLA specimens. The void distribution and elliptical printed filament are visible in the image (Fig. 40a). The voids are uniformly distributed in the cross-section of x-axis specimen and are located in the centre of four adjacent filament beads. The uniform distribution of voids matched with the wave of density profile abovementioned. The maximum porosity along and

across the layer thickness is approximately occurred at the mid-point of two printed layers. Due to the nonhomogeneous printing process in this study, the variation of size, shape and configuration of pores are investigated due to the final performance of the 3D printing parts is considerably dependent on the interlaminar pores.

(a) (b)
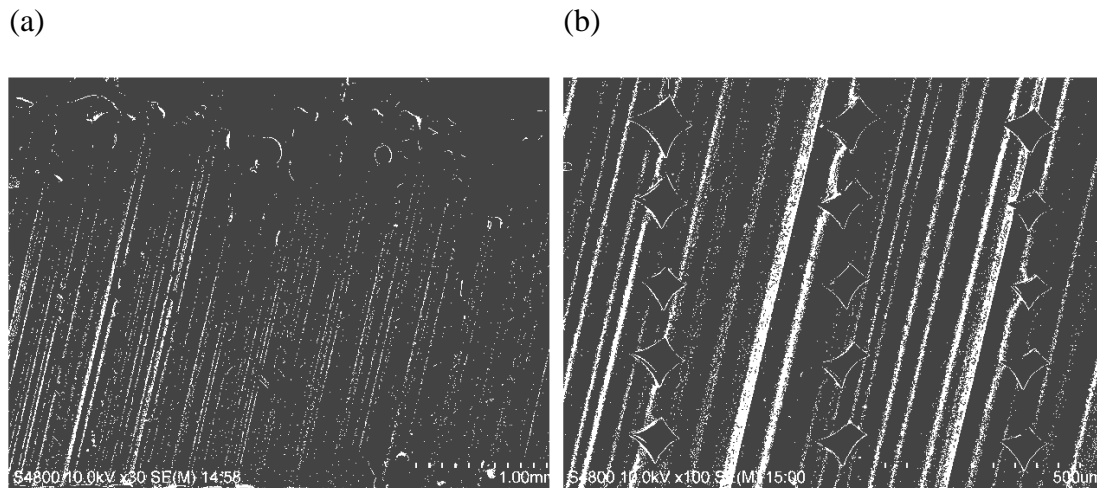
Fig. 40 The cross section of 3D printed PLA printed in x-axis orientation (a: ×30 cross section SEM image of x-axis PLA sample, b: ×100 cross section SEM image of x-axis PLA sample)

In the previous VDP analysis, the density of PLA specimen has a descending trend along with the layer thickness, the material density in the bottom is an averagely higher than the material near the top layers. The cross-section image in Fig. 40a has an opposite result, large pores generated in the first several layers, the lack of bonding is also occurred in few of the filament beads. One of the reasons for this poor printing quality is that for the consistency throughout the study, a raft is designed to all the printing programmes in case of the warpage occurrence. The printed 'platform' has an unsmooth surface and risk of geometry deformation. This uncertainty may lead to the printing disorder in first few layers printed upon the raft structure. The other potential causes are deviation of printing programme, the calibration of nozzle displacement in z-axis and the internal bubbles occurred in the printed filament may also affect the disorder. The bubbles are mainly occurred in the beginning of printing.

The size of the pores has similar ascending trend compared with the VDP result if the first three layers are neglected, the porosity of the specimen is inversely proportional to the density. To define the variation of the neck growth between adjacent filaments based on the mesostructured characteristics, the interlaminar bonding performance can

be evaluated by calculating the quantified geometrical neck growth between adjacent layers in Fig. 41.
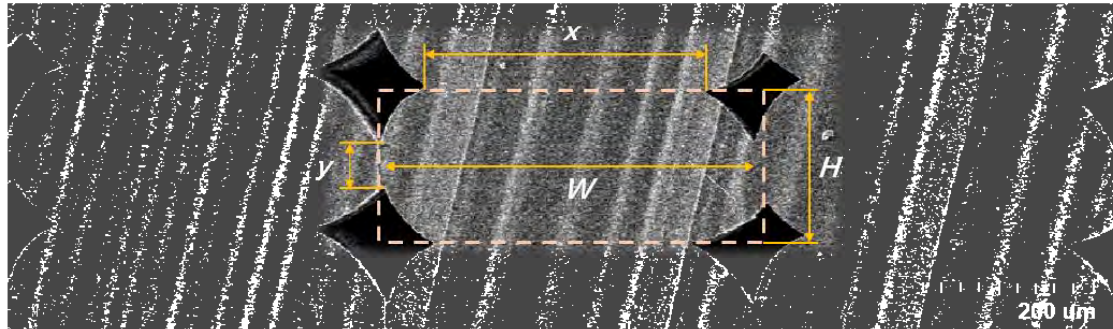
Fig. 41 Microstructure of the single filament cross-sectional area, W and H is the width and height of the filament respectively. x and y are the neck length among adjacent filaments in the two directions respectively

From the previous VDP studies, the neck growth between interlaminar layers is expected to be greater in the bottom than top layers. However, this trend in the small specimens is not as significant as VDP big samples. The experimental results are summarized in Table 17. The results confirm the expected variation that the bottom layers have higher average neck growth except the topside layer. To achieve a smooth appearance of printed objects, a lateral displacement is printed due to the setup of printing programme in the topside layer. Therefore, the bonding performance of the topside layer is negligible in this study.

The measurement result from the microstructure image is significantly lower than density profile abovementioned, the neck growth length is 30% and 36% compared with the width and height of the programmed filament respectively. The bottom layers have the highest neck length in x and y directions, which is 9 % and 17% higher than the following layers in x and y directions respectively.

Table 17 Average neck growth of the x and y axis among the adjacent layers

	Average neck growth length (µm)		Printed filament parameters (µm)	
	x	y	W	H
Bottom Layers (3 layers)	312	157		
Middle Layers (5 layers)	288	138	455	200
Top Layers (3 layers)	283	130		

The bonding process occurs during a short period of time after the material is extruded and laid between the glass transition temperature and critical sintering temperature. The formation of x neck length is mainly caused by the sintering in the beginning, and creep deformation due to the effect of gravity. The y neck length has less bonding performance is due to the creep caused by the down pressure from the nozzle orifice of the printer when the filament is being printed. The material is pressed to have a creep deformation and bonding with the transverse adjacent filament. This downforce can be adjusted and programmed by the calibration of the printer and different setup of the slicer software.

The physical boundaries among the printed filament can also be observed in the SEM image, but majority of the boundaries are not visible. The sample of visible boundaries are shown in Fig. 42. It can be observed that the physical boundaries occur in the transverse boundaries and the neck growth length is relatively low. It led to an insufficient creep deformation during the printing process. The chain diffusion occurs during the formation of the boundary, and it is expected that there are no physical boundaries in the microscope images. The nano-mechanical properties will be implemented to analyse whether the interlaminar boundary will deteriorate the

performance of the printed objects by weakening the interfacial bonding properties.
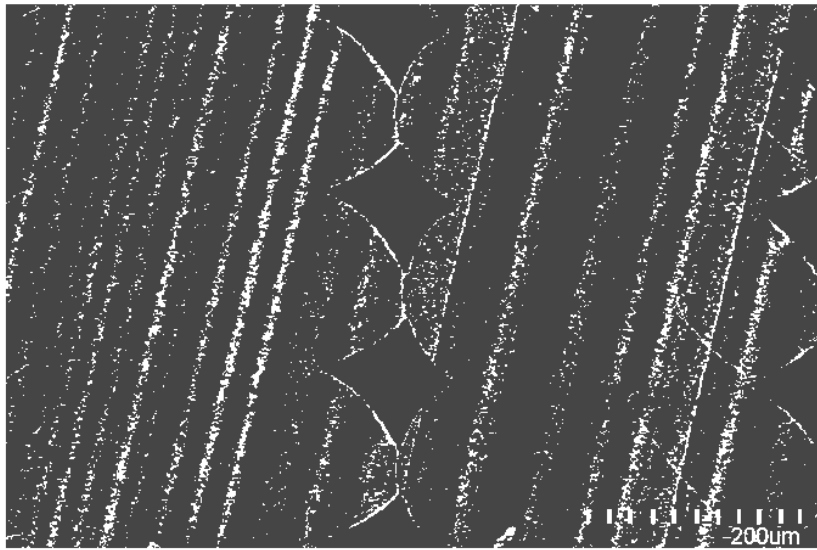
Fig. 42 Physical boundaries in the microstructure of the x-axis cross-section

(a)
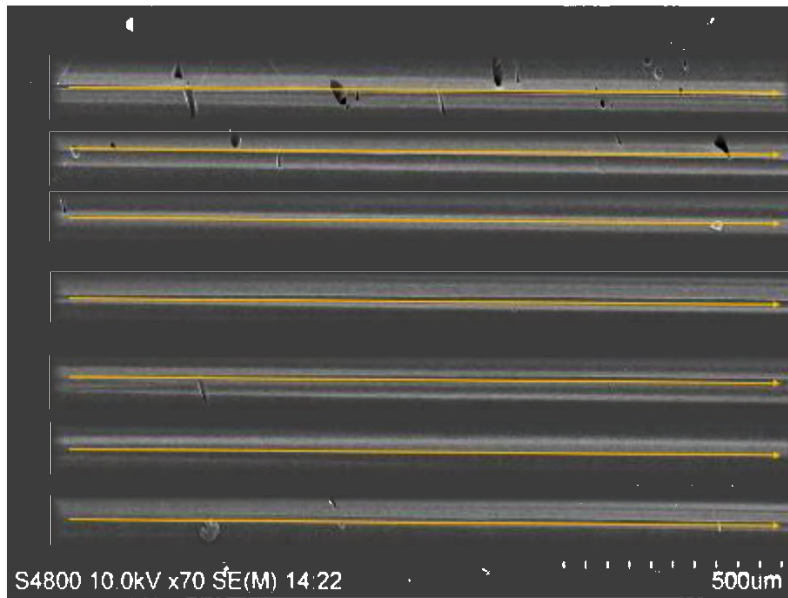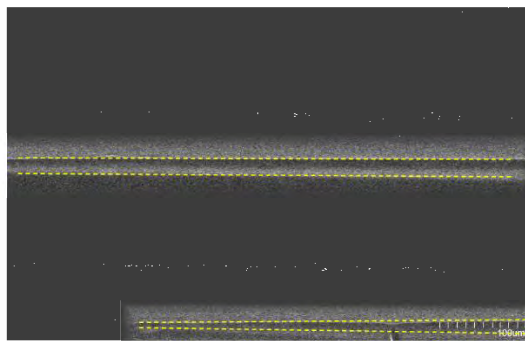
(b)   (c)
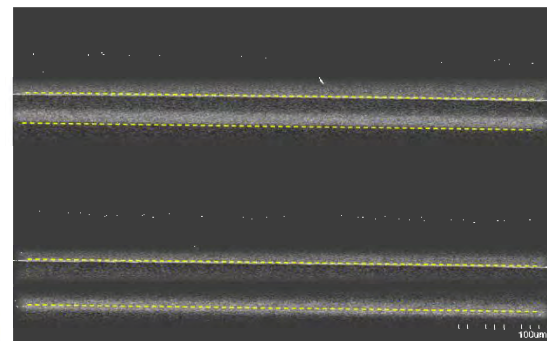
Fig. 43 The cross section of 3D printed PLA printed in y-axis orientation (a: ×70 cross section SEM image of y-axis PLA sample, b, c: grooves among printed layers)

Compared with the SEM image of x-axis cross-section, the y-axis has less observed pores, the grooves are expected which are an indication of the voids among the printed layers. Fig. 43a shows the microstructure of the y-axis cross section image, the interlaminar grooves are indicated by the marked arrows, which clearly matched with the 200 μm layer thickness. The variation of the grooves is similar to the fracture surface above, considerably smaller grooves at the side of the specimen than the groove in the middle (Fig. 43b and 43c). Some voids are observed in the image, similar to the x-axis specimen and the voids are mainly generated in the early stage of the printing process. The bubbles observed could be created when the filament is extruded before the printing

process due to the lack of pressure from the nozzle orifice in the beginning of the printing process. The bubbles remain after printing. Some impurities are also observed in both x and y axis specimen, the impurities in this study are mainly from the filament fabrication process. Various sources may contribute to the final impurities, such as, the dust which can be attached to the melt material after the compound process, impurities from the shredding process due to difficult to clean the machine thoroughly and some carbonized polymer remaining due to blocked extrusion process occurred.

4.6 Nanoindentation analysis of 3D printed PLA specimen

The aforementioned microstructure of 3D printed indicates that the interlaminar bonding is significantly critical to the mechanical performance of final printed parts, to further investigate the micromechanical performance of the interlaminar boundary, nanoindentation is implemented to analyse the mechanical properties at the potential boundary between printed layers.

Three areas, which cover the interface between two printing layers, have been selected in one testing specimen, the testing areas are shown in Fig. 44a (A, B and C areas). Nine indentations (3×3) have been implemented in one area, the microstructure images before-after testing is shown in Fig. 44b and 44c. The testing for the y-axis specimen has same area selection and procedure.

(a)   (b)   (c)
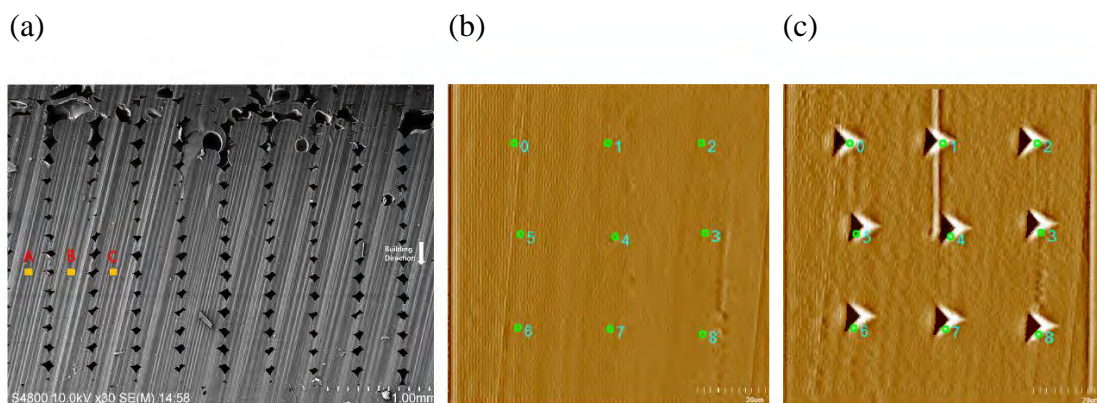
Fig. 44 Nanoindentation of x-axis PLA specimen (a: position of indentations, b: before indentation, c: after indentation)

Nanomechanical properties like hardness and modulus have insignificant difference between two printing orientations. However, the result has less dispersion and more

uniform in the x-axis, which lead to a better printing uniformity. The average hardness reaches 0.284 GPa and 0.288 GPa respectively, and the average modulus is almost identical, 5.69 GPa in x-axis and 5.67 GPa in y-axis (Fig. 45).

With a slight increase in hardness in the y-axis, but the deviation of y-axis specimen is 42% and 47% higher than the x-axis sample in hardness and modulus respectively. Both specimens have no observed mechanical deterioration in the interfacial boundary. The higher deviation in the y-axis specimen is mainly due to the longer printing process and higher complexity than x-axis specimen.

Due to the insufficient variation of mechanical properties tested by nanoindentation process and consider the previous microstructure analysis in the meanwhile. It can be concluded that the anisotropy property of 3D printed PLA is mainly caused by the inadequate physical contact area among printed filament beads rather than the weak interlaminar bonding properties.

(a)   (b)
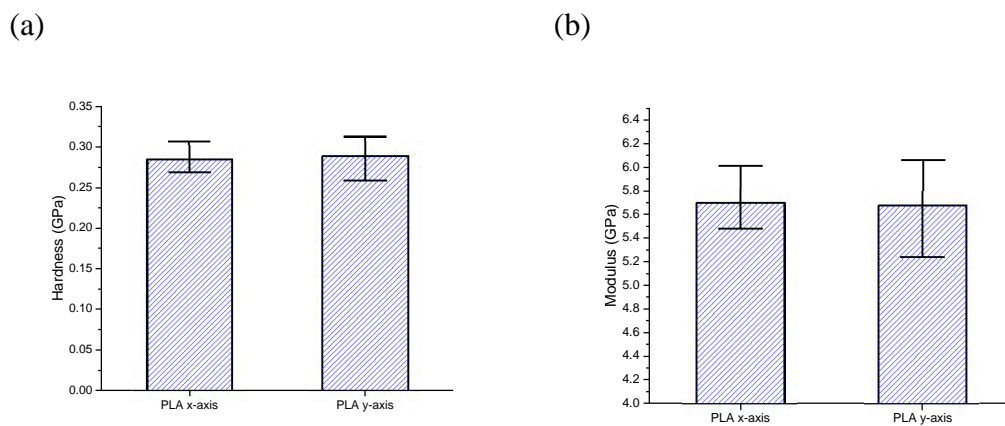
Fig. 45 The comparison of the hardness (a) and modulus (b) of PLA in different orientations

4.7 Discussion

The average densities and porosity distribution in the specimen have been investigated in 4.3, although the overall results were inconspicuous, the average density of specimen printed at the temperature 220 ˚C reached 1242.7kg/m^3 which was 1.7% higher than that at the 200 ˚C and a smoother density distribution was also achieved. This outcome was supported by following mechanical performance testing and microstructure morphology. The PLA specimens printed at the higher temperature had superior tensile strength to that printed at the low printing temperature (up to 7% and 24% in x and y-

axis respectively). Printing inhomogeneity has occurred when the printing temperature was low, similar comment was risen by other researchers [273]. Various printing parameters were investigated by pioneers, such as printing temperature, layer thickness, printing speed and orientations [6,171,172,190-192,273-281]. [281] Compared to the outcomes of this work, superior enhancements in tensile strength were achieved in their study. However, considering the other printing parameters they applied, such as ±45° printing orientation, the interlayer bonding might partially impacted the tensile strength.A higher printing speed (45 mm/s) could result in higher mechanical performance.

The anisotropy property of FDM 3D printing process was also reported severe. The average tensile strength of x-axis reached 54.6 MPa but only 21.9 MPa of the specimens printed in y-axis direction. Similar reduction was occurred in tensile strain, decreased from 2.9% to 1.1% in x and y axis respectively. The tensile strength and strain were decreased 59.8% and 62.8% respectively, this also supported most of the current studies, regardless of the material employed [188,189,192,194,273-278,282-284]. The mechanical properties of printed parts are highly dependent on the printing orientation. A study on [275] the anisotropy properties of 3D printed PLA showed that tensile and flexural strength is up to 78% and 350% higher when the printing orientation at 0° compared with those at 90°, which is similar to the outcome achieved in this study discussed in 4.5.3.

Opposite results were also reported [277], showing that the specimen printed in 0° and 90° had similar tensile strength when the layer thickness is higher than 0.1 mm, and the ± 45° orientation resulted in the maximum mechanical properties among three orientations, which indicated that the interfacial bonding among printed layers has much less influence to the final mechanical properties of printed objects. The reasons for these differences could also be the commercial PLA filament applied and insufficient filament specifications provided, or the unclear printing programme reported in this study.

The thermal post-process in this study was analysed by oven annealing curing, the tensile strength increased 19% to average 64.5 MPa. But the tensile strain decreased dramatically by 42% from 2.9% to 1.7%, which lead to a severe brittleness of the specimen. The improvement of mechanical performance by thermal post-process was

also reported by Wach et al. [281], up to 17% increase in flexural strength. The flexural strains were also slightly decreased, which also matches the testing result above in 4.4.2.

The microstructure characterizations of the fracture surface and cross-section were implemented, the failure mechanism was subtle in specimens printed at different temperatures. Brittle failure was occurred in all printed specimens, and the reason of the increase in mechanical properties of the y-axis specimen, may be the increase of physical interlayer bonding neck growth. [275] However, different failure modes have been reported [274]; the ductile fracture was achieved when the load is parallel to the printing orientation, while brittle facture was found when the printing orientation is perpendicular to the loading direction. The reason caused this could be the commercial printing filament applied in their research and no material composition can be found. Some additive or plasticizer might be employed during the filament extrusion. The interlayer bonding neck growth was measured and analysed by the help of x-axis cross-section image, same trend was found with the VDP result, the interlayer neck growth length in the bottom layers was up to 36% higher than that the top layers.

The melt rheological properties of printing material which is another important parameter when applying the material in FDM AM process. The melt flow index (MFI) of PLA increased considerably with the ascending temperature from 180 °C to 240 °C (from 2 to 36 g/10 min), hence strong delamination was reported when the printing temperature was 180 °C [190]. Although impressive mechanical performance was reported when the high temperature (240 °C) [190], strong overflow occurred when printing the PLA filament in our 3D printer. It must be noted that the long carbon fibre bundle embedded in the printing process could help reduce the matrix overflow.

4.8 Interim conclusions

The 3D printed PLA polymer is comprehensively studied in this chapter from nano to macro. The ascending printing temperatures have been evaluated and the optimized printing temperature for the PLA polymer is 220 ˚C

The printing temperature was one of the most critical features in 3D printing process, optimized printing temperature for the PLA polymer was generated in this chapter. When printing in y-axis orientation, the mechanical properties of 220 ˚C printed PLA was up to 24% higher than the PLA printed at 200 ˚C, less anisotropy property was also

achieved. Better interlaminar bonding properties and larger interlaminar contact area were considered the reasons when printed in y-axis direction by studying the fracture morphology.

Up to 19% improvement of tensile strength in x-axis printing orientation has been achieved when the post-process was applied, but severe brittleness and significant anisotropy restricted the further application of heat annealing process of 3D printed PLA polymer.

The failure mechanism of 3D printing objects was analysed in detail in two different printing orientation, the result showed that the final mechanical performance was affected by the interlaminar bonding properties, even the printing orientation aligned with the load applied. However, the y-axis specimen showed dramatically insufficient contact area between adjacent filament beads in the middle of the specimen, which was the main reason of weak mechanical performance in y-axis specimens.

There were no deteriorative interlaminar bonding properties among the printed layers, proven by nanoindentation process. The micro-mechanical properties have been tested at the interface of two printed layers, resulted in little variation in hardness and modulus. To reduce the anisotropy property of PLA biopolymer, further copolymers and additives were employed and analysed in the following chapters.

5. 3D Printing of PLA/PHBV Copolymer and Interface Structure

5.1 Introduction

Polyhydroxyalkanoates (PHAs) are another class of bio-based polymers, which are fabricated from bacterial fermentation process. PHAs have already been applied in a wide variety of applications such as packaging, biomedical implants, drug delivery and tissue engineering thanks to the biodegradability, biocompatibility and outstanding mechanical performance. With the reducing cost of PHBV polymers, an extension of potential applications has emerged. There are limited studies regarding PHBV polymer applied in additive manufacturing compared with PLA polymer, which is one of the most employed biopolymers in 3D printing industry. PHBV may also be applied in additive manufacturing to ease the inherent anisotropic property. This chapter introduces the investigation of 3D printed PLA/PHBV copolymer compounded in different proportion ratios.

5.2 Vertical density profile (VDP) of PLA/PHBV copolymers

Unlike the previous chapter, the density profile of small specimens was studied by the X-ray profile densimeter in this study. It must be noted that the relatively large deviation in the diameter of extruded filament leads to a slightly greater non-uniform printing process, as large specimen is difficult to be printed. This phenomenon has become more intensified with the increased weight-ratio of PHBV due to its thermo-rheologic properties.

5.2.1 Vertical density profile (VDP) of PLA/PHBV copolymers printed in x-axis orientation

The density profile of PLA/PHBV copolymer printed in x-axis orientation is tested and analysed. Two general observable phenomena can be identified before the detailed discussion to be followed. Firstly, a strong variable trend can be observed for the profile examined (Fig. 46). It can be seen that the waves are significantly variable with the addition of PHBV ratio. Secondly, unlike the PLA specimen, the density distribution at the early printing stage, especially when the thickness of specimen is below 1 mm, is

considerably lower than that of following printings. However, the difference of average densities for each copolymer are negligible.

Like the PLA specimen, the density wave of PLA/PHBV 90:10 wt% is relatively flat compared with other copolymers (Fig. 46a). The average amplitude of the density wave is around 50 kg/mm^3. It must be noted that there is no density trend in one tested specimen due to the limited thickness. The density variations of PLA/PHBV 70:30 wt% and PLA/PHBV 50:50 wt% are further magnified to a larger amplitude in the diagram (Fig. 46b and 46c). The amplitude in the density variation between layers of the PLA/PHBV 30:70 wt% could reach to 214 kg/m^3, which is more than four times that of the PLA/PHBV 90:10 wt% specimen (Fig. 46d). This may be due to the pores (loosen structure) between layers, which could be more significant in the PLA/PHBV 30:70 wt% copolymer, by contrast the PLA/PHBV 90:10 wt% may have the finest porosity. This will also be analysed with the microstructure images in the later section to confirm this assumption.

Besides, it can be observed from the diagram that in addition to the stronger variation with the addition of PHBV polymer, the densities of copolymer varied more randomly even without any regularity when the PHBV weight-ratio is increased. An inhomogeneous printing quality may be the case according to this phenomenon shown in the density profile diagram.
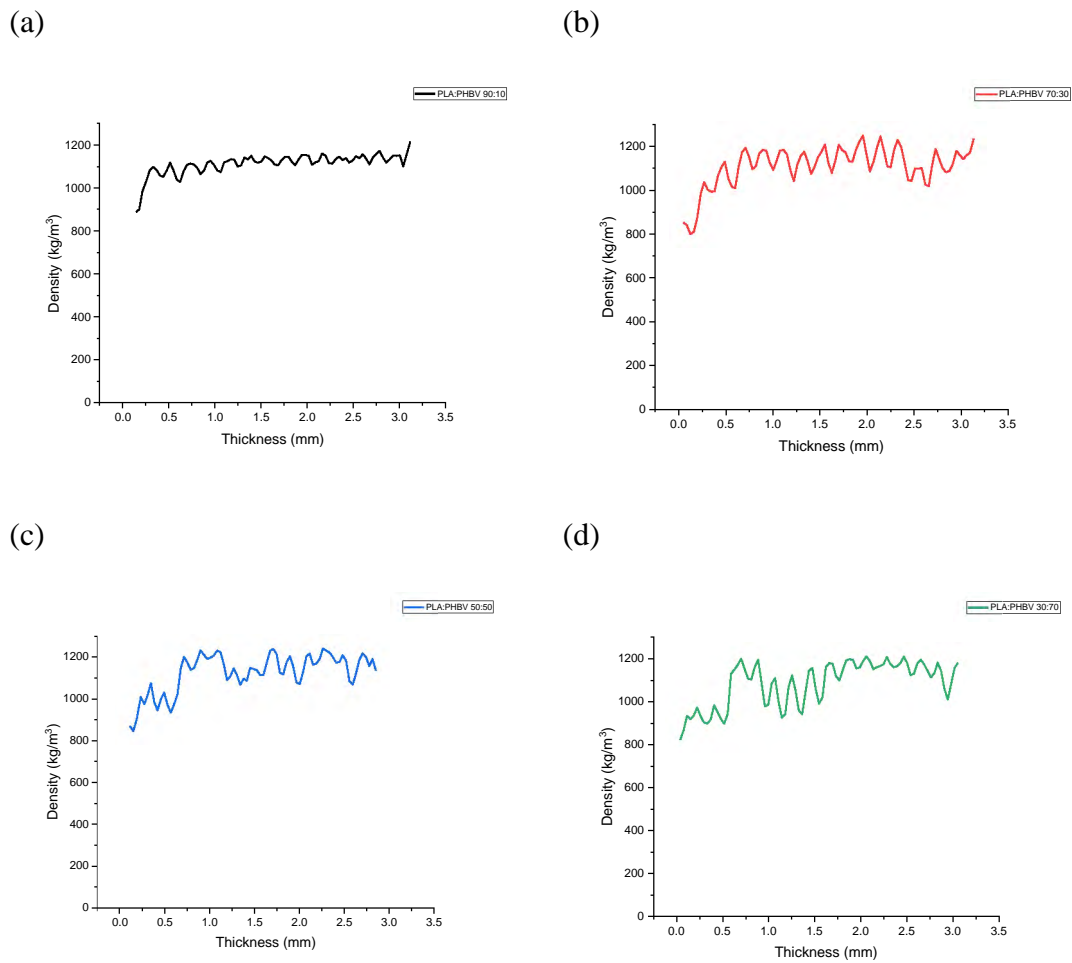
Fig. 46 Density profile of PLA/PHBV copolymers printed in x-axis (a: PLA/PHBV 90:10 wt%, b: PLA/PHBV 70:30 wt%, c: PLA/PHBV 50:50 wt%, d: PLA/PHBV 30:70 wt%,)

5.2.2 Vertical density profile (VDP) of PLA/PHBV copolymers printed in y-axis orientation

Compared with the samples in the x-axis direction, similar characteristics can be determined in the y-axis direction (Fig. 47). For example, in the early stage of printing (within a thickness of 1mm) the average density is much lower than the material density in the following printings. The density trend of all samples has no obvious variation after the early period, except for the PLA/PHBV 90:10 wt%, the average density has a slightly descending trend.

As for the tendency of the fluctuation amplitude, the two printing orientations have shown completely opposite characteristic. Compared with the increased PHBV weight-ratio in the x-direction, the higher the amplitude, the smaller the amplitude in the y-axis

direction with the addition of PHBV. The maximum amplitude in the PLA/PHBV 90:10 wt% reached 138 kg/m^3, compared to the 63 kg/m^3 and 54 kg/m^3 in the PLA/PHBV 50:50 wt% and PLA/PHBV 30:70 wt% respectively.

The reasons for this interesting result may be as follows: The first is that with the addition of PHBV, the variable material rheological property of the filament at the printing temperature and the solidification process of the melt deposited filament beads have been extended. As a result, the melt materials cannot be sufficiently cooled down before the following adjacent printed bead is deposited. The severe deformation has occurred in the PLA/PHBV 30:70 wt% specimen due to the insufficient solidification. Another reason is that when printing in the x-direction, except for the corners at both ends of the sample length, the rest of the printer's nozzles is printed at a set printing speed of 100% (50 mm/s). In the y-axis direction, since the set sample width is only 10 mm and the printer is set at every 180˚ corner, the printing speed is only 50% of the set speed. This results in an overstock at the corners when printing in the y-axis direction, which results in a final sample with a lower porosity and higher average density.

a

b
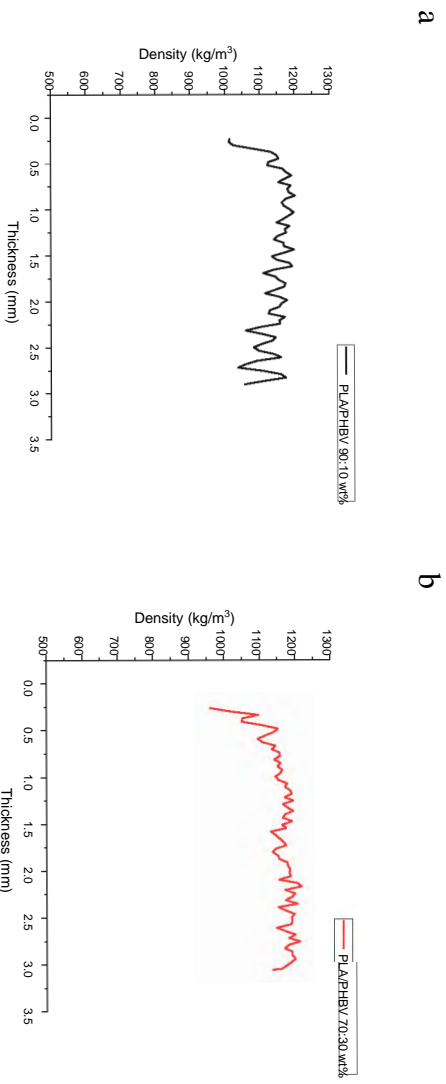
c
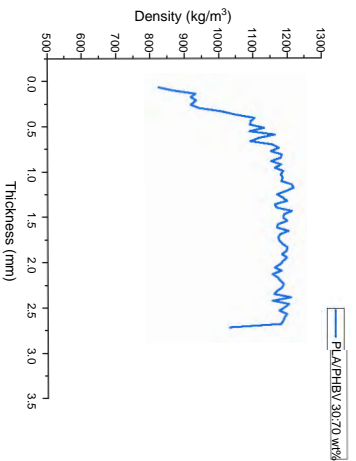
Fig. 47 Density profile of PLA/PHBV copolymers printed in y-axis (a: PLA/PHBV 90:10 wt%, b: PLA/PHBV 70:30 wt%, c: PLA/PHBV 30:70 wt%,)

5.3 Mechanical performance of PLA/PHBV copolymers

To achieve the consistency of research, the 3D printing specimens in this study were fabricated by employing the same printing programme and tested following the same standards with the PLA specimens in the previous chapter. The mechanical performance of PLA/PHBV copolymers is split into two printing orientations and a final summary will be given afterwards.

5.3.1 Tensile properties of PLA/PHBV copolymers in x-axis printing orientation

Similar to the PLA samples, the failure mode of PLA/PHBV copolymers is also brittle fracture. A monotonically increasing line is shown on all the stress/strain curves and

the anisotropy property is also unavoidable for the copolymers. The tensile strength and strain of copolymers are shown Fig. 48, neat PLA and PHBV are also provided as a benchmark. The tensile properties of pure PHBV polymer are lower than those of the printed neat PLA. The average tensile strength of 3D printed PHBV specimens is 35.6 MPa, which is 35% lower than that of the neat PLA samples. The PLA/PHBV 30:70% specimen has the lowest strength in the diagram, resulted in 33.1 MPa and 39% lower than the tensile strength of PLA samples. The tensile strength is even 7% lower than that of neat PHBV specimens, which may indicate a poor printing quality. The rest of copolymers have only slightly lower strength than that of PLA polymer, up to 13% lower in tensile strength.

The difference in tensile strains seems less significant than that in the tensile strength. The tensile strain of PLA/PHBV copolymers is comparative with both samples printed by two neat polymers. The strains of PLA and PHBV are very similar, resulting in average 2.87% and 2.78% respectively. There is a descending tendency occurred in tensile strain, when focused on the four copolymer variations. The highest strains occurred in PLA/PHBV 90:10% specimens, which is almost identical with the PLA. The PLA/PHBV 30:70% copolymer has the lowest tensile strains, which is 16% lower than the PLA specimens. Table 18 summaries the tensile properties of PLA/PHBV copolymers.
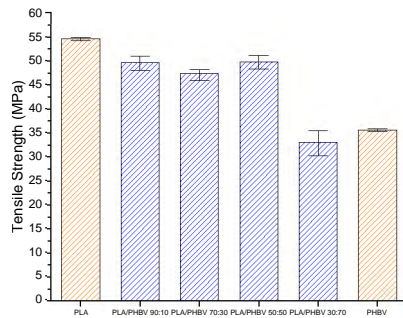
(a)   (b)
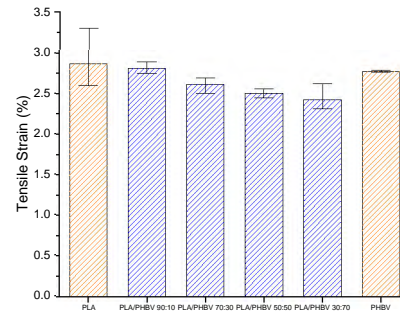
Fig. 48 Tensile strength and strain of x-axis PLA/PHBV copolymers (a: tensile strength, b: tensile strain)

Table 18 Average mechanical properties of PLA/PHBV copolymers in x-axis printing orientation

	Tensile Strength (MPa)	Tensile Strain (%)	Young's Modulus (GPa)
PLA	54.6	2.87	1.93
PLA/PHBV 90:10%	49.7	2.81	1.77
PLA/PHBV 70:30%	47.4	2.62	1.82
PLA/PHBV 50:50%	49.8	2.50	2.00
PLA/PHBV 30:70%	33.1	2.42	1.37
PHBV	35.6	2.78	1.29

5.3.2 Tensile properties of PLA/PHBV copolymers in y-axis printing orientation

Although the copolymer specimens printed in y-axis orientation have all resulted in lower tensile strength than PLA polymer (Fig. 49), the reduction is significantly less compared with the reduction in x-axis. The weakest tensile strength occurred in PLA/PHBV 30:70% specimens, which is 14% lower than the PLA. It can be assumed

that the interlaminar bonding performance of PHBV is superior to that of PLA polymer in 3D printing. Further discussion will be provided in the following sections.

The tensile strain of copolymers is superior to that of the PLA samples. The maximum tensile strain has resulted in PLA/PHBV 50:50% (1.94%), which is 43% higher than the strain of PLA. Table 19 shows the average mechanical properties of PLA/PHBV copolymers, benchmarked with PLA samples. The improvement in tensile strains is probably due to the improved bonding performance between layers for the PLA/PHBV copolymer, which will also be investigated in the next section, compared with the mechanical properties of neat PHBV. The improvement of ductility is dramatic even in the small PHBV proportion like PLA/PHBV 90:10%, resulting in 1.75% and 37% higher than those of the PLA. Fig. 49 summarizes the tensile properties of PLA/PHBV copolymers compared with the PLA which are printed in 220 ˚C.

Table. 19 Average mechanical properties of PLA/PHBV copolymers in y-axis printing orientation

	Tensile Strength (MPa)	Tensile Strain (%)	Young's Modulus (GPa)
PLA	21.9	1.1	2.11
PLA/PHBV 90:10%	20.0	1.75	1.14
PLA/PHBV 70:30%	21.4	1.60	1.34
PLA/PHBV 50:50%	21.0	1.94	1.08
PLA/PHBV 30:70%	18.9	1.75	1.09
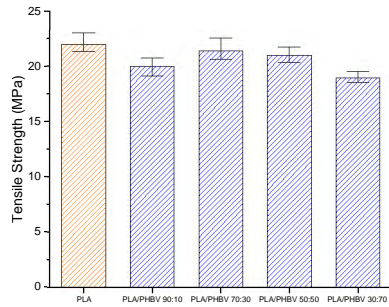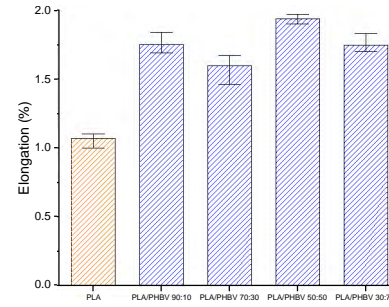
Fig. 49 Tensile strength and strain of y-axis PLA/PHBV copolymers (a: tensile strength, b: tensile strain)

The tendency of tensile properties of PLA/PHBV copolymers printed in x-axis and y-axis orientations is compared (Fig. 50a). With the increase of PHBV proportion, the tensile strength is reduced visibly in the x-axis, but there is no tendency for the y-axis specimens. The tensile strength of PLA/PHBV 30:70% copolymer printed in y-axis is 39% lower than that of the sample printed in x-axis. Although it is premised that the tensile strength decreases in the x-axis direction, the anisotropy of tensile strength is significantly reduced by the addition of PHBV.

Meanwhile, the ductility of copolymer specimen printed in y-axis orientation is considerably improved when the PHBV polymer is presented in Fig. 50b. In the PLA/PHBV 50:50% proportion samples, the tensile strain in the y-axis orientation is only 22% less than that of the specimen printed in x-axis, which is significantly improved compared to the 62% reduction in the PLA specimens. Same reductions have occurred in the Young's modulus of specimens, in the PLA/PHBV 70:30% and PLA/PHBV 30:70%, there are 26% and 20% lower in y-axis specimen respectively compared to the outcomes of x-axis, the difference of which is lower than that of other proportions of copolymer, shown in Fig. 50a. The testing outcomes have proved that the PLA/PHBV copolymers have less anisotropy properties than 3D printed neat PLA polymer.
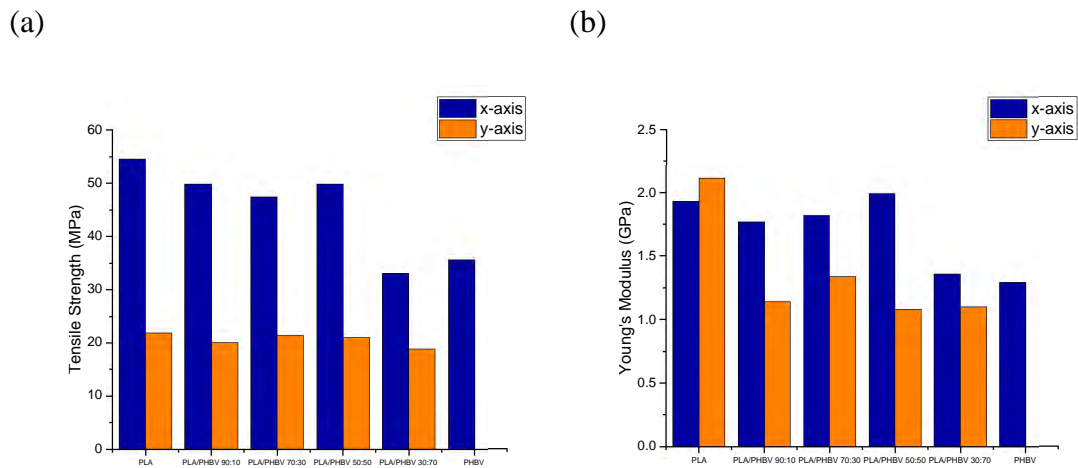
Fig. 50 Comparison of tensile strength and Young's modulus of PLA and PLA/PHBV copolymer

5.4 Microstructure of PLA/PHBV copolymers

5.4.1 Fracture surface of PLA/PHBV copolymers printed in x-axis orientation

Similar to the previous chapter, the copolymer specimens were implemented to SEM to acquire the fracture morphology. To further compare the failure mechanisms between different weight-ratios of copolymer, the analysis of fracture surface is separately discussed for different printing orientations.

Fig. 51 shows representative SEM images of fracture surface of PLA and PLA/PHBV copolymers. Firstly, no visible cluster or domain is observed in all the copolymers, which the miscible blends have been determined. The PLA/PHBV 90:10% and PLA/PHBV 70:30% have overall similar failure surfaces compared with PLA specimen. A brittle failure mode have been indicated with large smooth fracture surface. However, with the increasing weight ratio of PHBV, more rough surfaces have been observed which may indicate a different failure mechanism.

In the Fig. 51b, three surface areas which are combined with both clean and rough surfaces have been marked in the image. Debonding and delamination have also occurred during the tension testing in the area 1; the bottom layers are pulled-out from the top layers and there is also a multistep structure between area 1 and 2, which

indicates the direction of crack propagation. A quick brittle failure is indicative in the area 2 due to the smooth fracture surface, whereas a rough and ductile fracture surface in area 3 has been distinguished from other areas. Like the PLA specimen, the crack is propagated along with the horizontally adjacent filament beads.

The fracture morphology of PLA/PHBV 30:70% on the contrary in the Fig. 51d, has shown a relatively clear fracture surface. Severe delamination has occurred in both horizontal and vertical interlaminar boundaries. It can be observed that the insufficient deposition during printing process has occurred in the first 7 printing layers, which caused a weak interlaminar bonding properties and the following horizontal delamination during tension testing. Same phenomenon in the adjacent filament beads leads to another vertical delamination at the middle of the specimen.
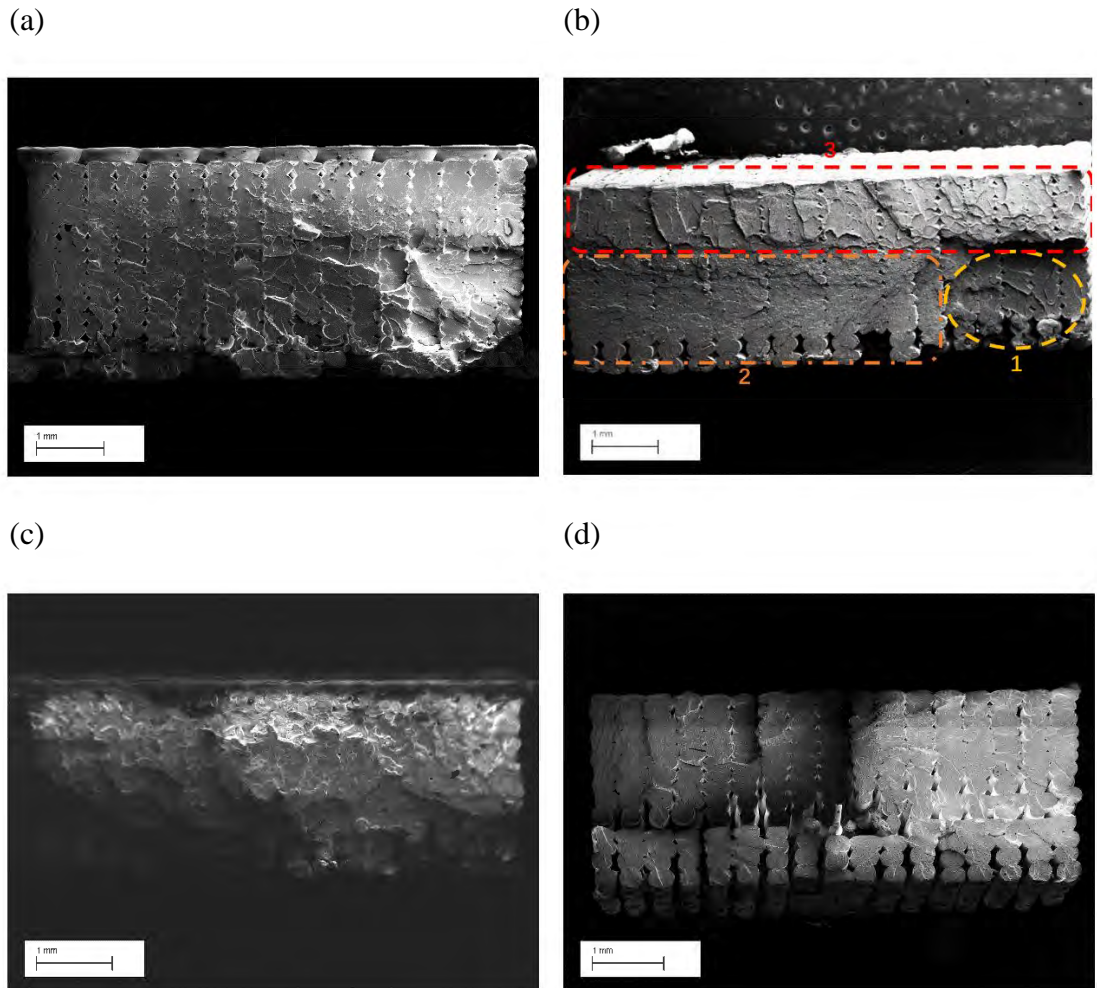
Fig. 51 Fracture morphology of PLA/PHBV copolymers printed in x-axis (a: PLA, b: PLA/PHBV 90:10 wt%, c: PLA/PHBV 70:30 wt%, d: PLA/PHBV 30:70 wt%)

5.4.2 Fracture surface of PLA/PHBV copolymers printed in y-axis orientation

Unlike the insufficient difference in mechanical properties of x-axis specimens, the PLA/PHBV copolymers printed in y-axis have impressively enhanced the tensile strain at break compared with neat PLA polymers. The fracture morphology of copolymers has been investigated to analyse the cause of this improvement.

As aforementioned, the improved mechanical properties have been achieved in the y-axis specimens. The microstructure images are shown in Fig. 52. The improved contact areas of fracture surfaces can be observed in the Fig. 52b, 52c and 52d. The increased physical contact areas can lead to an improved endurance to the applied load, then a tougher mechanical performance is achieved.

Similar to the surface morphology of PLA specimen, the fracture surface shows a symmetrical structure. Overstocked material is deposited at the end of the y-axis printing path, where the nozzle is making a U-turn (Fig. 52b and 52c). However, there are two different features compared with PLA. Firstly, the interlaminar bonding between adjacent beads is improved in the middle of the specimen with the increasing weight ratio of PHBV, the bonding performance is improving faster at the top of the specimen than the bottom. Another interesting feature is that two different fracture surfaces have been observed in Fig. 52c, a rough surface on the right and a smooth failure on the left. Although they both indicate a brittle failure morphology, a faster crack propagation normally took place in a smooth fracture surface than in the rough surface. These two failure modes occurred separately in a very short period of time. The crack was initiated at the middle of the specimen due to the lack of physical bonding, then propagated horizontally to both sides of the sample. The reason of these impressively different fracture morphologies is potentially the direction of applied tensile load. There may be an error occurred during the testing, which may finally cause uneven load applied on the two edges of sample.

As for the PLA/PHBV 30:70%, only little area has no physical bonding in the fracture surface. The failure mode in the Fig. 52d is like that in the x-axis specimen, which the crack is integrally propagated across the sample, different failure modes are physically linked, rather than two separated cracks, such as Fig. 52b and 52c. The optimized anisotropy property in all the copolymers has achieved in this weight ratio due to the

maximum physical bonding performance, whereas the printing geometry accuracy in this proportion ratio is the lowest. Interestingly, the PLA/PHBV 30:70% specimens printed in x and y axis orientations have completely polarized deposition result. Strong deformation occurred in the PLA/PHBV 30:70% specimen and an inverted trapezoidal outline of the fracture surface is observed in the y-axis specimen except few bottom layers, which indicated an over-deposition of the copolymer during the printing process. This appearance has occurred in all the copolymers, which when printed in y-axis orientation and with the increasing PHBV added, more severe overstocked material is deposited upon the previous layer at turning area of the specimen.

The improvement of interlaminar bonding performance, when the PLA/PHBV copolymers are printed in y-axis orientation, is potentially due to the over-deposition of the printer by sacrificing printing geometry accuracy. The origin of this insufficient and over-sufficient material deposition which occurred in the same copolymer is not fully understood yet, but one explanation may be proposed relating to the thermal properties of PHBV, which will be further discussed in the following sections.

(a)   (b)

(c)   (d)
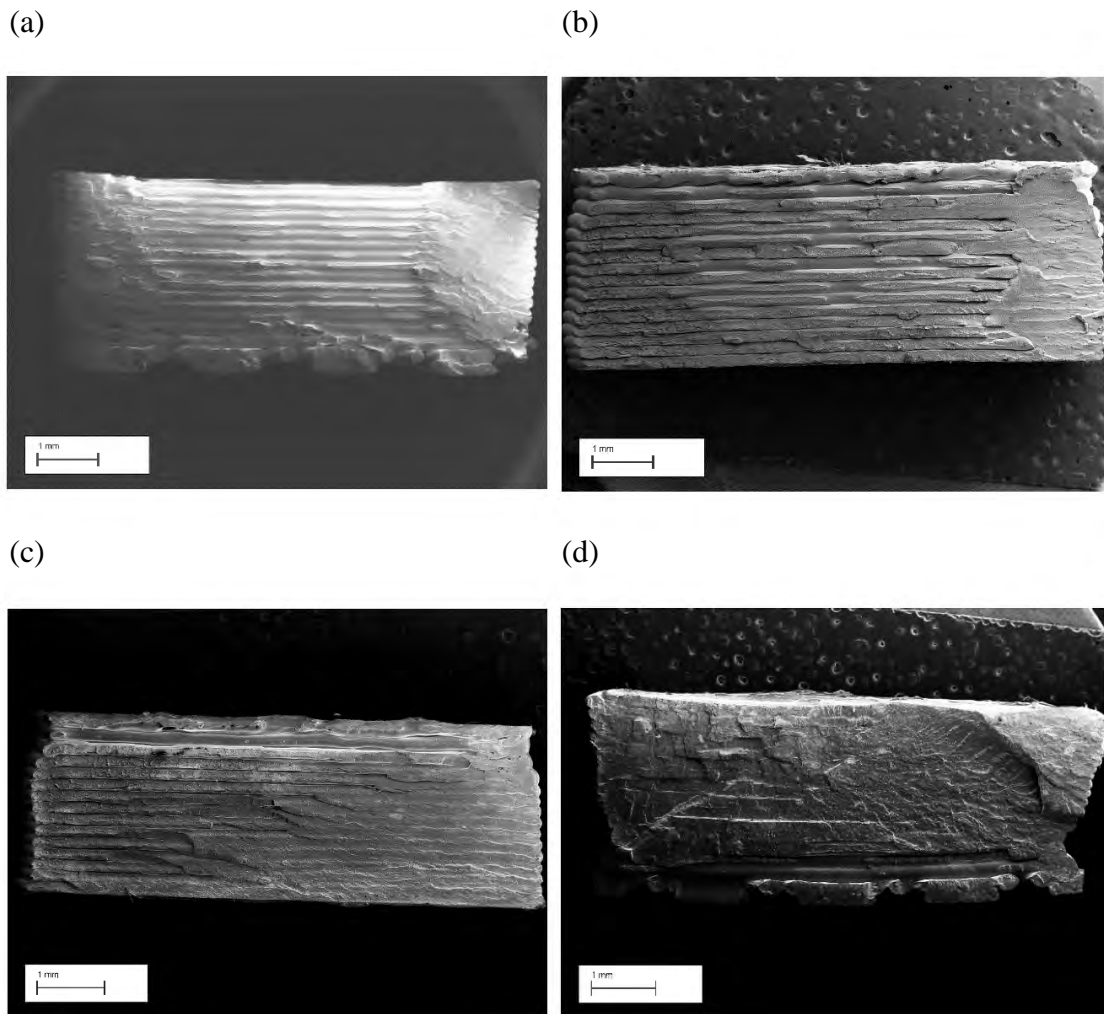
Fig. 52 Fracture morphology of PLA/PHBV copolymers printed in y-axis (a: PLA, b: PLA/PHBV 90:10 wt%, c: PLA/PHBV 70:30 wt%, d: PLA/PHBV 30:70 wt%)

5.4.3 The cross-section morphology of PLA/PHBV copolymer printed in x-axis orientation

In this section, the PLA/PHBV 70:30 wt% and PLA/PHBV 50:50 wt% are employed to study the cross-section morphology of the copolymers. Fig. 53 shows the cross-section of x-axis specimens, compared to the cross-section of neat PLA, the porosity and size of pores are impressively improved. It is also worth mentioning that the pores among filament beads are halved in some printed layers, shown in Fig. 53a. Unlike the relatively uniform pores in PLA specimen, the shape and size of the pores in PLA/PHBV 70:30 wt% are somehow variable. The thermal properties may be one of the reasons for these reduced and variable pores, and the copolymer has shown more sufficient deposition and neck growth during printing process. Beside the pores

generated during the printing process, another proposed explanation is that some of the residual material is displaced during the cutting process when preparing the cross-section specimen. Interestingly, when observing the cross-section image, pores are horizontally absented every other adjacent filament beads. This phenomenon is clearer at the bottom and in the middle than top parts of the sample, and it can also be observed in the fracture surface shown in Fig. 51c.

Compared with the PLA/PHBV 70:30 wt% copolymer, a further integrated cross-section is acquired in the PLA/PHBV 50:50 wt% copolymer. The size of pores in the image is further decreased to nearly invisible. Like the PLA/PHBV 70:30 wt% copolymer, the grooves between layers are subtle and the shape of pores is still considerably disordered.

Beside the pores generated during the printing process, another proposed explanation is that some of the residual material could be displaced during the cutting process when preparing the cross-section specimen. Fig. 54 compares the shape of the pores in the fracture surface and cut cross-section image. Excessive adhesion material can be observed in the Fig. 54b in comparison with the pore which presented in the fracture surface of Fig. 54a, from the size of the pores in the copolymers, it is not convincible that this is due to the disordered pores in the cross-section image.

Both PLA/PHBV 70:30 wt% and PLA/PHBV 50:50 wt% copolymers had a more integrated cross-section and less porosity than neat PLA, but the morphology of the pores cannot be determined due to the pores in the cross-section images are damaged during the cutting process.

(a) (b)
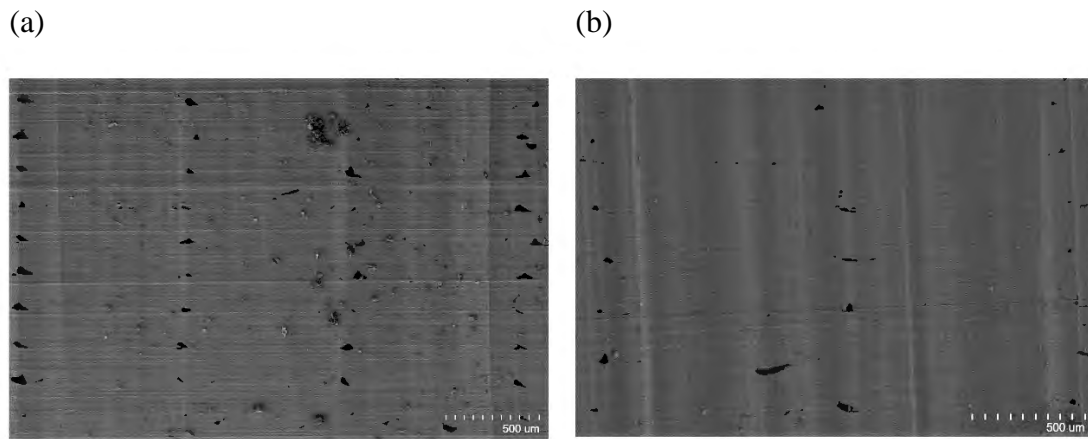
Fig. 53 Cross-section SEM image of PLA/PHBV 70:30 wt% and PLA/PHBV 50:50 wt%

(a) (b)
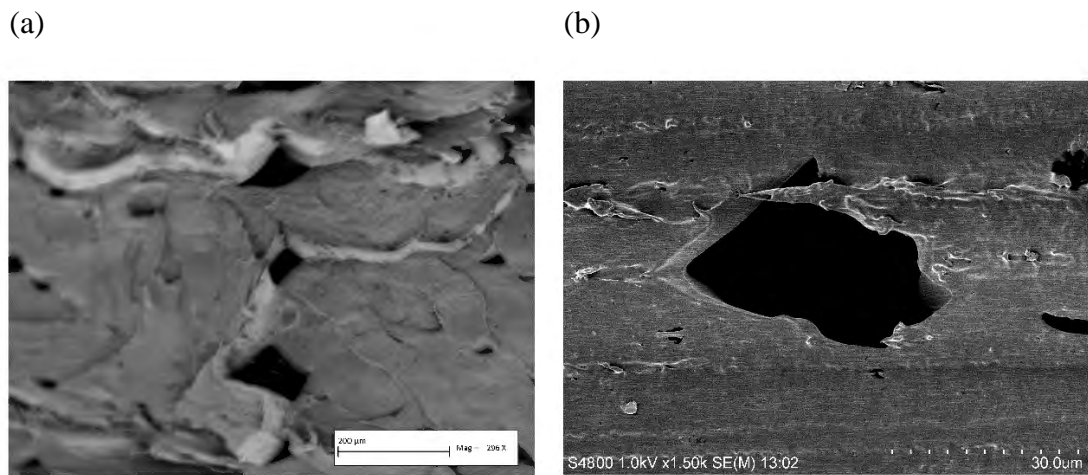
Fig. 54 Comparison of the interlaminar pore between fracture surface and cross-section SEM image in PLA/PHBV 50:50 wt%

5.4.4 The cross-section morphology of PLA/PHBV copolymer printed in y-axis orientation

In the cross-section image of y-axis samples, similar phenomenon has occurred. The grooves in the image are physically smaller and thinner compared with those of PLA specimen, shown in Fig. 55. An improved bonding performance has been achieved. The grooves in the image illustrates the pores among printed filament beads and among the printed layers. The cross-section shows similar variation with the fracture surface, the grooves is considerably smaller at the side of the specimen than in the middle.

However, there are two concerns shown on the images. Firstly, the appearance of the grooves from the image shows non-uniform layout and spread. One of the reasons is the large deviation of filament diameter, leading to a variable deposition during the printing process. It can be observed that there are some of the cavities in the cross-section image, shown in the bottom right of Fig. 55a. Unlike the bubbles in the PLA specimen, which are mainly located in one area, the cavities are randomly scattered in the cross-section of copolymers. The size of the cavities is normally large, almost as big as one printed layer. It is possible that the clogging of nozzle orifice occurs during the printing process and the cavities are formed when the clogging happened. The remaining impurities in the filament may also have been removed during the cutting process, thus resulting in cavities. Fig. 56 indicates the cavities caused by impurities.

(a)   (b)
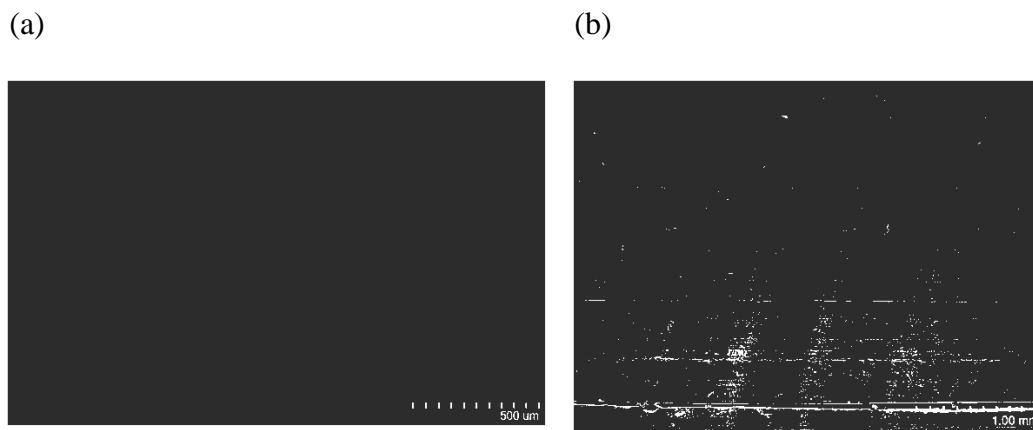
Fig. 55 The cross-section SEM images of PLA/PHBV 70/30 wt% and PLA/PHBV 50/50 wt%

Fig. 56 The cavity presented in the PLA/PHBV 70:30 wt% y-axis specimen

5.5 Nanoindentation analysis of 3D printed PLA/PHBV copolymers

With the addition of PHBV, the micromechanical determination of boundary performance needs to be evaluated. The ratios of PLA/PHBV 70:30 wt% and PLA/PHBV 30:70 wt% were chosen to analyse the micromechanical properties of the 3D printed copolymers like the previous chapter. Fig. 57 shows three testing locations selected for nanoindentation, which are considered possible print boundary locations. Fig. 57b and 57c show the micrographs before and after the nanoindentation at the test site under the microscope.

(a) Position of indentations　　(b) Before　　(c) After
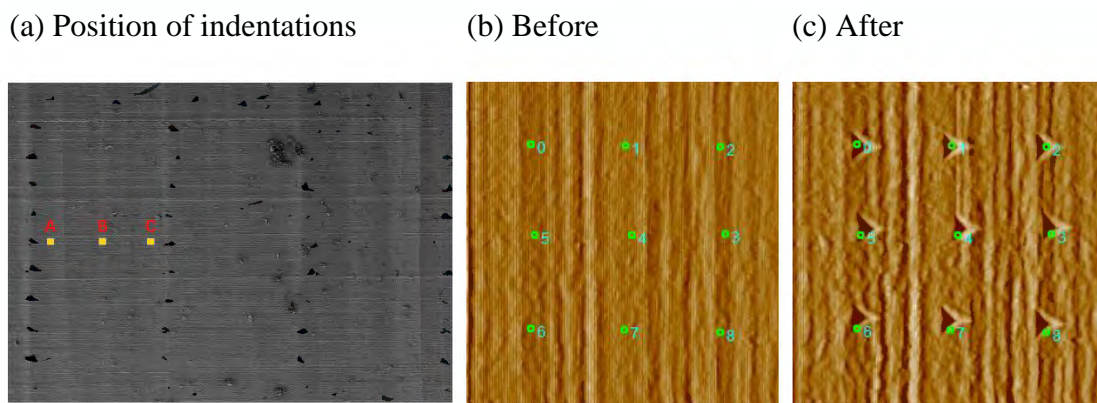
Fig. 57 Position of indentations were implemented in PLA/PHBV 70:30 wt% and the microstructure morphology before-after testing

The average hardness and modulus of the material obtained after nanoindentation testing are shown in Fig. 58. Similar to the previous chapter, the micromechanical properties of copolymer did not show a significant attenuation of interlaminar bond strength. The results obtained at all test points are within an acceptable tolerance range. It can be concluded that, like the PLA, copolymer has little interlaminar bonding surface that will affect the mechanical properties. The main reasons for affecting the mechanical properties may still be the neck growth length of physical interlaminar bonding.

Like the results of mechanical properties after tensile test, the average modulus of PLA/PHBV 30:70 wt% is 8% higher than that of PLA/PHBV 70:30 wt% in the results of nanoindentation test, which is presented in Fig. 58b. Hardness is almost identical

(Fig. 58a), being in 0.31 GPa and 0.32 GPa respectively. Due to the lower printing quality of PLA/PHBV 30:70 wt%, the greater deviation in material hardness has been obtained in the nanoindentation result.

(a)   (b)
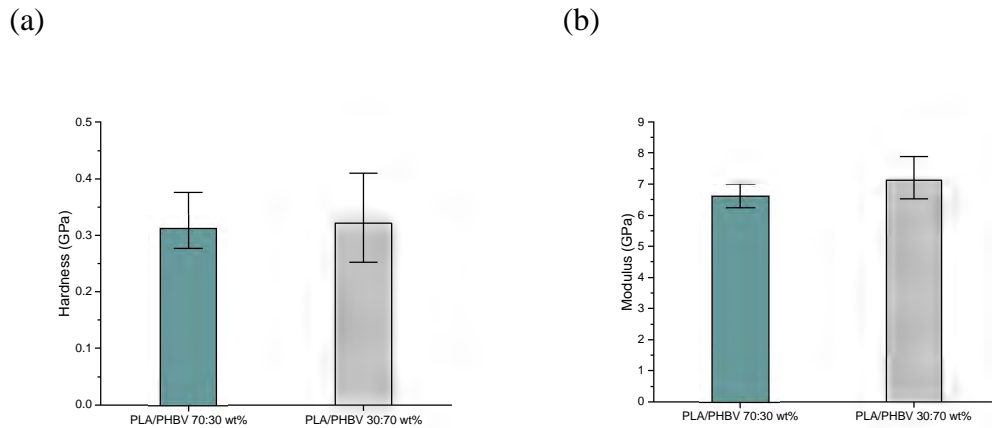
Fig. 58 The hardness and modulus of the PLA/PHBV copolymer

It is worth mentioning that fine vertical grooves can be seen on the surface of the copolymers and the spacing of the grooves is random from nanometers to micrometers. The material surface characterization may image the bond strength between the printed layers and whether these grooves are related to the interlaminar bonding properties. To determine the influence of the grooves on the material properties, some indention points were selected to be pressed on the grooves in the nanoindentation testing process.

As aforementioned, two nanoindentation samples (one for each material weight-ratios) are selected to determine whether final performance will be affected by the micro-grooves. The microstructure of two selected samples is shown in Fig. 59, in the Fig. 59a, inline indentation number 1-4-7 and 2-3-8 are considered points on the groove and 0-5-6 is the normal indentation points. Similarly, the indentation number 0-5-6 and 2-3-8 in the Fig. 59b are chosen as a comparison with the normal indentation point.

The test results of two samples are shown in the Fig. 60, comparing each inline indentation points (result of each point is shown in Appendix). Two different phenomena are achieved in different material weight-ratios, insignificant variation is shown in the Fig. 60a, but the results of inline indentation points on the grooves are slightly higher than the points off the grooves in the PLA/PHBV 30:70 wt%. The average modulus of the 1-4-7 points, which is considered off the grooves, is on average

7% higher than that of the points on the grooves. However, it is still unknown that the origin of this variation and the variates may cause this difference are numerous, such as the cutting procedure before the nanoindentation implemented, the system error of nanoindentation process and immiscible material domains. There is no evidence that this loss comprehensively existed in all over the printed specimen, and this phenomenon may not be considered novel material properties in the PLA/PHBV copolymer and the material interface between printed beads, but it is still worth digging based on this phenomenon.

(a)   (b)

PLA/PHBV 70:30 wt%   PLA/PHBV 30:70 wt%
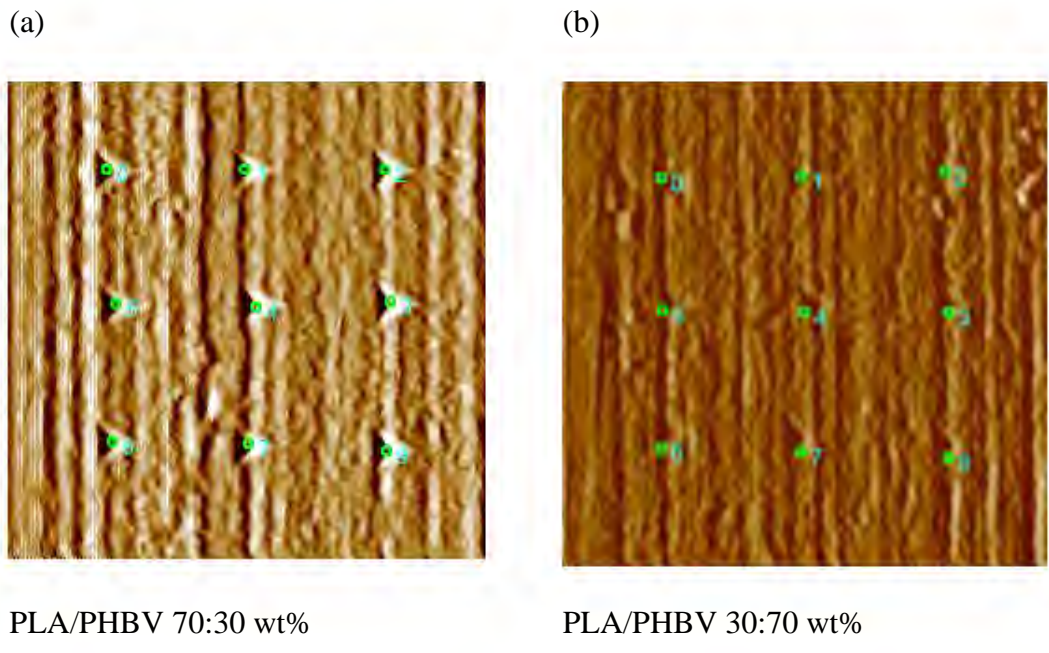
Fig. 59 Selected nanoindentation samples applied on the micro-grooves

(a)   (b)
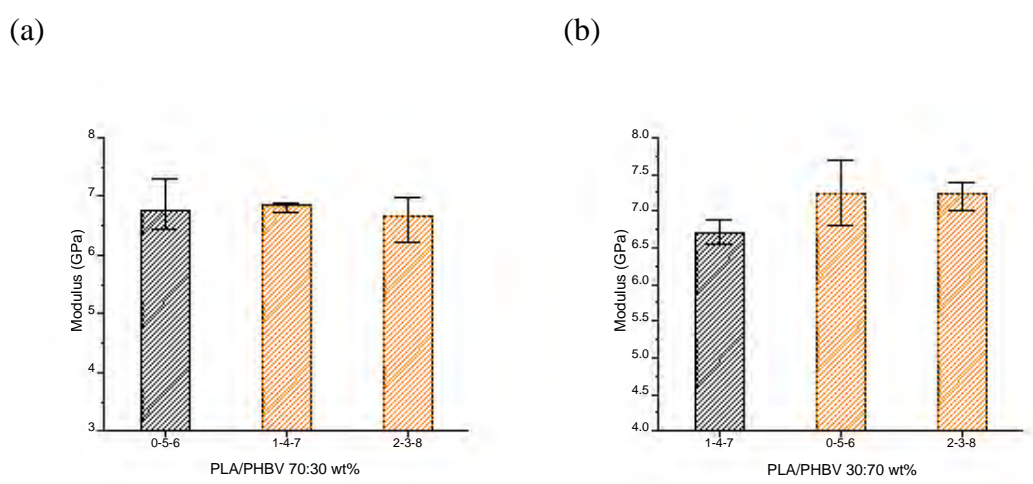
Fig. 60 Comparison of the nanoindentation results that on and off the grooves

5.6 Thermal properties of PLA/PHBV copolymers

To further study the cause of the variation on the printing performance occurred, the thermal properties of PLA/PHBV copolymers are analysed by TGA. Two blend compositions (PLA/PHBV 70:30 wt% and PLA/PHBV 30:70 wt%) are selected in this study. The TGA diagram is described in Fig. 61. Generally, the degradation of two blends occurred differently as expected and the degradation ranges of copolymers are

both relatively narrow. Both copolymers have more than one stage of degradation. Table 20 summarises the corresponding stages of decomposition (2%, 5%, 10% and 50%).

Based on the Table 20, the degradations have initiated at the temperature of 263 °C for the PLA/PHBV 70:30 wt% earlier than the 273 °C for the PLA/PHBV 30:70 wt%, when the weight loss is reached 2%. However, a rapid degradation on the PLA/PHBV 30:70 wt% is observed, at 279, 284, 298 °C when the weight loss is 5%, 10% and 50% respectively. The range of weight loss from 2% to 50% is only 25 °C in comparison with that on PLA/PHBV 70:30 wt% which is 65 °C. The residues at 550 °C of both copolymers are around 1%, which is very little quantity, it is worth mentioning that the PLA/PHBV 70:30 wt% has a higher residue due to the mineral fillers which are acted as stabilizers or nucleating agents in PHBV polymer, but it's not mentioned in the datasheet of the PHBV, which is provided by the material supplier.

The maximum rate of weight loss which corresponds with temperature is also critical to the thermal characteristic, the curve is presented, which the maximum rate is determined as the peak value of the 1st derivative of the TGA curve, shown in the Fig. 62 as derivative thermogravimetry (DTG). The decomposition feature of the material can be improved from the investigation by the DTG curve, and decomposition temperatures (T_{max}) can be found and listed in Table 21.

A bimodal peak has been obtained in the DTG curves of both copolymers; the first peak of weight loss in the PLA/PHBV 70:30 wt% is 298 °C which is almost identical with the 297 °C of PLA/PHBV 30:70 wt%. However, the decomposition rate of PLA/PHBV 30:70 wt% is 59%, which is considerably higher than that of the other copolymer. The immiscibility of PLA and PHBV blends can also be confirmed by the bimodal peak curve.

It can be concluded that the decomposition of both blends occurred within a narrow range of temperature and the thermal stability of PLA/PHBV 70:30 wt% is slightly improved compared with that of the other blend compositions.
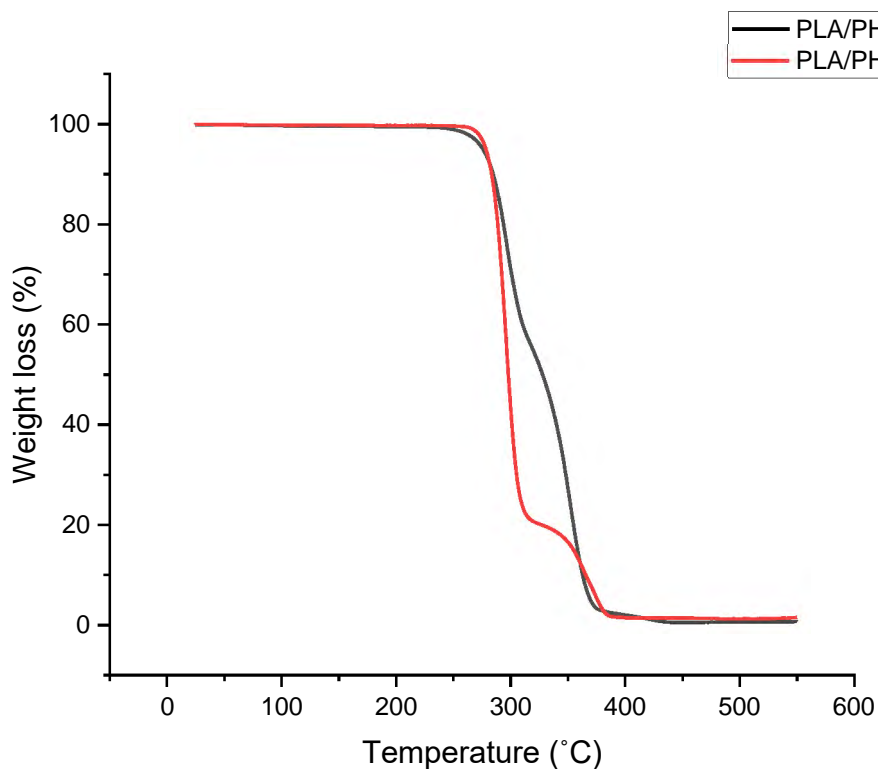
Fig. 61 TGA curves of the PLA/PHBV blends.

Table 20 Decomposition temperature of PLA/PHBV blends when the weight loss is reached 2%, 5%, 10% and 50%, and char yields at 550 ˚C.

	T$_{2\%}$ (˚C)	T$_{5\%}$ (˚C)	T$_{10\%}$ (˚C)	T$_{50\%}$ (˚C)	Char yield (%)
PLA/PHBV 70:30 wt%	263	276	285	328	0.85
PLA/PHBV 30:70 wt%	273	279	284	298	1.67
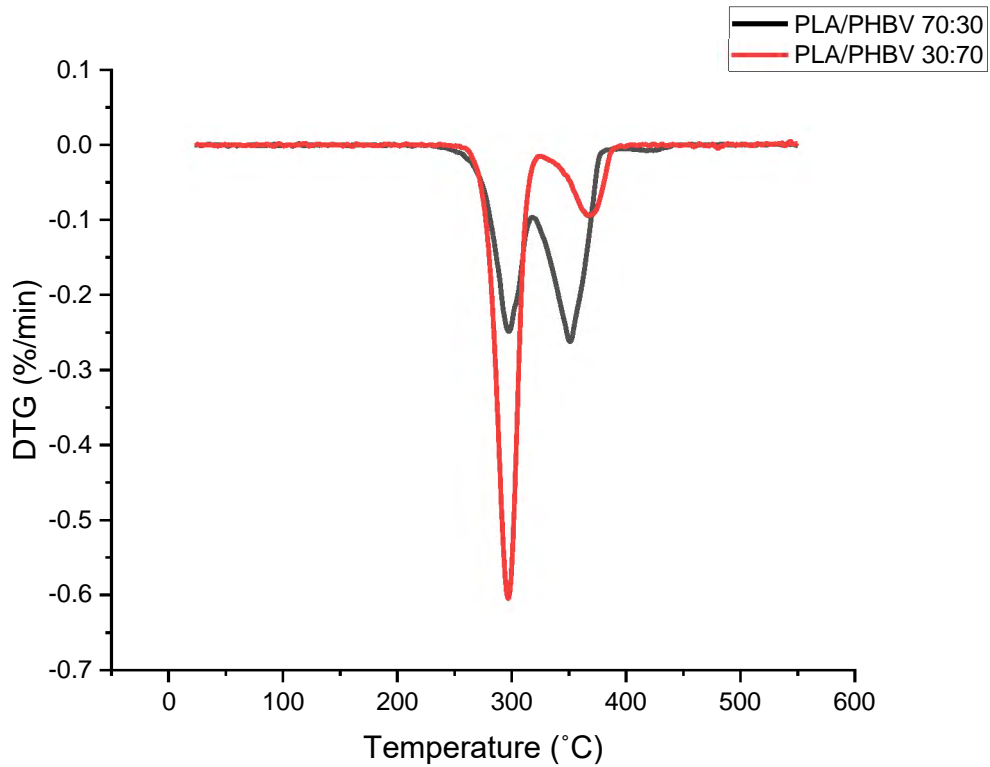
Fig. 62 DTG curves of the PLA/PHBV blends

Table 21 Decomposition temperatures of PLA/PHBV blends

	Decomposition temperatures (T_{max})
PLA/PHBV 70:30 wt%	298-351 ˚C
PLA/PHBV 30:70 wt%	297-366 ˚C

5.7 Discussion

PHBV, as a gaining immense attention in the bio-based polymer industry, has been applied in various processes except AM. The AM produced PHBV and its copolymers require further exploration. This chapter investigated the performance of PLA/PHBV copolymers applied in FDM. The wave non-uniform density distribution in x-axis specimen was found when the PHBV content is high, such as PLA/PHBV 30:70 wt%, which indicated a higher porosity, but the opposite result was achieved in y-axis

specimen. An overstock was reported when the copolymer printed in the y-axis orientation.

With the addition of PHBV, mechanical properties of the copolymers were decreased in both printing orientation, but except the PHBV content was 70 wt%, the reduction in tensile strength was negligible (7% and 4% in a-axis and y-axis respectively when the PHBV content was 50 wt%). However, opposite results occurred in tensile strain, the tensile strain reduced slightly (up to 16%) when the printing orientation was x-axis. The tensile strain improved considerably with increased PHBV content (1.94% in PLA/PHBV 50:50 wt% compared to the 1.1% in neat PLA). The outcome of results achieved is not fully in agreement with the previous report [285], where the specimen printed in vertical had higher tensile strength compared to the horizontal and the tensile strains of PLA/PHBV were impressively higher than that of the PLA in vertical printing orientation.[286] The actual density and overall thickness of the printed parts were considered for these abnormal results. Fuentes et al. [287] have also studied the PLA/PHBV copolymer filament using FDM process, different PHBV contents were studied (40, 50, 60 wt%). When the printing orientation was ± 45°, little deterioration was found in tensile properties with the PHBV content increased, but the flexural and impact strength had an impressive decrease when the PHBV content was over 50 wt%. Compared to the results in this study mentioned in 5.3, the tensile strength of PLA/PHBV 30:70 wt% was 33% lower than that of the 50:50% specimens. The potential reasons may be summarised as follows:

- The printing was carried out without any addition of additive, while an epoxy functionalized styrene-acrylate copolymer compatibilizer was used as a chain extender (CE) in previous research, which could lead to a better processability, shown in Fig. 63.

- The cooling process (Fig. 63) after the filament extruded from the die was also different, where the water cooling applied could result in a more homogeneous outline of the filament.

- There may be a difference in the quality of filaments used. For instance, a less contaminated printing filament could be generated with a direct extrusion by a twin-screw extruder compared to a 3-step process used in this study.
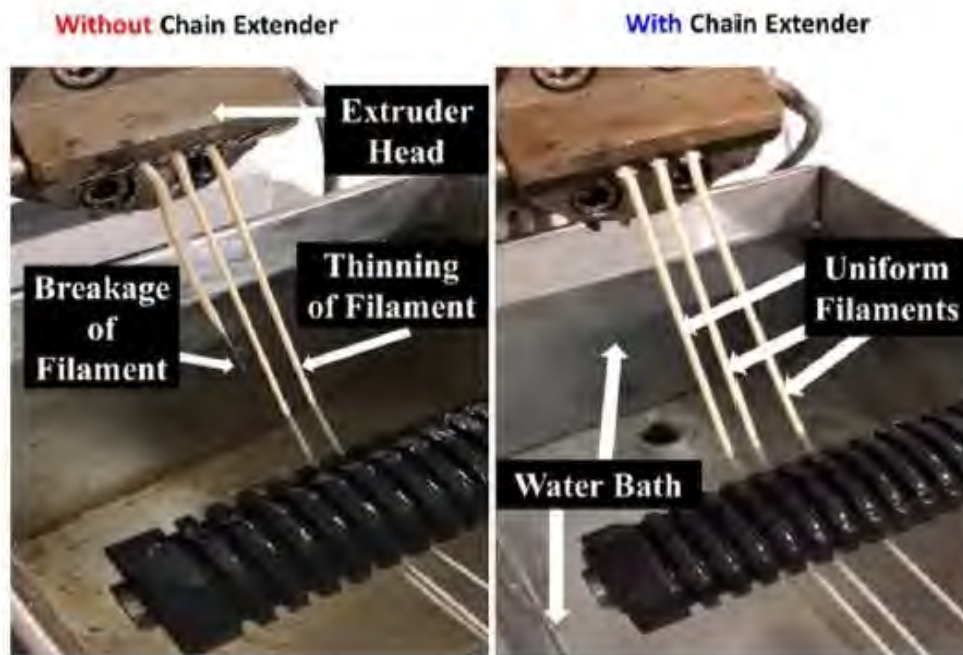
Fig. 63 The water bath cooling process and the filament extruded with and without chain extender.

The interlayer bonding of the PLA/PHBV polymers was also investigated and the bonding performance was evaluated by visual fracture morphological characterization. Similar to the fracture surface of the PLA specimen, brittle failure occurred in all specimens and fewer voids were observed in both x and y axis specimens compared to the neat PLA. The interlayer bonding improved with the increasing content of PHBV but the non-uniform printing also occurred. The filament fusion and residual stresses were considered as two main factors involved. As the various platform temperatures and layer thicknesses were applied from other studies [287], some visible interfaces were shown (Fig. 64). As the ± 45° printing orientation was applied, shear fracture occurred (Fig. 64b) [287]. Smaller layer thickness was suggested to reduce the residual stress [288].

The miscibility and decomposition properties were analysed by TGA process, immiscibility was found due two peaks were observed in DTG curve. Gerard and Budtova [288] studied the PLA and PHBV blend in various compositions, the immiscibility of two polymers was also supported by differential scanning calorimetry (DSC) and morphology characterization SEM image, which can match the thermal properties result in this study, section 5.6. More additives or plasticizers are still attractive to PLA/PHBV printing.
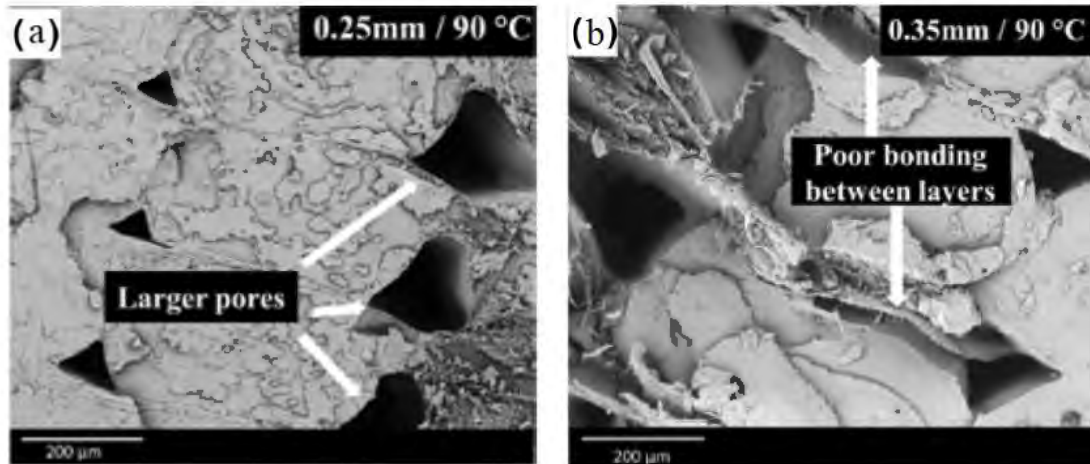
Fig. 64 Fracture surface of PHBV:PLA:CE (40:60:0.25) [287].

5.8 Interim conclusions

The performance of 3D printed PLA/PHBV copolymer was investigated and analysed in this chapter. The different variations of the copolymer printed in the x-axis and y-axis have been achieved in the VDP results. With the increasing weight ratio of PHBV, the amplitude of the density distribution waves is decreased from 138 kg/m^3 to the minimum 54 kg/m^3 in the PLA/PHBV 90:10 wt% and PLA/PHBV 30:70 wt% respectively. Two opposite tendencies have been obtained in x-axis and y-axis specimen, the variation was also supported by the results from the examination of mechanical properties and microstructure characteristics. Despite the fact that the printing quality has deteriorated with the increased weight ratio of PHBV, especially the tensile strength of PLA/PHBV 30:70 wt% was achieved only 33.1 MPa in x-axis, which was 39% lower than PLA. There was strong evidence that the anisotropy property in the 3D printing objects was relieved by the addition of PHBV polymer. Compared to the y-axis specimens to the x-axis, anisotropy in tensile strain has been considerably enhanced from 62% to 20% in PLA/PHBV 30:70 wt%.

The microstructure characterisation explained the enhancement of anisotropy mainly due to the improved interfacial bonding in printed y-axis specimens of PLA/PHBV blends. However, there was no clear evidence of the interlayer boundaries when implementing the nanoindentation process.

Although the mechanical performance and the printing accuracy were deteriorated corresponding to the increased weight-ratio of PHBV, but the PLA/PHBV copolymer

could still be attractive as the potentially improved anisotropy property has been emerged in forementioned studies.

6. Improvement and Modification of PLA and PHBV Polymers for 3D Printing

6.1 Introduction

With the PLA/PHBV copolymers studied in the previous chapter, a dramatic potential has appeared for the application of biopolymer applied in additive manufacturing. However, besides the reduced anisotropy property when printing in different orientations, there exist several defects:

1) Different deposition disorders during the printing process;

2) The poor geometry accuracy and warpage when the PHBV weight ratio is high;

3) The decreased mechanical properties;

4) Severe brittleness in all the specimens.

This chapter offers a further study that attempts to improve the issues above based on the previous chapters. The modification and improvement are implemented by the addition of some other biopolymers, those copolymers and additives like Polycaprolactone (PCL), Polybutylene Succinate (PBS) and Polyethylene glycol (PEG).

6.2 Vertical density profile (VDP) of 3D printed PLA and PHBV with modifications

The modified specimens were compared with their benchmarks, which are the PLA and PLA/PHBV 30:70 wt% specimens due to the incomplete data acquired of neat PHBV. The porosity distributions were investigated to firstly determine the printing quality of the modified printing materials. Similar to previous chapters, the x-axis and y-axis printing orientations were analysed separately.

6.2.1 VDP of modified materials printed in x-axis

6.2.1.1 VDP of modified PLA based polymers printed in x-axis

The PLA and two of the blends based on the PLA polymer are analysed in this section. The density distributions are presented in Fig. 65a. Three printed specimens have

overall similar results in average density. The average density of neat PLA has the highest density of 1140 kg/m^3, which is slightly higher than other two modifications. The PLA/PBS and PLA/PBS/PEG copolymers have almost identical average throughout the specimens, resulting in 1110 and 1112 kg/m^3.

The amplitudes of the wave are also similar between three specimens, the maximum amplitude is occurred in the neat PLA, which is 71 kg/m3. The modifications have slightly lower amplitude obtained from the result, which indicates a lower porosity compared with the PLA. However, the argument has been raised that the density of copolymers should have a higher density compared with PLA due to the present of PBS, but lower peak density occurred during the VDP testing. Besides considering the system error, the geometry disorder is also one of the reasons led to this phenomenon. The air gap between specimen and sample holder is also counted during the testing procedure and lead to the final lower peak density.

Generally, it can be concluded that two modification specimens are printed in an adequate quality and uniformity, which are close to the neat PLA specimen, whereas the specific density distributions in the diagram varied. The distinguishing variations of density scanning from the bottom to top of specimen are observed in the diagram below (Fig. 65b). A 'smooth' diagram is provided to further study the tendency of specimens, shown in Fig. 65b. The PLA and PLA/PBS have a relatively flat density distribution, the average density in the top of the sample is very close to the density in the bottom. However, like the density trend of PLA polymer studied in Chapter 4, a descending density is also presented in the small PLA specimen except the first few deposited layers. The distribution trend of PLA/PBS and PLA/PBS/PEG in the opposite, presented an ascending density along with the printed layers, especially PLA/PBS/PEG specimen. The density of the top layer is 9% higher than the density at the bottom of the specimen (at layer thickness is 1mm). The reason of this tendency is still unclear and it will be further investigated at the following microstructure sections.
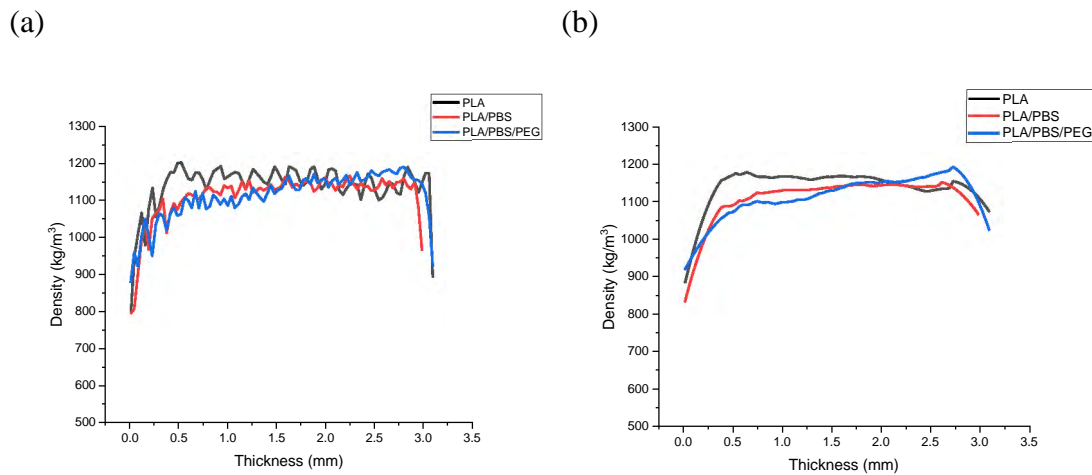
Fig. 65 VDP of PLA and modified copolymers (a) and smooth processed density diagram (b)

6.2.1.2 VDP of modified PHBV based polymers printed in x-axis

PHBV with modifications are compared with the PHBV/PLA 30:70 wt%, which have studied in the last chapter as a benchmark for all PHBV modifications. The density profile of PHBV modifications is presented in the Fig. 66a. Significant diversifications of density profile are obtained in the diagram (Fig. 66a), which need to be thoroughly introduced and discussed. The red PHBV/PBS and blue PHBV/PCL 90:10 lines present relatively smooth density distribution and variation compared with those of the benchmark. The average densities of these two modifications are almost identical, PHBV/PBS and PHBV/PCL 90:10 have average densities of 1180 kg/m^3 and 1178 kg/m^3, respectively. The PHBV/PCL 80:20, which is beyond expectations, has the lowest average density and greatest amplitude of wave. Although, it cannot be concluded what is the reason caused this dramatically differences between two close weight ratios.

From the variation of waves shown in the diagram (Fig. 66a), it can be expected that the porosity between different modifications varies dramatically. The pores in PHBV/PCL 80:20 specimen are expected large due to the greatest amplitude of wave. The PHBV/PBS and PHBV/PCL 90:10 in the opposite, smaller pores and lower overall porosity than the PHBV/PLA 70:30 copolymer can be determined. The maximum amplitude of PHBV/PCL 80:20 is 195 kg/m3 and its 88% and 157% greater than the PHBV/PBS and PHBV/PCL 90:10 respectively. However, all the modifications are

143

resulted in lower average density compared with the benchmark which the printing geometry disorder may be indicated.

The density distributions of PHBV/PLA/PCL copolymers are presented in Fig. 66b and the tendencies are provided in Fig. 64d, the two copolymers have similar tendency along the thickness with more stable density profile is observed in PHBV/PLA/PCL 70:20:10 wt% except the bottom of the specimen. Both copolymers have lower average density compared with the benchmark PHBV/PLA 70:30 wt%. Similar to the PHBV/PCL 90:10 wt%, the 10 wt% PCL polymer leads to a smoother density distribution rather than only 5 wt%. The copolymer with 5 wt% of PCL has a large amplitude similar to the benchmark specimen, which is unexpected. The addition of 5 wt% of PCL doesn't result in smaller interlayer pores. It is worth noting that further analysis of the VDP waves with a bigger sample size is highly desirable. The sample size in this research is limited due to poor processibility and non-uniform filament extruded.
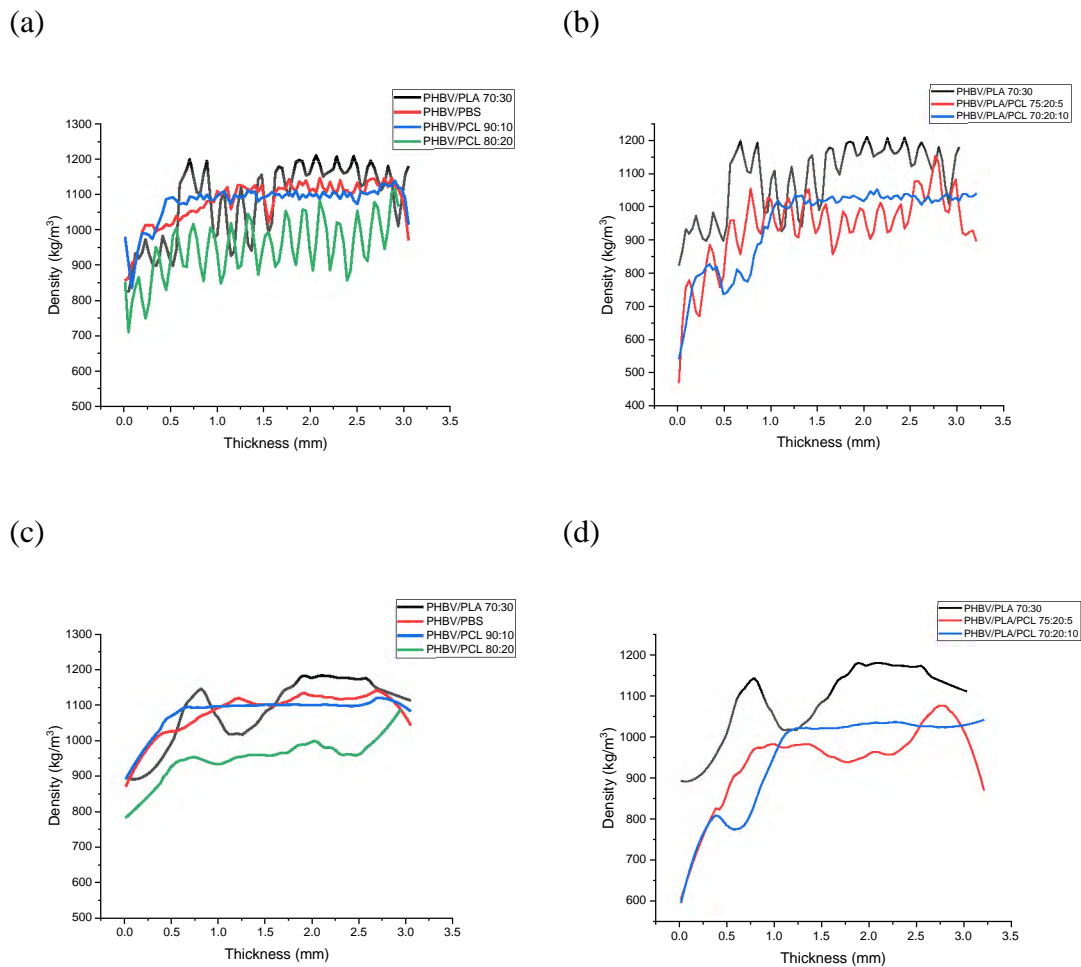
Fig. 66 VDP of PHBV and modified copolymers (a) and smooth processed density diagram (c)

6.2.2 VDP of modified material printed in y-axis

6.2.2.1 VDP of modified PLA based polymers printed in y-axis

The y-axis specimens are carried out in a similar to the x-axis, the density profiles of PLA based modifications are tested and compared with neat PLA y-axis specimen. The density profile of PLA and PLA based copolymers are presented in the Fig. 67a. It is apparent that the overall density distribution of PLA copolymers is similar to x-axis specimen compared with neat PLA. The same as the x-axis specimen, the average amplitudes of the modified copolymers are smaller than those of the PLA, which minor interlaminar pores can be expected. The overall average density of PLA/PBS/PEG is slightly superior to that of the neat PLA and the density of PLA/PBS is the lowest due to the unstable density distribution throughout the specimen.

Interestingly, the average density of all y-axis orientation specimens is higher than that of the other printing orientation, the reason caused this phenomenon is still unclear, but one of the reasons that can be proposed is that, besides the system error during testing, the overstocked material at both sides of the specimen could lead to a minor porosity of the entire specimen.

When analysing the waves of modified PLA printed in y-axis, beside the minor amplitudes compared with the neat PLA, the tendencies of density distribution are also investigated, the smoothed waves are presented in Fig. 67b. The PLA/PBS and PLA/PBS/PEG have almost identical composition but different density profile after the printing process, a relatively flat wave of PLA/PBS/PEG is similar to that of the neat PLA except the regression at the top of sample. The PLA/PBS has an ascending density profile along with the printed layers which is distinguished against the other two waves. The different density tendencies and the regression of PLA/PBS/PEG composition are mainly due to the printing uniformity rather than the material compositions, it could be assumed that the microstructures of PLA/PBS and PLA/PBS/PEG have very similar internal morphologies but different outline dimensions, the fracture morphology will be investigated later in 6.5.

(a)

(b)
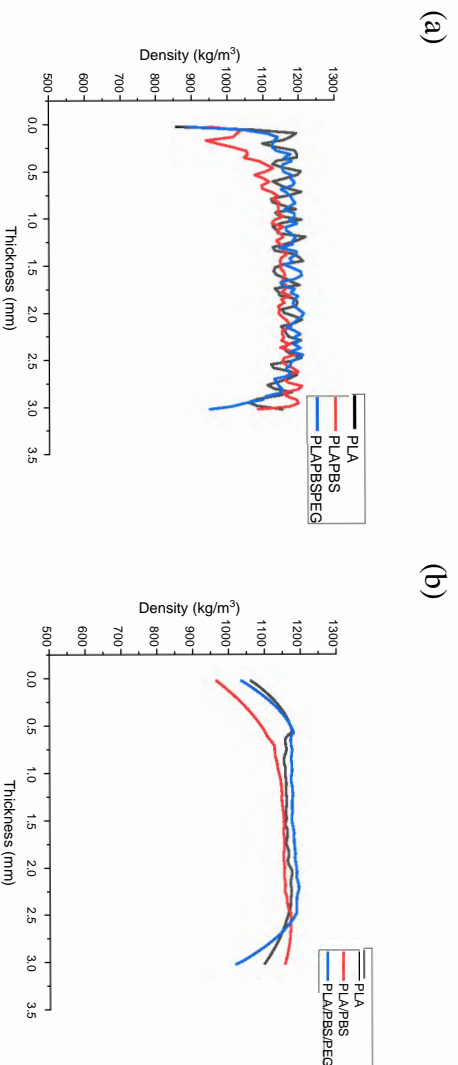
Fig. 67 VDP of PLA and modified copolymers (a) printed in y-axis orientation and smooth processed density diagram (b)

6.2.2.2 VDP of modified PHBV based polymers printed in y-axis

The density profiles of PHBV based modifications in y-axis are investigated and the density distribution diagrams have been summarised in Fig. 68a, various wave forms

like the abovementioned PHBV x-axis specimens, have been presented and the discussion for each specific wave needs to be provided. Some of the waves are varied when comparing the wave forms of x-axis with those of y-axis specimens like PHBV/PCL 90:10 wt%.

Generally, the common characteristic of all waves in the diagram is the minor overall amplitude compared with PLA based specimens, although there are several points which have relatively large variation in density, but these variations are caused by either the printing nonuniformity during fabrication or the disorder of geometry outlines. Further investigation will be provided in the following microstructure characterization to testify this deduction.

When comparing the average density of the specimens, except the PHBV/PCL 90:10 wt% specimen, the average density of other two modifications are all superior to the benchmark which is PHBV/PCL 30:70 wt%, the average densities are presented in the Table. 22. However, the comparison of y-axis average densities is less accurate than that of the x-axis specimens due to the geometry disorders occur extremely often in the y-axis specimen when the PHBV weight-ratio is high, but further evidence needs to be given.

The tendencies of modifications are impressively varied when printing in different orientations especially the PCL modified PHBV specimens, shown in Fig. 68b. In the y-axis orientation specimens, PHBV/PCL specimen has an ascending density along with the printed layers and PHBV/PCL 90:10 wt% sample when printing in y-axis compared with the adequate printing quality printed in x-axis orientation. The red PBS copolymer has the only similar density distribution and relatively high average density in both printing orientations which may indicate a decent printing quality.

(a)   (b)
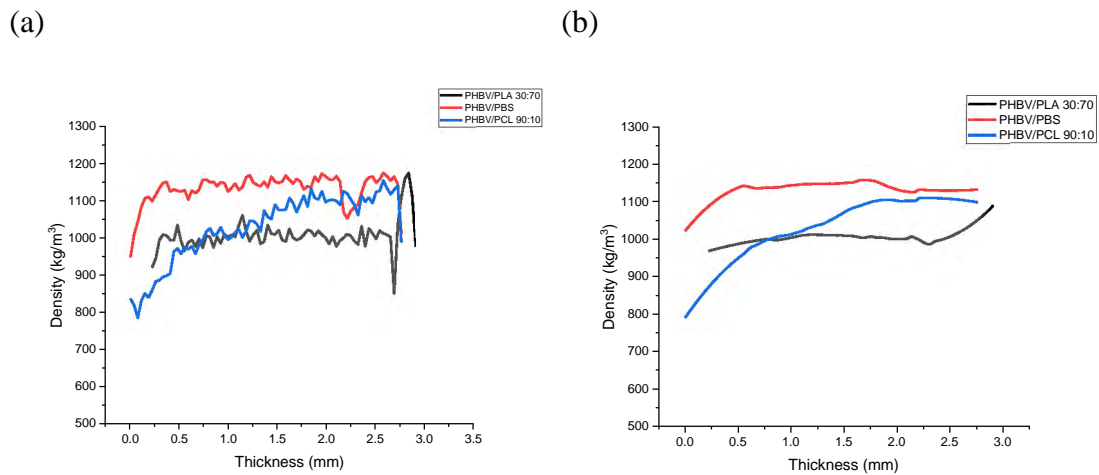
Fig. 68 VDP of PHBV/PLA and modified copolymers (a) printed in y-axis orientation and smooth processed density diagram (b)

Table 22 Comparison of the average densities of PHBV based modifications printed in y-axis

	PHBV/PCL 30:70 wt%	PHBV/PBS	PHBV/PCL 90:10 wt%
Density (kg/m^3)	1007	1120	989

Unlike the incoherent density tendencies of PHBV based modifications, the PHBV/PLA modifications show an adequate constant variation which presented in Fig. 69a. The average density of modifications is slightly higher than that of the PHBV/PLA copolymer and smoother fluctuations of wave are observed. Similar tendencies are also obtained that the wave of modifications has an ascending density along with the printed layers.

Compared the two modifications of PHBV/PLA, the PHBV/PLA/PCL 70:20:10 wt% has a greater ascending trend than other modifications due to the increased weight-ratio of PCL polymer. The PHBV/PLA/PCL 75:20:5 wt% sample has a relatively flat wave except the bottom and top of the sample, considerably low density is appeared at the bottom of the sample which may indicate a warpage occurred. Both modified specimens are expected a disorder in the outline dimension based on the experience from previous chapter in 5.5.
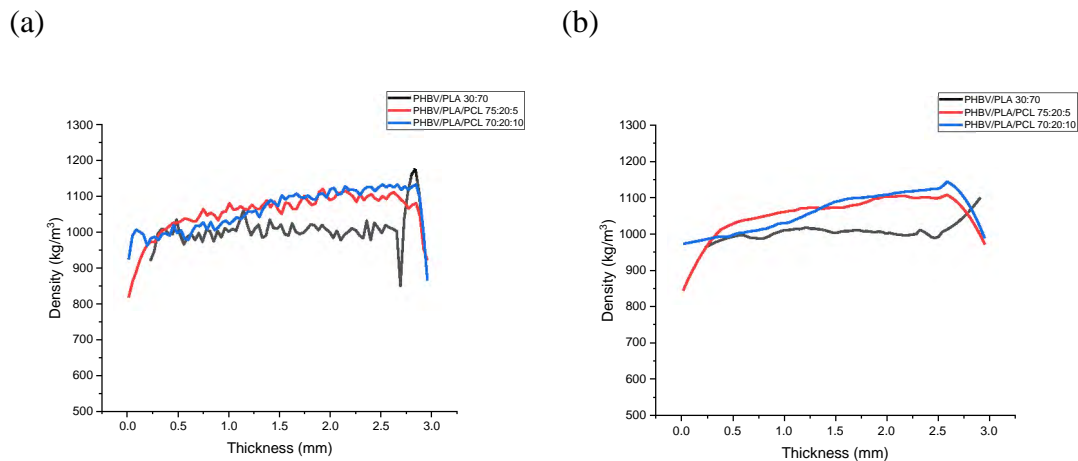
Fig. 69 VDP of PHBV/PLA and modified PHBV/PLA/PCL copolymers (a) printed in y-axis orientation and smooth processed density diagram (b)

6.3 Mechanical performance of 3D printed PLA and PHBV with modifications

6.3.1 Tensile properties of PLA and PHBV with modifications in x-axis printing orientation

6.3.1.1 Tensile properties of PLA modifications in x-axis orientation

Since the tensile performance of PLA polymer has been evaluated in the Chapter 4 and the brittle fracture has been observed in all the specimens, to ease the brittleness of the PLA polymer, the addition of PBS and following PEG polymers has been implemented since these two polymers have been employed and proven as plasticizers to the PLA [289,290]. The comparison of tensile strength and strain of the modified polymers and PLA specimens are shown below in Fig. 70, the tensile strains of modifications are impressively enhanced compared to the neat PLA.

The tensile strengths are slightly reduced by maximum 11% in PLA/PBS/PEG specimen compared with the neat PLA and the intermediate result has been obtained in PLA/PBS. The tensile strain however, the result of both modifications is considerably higher than the neat PLA, the increase of average tensile strain in PLA/PBS and PLA/PBS/PEG is 57% and 86% respectively. The result which the PBS and PEG modified PLA has proven the ductility can be improved by these two plasticizers.

(a)   (b)

Fig. 70 The tensile strength (a) and strain (b) of the PLA based modifications printed in x-axis orientation

6.3.1.2 Tensile properties of PHBV modifications in x-axis orientation

The PHBV polymer in this study is modified by various copolymers and additives such as PBS, PCL and PLA/PCL. The tensile properties of modified PHBV are obtained and presented below in Fig. 71. The modifications have shown insufficient improvement in both tensile strength and strain, compared with PHBV/PLA 70:30 wt% specimens, lower tensile strength have been obtained in PHBV/PBS and PHBV/PCL copolymers, but all the modifications have improved tensile strain compared with the benchmark.

From the Fig. 71a, only the PHBV/PLA/PCL copolymers have slightly improved strengths which the tensile strength of PHBV/PLA/PCL 75:20:5 wt% and PHBV/PLA/PCL 70:20:10 wt% is 22% and 15% higher than the benchmark respectively. However, the weakest tensile strength has been obtained by PHBV/PCL 80:20 wt% which is 30% lower than the PHBV/PLA, the abnormal result is achieved since this result is 22% lower than the similar material composition (PHBV/PCL 90:10 wt%). The reason of this reduction is currently unknow and further investigation will be provided in the following section. Apart from the lowest tensile strength, the maximum tensile strain has been obtained by the addition of 20 wt% of PCL, the result is 48% higher than the benchmark specimen.

Higher tensile strength has been achieved by both PHBV/PLA/PCL copolymers, but the ductility is negligibly improved. Unlike the PLA, limited improvement is achieved by addition of PBS polymer, immiscibility of PHBV and PBS polymer may be

indicated. Overall the modifications of PHBV polymer have resulted in insufficient improvement in mechanical performance.

(a)   (b)
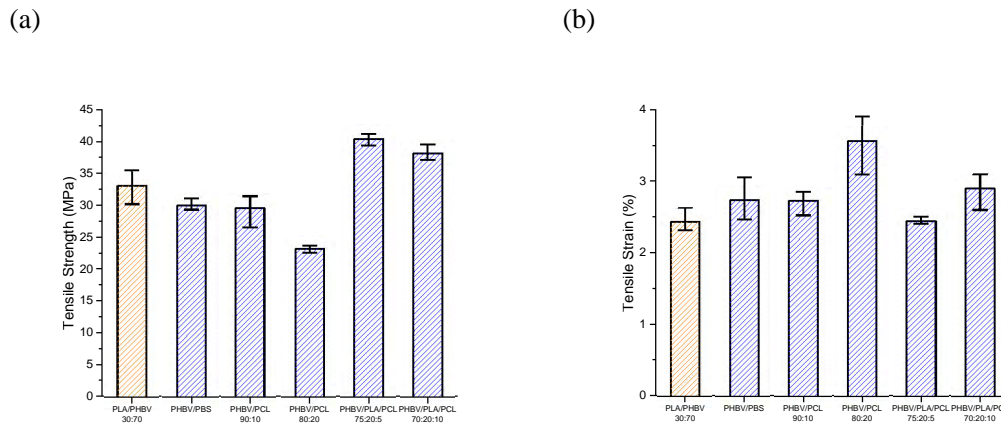
Fig. 71 The tensile strength (a) and strain (b) of the PHBV based modifications printed in x-axis orientation

6.3.2 Tensile properties of PLA and PHBV with modifications in y-axis printing orientation

6.3.2.1 Tensile properties of PLA modifications in y-axis orientation

The tensile properties of the modified PLA polymer printed in y-axis have been tested and presented below in Fig. 72, similar to the x-axis specimens above, the tensile strain (Fig. 72b) has been improved impressively but the insufficient difference has been observed in tensile strength (Fig. 72a). The tensile strength of modified specimens has slightly improvement (11% and 3% respectively) probably due to the increased interlaminar bonding area compared with the neat PLA, the reduced increase is occurred in PLA/PBS/PEG specimen due to the addition of plasticizer will reduce the strength [291].

In the meanwhile, with the plasticizer employed in the modification, the ductility of the specimen printed in y-axis has improved dramatically, the average tensile strains of PLA/PBS and PLA/PBS/PEG are enhanced 57% and 80% respectively compared with the neat PLA. Although the improvement of specimen printed in y-axis is very similar to x-axis, and beside the effect of added plasticizer, the improved performance of interlaminar bonding is also expected. It will be evaluated in the following fracture morphology section.

151
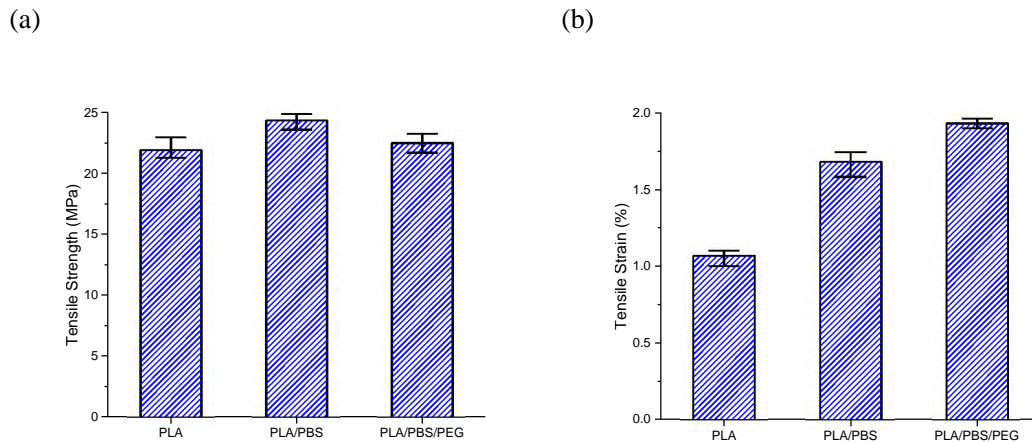
Fig. 72 The tensile strength (a) and strain (b) of the PLA based modifications printed in y-axis orientation

6.3.2.2 Tensile properties of PHBV modifications in y-axis orientation

Due to the various processibility of PHBV based modifications, two modifications are finally selected in the tensile properties study, the tensile strength and strain diagrams are provided below in Fig. 73. Although the reduction of sample size provided, PBS and PCL polymers are compounded with PHBV in each modification. Slightly reduced tensile strengths have been obtained in both modifications and only PHBV/PBS shows limited improvement in the tensile strain.

Large deviations of PHBV/PCL 90:10 wt% specimen have been observed in both diagrams since the non-uniform printing quality, significant warpage has occurred during the printing process. It can be concluded that the addition of PCL polymer cannot improve the processibility of PHBV based printing filament.

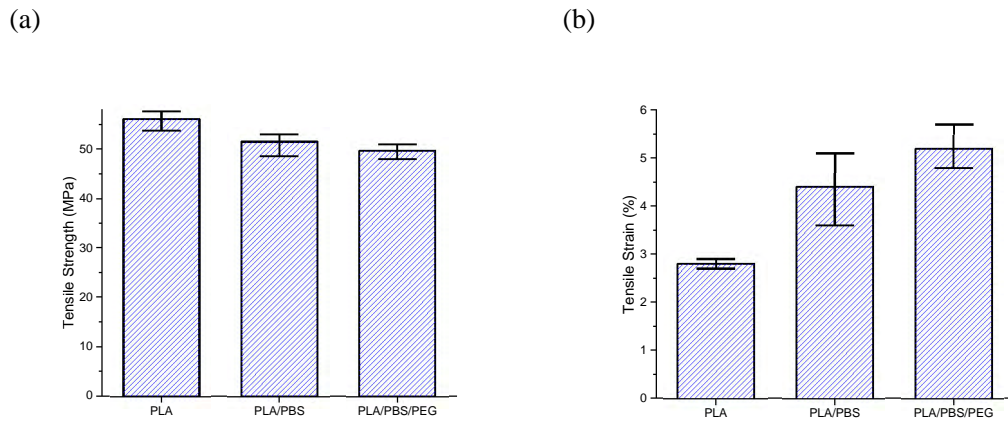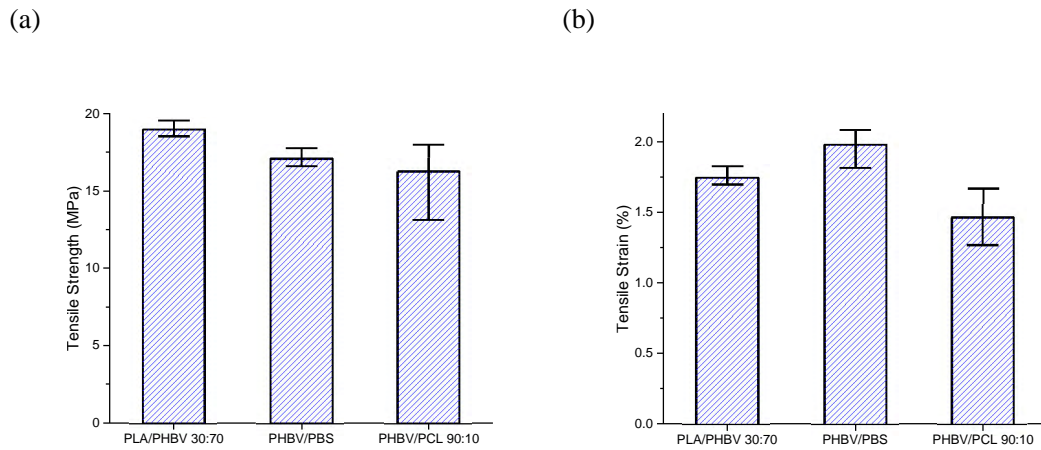Fig. 73 The tensile strength (a) and strain (b) of the PHBV based modifications printed in y-axis orientation

6.4 Microstructure of the modified PLA and PHBV polymers

6.4.1 Fracture surface of the modified PLA and PHBV printed in x-axis orientation

6.4.1.1 Fracture surface of modified PLA printed in x-axis orientation

Based on the previous studies of VDP and mechanical properties, a distinguishing microstructure of the modified PLA is anticipated. The same with last two chapters, the fracture morphologies of the x-axis specimens are taken by SEM to offer a visible further analysis of the effect of modifications and failure mechanisms.

The general view of fracture surface after the tensile testing is presented in Fig. 74 and the PLA has been employed in Fig. 74a as a benchmark. The fracture morphologies of PLA/PBS and PLA/PBS/PEG specimens are shown in the Fig. 74b and 74c respectively. With the addition of PBS and following PEG, the fracture surfaces of the modified PLA are varied dramatically from the neat PLA. The size and distribution of the pores are visually verified and matched with the VDP result, which are observed that smaller pores are evenly distributed in the modified specimens compared with neat PLA. Besides both modifications have a smooth failure surface like the PLA, the tearing failure between the adjacent filament beads is also commonly presented at an impressive large area of the sample. Ductile fractures are also observed in the

modification samples, which are matched with the higher strain in the result of mechanical properties.

However, besides the improved porosity and failure mechanisms, there are two concerns regarding the modified specimens.

- The printing processes are less uniform compared with the neat PLA, especially in the bottoms of the sample. The detached adjacent filament beads commonly appeared in both specimens.

- The final outline dimension of the printed parts from both modifications is less accurate compared with neat PLA. The reason is still opening to discussion, but it is suspected that the inhomogeneous printing process and unstable filament diameters could be one of the reasons.

Comparing the overview of PLA/PBS and PLA/PBS/PEG fracture surfaces, it can be concluded that both copolymers have very similar failure modes and mechanisms, and a larger area of smooth failure surface (marked red circles) is obtained in the PLA/PBS than in PLA/PBS/PEG, which indicates a greater brittle failure mode and in which the crack propagated fast along this area. Then the failure mode has also turned to more ductile, as the presence of the crazing is observed between the adjacent filament beads and a further delaminated bead has also been achieved (marked blue circles).

(a)   (b)   (c)
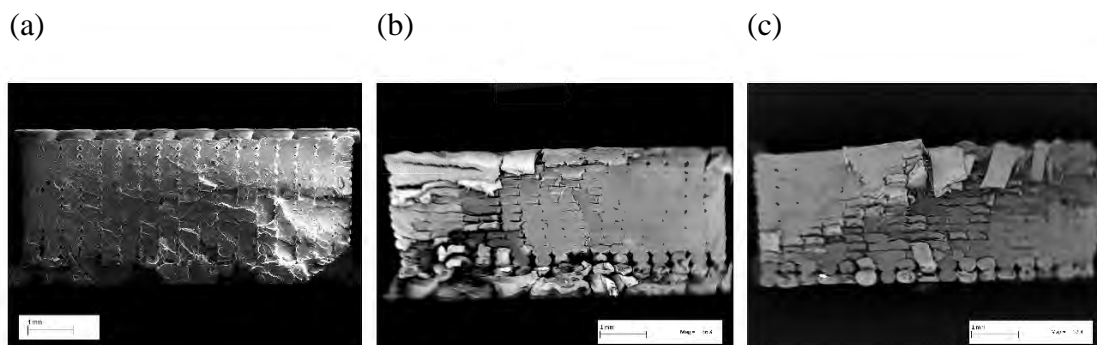
Fig. 74 Fracture morphology of PLA based modifications printed in x-axis. (a: PLA, b: PLA/PBS, c: PLA/PBS/PEG)

In the fracture morphologies of PLA based modifications, the area with crazing between adjacent beads and the delamination are very interesting for a deep study due to a potential inadequate interfacial bonding among adjacent layers and final ductility of the

sample. Fig. 75 presents the SEM images of the crazing and delamination areas in PLA/PBS and PLA/PBS/PEG specimens respectively.

(a)   (b)
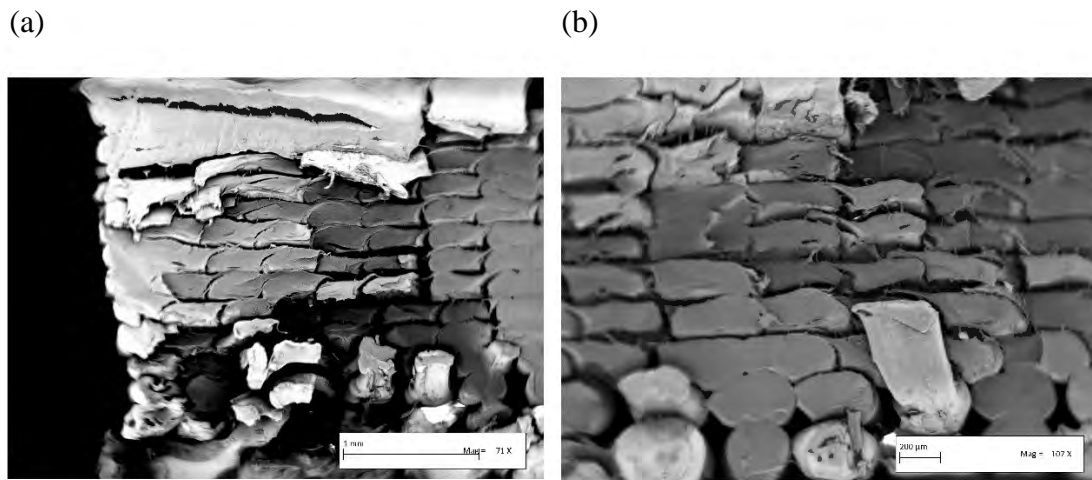
Fig. 75 Fracture morphology of crazing and delamination areas in PLA/PBS and PLA/PBS/PEG

From the microscopic images, a fish scale crazing morphology has been observed in both samples and the crazing is uniformly spread through the sample between the transversely adjacent filament beads. Most of the crazing has very similar orientation which indicates a single direction of crack propagation. The delamination of the printed filament beads normally occurred next to the fish scale area, as the further shrinkage of the diameter occurs in the filament beads during separated ductile fracture of single filament bead. Due to the increased interlaminar neck growth, the rectangular cross-sections of the delaminated filament beads are often obtained rather than the ellipse outline in the PLA specimen.

However, due to the shape of single filament bead in the fracture morphology, the weak interfacial bonding between layers is also potentially existed. It is still worth investigating the relationship between filament interfacial bonding and the failure mechanism in the PLA/PBS and PLA/PBS/PEG specimens.

The fracture surface of four filament beads is presented in Fig. 76 as an example for the study. The cracks are presented in both vertical and horizontal directions. The torn single printed filament bead has been found with the deformation to certain direction. From the image, the original pores between adjacent layers are marked, which is considered crack initiation. The crack propagates transversely till the next pore and the delamination between printed layers is generated, which is matched with the interface

of the layers. On the other hand, insufficient evidence has been provided by the image as the two pores are not connected vertically through the crack propagation. Hence the further study should be carried out in the following section.
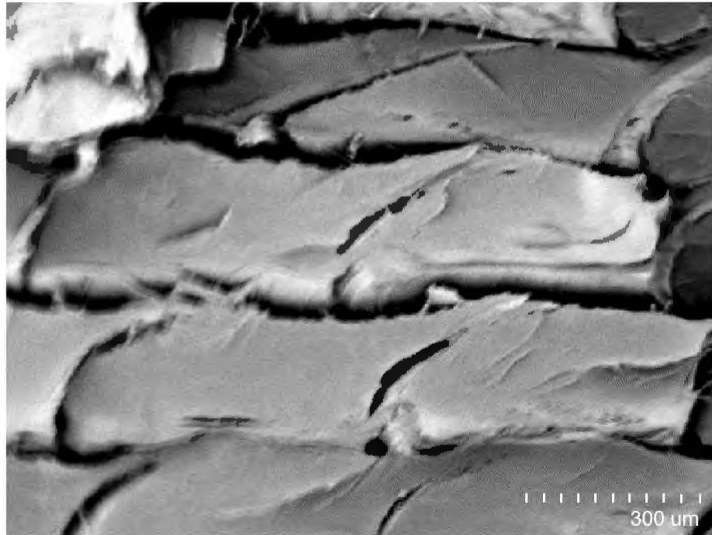
Fig. 76 Fracture mode of single filament in PLA/PBS specimen

6.4.1.2 Fracture surface of modified PHBV printed in x-axis orientation

The SEM fracture morphologies of PHBV based specimens printed in x-axis has also been implemented. Due to two different modifications, the microstructure of modifications is various, shown in Fig. 77. Aforementioned PHBV/PCL 80:20 wt% has an unexpected density profile compared to the other weight-ratio and the SEM image of its fracture morphology has matched with the features of the density profile; lower average density and larger amplitude throughout the specimen. The density profile of other two modifications are also proven by the SEM images, and the overall low porosity of PHBV/PBS and PHBV/PCL 90:10 wt% has been observed in Fig. 77b and 77c. The area with large amplitude in the middle stage of PHBV/PBS specimen is also shown as an area with relatively large pores. The PHBV/PLA/PCL specimen has on average the lowest porosity which is shown in Fig. 77, even in the bottom layers. Moreover, the geometry accuracy of PHBV/PBS and PHBV/PCL 90:10 wt% is both adequate except the bottom layers, in which normally high porosity is obtained.

Similar to the PHBV/PLA specimen in Fig. 77a, the single failure mechanism is observed in all the three modifications, which has the fast brittle fracture without noticeable ductile fracture. The fracture surfaces are mainly smooth, and groove and

ridge having a rough fracture surface are rarely observed in the samples. The rough surface of both PHBV/PBS and PHBV/PCL 90:10 wt% is in the middle of the sample, and the PHBV/PBS has only a small area of the rough surface. Similar to the PLA specimen, the crack is initiated at the rough area and then propagates transversely to both sides of the sample.

In the SEM image of PHBV/PCL 80:20 wt% fracture surface, the lack of lateral material bonding indicates the insufficient deposition during the printing process. The clogging or absence of the printing filament have also occurred in the middle of the specimen. The insufficient material deposition can be caused by the relatively small diameter of the printing filament or because the degradation of the PCL polymer has occurred during the printing process. However, both reasons are not fully convincible. Since the minimum filament diameter is limited by the feed roller of the printer, the filament with small diameter cannot be pinched and feed to the heatsink of printer, therefore no deposited material would be printed. The degradation of PCL will be investigated in the thermal properties of PHBV/PCL copolymer in next sections.

The reason of this phenomenon is probably due to that the PCL polymer cannot be embedded in the main PHBV polymer with the increased weight ratio and the melting temperatures of two compositions are considerably varied. The melting point of PCL (55-65 °C) is dramatically lower than that of the PHBV. The PCL will not be embedded by the based PHBV polymer if two compositions are immiscible and the melt flow properties of two polymers also considerably varied based on previous studies. The melt flow index of PHBV is significantly lower than that of PCL [292,293]. The experimental result shows that the overall filling quality is improved when the weight ratio of PCL polymer is 10 wt%, but the processability of filament is significantly deteriorated when the weight ratio of PCL increased to 20 wt%.

(a)

(b)

(c)

(d)

(e)
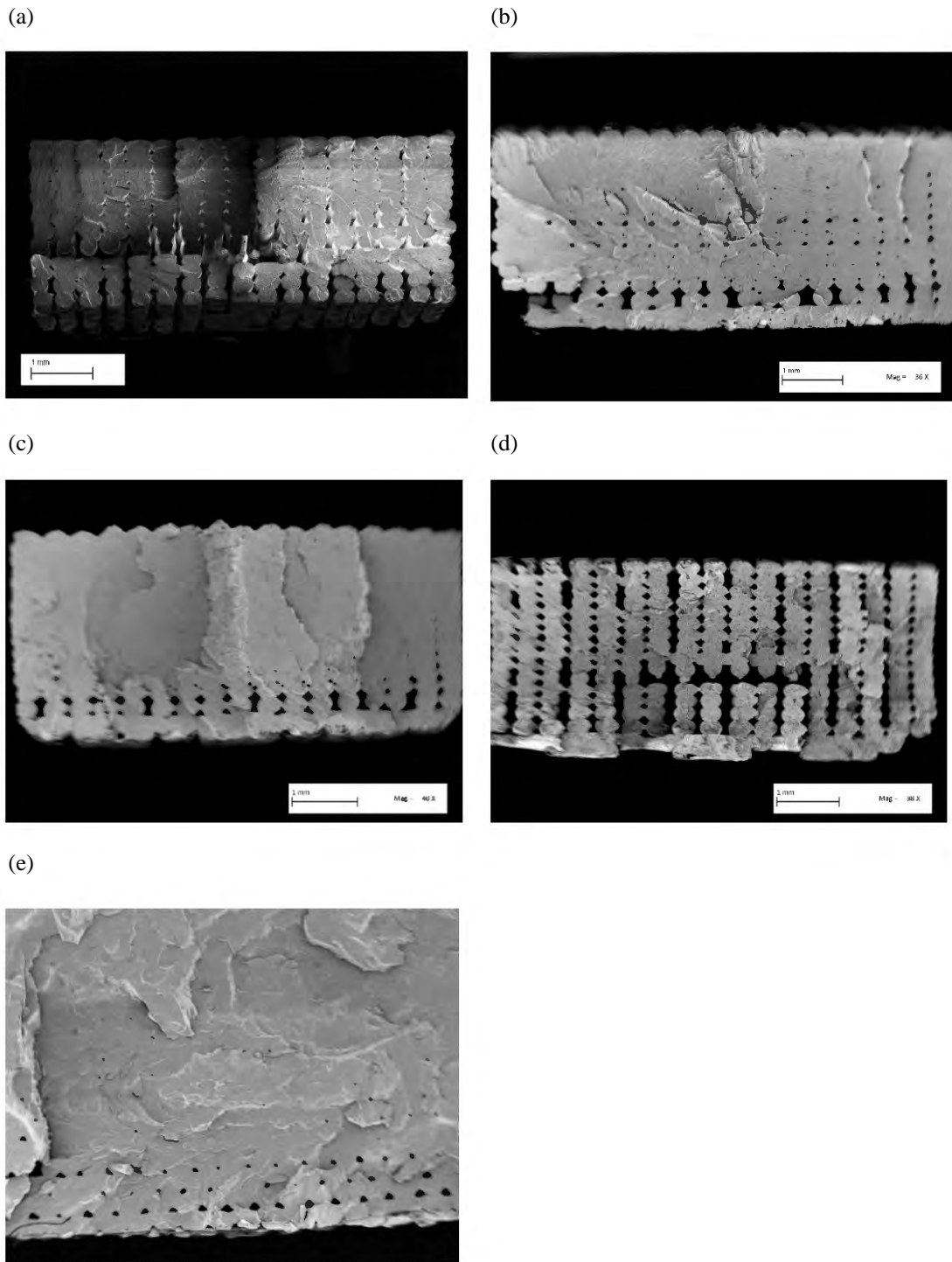
Fig. 77 Fracture morphology of PHBV based modifications printed in x-axis (a: PHBV/PLA 30:70wt%, b: PHBV/PBS, c: PHBV/PCL 90:10 wt%, d: PHBV/PCL 80:20 wt%, e: PHBV/PLA/PCL 70:20:10 wt%)

6.4.2 Fracture surface of modified PLA and PHBV printed in y-axis orientation

6.4.2.1 Fracture surface of modified PLA printed in y-axis orientation

The fracture surfaces of modified PLA, which is printed in y-axis orientation, have also been analysed by the SEM. From the previous study of VDP, a trapezoid outline of the sample is expected due to the ascending density profile. The fracture morphologies of PLA and modification samples are presented in Fig. 78, a trapezoid outline of both modified samples has been obtained. The improved interlaminar bonding area has also been observed in the modification in comparison with the neat PLA. Similar fracture morphologies of modified PLA are observed when compared with PLA/PHBV 70:30 wt% copolymer from the overview of SEM image in Fig. 78b and 78c.

The single failure mechanism is also observed in the modified PLA specimens, which the smooth brittle fracture surface is achieved without noticeable ductile fracture. The two modifications have similar size of the smooth fracture surface, but the interlaminar contact neck growth of PLA/PBS/PEG specimen is expected greater than that of the PLA/PBS and it will be shown and evaluated in the following cross-section microstructure section, as the PEG is commonly employed as the plasticizer with PLA polymer. In general, the interlaminar bonding performance and the anisotropy property of the modified PLA are improved by slightly compensating the geometry accuracy.

(a)   (b)   (c)
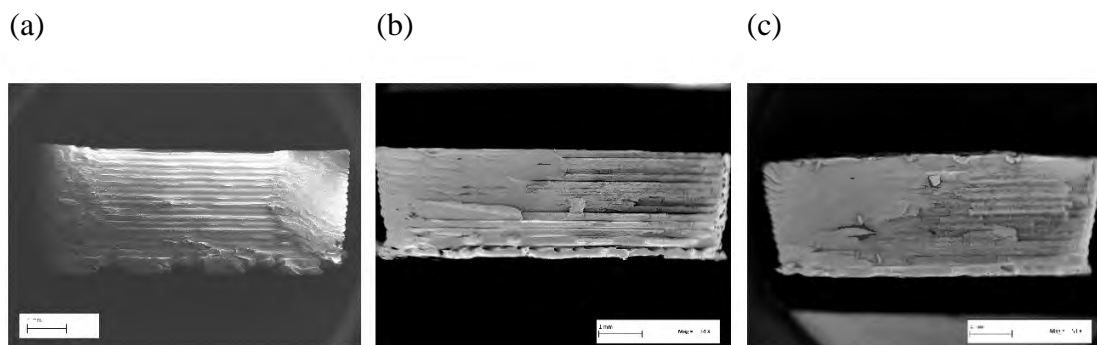
Fig. 78 Fracture morphology of PLA based modifications printed in y-axis. (a: PLA, b: PLA/PBS, c: PLA/PBS/PEG)

6.4.2.2 Fracture surface of modified PHBV printed in y-axis orientation

Since the various density profiles have shown in the previous chapters, the diverse morphologies of the fracture surface are also expected for this copolymer. However, the SEM images of fracture surface, which are presented in the Fig. 79, have similar morphologies except few noticeable features. The disorder of outline dimension has been acquired in all the modifications like the PHBV/PLA 70:30 wt% specimen, and the lack of physical interlaminar bonding is not significant in all the samples, which decrescent anisotropy is indicative.

The printed layers are only noticeable in the PHBV/PBS copolymer, which is shown in Fig. 79b. It is apparent that there is an insufficient neck growth of interlaminar bonding. The failure mechanism of the modifications is also similar to that of the PHBV/PLA copolymer shown in Fig. 79a, except the minor sign of ductile fracture has shown in the middle of Fig. 79c. From the outlines of PHBV/PLA and PHBV/PCL 90:10 wt% shown in the Fig. 79a and 79c respectively, it can be proposed that the addition of PCL will not deteriorate the printing geometry accuracy, and the deposition filling property is also improved with the addition of 10 wt% PCL based on the comparison of x-axis specimen, which reflected the low porosity in the Fig. 79c.

(a) (b)

(c)
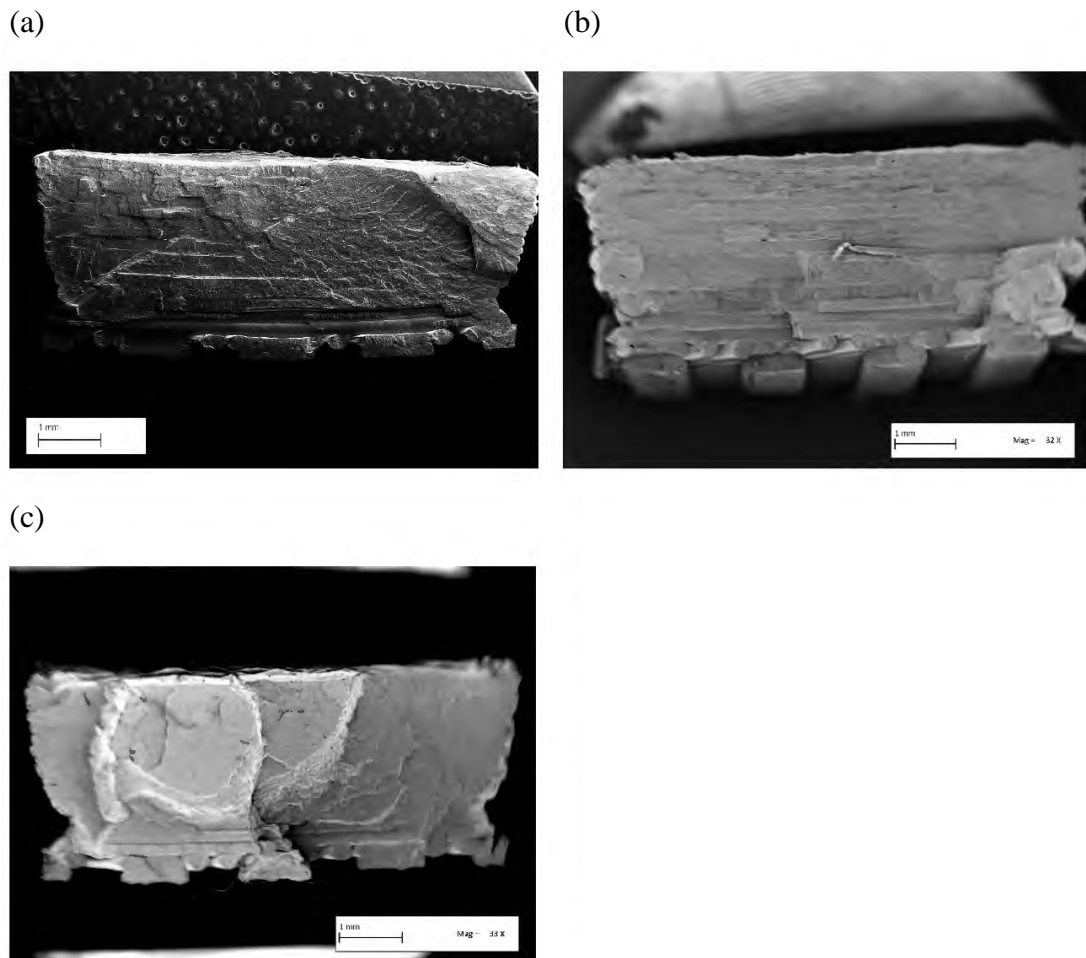
Fig. 79 Fracture morphology of PHBV based modifications printed in y-axis (a: PHBV/PLA 30:70wt%, b: PHBV/PBS, c: PHBV/PCL 90:10 wt%

6.4.3 The cross-section morphology of modified PLA and PHBV printed in x-axis orientation

6.4.3.1 The cross-section morphology of modified PLA printed in x-axis orientation

From the results of density profile and images of fracture surface, the porosity of the PLA based modifications is expected smaller than the neat PLA. To evaluate the size and distribution of the pores in the specimens, the cross-section samples are cut and the microstructure morphologies have been obtained by SEM. Fig. 80 presents the comparison between the neat PLA, PLA/PBS and PLA/PBS/PEG, shown in Fig. 80a, 80b and 80c respectively, the pores generated during the 3D printing process are barely visible in both modifications, especially for the PLA/PBS/PEG specimen, it indicates

the superior neck growth and smaller amplitude in density distribution, which matched with the outcome of VDP and fracture morphology.

Due to the size of pores are dramatically reduced in the modified specimens, it is difficult and unnecessary to compare the specific size or diameter of the pores. The pores are partially visible in only the top and bottom of PLA/PBS specimen, which is presented as an example in Fig. 81. Compared the image of the fracture surface above, the rectangular outline for the single filament bead is reasonable after the fracture of the sample. Like the cross-section of PLA/PHBV copolymer, excessive adhesion is also observed and marked in the Fig. 81, and when comparing the cross-section image with the fracture morphologies, some pores are potentially concealed due to the adhesion in PLA/PBS and PLA/PBS/PEG specimens. The pores in the PLA/PBS sample are also uniform in a triangle shape and the size is also slightly varied. The average size of the pore is around 15 μm and the image of the pore is presented in Fig. 82. It can be concluded that an adequate printing quality and uniformity are achieved in PLA/PBS specimen.

The pores are further decreased in the PLA/PBS/PEG specimen shown in Fig. 80c. The pores between adjacent layers are rarely observed throughout the cross-section image and the size is only around 10 μm. The shape of the pores varied and the rounded pores are also presented with the commonly triangular pore. However, there are also potential concealed pores along the specimen, when comparing the SEM image of the cross-section and fracture surface.
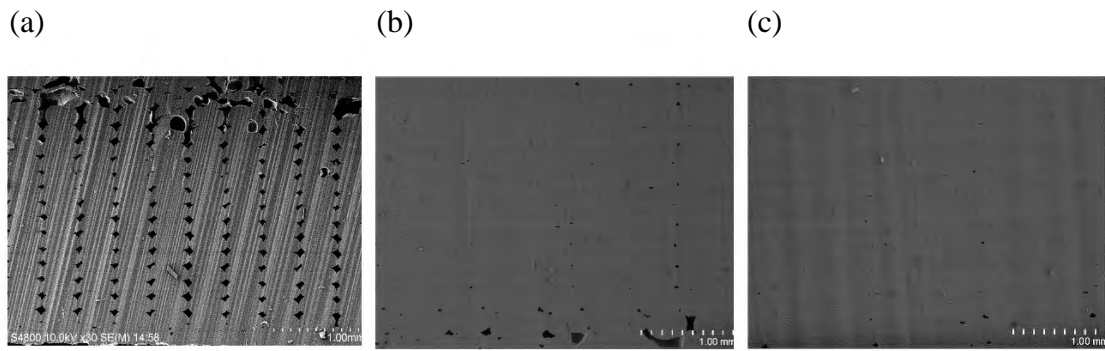
Fig. 80 Cross-section microscopic images of PLA based modifications printed in x-axis. (a: PLA, b: PLA/PBS, c: PLA/PBS/PEG)
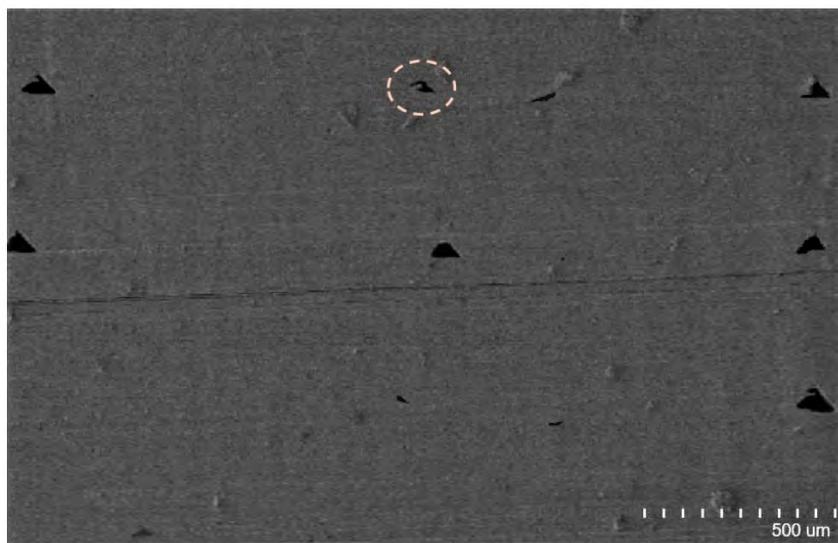
Fig. 81 Pore distribution in PLA/PBS specimen
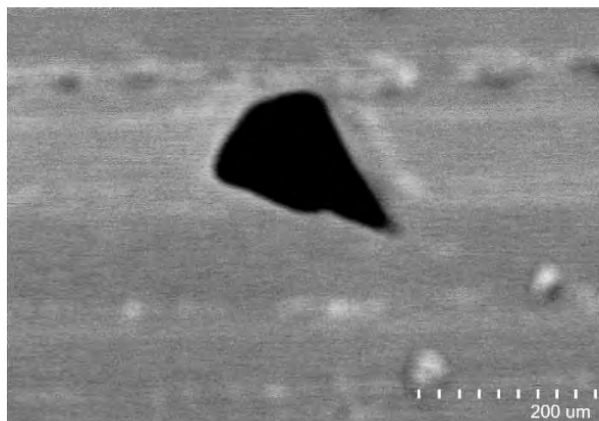
Fig. 82 The size and shape of the pore in PLA/PBS specimen

6.4.3.2 The cross-section morphology of modified PHBV printed in x-axis orientation

The cross-section SEM image of PHBV based modifications printed in x-axis is obtained after cutting the specimen with a diamond cutter. Frome the observation during the cutting process, it can be confirmed that there is no error during the printing process of PHBV/PCL 80:20 wt% copolymer, as the sample is damaged after cutting by a diamond cutter. The other two modifications are compared with the PHBV/PLA 50:50 wt% specimen and presented in Fig. 83. Both modifications have no obvious pores shown in the cross-section image, especially the PHBV/PCL 90:10 wt% specimen, which shows no sign of pore throughout the specimen.

However, when comparing the images of fracture surface and cross-section, some certain pores may be concealed in the cross-section image of PHBV/PBS specimen shown in Fig. 83b compared with the fracture surface of Fig. 83b if the nonuniformity of printing process is neglected. Even through the nonuniformity of printing process is indeterminate in this study, the abovementioned excessive adhesion of material during the cutting process is not neglectable. The precise cross-section image of PHBV copolymers and modifications is difficult to acquire through diamond cutting process.

    (a)   (b)   (c)
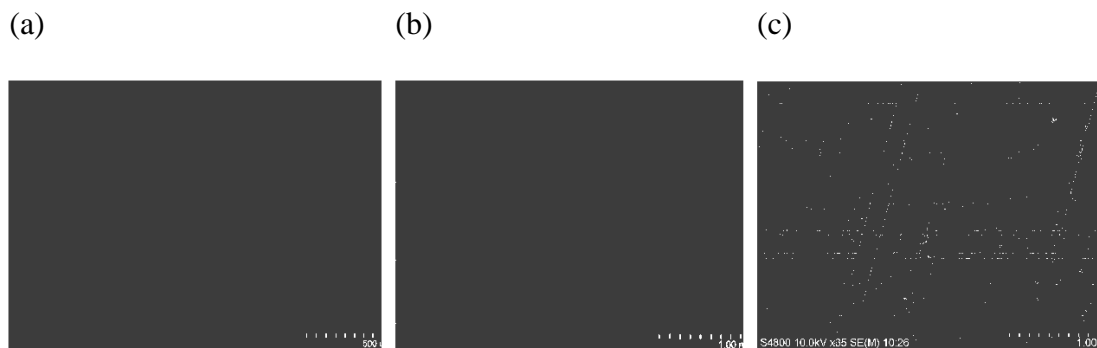
Fig. 83 Cross-section microscopic images of PLA based modifications printed in in x-axis (a: PHBV/PLA 50:50 wt%, b: PHBV/PBS, c: PHBV/PCL 90:10 wt%)

6.4.4 The cross-section morphology of modified PLA and PHBV printed in y-axis orientation

6.4.4.1 The cross-section morphology of modified PLA printed in y-axis orientation

Based on the previous study regarding the fracture morphology of PLA based modification specimens, the SEM image of cross-section of the specimen is also

implemented and presented in Fig. 84. The images of modification are uniform without noticeable grooves compared with the neat PLA specimen in Fig. 84a. Few exceptions are observed in the top or the bottom of the specimen in Fig. 84b and 84c. It is difficult to locate the printed layers along the thickness of specimen in the modified PLA except few micro grooves observed in the Fig. 85. Both the lengths of the groove are less than 200 μm and they may not be confirmed as interlaminar pores due to insufficient evidence. The overall filling quality of modified PLA specimen printed in y-axis is adequate, but the geometry accuracy of the final object is deteriorated slightly.

(a)   (b)   (c)
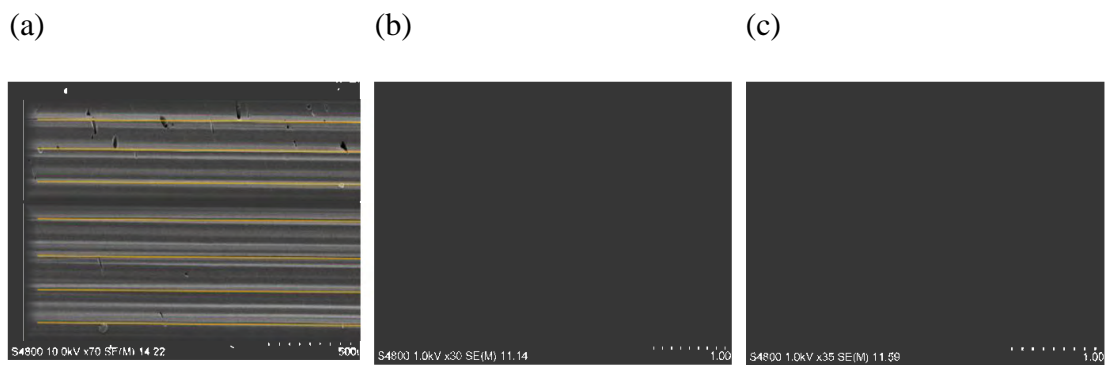
Fig. 84 Cross-section microscopic images of PLA based modifications printed in y-axis (a: PLA, b: PLA/PBS, c: PLA/PBS/PEG)
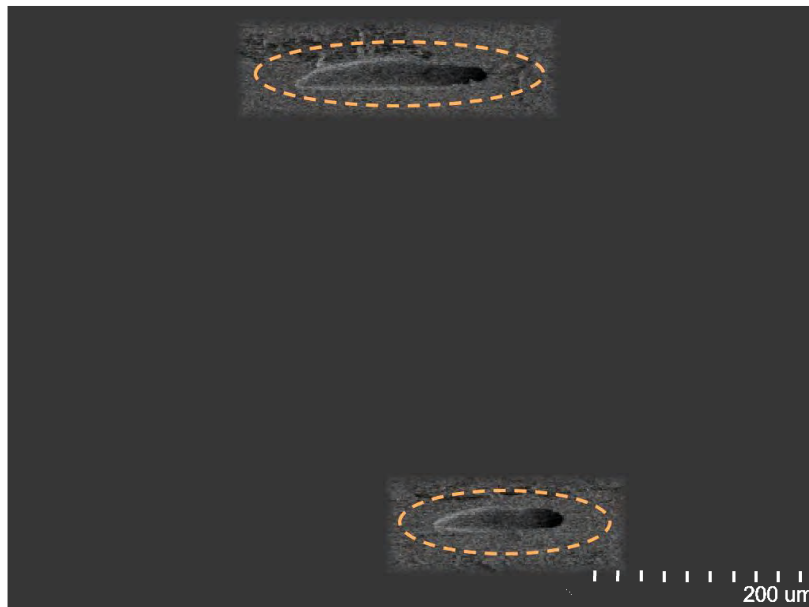
Fig. 85 Micro grooves in the PLA/PBS/PEG specimen

6.4.4.2 The cross-section morphology of modified PHBV printed in y-axis orientation

The reduction of interlaminar grooves is also observed in the PHBV based modifications, shown in Fig. 86. The cross-section images of modified PHBV presents minimum grooves compared with the PHBV/PLA copolymer similar to that of modified PLA. There are no visible printed layers on both PHBV/PBS and PHBV/PCL specimens, which indicates a sufficient deposition and neck growth between the printed layers. A dot of impurity has been observed in the PHBV/PCL specimen, from which a degradation of PCL may be indicated due to the difference of thermal properties of PHBV and PCL. A further study regarding the thermal properties of modified PHBV will be presented in the following section.

(a)   (b)

(c)
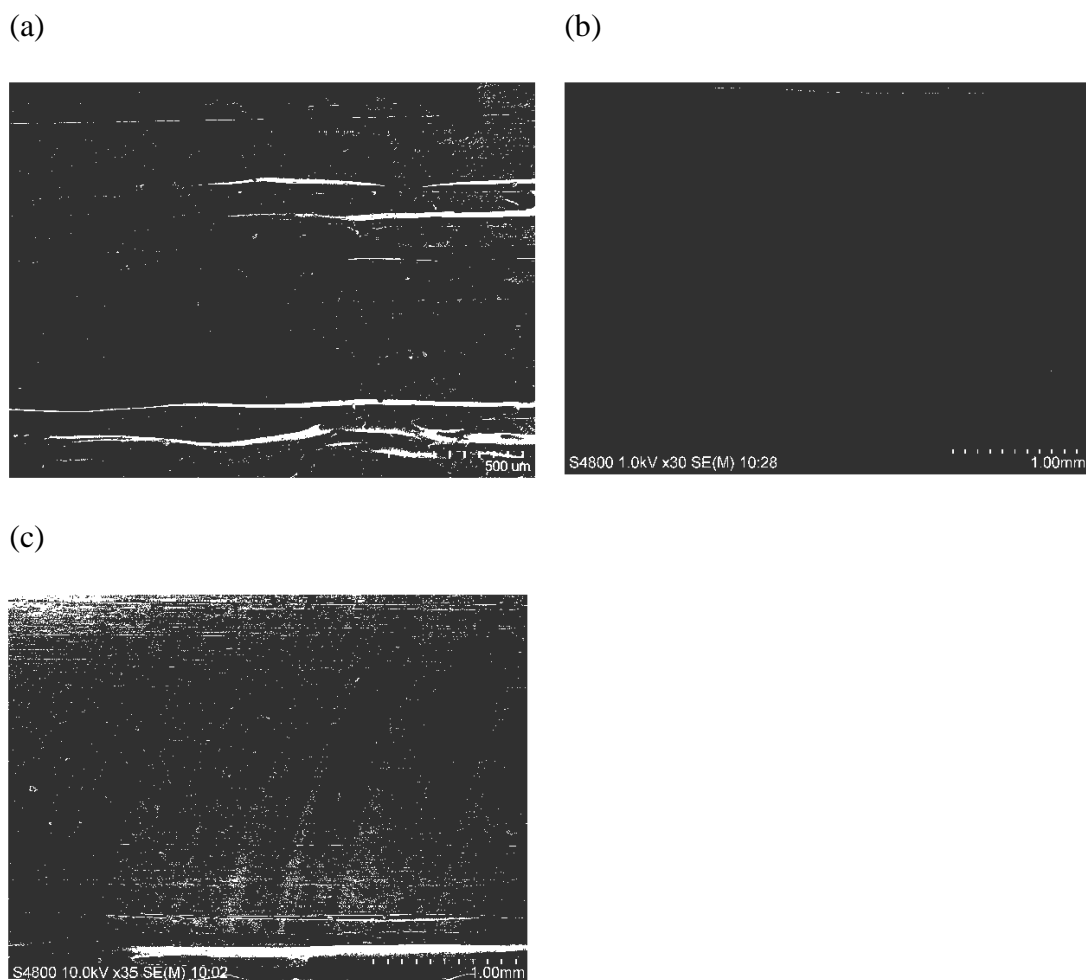
Fig. 86 Cross-section of PHBV based modifications printed in y-axis. (a: PHBV/PLA 30:70wt%, b: PHBV/PBS, c: PHBV/PCL 90:10 wt%)

6.5 Nanoindentation analysis of 3D printed PLA and PHBV with modifications

Based on the nanoindentation investigated previously, insufficient evidence has been provided that the effect of interlaminar neck growth will deteriorate the mechanical properties between adjacent filament beads in both neat PLA and PLA/PHBV copolymers. There is no need to implement all modifications into the micro-mechanical performance investigation. In this section, the PHBV/PCL 80:20 wt% specimen printed in x-axis has been selected in this study, since more remarkable difference in the interfacial bonding may be caused by insufficient neck growth in this material composition.

Due to the poor printing quality, it's difficult to cut and prepare quality cross-section surface, the nanoindentation of PHBV/PCL 80:20 wt% is implemented on the fracture surface. The Fig. 87 shows three testing locations selected for nanoindentation, which are considered possible print boundary locations. Fig. 87b and 87c show the micrographs before and after the nanoindentation at the test site under the microscope. From the images of Fig. 87b and 87c, there is no sign of vertical grooves, which are discussed in previous chapter.

The results of the hardness and modulus of indentations are obtained and presented in Fig. 88, each and the variation of the mechanical properties are unsurprisingly limited, and no apparent reduction in hardness and modulus at the interface has been observed. Three testing positions are separately analysed and the average of both hardness and modulus are almost identical. The position A with the lowest hardness (0.192 GPa) is only 4% lower than the position C, which has the highest hardness (0.200 GPa). The range of the results in one position is also insufficient and the greatest rnage/gap in one position occurs in position B. The indentation 'point 0' is 22% higher than the 'point 2'. The potential interface could be found due to this variation, whereas the further evidence cannot be obtained in the following indentation points. The results of following three points are 0.193, 0.187 and 0.189 GPa respectively, which shows negligible differences. Therefore, there is no sufficient evidence on where the interface between adjacent layers can be.

(a) Position of indentations   (b) Before   (c) After
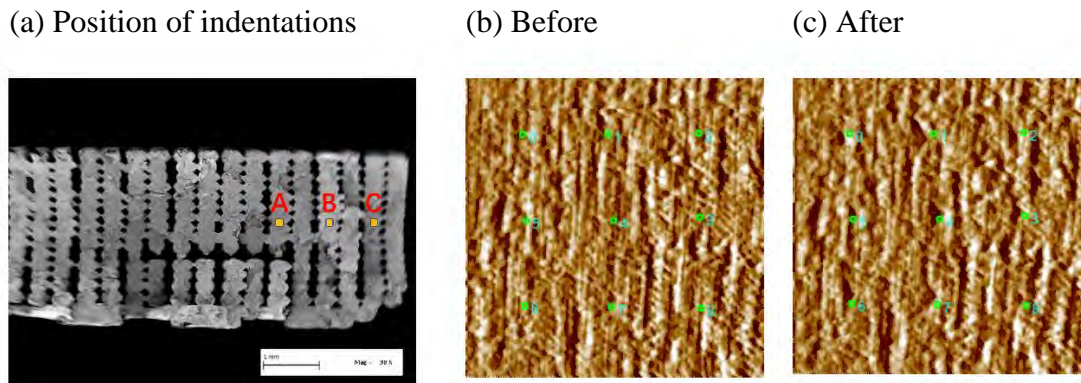
Fig. 87 Position of indentations implemented in PHBV/PCL 80:20 wt%, and the microstructure morphology before and after testing

(a)   (b)
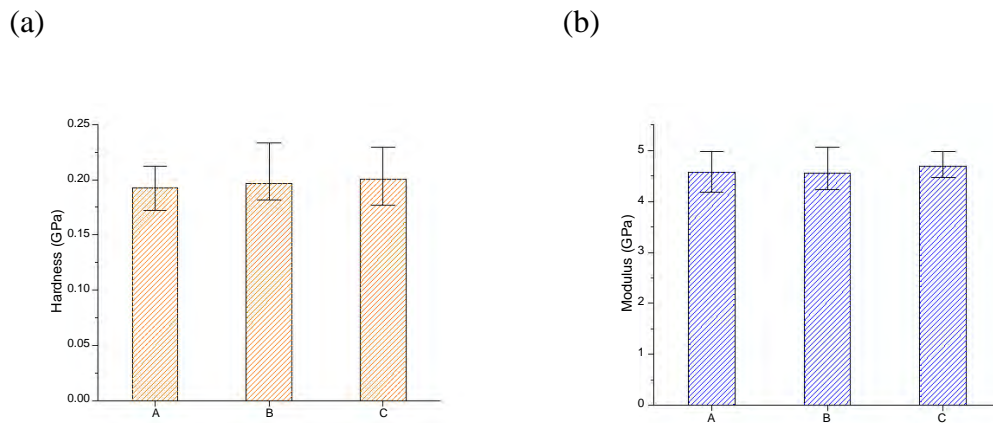
Fig. 88 The hardness and modulus of the PHBV/PCL 80:20 wt%

6.6 Thermal properties of PLA and PHBV modifications

Three specimens are selected in the TGA analysis and one for each category, the PHBV/PCL 80:20 wt%, PHBV/PLA/PCL 70:20:10% wt% and PLA/PBS 80:20 wt% are employed in the study. The following is abbreviated as PHBV/PCL, PHBV/PLA/PCL and PLA/PBS. The weight loss diagram of TGA is presented in Fig. 89. The PHBV/PCL and PHBV/PLA/PCL show an immiscibility, which indicates varied melt flow during printing, this is in line with the poor printed products as discussed in section 6.5.1.2.

Based on the printing properties, the TGA analysis has been implemented. The first two specimens with the majority of PHBV composition are similar compared with the PLA

based specimen. The degradation of PHBV/PCL and PHBV/PLA/PCL specimen is initiated earlier than the PLA/PBS, which started at around 251 ˚C and 259 ˚C respectively compared with the 271 ˚C for the PLA/PBS specimen. Similar to the TGA results from last chapters, the degradation is developed faster in these two specimens, for which the PHBV is the main composition.

The temperature of each milestone when the weight loss is reached 2%, 5%, 10% and 50% has been summarised and presented in Table 23. The PHBV/PCL and PHBV/PLA/PCL modifications have extremely similar degradation procedures when the weight loss is lower than 50%. The degradation procedure of PLA/PBS is significantly delayed by increasing temperature, which indicates a better thermal stability than other two specimens. The residues at 550 ˚C of all three specimens are similar at more than 1%, compared with the result from previous chapter. The mineral filler in the PBS polymer is ought to be high, as low mineral composition is proven in the PLA polymer.

The rate of weight loss corresponded with temperature is figured by the derivative thermogravimetry (DTG) curves presented in the Fig. 90. The peaks of weight loss are obtained, the same in PHBV/PCL and PHBV/PLA/PCL at 296 ˚C, which is almost identical to the PLA/PHBV 30:70 wt% specimen (297 ˚C) in the previous chapter, but the rate of PHBV/PLA/PCL is 18% lower than the PHBV/PCL specimen due to the reduced PHBV weight ratio. The peak of copolymers like PCL is observed in the diagram, which shows a degradation far behind at around 388 ˚C in the PHBV/PCL specimen. However, there are only two peaks observed in the PHBV/PLA/PCL specimen, which are the degradation peak of PHBV and PLA. The peak of PLA occurred at 348 ˚C which is almost identical to that of the PLA/PBS specimen (352 ˚C). The curve of PLA/PBS specimen varied with all other specimens, as a uniform and unimodal curve is obtained, which indicate a miscibility of PLA and PBS polymer. The result matches with the previous result that the mixing of PLA and PBS polymer is following the solubility concept [294,295]. It is also supported by the TGA diagram due to the single tendency and rectilinear weight loss in the curve.
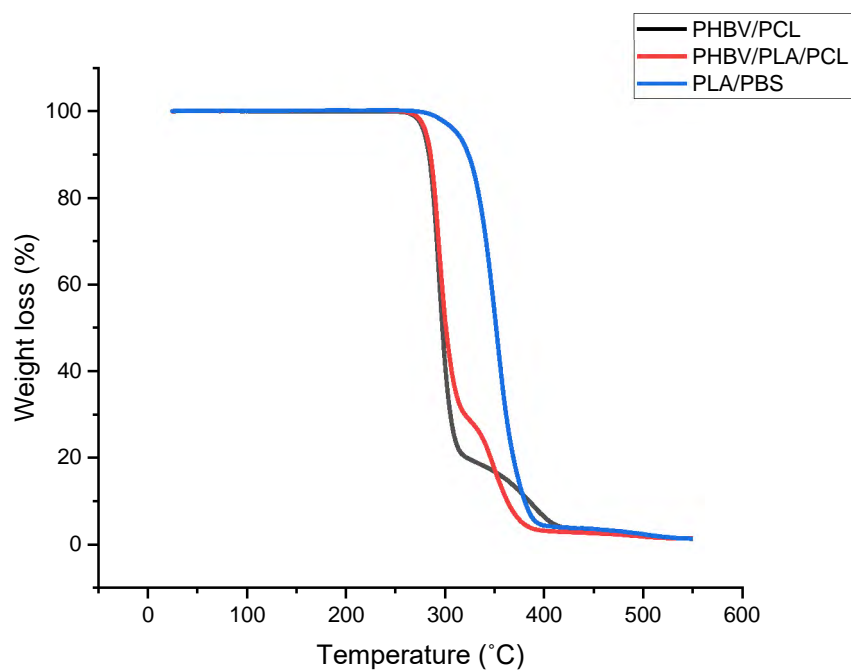
Fig. 89 TGA curves of the PHBV/PCL, PHBV/PLA/PCL and PLA/PBS polymers

Table. 23 Decomposition temperature of copolymers when the weight loss is reached 2%, 5%, 10% and 50%, and char yields at 550 ˚C

	$T_{2\%}$ (˚C)	$T_{5\%}$ (˚C)	$T_{10\%}$ (˚C)	$T_{50\%}$ (˚C)	Char yield (%)
PHBV/PCL	273	279	284	297	1.41
PHBV/PLA/PCL	275	281	285	301	1.44
PLA/PBS	296	312	323	352	1.38
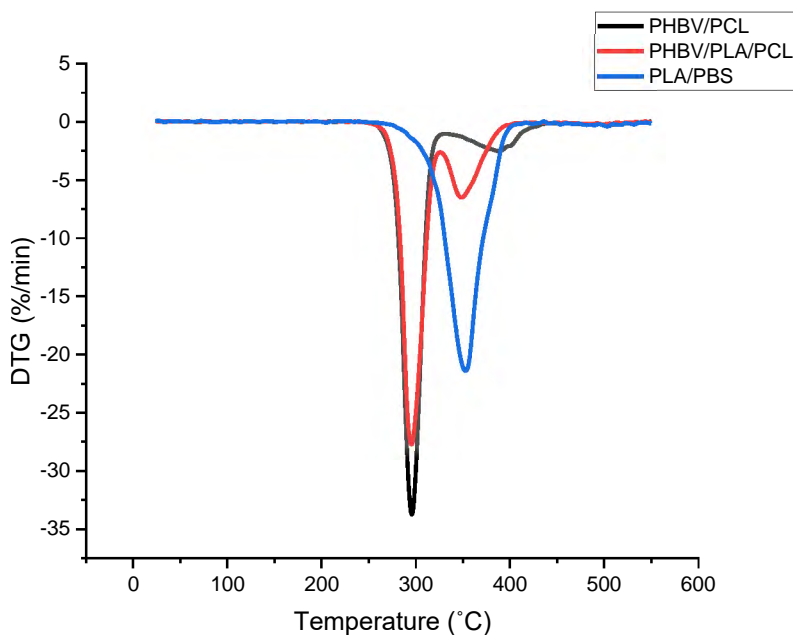
Fig. 90 DTG curves of the PHBV/PCL, PHBV/PLA/PCL and PLA/PBS polymers

6.7 Discussion

6.7.1 PLA modifications

The PLA/PBS copolymer has also been investigated via injection molding [296,297] and 3D printing [298,299], further study of 3D printed PLA/PBS was still required. Table 24 compared the mechanical performance of current studies on 3D printed PLA/PBS. With the increase of the PBS content, the tensile strengths decreased stepwise. The tensile strength reduced 8% when the PBS content was 20 wt% compared to the neat PLA in x-axis orientation, but there was an improvement in y-axis specimen, the tensile strength enhanced 11% due to the addition of PBS. The addition of PEG plasticizer further decreased the strength compared to the PLA/PBS copolymer (3% and 8% reduction in x and y axis respectively). The elasticities increased with the addition of PBS, 57% improvement in tensile strain of PLA/PBS copolymer has been achieved in both x and y axis specimen, further enhancement in the elasticity of the specimen was obtained with the addition of PEG (86% and 80% increase in x and y axis respectively). However, the tensile strain varied dramatically among the studies (Table 24) and two reasons may cause this difference. Firstly, different molecular weight of raw materials may lead to different mechanical performance of the final specimens. The result of

elongation at break was not suitable for comparing to our data due to different grade of PLA or PBS employed in the study.

Table 24 Comparison of the mechanical performance of PLA/PBS blends in 3D printing

		Ou-Yang et al. [298]		Qahtani et al. [299]		Our data	
Weight ratio PLA:PBS (wt%)		80:20	60:40	Neat PLA	80:20	Neat PLA	80:20
Tensile strength (MPa)	x-axis	55.6 (IM)	51.2 (IM)	66.2	64.9	56.1	51.5
	y-axis	-	Up to 21.4	-	-	21.9	24.4
Tensile strain (%)	x-axis	93	159	-	-	2.8	4.4
	y-axis			-	-	1.1	1.7

The PLA/PBS 80:20 wt% was also found miscible as aforementioned when the single peak was observed in the DTG curve (Fig. 90), this is in agreement with the results from other reports [297-300], where the PLA/PBS blends were reported miscible when the PBS weight ratio was less than 20 wt%. The complex viscosity (η^*) which can be acquired by Power law model described below:

$$\eta^* = K \cdot \dot{\gamma}^{n-1}$$

Where, K is the constant prefactor and n is the power law exponent, $\dot{\gamma}$ is the shear rate. And the shear rate in the FDM process can be estimated as:

$$\dot{\gamma} = \frac{8\bar{v}}{D}$$

Where, $\bar{v}$ and D are the average deposition speed of the melt filament and the diameter of the nozzle. FDM printing used a nozzle with an inner diameter of approximately 0.0004 m, resulting in a shear rate of approximately 400 s^{-1}. A sharp increase in complex viscosity was reported when the PBS content was higher than 30 wt%, which can impact the printability of the filament, as swelling could happen when the melt filament was extruded from the nozzle, leading to insufficient interlayer bonding [297,299]. Also an inconsistent printing was reported for the PBS content over 50 wt% [299]. The

PLA/PBS copolymer shows promising material performance and printability for further applications in 3D printing.

PEG worked as a plasticizer with PLA in 3D printing can increase the tensile strength and strain. In this study, up to 86% increase was achieved when the PEG content was 2 wt%, and the enhancement of elasticity in x and y axis printing orientation was almost identical. However, the tensile strength was decreased with the addition of PEG. Compared to other study, up to 19% and 35% increase respectively in tensile strength and strain was achieved when 2 wt% of PEG was added to the PLA/lignin composite in 3D printing [301], compared to the 3% reduction in tensile strength and 80% improvement in tensile strain of PLA/PBS/PEG, aforementioned in 6.3.2.1. The reason may be due to the PLA-lignin interface can be improved by the addition of PEG.

6.7.2 PHBV modifications

The PCL and PBS were employed to blend with PHBV to modify the printability and mechanical properties. The printability was obtained by the modified blends but the printing quality was limited due to warpage. Severe insufficient filament deposition occurred when PHBV/PCL was 80:20 wt%. The mechanical performance of the blends was unremarkable. The tensile strength of PHBV/PBS and PHBV/PCL blends was lower than the benchmark PHBV/PLA (30% and 22% lower in x-axis respectively), although the tensile strains were improved (13% higher in x-axis). Similar trend was reported that up to 700% increase in tensile strain could be achieved when 25 wt% of PCL added into the PHBV and the tensile strength and modulus decreased by 50% and 20% respectively [303]. The blends of PHBV/PBS slightly improved both tensile strength and strain with the increase of PBS from 0% to 20 wt% [304]. [302]The PBS and PCL polymer can be mixed with PHBV and the processibility could be improved except PHBV/PCL 80:20 wt%, but the little improvement in mechanical properties.

This study innovatively utilized the PBS as a copolymer with the PHBV and improved the printability of neat PHBV. The viscosities of PHBV/PBS blends were also studied and the complex viscosity decreased with increasing PBS content [302]. The MFI of PLA/PHBV/PBS blends were reported remain relatively high (28.5-29.1 g/10 min) when the PHBV content was 60 wt%, which was significantly higher than the neat PHBV (13.9 g/10 min) [306]. With the addition of PBS to PHBV or PHBV/PLA, better

rheology properties were achieved by both viscosity and MFI results, which could result in a better printability.

The immiscibility was also found in the blends of PHBV and PCL, and also due to the considerably varied thermal-rheological properties of two blends, the PCL cannot be embedded by the PHBV and the blends cannot be deposited homogeneously, causing the deteriorated printing performance. Similar outcome was also found by Qiu et al. [303]. Both the tensile strength and strain decreased in PHB/PCL copolymers compared to the neat PHB, which in agreement with the testing result as presented in 6.3[304]. However, Laoutid et al. [304] modified the PHB/PCL blends by dicumyl peroxide (DCP) as a free-radical promotor of polyester interchain reactions and PEG as a plasticizer, and successfully applied the blends in FDM 3D printing. Adequate printability and mechanical performance of the blends ware reported. The addition of the DCP and plasticizer could inspire the further study and application of PHB/PCL or PHBV/PCL blends.

6.8 Interim conclusions

Various modified PLA and PHBV have been evaluated comprehensively by different analysis processes. Some of the modifications showed potentially improved performance compared with PLA or PLA/PHBV polymers in various properties.

Although the lack of improvement in mechanical performance of PHBV based modifications, the addition of PBS in both PLA and PHBV polymers showed promising performance especially in the PLA/PBS copolymers. Significantly improved interlaminar bonding performance was observed in both x and y-axis specimens which the anisotropy property was inadequately reduced compared to the neat PLA. The ductility of the specimen was also enhanced (up to 86%) from the examined result of tensile testing and following fracture morphology images due to the addition of PBS and further PEG polymer as a plasticizer. The miscibility of PLA and PBS was also found potential in favour of thermal properties.

The results of PHBV based modifications showed different from those of the improved PLA based polymers. The printability of PHBV based polymers was unpredictable like the PHBV/PCL 80:20 wt% due to varied rheological properties of melt material. The warpage dramatically occurred in some of the PHBV specimens. Nevertheless, the

printability of PHBV based polymers was improved by employing the blends and additives in the PHBV. An adequate printed objected could be fabricated by 3D printer by adding small amount of blends or additive, such as 10 wt% of PCL polymer. The results of PHBV based modifications were generally appropriate when comparing to the benchmarked PHBV/PLA 30:70 wt% composition. The elasticity was improved slightly (up to 13% increase in x-axis) but the strength was compromised (up to 30% reduction in x-axis). Although the VDP process was not so accurate as firstly expected due to the influence of the outline dimension of printing objects, the results of mechanical performance and corresponding microstructures were competitive, especially the improved ductility of final objects. The immiscibility has been proven when the PHBV was compounded with PCL polymer by investigating the thermal properties of modifications.

Overall, several potential modifications such as PLA/PBS and PHBV/PLA/PCL have been found during this study, but further investigation is still strongly required.

7. Final Appraisal and Recommendations

7.1 Conclusions

In this study, various bio-based polymers were employed into the filaments of FDM 3D printing technology, from the commercially available PLA polymer to the highly potential PHBV, and different possible copolymers and additives were also implemented for the modification of the PLA and PHBV biobased materials. The interfacial bonding properties of 3D printing process was the focus throughout the study. All the material compositions were fabricated by FDM printer and comprehensively evaluated from the nano-size to the macro-size.

Novel analysis procedures were introduced and implemented in this work, like VDP and nanoindentation, which has revealed various performance of 3D printed objects. The printing performance and porosity distribution of the final parts were illustrated by the VDP diagrams along with the thickness of the sample, where the general size and tendency of the pores were revealed for further micro-size study of the interface of the printed parts. The VDP testing showed great potential for the determination of the density distribution of the 3D printed objects, but the result could be considerably affected by the geometry disorder of the final printed parts. The micro-mechanical properties of the potential interfacial bonding areas were tested and analysed by nanoindentation process and the result revealed that there was no deterioration among the adjacent printed layers within the interfacial bonding area. In addition, conventional analysis processes, such as mechanical properties testing and microstructure evaluation (fracture morphology and cross-section studies), have also been employed to complete this comprehensive study. Overall, this study provided a novel and complete methodology to investigate the interfacial performance of 3D printing part and the material properties when employing the FDM 3D printing process.

From the material point of view, PLA which has been widely applied in the additive manufacturing for years, was optimized by this method in printing temperature. Detailed analysis regarding the effects of ascending printing temperatures to the final performance of the printed parts has been provided. The optimized printing temperature was found at 220 ˚C, which was 24% higher in tensile strength than the specimens printed at 200 ˚C in y-axis orientation. Stronger anisotropy property has been found in

low printing temperature like 200 ˚C, the average tensile strength of the specimen printed in x-axis was 52.4 MPa, which was dramatically higher than the sample printed in y-axis (14.7 MPa). The oven curing post-process led to a different failure mechanisms and morphology due to the varied crystallinity degree for the PLA polymer. Severe brittleness (the tensile strain reduced by 42%) and more significant anisotropy property have been observed even through the tensile strength was improved inadequately.

The PHBV polymer which was produced by cell of bacteria was innovatively employed in the 3D printing as a main composition with the combination of PLA, and other polymers like PEG and PCL as an additive to the PHBV. Beside the PLA which has widely been applied in the FDM 3D printing, the PHBV/PLA copolymers also have potential application with the reduced anisotropy property and better infill performance compared with neat PLA, enhanced interlayer bonding was found. When the weight ratio of PHBV was no more than 50 wt%, the mechanical properties of the PLA/PHBV blends were competitive with the impressively improved strains when printed in y-axis orientation (increased up to 86% in tensile strain). The investigation of thermal properties has proven the immiscibility of PLA and PHBV polymers. However, the final printing geometry accuracy, insufficient tensile strength and strain, and warpage during printing could limit the further industrial and commercial applications of PHBV polymer in 3D printing.

For the additives applying in the PLA and PHBV biopolymers, additives like PBS, PLA and PEG were investigated as a copolymer to improve the performance of 3D printed objects, the modified material showed significant prospect in further industrial applications. The brittleness and anisotropy property of PLA and PLA/PHBV copolymers were also reduced by addition of the PCL, PBS and PEG polymers. The final mechanical performance of the bio-based modified copolymers was also competitive with that of the synthetic polymer like ABS in additive manufacturing. The improved ductility of the modified material was achieved especially in the PLA/PBS and PLA/PBS/PEG, the tensile strains were enhanced by 57% and 86% in x-axis respectively, the tensile strengths were slightly compensated by 3% and 11% respectively. The performance of polymers added into PHBV varied and the elasticity was slightly improved, but the printing quality was unpredictable.

3D printed bio-based PLA, PLA/PHBV and their modifications were investigated comprehensively in this study focusing on the interfacial bonding and anisotropy properties by employing novel analysis processes. The anisotropy properties were improved by addition of PHBV and following additives (decreased from 62% reduction in tensile strain to 22%). The performance of interfacial bonding between adjacent printed layers was investigated by nanoindentation, although none of clear interface was found in various materials throughout this study. The novel bio-based printing materials were printed and tested, which resulted in impressive performance but the PLA was still on the top among all the material compositions. However, the disorders occasionally occurred during the printing process like warpage and over-stocked material, which led to the poor final geometry accuracy. They may be alleviated by optimizing the printing process, such as applying industrial printer, improved filament diameter or optimized printing environment.

7.2 Challenges and possible future study

This study has proven that the novel biobased polymers like PHBV, PBS and PCL can be applied into FDM 3D printing process with some certain challenges:

1) The difficult-to-print properties of PHBV polymer commonly occurs during the printing process, and the geometric disorder of final printed objects and the warpage often occur during the printing. The processability of PHBV and PHBV based copolymer requires further improvement.

2) The ductility of the printed parts is improved with the increasing weight ratio of additives like PBS, PCL and PEG, but the tensile strength is reduced in the meanwhile.

3) The anisotropy properties still hereditarily existed when different printing orientations are taken, which will further limit the industrial application of 3D printed biopolymers.

4) The efficacy of additives added into the PLA or PHBV polymer varies even through the better printability and less warpage are obtained. The optimisation of the material composition, which has the maximum performance, is significantly challenging.

In this study, all the printed filaments applied on the 3D printer were self-fabricated and the diameter accuracy of the filament extruded was not competitive with the commercial filament, the impurities were also found during the study of microstructure. Due to the final printing performance was highly dependent on the quality of the filament extruded and the printer utilized was open-end desktop 3D printer, the printing quality was affected by the ambient environment like temperature and humidity. Therefore, it is very likely that the printability could be enhanced by optimising the processing quality. The warpage of the printed object was difficult to be minimised by this method, but the modification of PHBV polymer could ease this difficulty during printing process.

Although the ductility has been proven that was significantly increased by the addition of additive polymers, it is still far lower than the majority of synthetic polymer such as PP or PC. Further study regarding the common brittleness of bio-based polymers is required. Some other additives are potential for PLA and PHBV, such as PBAT, and the inherited anisotropy properties of FDM 3D printing process can be considerably eased by various design methods on the slicing software, such as the $\pm 45°$ printing orientation, alternate printing directions and various infill patterns.

The printed PHBV based polymer has proven that the warpage often occurred when the composition of PHBV is high. The optimised material composition, which can minimise the warpage, is necessary for the further study. The overall mechanical properties of bio-based printing material can also be maximised by investigating various material compositions. Several valuable features have been offered by this study like the miscibility of material, density distribution, failure mechanisms and interfacial bonding properties. Meanwhile, the development of novel biobased polymer, which can be benchmarked with high-performance synthetic polymer like PA, PC or PEEK, is also required for expanding the application, especially in automotive or aerospace engineering.

An innovative and promising route has been provided by this study to potentially expand the industrial and commercial applications of bio-based polymers applied in additive manufacturing. The functional properties of PHBV, for instance, have been observed in processability and mechanical performance, when appropriate proportions

of additive or copolymer were added. Commercially used PLA is also optimised in printing parameters and finely tuned by postprocess and modifications.

Reference

1. Leary M. 4 - Detail DFAM. In: Leary M, editor. Design for Additive Manufacturing. : Elsevier, 2020. p. 91-122.

2. Diegel O. 10.02 - Additive Manufacturing: An Overview. In: Hashmi S, Batalha GF, Van Tyne CJ, Yilbas B, editors. Comprehensive Materials Processing. Oxford: Elsevier, 2014. p. 3-18.

3. Greene JP. 10 - Bio-Based and Biodegradable Plastics. In: Greene JP, editor. Automotive Plastics and Composites. : William Andrew Publishing, 2021. p. 149-174.

4. Zia KM, Akram N, Tabasum S, Noreen A, Akbar MU. 6 - Processing of bio-based polymers for industrial and medical applications. In: Zia KM, Akram N, Tabasum S, Noreen A, Akbar MU, editors. Processing Technology for Bio-Based Polymers. : Elsevier, 2021. p. 191-238.

5. Lin W, Shen H, Xu G, Zhang L, Fu J, Deng X. Single-layer temperature-adjusting transition method to improve the bond strength of 3D-printed PCL/PLA parts. Composites Part A: Applied Science and Manufacturing 2018;115:22-30.

6. Chacón JM, Caminero MA, García-Plaza E, Núñez PJ. Additive manufacturing of PLA structures using fused deposition modelling: Effect of process parameters on mechanical properties and their optimal selection. Mater Des 2017;124:143-157.

7. Steve U. The rapid prototyping technologies. Assem Autom 2003;23(4):318-330.

8. Bernhard M. Additive Manufacturing Technologies â€" Rapid Prototyping to Direct Digital Manufacturing. Assem Autom 2012;32(2).

9. Hopkinson N, Hague R, Dickens P, Gornet T. Introduction to Rapid Manufacturing; Materials and Process Control for Rapid Manufacture. Rapid Manufacturing; Rapid Manufacturing 2005:1; 125-4; 146.

10. Cooper KG. Rapid Prototyping Technology: Selection and Application. New York, NY, USA: Marcel Dekker, Inc, 2001.

11. Grimm T. User's guide to rapid prototyping. Society of Manufacturing Engineers 2004.

12. Bikas H, Stavropoulos P, Chryssolouris G. Additive manufacturing methods and modelling approaches: a critical review. The International Journal of Advanced Manufacturing Technology 2016;83(1-4):389-405.

13. BASF 3D Printing. Metal SolutionsEasy and cost effective 3D printing of metal parts. ;2019.

14. Wong KV, Hernandez A. A Review of Additive Manufacturing. ISRN Mechanical Engineering 2012;2012:10.

15. Kazmer D. Three-dimensional printing of plastics. In: Anonymous Applied Plastics Engineering Handbook. : Elsevier, 2017. p. 617-634.

16. Nancharaiah T, Ranga Raju D, Ramachandra Raju V. An Experimental Investigation on Surface Quality and Dimensional Accuracy of FDM Components. , 2010.

17. Chung WC. Optimizing the rapid prototyping process by integrating the Taguchi method with the Gray relational analysis. Rapid Prototyping Journal 2007;13(5):304-315.

18. Zhang Y, Chou K. A parametric study of part distortions in fused deposition modelling using three-dimensional finite element analysis. Proc Inst Mech Eng Pt B: J Eng Manuf 2008;222(8):959-968.

19. Galantucci LM, Lavecchia F, Percoco G. Quantitative analysis of a chemical treatment to reduce roughness of parts fabricated using fused deposition modeling. CIRP annals 2010;59(1):247-250.

20. Galantucci LM, Lavecchia F, Percoco G. Experimental study aiming to enhance the surface finish of fused deposition modeled parts. CIRP annals 2009;58(1):189-192.

21. Percoco G, Lavecchia F, Galantucci LM. Compressive properties of FDM rapid prototypes treated with a low cost chemical finishing. Research Journal of Applied Sciences, Engineering and Technology 2012;4(19):3838-3842.

22. Rao AS, Dharap MA, Venkatesh JVL, Ojha D. Investigation of Post Processing Techniques to Reduce the Surface Roughness of Fused Deposition Modeled Parts. , 2012.

23. Garg A, Bhattacharya A, Batish A. On surface finish and dimensional accuracy of FDM parts after cold vapor treatment. Mater Manuf Process 2016;31(4):522-529.

24. Jin Y, Wan Y, Zhang B, Liu Z. Modeling of the chemical finishing process for polylactic acid parts in fused deposition modeling and investigation of its tensile properties. Journal of Materials Processing Technology 2017;240:233-239.

25. Pandey PM, Venkata Reddy N, Dhande SG. Improvement of surface finish by staircase machining in fused deposition modeling. Journal of Materials Processing Technology 2003;132(1):323-331.

26. Boschetto A, Bottini L, Veniali F. Finishing of Fused Deposition Modeling parts by CNC machining. Robot Comput Integrated Manuf 2016;41:92-101.

27. Torres J, Cotelo J, Karl J, Gordon AP. Mechanical property optimization of FDM PLA in shear with multiple objectives. JOM 2015;67(5):1183-1193.

28. Hull CW. No title. Apparatus for production of three-dimensional objects by stereolithography 1986.

29. Wang X, Jiang M, Zhou Z, Gou J, Hui D. 3D printing of polymer matrix composites: A review and prospective. Composites Part B: Engineering 2017;110:442-458.

30. Maruo S, Ikuta K. Submicron stereolithography for the production of freely movable mechanisms by using single-photon polymerization. Sensors and Actuators A: Physical 2002;100(1):70-76.

31. Cho YH, Lee IH, Cho D. Laser scanning path generation considering photopolymer solidification in micro-stereolithography. Microsystem technologies 2005;11(2-3):158-167.

32. Andrzejewska E. Photopolymerization kinetics of multifunctional monomers. Progress in Polymer Science 2001;26(4):605-665.

33. Mapili G, Lu Y, Chen S, Roy K. Laser-layered microfabrication of spatially patterned functionalized tissue-engineering scaffolds. Journal of Biomedical Materials Research Part B: Applied Biomaterials: An Official Journal of The Society for Biomaterials, The Japanese Society for Biomaterials, and The Australian Society for Biomaterials and the Korean Society for Biomaterials 2005;75(2):414-424.

34. Arcaute K, Mann BK, Wicker RB. Stereolithography of three-dimensional bioactive poly (ethylene glycol) constructs with encapsulated cells. Ann Biomed Eng 2006;34(9):1429-1441.

35. Tumbleston JR, Shirvanyants D, Ermoshkin N, Janusziewicz R, Johnson AR, Kelly D, Chen K, Pinschmidt R, Rolland JP, Ermoshkin A, Samulski ET, DeSimone JM. Additive manufacturing. Continuous liquid interface production of 3D objects. Science 2015;347(6228):1349-1352.

36. Bishop GW, Satterwhite-Warden JE, Kadimisetty K, Rusling JF. 3D-printed bioanalytical devices. Nanotechnology 2016;27(28):284002.

37. Nowicki M, Castro NJ, Rao R, Plesniak M, Zhang LG. Integrating three-dimensional printing and nanotechnology for musculoskeletal regeneration. Nanotechnology 2017;28(38):382001.

38. Hinczewski C, Corbel S, Chartier T. Ceramic suspensions suitable for stereolithography. Journal of the European Ceramic Society 1998;18(6):583-590.

39. Melchels FPW, Feijen J, Grijpma DW. A review on stereolithography and its applications in biomedical engineering. Biomaterials 2010;31(24):6121-6130.

40. Chu T-G, Orton DG, Hollister SJ, Feinberg SE, Halloran JW. Mechanical and in vivo performance of hydroxyapatite implants with controlled architectures. Biomaterials 2002;23(5):1283-1293.

41. Licciulli A, Esposito Corcione C, Greco A, Amicarelli V, Maffezzoli A. Laser stereolithography of ZrO2 toughened Al2O3. Journal of the European Ceramic Society 2005;25(9):1581-1589.

42. Hyuk Moon J, Yang S. Creating Three-Dimensional Polymeric Microstructures by Multi-Beam Interference Lithography. Journal of Macromolecular Science, Part C 2005;45(4):351-373.

43. Lee K, Kim RH, Yang D, Park SH. Advances in 3D nano/microfabrication using two-photon initiated polymerization. Progress in Polymer Science 2008;33(6):631-681.

44. Zguris Z. How mechanical properties of stereolithography 3D prints are affected by UV curing. Formlabs Inc., Somerville, MA, accessed Mar 2016;7:2017.

45. Salmoria GV, Ahrens CH, Fredel M, Soldi V, Pires A. Stereolithography somos 7110 resin: mechanical behavior and fractography of parts post-cured by different methods. Polym Test 2005;24(2):157-162.

46. Stratasys Ltd. Connex3 Objet260. ;2019.

47. Barclift MW, Williams CB, Examining variability in the mechanical properties of parts manufactured via polyjet direct 3D printing. In: International Solid Freeform Fabrication Symposium. , 2012. p. 6-8.

48. Meisel NA, Elliott AM, Williams CB. A procedure for creating actuated joints via embedding shape memory alloys in PolyJet 3D printing. J Intell Mater Syst Struct 2015;26(12):1498-1512.

49. Feygin M, Hsieh B, Laminated object manufacturing (LOM): a simpler process. In: 1991 International Solid Freeform Fabrication Symposium. , 1991.

50. Huang SH, Liu P, Mokasdar A, Hou L. Additive manufacturing and its societal impact: a literature review. The International Journal of Advanced Manufacturing Technology 2013;67(5-8):1191-1203.

51. Kamrani AK, Nasr EA. Engineering Design and Rapid Prototyping. : Springer Science & Business Media, 2010.

52. Kechagias J. An experimental investigation of the surface roughness of parts produced by LOM process. Rapid Prototyping Journal 2007;13(1):17-22.

53. Gomes CM, Oliveira APN, Hotza D, Travitzky N, Greil P. LZSA glass-ceramic laminates: Fabrication and mechanical properties. Journal of Materials Processing Technology 2008;206(1):194-201.

54. Tang H, Chiu M, Yen H. Slurry-based selective laser sintering of polymer-coated ceramic powders to fabricate high strength alumina parts. Journal of the European Ceramic Society 2011;31(8):1383-1388.

55. Gomes C, Travitzky N, Greil P, Acchar W, Birol H, Pedro Novaes de Oliveira A, Hotza D. Laminated object manufacturing of LZSA glass-ceramics. Rapid Prototyping Journal 2011;17(6):424-428.

56. Mazzoli A. Selective laser sintering in biomedical engineering. Med Biol Eng Comput 2013;51(3):245-256.

57. Dupin S, Lame O, Barrès C, Charmeau J. Microstructural origin of physical and mechanical properties of polyamide 12 processed by laser sintering. European Polymer Journal 2012;48(9):1611-1621.

58. Drummer D, Rietzel D, Kühnlein F. Development of a characterization approach for the sintering behavior of new thermoplastics for selective laser sintering. Physics Procedia 2010;5:533-542.

59. Tolochko NK, Khlopkov YV, Mozzharov SE, Ignatiev MB, Laoui T, Titov VI. Absorptance of powder materials suitable for laser sintering. Rapid Prototyping Journal 2000;6(3):155-161.

60. Anestiev LA, Froyen L. Model of the primary rearrangement processes at liquid phase sintering and selective laser sintering due to biparticle interactions. J Appl Phys 1999;86(7):4008-4017.

61. Kruth JP, Froyen L, Van Vaerenbergh J, Mercelis P, Rombouts M, Lauwers B. Selective laser melting of iron-based powder. Journal of Materials Processing Technology 2004;149(1):616-622.

62. Bugeda Miguel Cervera G, Lombera G. Numerical prediction of temperature and density distributions in selective laser sintering processes. Rapid Prototyping Journal 1999;5(1):21-26.

63. Traini T, Mangano C, Sammons RL, Mangano F, Macchi A, Piattelli A. Direct laser metal sintering as a new approach to fabrication of an isoelastic functionally graded material for manufacture of porous titanium dental implants. Dental Materials 2008;24(11):1525-1533.

64. Kruth J, Mercelis P, Van Vaerenbergh J, Froyen L, Rombouts M. Binding mechanisms in selective laser sintering and selective laser melting. Rapid prototyping journal 2005;11(1):26-36.

65. Redwood B. Learn about the most common SLS post processing methods from dyeing to metal plating. ;2019.

66. Zarringhalam H, Hopkinson N, Post-processing of Duraform™ parts for rapid manufacture. In: Solid Free Form Fabrication Symposium, University of Texas-Austin. , 2003. p. 596-606.

67. Utela B, Storti D, Anderson R, Ganter M. A review of process development steps for new material systems in three dimensional printing (3DP). Journal of Manufacturing Processes 2008;10(2):96-104.

68. Cima LG, Cima MJ. No title. Preparation of medical devices by solid free-form fabrication methods 1996.

69. Sachs EM, Haggerty JS, Cima MJ, Williams PA. No title. Three-dimensional printing techniques 1993.

70. Liu J, Ryneson ML. No title. Blended powder solid-supersolidus liquid phase sintering 2004.

71. Bredt JF, Anderson TC, Russell DB. No title. Three dimensional printing materials system 2002.

72. Lorenz AM, Sachs EM, Allen SM. No title. Techniques for infiltration of a powder metal skeleton by a similar alloy with melting point depressed 2004.

73. Sachs EM, Cima MJ, Caradonna MA, Grau J, Serdy JG, Saxton PC, Uhland SA, Moon J. No title. Jetting layers of powder and the formation of fine powder beds thereby 2003.

74. Tay BY, Evans JRG, Edirisinghe MJ. Solid freeform fabrication of ceramics. International Materials Reviews 2003;48(6):341-370.

75. Greil P. Polymer derived engineering ceramics. Advanced engineering materials 2000;2(6):339-348.

76. Bredt JF, Anderson T. No title. Method of three dimensional printing 1999.

77. Ho Y, Huang F, Chang Y. Cytotoxicity of formaldehyde on human osteoblastic cells is related to intracellular glutathione levels. Journal of Biomedical Materials Research Part B: Applied Biomaterials: An Official Journal of The Society for Biomaterials, The Japanese Society for Biomaterials, and The Australian Society for Biomaterials and the Korean Society for Biomaterials 2007;83(2):340-344.

78. Bredt JF, Clark S, Gilchrist G. No title. Three dimensional printing material system and method 2006.

79. Shen J. No title. Material system for use in three dimensional printing 2006.

80. Bredt JF. No title. Binder composition for use in three dimensional printing 1998.

81. Pfister A, Landers R, Laib A, Hübner U, Schmelzeisen R, Mülhaupt R. Biofunctional rapid prototyping for tissue-engineering applications: 3D bioplotting versus 3D printing. Journal of Polymer Science Part A: Polymer Chemistry 2004;42(3):624-638.

82. Khoshnevis B. No title. Selective inhibition of bonding of power particles for layered fabrication of 3-D objects 2003.

83. Butscher A, Bohner M, Hofmann S, Gauckler L, Müller R. Structural and material approaches to bone tissue engineering in powder-based three-dimensional printing. Acta biomaterialia 2011;7(3):907-920.

84. Seitz H, Deisinger U, Leukers B, Detsch R, Ziegler G. Different Calcium Phosphate Granules for 3-D Printing of Bone Tissue Engineering Scaffolds. Advanced engineering materials 2009;11(5):B41-B46.

85. Impens D, Urbanic RJ. Assessing the impact of post-processing variables on tensile and compression characteristics for 3D printed components. IFAC-PapersOnLine 2015;48(3):652-657.

86. ExOne. 3D Printing Systems Experience an innovative, faster, and more agile method of generating parts for rapid product development and production. ;2019.

87. Additive Manufacturing. ExOne Announces Exerial™ 3D Printing System Designed for Industrial Series Production. 2015;2019.

88. Von Obel M. 2019 3D Printing Materials Guide – All You Need to Know. 2019;2019.

89. Xu X, Meteyer S, Perry N, Zhao YF. Energy consumption model of Binder-jetting additive manufacturing processes. Int J Prod Res 2015;53(23):7005-7015.

90. Hopkinson N, Hague R, Dickens P. Rapid Manufacturing: An Industrial Revolution for the Digital Age. , 2006.

91. Wang X, Jiang M, Zhou Z, Gou J, Hui D. 3D printing of polymer matrix composites: A review and prospective. Composites Part B: Engineering 2017;110:442-458.

92. Additively. Overview over 3D printing technologies. ;2019.

93. Ahn D, Kweon J, Choi J, Lee S. Quantification of surface roughness of parts processed by laminated object manufacturing. Journal of Materials Processing Technology 2012;212(2):339-346.

94. Gao W, Zhang Y, Ramanujan D, Ramani K, Chen Y, Williams CB, Wang CCL, Shin YC, Zhang S, Zavattieri PD. The status, challenges, and future of additive manufacturing in engineering. Computer-Aided Design 2015;69:65-89.

95. Osswald TA, Baur E, Brinkmann S, Oberbach K, Schmachtenberg E. International Plastics Handbook. In: Anonymous International Plastics Handbook. : Carl Hanser Verlag GmbH & Co. KG, 2006. p. i-xvii.

96. Kulich DM, Gaggar SK, Lowry V, Stepien R. Acrylonitrile–butadiene–styrene polymers. Encyclopedia of Polymer Science and Technology 2002;1.

97. Baguley R. 3D Printing Materials: The Pros and Cons of Each Type. 2017;2019.

98. Scheirs J, Priddy D. Modern Styrenic Polymers: Polystyrenes and Styrenic Copolymers. : John Wiley & Sons, 2003.

99. Fink JK. Handbook of Engineering and Specialty Thermoplastics, Volume 1: Polyolefins and Styrenics. : John Wiley & Sons, 2010.

100. Carneiro OS, Silva AF, Gomes R. Fused deposition modeling with polypropylene. Materials & Design 2015;83:768-776.

101. Van de Velde K, Kiekens P. Biopolymers: overview of several properties and consequences on their applications. Polymer Testing 2002;21(4):433-442.

102. Crawford RJ. Plastics Engineering. : Elsevier, 1998.

103. Batchelder JS, Crump SS. No title. Method for rapid prototyping of solid models 1999.

104. Bártolo PJ. Stereolithography: Materials, Processes and Applications. : Springer Science & Business Media, 2011.

105. 3Dprinting.com. 3D Printing Materials. 2019;2019.

106. Li H, Zhang S, Yi Z, Li J, Sun A, Guo J, Xu G. Bonding quality and fracture analysis of polyamide 12 parts fabricated by fused deposition modeling. Rapid Prototyping Journal 2017;23(6):973-982.

107. Lederle F, Meyer F, Brunotte G, Kaldun C, Hübner EG. Improved mechanical properties of 3D-printed parts by fused deposition modeling processed under the exclusion of oxygen. Progress in Additive Manufacturing 2016;1(1-2):3-7.

108. Rahim T, Abdullah AM, Akil HM, Mohamad D, Rajion ZA. The improvement of mechanical and thermal properties of polyamide 12 3D printed parts by fused deposition modelling. eXPRESS Polymer Letters 2017;11(12):963-982.

109. Schmidt M, Pohle D, Rechtenwald T. Selective laser sintering of PEEK. CIRP annals 2007;56(1):205-208.

110. Vink D. Designs on the future of manufacturing. 2009;2019.

111. Garcia-Gonzalez D, Rusinek A, Jankowiak T, Arias A. Mechanical impact behavior of polyether–ether–ketone (PEEK). Composite Structures 2015;124:88-99.

112. Wu WZ, Geng P, Zhao J, Zhang Y, Rosen DW, Zhang HB. Manufacture and thermal deformation analysis of semicrystalline polymer polyether ether ketone by 3D printing. Materials Research Innovations 2014;18(sup5):S5-16.

113. TRACTUS 3D. PEEK 3D printing - Tips, examples, advantages and more... ;2019.

114. Yang C, Tian X, Li D, Cao Y, Zhao F, Shi C. Influence of thermal processing conditions in 3D printing on the crystallinity and mechanical properties of PEEK material. J Mater Process Technol 2017;248:1-7.

115. Wang P, Zou B, Xiao H, Ding S, Huang C. Effects of printing parameters of fused deposition modeling on mechanical properties, surface quality, and microstructure of PEEK. J Mater Process Technol 2019;271:62-74.

116. Deng X, Zeng Z, Peng B, Yan S, Ke W. Mechanical properties optimization of poly-ether-ether-ketone via fused deposition modeling. Materials 2018;11(2):216.

117. Nair LS, Laurencin CT. Biodegradable polymers as biomaterials. Progress in Polymer Science 2007;32(8):762-798.

118. Gross RA, Kalra B. Biodegradable polymers for the environment. Science 2002;297(5582):803-807.

119. Galactic. Galactic at a glance. ;2019.

120. Baroli B. Hydrogels for Tissue Engineering and Delivery of Tissue-Inducing Substances. Journal of Pharmaceutical Sciences 2007;96(9):2197-2223.

121. Kurtis Kasper MS, F., Mikos AG. Chapter II.6.3 - Tissue Engineering Scaffolds. In: Ratner BD, Hoffman AS, Schoen FJ, Lemons JE, editors. Biomaterials Science (Third Edition). : Academic Press, 2013. p. 1138-1159.

122. Mohanty AK, Misra Ma, Hinrichsen GI. Biofibres, biodegradable polymers and biocomposites: An overview. Macromolecular materials and Engineering 2000;276(1):1-24.

123. Avella M, Immirzi B, Malinconico M, Martuscelli E, Volpe MG. Reactive blending methodologies for Biopol. Polym Int 1996;39(3):191-204.

124. Barham PJ, Keller A. The relationship between microstructure and mode of fracture in polyhydroxybutyrate. Journal of Polymer Science Part B: Polymer Physics 1986;24(1):69-77.

125. Doi Y, Microbial synthesis, physical properties, and biodegradability of polyhydroxyalkanoates. In: Macromolecular Symposia. , 1995. p. 585-599.

126. Hocking PJ, Marchessault RH, Timmins MR, Lenz RW, Fuller RC. Enzymatic degradation of single crystals of bacterial and synthetic poly (β-hydroxybutyrate). Macromolecules 1996;29(7):2472-2478.

127. Pool R. In search of the plastic potato. Science 1989;245(4923):1187-1190.

128. Pereira TF, Oliveira MF, Maia IA, Silva JV, Costa MF, Thiré RM, 3D Printing of Poly (3-hydroxybutyrate) Porous Structures Using Selective Laser Sintering. In: Macromolecular Symposia. , 2012. p. 64-73.

129. Loureiro NC, Esteves JL, Viana JC, Ghosh S. Development of polyhydroxyalkanoates/poly(lactic acid) composites reinforced with cellulosic fibers. Composites Part B: Engineering 2014;60:603-611.

130. Li X, Cui R, Sun L, Aifantis KE, Fan Y, Feng Q, Cui F, Watari F. 3D-printed biopolymers for tissue engineering application. International Journal of Polymer Science 2014;2014.

131. Duan B, Wang M. Customized Ca–P/PHBV nanocomposite scaffolds for bone tissue engineering: design, fabrication, surface modification and sustained release of growth factor. Journal of the Royal Society Interface 2010;7(suppl_5):S615-S629.

132. Wu C, Liao H, Cai Y. Characterisation, biodegradability and application of palm fibre-reinforced polyhydroxyalkanoate composites. Polymer Degradation and Stability 2017;140:55-63.

133. Brothers R. 3D Printing with Bamboo Wood Filament. 2019.

134. Scaffaro R, Lopresti F, Botta L, Maio A. Mechanical behavior of polylactic acid/polycaprolactone porous layered functional composites. Composites Part B: Engineering 2016;98:70-77.

135. Kundu J, Shim J, Jang J, Kim S, Cho D. An additive manufacturing-based PCL–alginate–chondrocyte bioprinted scaffold for cartilage tissue engineering. Journal of tissue engineering and regenerative medicine 2015;9(11):1286-1297.

136. Patrício T, Domingos M, Gloria A, Bártolo P. Characterisation of PCL and PCL/PLA Scaffolds for Tissue Engineering. Procedia CIRP 2013;5:110-114.

137. Melchels FPW, Domingos MAN, Klein TJ, Malda J, Bartolo PJ, Hutmacher DW. Additive manufacturing of tissues and organs. Progress in Polymer Science 2012;37(8):1079-1104.

138. Cheung H, Lau K, Lu T, Hui D. A critical review on polymer-based bio-engineered materials for scaffold development. Composites Part B: Engineering 2007;38(3):291-300.

139. Gilding DK, Reed AM. Biodegradable polymers for use in surgery—polyglycolic/poly (actic acid) homo-and copolymers: 1. Polymer 1979;20(12):1459-1464.

140. Chung H, Das S. Processing and properties of glass bead particulate-filled functionally graded Nylon-11 composites produced by selective laser sintering. Materials Science and Engineering: A 2006;437(2):226-234.

141. Nikzad M, Masood SH, Sbarski I. Thermo-mechanical properties of a highly filled polymeric composites for Fused Deposition Modeling. Materials & Design 2011;32(6):3448-3456.

142. Boparai KS, Singh R, Fabbrocino F, Fraternali F. Thermal characterization of recycled polymer for additive manufacturing applications. Composites Part B: Engineering 2016;106:42-47.

143. Kurimoto M, Yamashita Y, Ozaki H, Kato T, Funabashi T, Suzuoki Y, 3D printing of conical insulating spacer using alumina/UV-cured-resin composite. In: 2015 IEEE Conference on Electrical Insulation and Dielectric Phenomena (CEIDP). , 2015. p. 463-466.

144. Isakov DV, Lei Q, Castles F, Stevens CJ, Grovenor CRM, Grant PS. 3D printed anisotropic dielectric composite with meta-material features. Materials & Design 2016;93:423-430.

145. Shemelya CM, Rivera A, Perez AT, Rocha C, Liang M, Yu X, Kief C, Alexander D, Stegeman J, Xin H. Mechanical, electromagnetic, and X-ray shielding characterization of a 3D printable tungsten–polycarbonate polymer matrix composite for space-based applications. J Electron Mater 2015;44(8):2598-2607.

146. Hwang S, Reyes EI, Moon K, Rumpf RC, Kim NS. Thermo-mechanical characterization of metal/polymer composite filaments and printing parameter study for fused deposition modeling in the 3D printing process. J Electron Mater 2015;44(3):771-777.

147. Kalsoom U, Peristyy A, Nesterenko PN, Paull B. A 3D printable diamond polymer composite: a novel material for fabrication of low cost thermally conducting devices. RSC Advances 2016;6(44):38140-38147.

148. Castles F, Isakov D, Lui A, Lei Q, Dancer C, Wang Y, Janurudin JM, Speller SC, Grovenor C, Grant PS. Microwave dielectric characterisation of 3D-printed BaTiO 3/ABS polymer composites. Scientific reports 2016;6:22714.

149. Skorski MR, Esenther JM, Ahmed Z, Miller AE, Hartings MR. The chemical, mechanical, and physical properties of 3D printed materials composed of TiO2-ABS nanocomposites. Science and Technology of Advanced Materials 2016;17(1):89-97.

150. Perez ART, Roberson DA, Wicker RB. Fracture surface analysis of 3D-printed tensile specimens of novel ABS-based materials. Journal of Failure Analysis and Prevention 2014;14(3):343-353.

151. Khatri B, Lappe K, Noetzel D, Pursche K, Hanemann T. A 3D-printable polymer-metal soft-magnetic functional composite—Development and characterization. Materials 2018;11(2):189.

152. Kokkinis D, Schaffner M, Studart AR. Multimaterial magnetically assisted 3D printing of composite materials. Nature communications 2015;6:8643.

153. Paul DR, Robeson LM. Polymer nanotechnology: nanocomposites. Polymer 2008;49(15):3187-3204.

154. Lin D, Jin S, Zhang F, Wang C, Wang Y, Zhou C, Cheng GJ. 3D stereolithography printing of graphene oxide reinforced complex architectures. Nanotechnology 2015;26(43):434003.

155. Fang M, Wang K, Lu H, Yang Y, Nutt S. Covalent polymer functionalization of graphene nanosheets and mechanical properties of composites. Journal of Materials Chemistry 2009;19(38):7098-7105.

156. Rafiee MA, Rafiee J, Srivastava I, Wang Z, Song H, Yu Z, Koratkar N. Fracture and fatigue in graphene nanocomposites. small 2010;6(2):179-183.

157. Gong L, Young RJ, Kinloch IA, Riaz I, Jalil R, Novoselov KS. Optimizing the reinforcement of polymer-based nanocomposites by graphene. ACS nano 2012;6(3):2086-2095.

158. Stankovich S, Dikin DA, Dommett GH, Kohlhaas KM, Zimney EJ, Stach EA, Piner RD, Nguyen ST, Ruoff RS. Graphene-based composite materials. Nature 2006;442(7100):282.

159. Kahng YH, Lee S, Park W, Jo G, Choe M, Lee J, Yu H, Lee T, Lee K. Thermal stability of multilayer graphene films synthesized by chemical vapor deposition and stained by metallic impurities. Nanotechnology 2012;23(7):075702.

160. Vlassiouk I, Smirnov S, Ivanov I, Fulvio PF, Dai S, Meyer H, Chi M, Hensley D, Datskos P, Lavrik NV. Electrical and thermal conductivity of low temperature CVD graphene: the effect of disorder. Nanotechnology 2011;22(27):275716.

161. Che J, Wu K, Lin Y, Wang K, Fu Q. Largely improved thermal conductivity of HDPE/expanded graphite/carbon nanotubes ternary composites via filler network-network synergy. Composites Part A: Applied Science and Manufacturing 2017;99:32-40.

162. Li Y, Feng Z, Huang L, Essa K, Bilotti E, Zhang H, Peijs T, Hao L. Additive manufacturing high performance graphene-based composites: A review. Composites Part A: Applied Science and Manufacturing 2019;124:105483.

163. Wang D, Huang X, Li J, He B, Liu Q, Hu L, Jiang G. 3D printing of graphene-doped target for "matrix-free" laser desorption/ionization mass spectrometry. Chemical communications 2018;54(22):2723-2726.

164. Lin D, Jin S, Zhang F, Wang C, Wang Y, Zhou C, Cheng GJ. 3D stereolithography printing of graphene oxide reinforced complex architectures. Nanotechnology 2015;26(43):434003.

165. Gao Y, Picot OT, Tu W, Bilotti E, Peijs T. Multilayer coextrusion of graphene polymer nanocomposites with enhanced structural organization and properties. J Appl Polym Sci 2018;135(13):46041.

166. Zhu D, Ren Y, Liao G, Jiang S, Liu F, Guo J, Xu G. Thermal and mechanical properties of polyamide 12/graphene nanoplatelets nanocomposites and parts fabricated by fused deposition modeling. J Appl Polym Sci 2017;134(39):45332.

167. Feng Z, Li Y, Xin C, Tang D, Xiong W, Zhang H. Fabrication of Graphene-Reinforced Nanocomposites with Improved Fracture Toughness in Net Shape for Complex 3D Structures via Digital Light Processing. C 2019;5(2):25.

168. Bai J, Goodridge RD, Hague RJ, Song M, Okamoto M. Influence of carbon nanotubes on the rheology and dynamic mechanical properties of polyamide-12 for laser sintering. Polym Test 2014;36:95-100.

169. Gnanasekaran K, Heijmans T, Van Bennekom S, Woldhuis H, Wijnia S, de With G, Friedrich H. 3D printing of CNT-and graphene-based conductive polymer nanocomposites by fused deposition modeling. Applied materials today 2017;9:21-28.

170. Salmoria GV, Paggi RA, Lago A, Beal VE. Microstructural and mechanical characterization of PA12/MWCNTs nanocomposite manufactured by selective laser sintering. Polym Test 2011;30(6):611-615.

171. Plymill A, Minneci R, Greeley DA, Gritton J. Graphene and carbon nanotube PLA composite feedstock development for fused deposition modeling. 2016.

172. Nadernezhad A, Unal S, Khani N, Koc B. Material extrusion-based additive manufacturing of structurally controlled poly (lactic acid)/carbon nanotube nanocomposites. The International Journal of Advanced Manufacturing Technology 2019;102(5-8):2119-2132.

173. Cholleti ER, Gibson I, ABS Nano Composite Materials in Additive Manufacturing. In: IOP Conference Series: Materials Science and Engineering. , 2018. p. 012038.

174. Meng S, He H, Jia Y, Yu P, Huang B, Chen J. Effect of nanoparticles on the mechanical properties of acrylonitrile–butadiene–styrene specimens fabricated by fused deposition modeling. J Appl Polym Sci 2017;134(7).

175. Kim K, Park J, Suh J, Kim M, Jeong Y, Park I. 3D printing of multiaxial force sensors using carbon nanotube (CNT)/thermoplastic polyurethane (TPU) filaments. Sensors and Actuators A: Physical 2017;263:493-500.

176. Postiglione G, Natale G, Griffini G, Levi M, Turri S. Conductive 3D microstructures by direct 3D printing of polymer/carbon nanotube nanocomposites via liquid deposition modeling. Composites Part A: Applied Science and Manufacturing 2015;76:110-114.

177. Ko FK, Wan Y. Introduction to Nanofiber Materials. : Cambridge University Press, 2014.

178. Francis V, Jain PK. 3D printed polymer dielectric substrates with enhanced permittivity by nanoclay inclusion. Virtual and Physical Prototyping 2017;12(2):107-115.

179. Francis V, Jain PK. Experimental investigations on fused deposition modelling of polymer-layered silicate nanocomposite. Virtual and Physical Prototyping 2016;11(2):109-121.

180. Francis V, Jain PK. Investigation on the effect of surface modification of 3D printed parts by nanoclay and dimethyl ketone. Mater Manuf Process 2018;33(10):1080-1092.

181. Weng Z, Zhou Y, Lin W, Senthil T, Wu L. Structure-property relationship of nano enhanced stereolithography resin for desktop SLA 3D printer. Composites Part A: Applied Science and Manufacturing 2016;88:234-242.

182. Liu T, Zhou T, Yao Y, Zhang F, Liu L, Liu Y, Leng J. Stimulus methods of multi-functional shape memory polymer nanocomposites: A review. Composites Part A: Applied Science and Manufacturing 2017;100:20-30.

183. Liu W, Wu N, Pochiraju K. Shape recovery characteristics of SiC/C/PLA composite filaments and 3D printed parts. Composites Part A: Applied Science and Manufacturing 2018;108:1-11.

184. Blok LG, Longana ML, Yu H, Woods BK. An investigation into 3D printing of fibre reinforced thermoplastic composites. Additive Manufacturing 2018;22:176-186.

185. Ferreira RTL, Amatte IC, Dutra TA, Bürger D. Experimental characterization and micrography of 3D printed PLA and PLA reinforced with short carbon fibers. Composites Part B: Engineering 2017;124:88-100.

186. Tekinalp HL, Kunc V, Velez-Garcia GM, Duty CE, Love LJ, Naskar AK, Blue CA, Ozcan S. Highly oriented carbon fiber–polymer composites via additive manufacturing. Composites Sci Technol 2014;105:144-150.

187. Zhang W, Cotton C, Sun J, Heider D, Gu B, Sun B, Chou T. Interfacial bonding strength of short carbon fiber/acrylonitrile-butadiene-styrene composites fabricated by fused deposition modeling. Composites Part B: Engineering 2018;137:51-59.

188. Ning F, Cong W, Qiu J, Wei J, Wang S. Additive manufacturing of carbon fiber reinforced thermoplastic composites using fused deposition modeling. Composites Part B: Engineering 2015;80:369-378.

189. Spoerk M, Savandaiah C, Arbeiter F, Traxler G, Cardon L, Holzer C, Sapkota J. Anisotropic properties of oriented short carbon fibre filled polypropylene parts fabricated by extrusion-based additive manufacturing. Composites Part A: Applied Science and Manufacturing 2018;113:95-104.

190. Tian X, Liu T, Yang C, Wang Q, Li D. Interface and performance of 3D printed continuous carbon fiber reinforced PLA composites. Composites Part A: Applied Science and Manufacturing 2016;88:198-205.

191. Matsuzaki R, Ueda M, Namiki M, Jeong T, Asahara H, Horiguchi K, Nakamura T, Todoroki A, Hirano Y. Three-dimensional printing of continuous-fiber composites by in-nozzle impregnation. Scientific reports 2016;6:23058.

192. Bettini P, Alitta G, Sala G, Di Landro L. Fused deposition technique for continuous fiber reinforced thermoplastic. Journal of Materials Engineering and Performance 2017;26(2):843-848.

193. Dickson AN, Barry JN, McDonnell KA, Dowling DP. Fabrication of continuous carbon, glass and Kevlar fibre reinforced polymer composites using additive manufacturing. Additive Manufacturing 2017;16:146-152.

194. Caminero MA, Chacón JM, García-Moreno I, Reverte JM. Interlaminar bonding performance of 3D printed continuous fibre reinforced thermoplastic composites using fused deposition modelling. Polym Test 2018;68:415-423.

195. Sugiyama K, Matsuzaki R, Ueda M, Todoroki A, Hirano Y. 3D printing of composite sandwich structures using continuous carbon fiber and fiber tension. Composites Part A: Applied Science and Manufacturing 2018;113:114-121.

196. Liao G, Li Z, Cheng Y, Xu D, Zhu D, Jiang S, Guo J, Chen X, Xu G, Zhu Y. Properties of oriented carbon fiber/polyamide 12 composite parts fabricated by fused deposition modeling. Mater Des 2018;139:283-292.

197. Ye W, Lin G, Wu W, Geng P, Hu X, Gao Z, Zhao J. Separated 3D printing of continuous carbon fiber reinforced thermoplastic polyimide. Composites Part A: Applied Science and Manufacturing 2019;121:457-464.

198. ASM. Aluminum 6061-T6; 6061-T651. ;2019.

199. Quan Z, Larimore Z, Wu A, Yu J, Qin X, Mirotznik M, Suhr J, Byun J, Oh Y, Chou T. Microstructural design and additive manufacturing and characterization of 3D orthogonal short carbon fiber/acrylonitrile-butadiene-styrene preform and composite. Composites Science and Technology 2016;126:139-148.

200. Fu S, Lauke B, Mäder E, Yue C, Hu X. Tensile properties of short-glass-fiber-and short-carbon-fiber-reinforced polypropylene composites. Composites Part A: Applied Science and Manufacturing 2000;31(10):1117-1125.

201. Fan M, Naughton A. Mechanisms of thermal decomposition of natural fibre composites. Composites Part B: Engineering 2016;88:1-10.

202. Naughton A, Fan M, Bregulla J. Fire resistance characterisation of hemp fibre reinforced polyester composites for use in the construction industry. Composites Part B: Engineering 2014;60:546-554.

203. Stokke DD, Wu Q, Han G. Introduction to Wood and Natural Fiber Composites. : John Wiley & Sons, 2013.

204. Rao J, Bao L, Wang B, Fan M, Feo L. Plasma surface modification and bonding enhancement for bamboo composites. Composites Part B: Engineering 2018;138:157-167.

205. Pickering KL, Efendy MA, Le TM. A review of recent developments in natural fibre composites and their mechanical performance. Composites Part A: Applied Science and Manufacturing 2016;83:98-112.

206. Kabir MM, Wang H, Lau KT, Cardona F. Chemical treatments on plant-based natural fibre reinforced polymer composites: An overview. Composites Part B: Engineering 2012;43(7):2883-2892.

207. Yu Y, Wang H, Lu F, Tian G, Lin J. Bamboo fibers for composite applications: a mechanical and morphological investigation. J Mater Sci 2014;49(6):2559-2566.

208. Barkoula N, Alcock B, Cabrera NO, Peijs T. Fatigue properties of highly oriented polypropylene tapes and all-polypropylene composites. Polymers and Polymer Composites 2008;16(2):101-113.

209. Eichhorn SJ, Baillie CA, Zafeiropoulos N, Mwaikambo LY, Ansell MP, Dufresne A, Entwistle KM, Herrera-Franco PJ, Escamilla GC, Groom L. Current international research into cellulosic fibres and composites. J Mater Sci 2001;36(9):2107-2131.

210. Cai M, Takagi H, Nakagaito AN, Li Y, Waterhouse GI. Effect of alkali treatment on interfacial bonding in abaca fiber-reinforced composites. Composites Part A: Applied Science and Manufacturing 2016;90:589-597.

211. Kumar RP, Chandan GK, Ramamoorthi R. Fabrication and testing of natural fiber hybrid composites. Int J Eng Res 2016;5:285e8.

212. Sreekala MS, Kumaran MG, Thomas S. Oil palm fibers: Morphology, chemical composition, surface modification, and mechanical properties. J Appl Polym Sci 1997;66(5):821-835.

213. Kim NK, Bhattacharyya D. Development of fire resistant wool polymer composites: Mechanical performance and fire simulation with design perspectives. Materials & Design 2016;106:391-403.

214. Gurunathan T, Mohanty S, Nayak SK. A review of the recent developments in biocomposites based on natural fibres and their application perspectives. Composites Part A: Applied Science and Manufacturing 2015;77:1-25.

215. Fiore V, Scalici T, Di Bella G, Valenza A. A review on basalt fibre and its composites. Composites Part B: Engineering 2015;74:74-94.

216. Zhou Y, Fan M, Chen L. Interface and bonding mechanisms of plant fibre composites: An overview. Composites Part B: Engineering 2016;101:31-45.

217. Shah DU, Schubel PJ, Licence P, Clifford MJ. Determining the minimum, critical and maximum fibre content for twisted yarn reinforced plant fibre composites. Composites Sci Technol 2012;72(15):1909-1917.

218. Stoof D, Pickering K. Sustainable composite fused deposition modelling filament using recycled pre-consumer polypropylene. Composites Part B: Engineering 2018;135:110-118.

219. Hu R, Lim J. Fabrication and mechanical properties of completely biodegradable hemp fiber reinforced polylactic acid composites. J Composite Mater 2007;41(13):1655-1669.

220. Zhou Y, Fan M. Recycled tyre rubber-thermoplastic composites through interface optimisation. RSC advances 2017;7(47):29263-29270.

221. Le Duigou A, Castro M, Bevan R, Martin N. 3D printing of wood fibre biocomposites: From mechanical to actuation functionality. Materials & Design 2016;96:106-114.

222. Navarrete JIM, Hidalgo-Salazar MA, Nunez EE, Arciniegas AJR. Thermal and mechanical behavior of biocomposites using additive manufacturing. International Journal on Interactive Design and Manufacturing (IJIDeM) 2018;12(2):449-458.

223. Baghaei B, Skrifvars M, Salehi M, Bashir T, Rissanen M, Nousiainen P. Novel aligned hemp fibre reinforcement for structural biocomposites: Porosity, water absorption, mechanical performances and viscoelastic behaviour. Composites Part A: Applied Science and Manufacturing 2014;61:1-12.

224. Li H, Sain MM. High stiffness natural fiber-reinforced hybrid polypropylene composites. Polym Plast Technol Eng 2003;42(5):853-862.

225. Sang L, Han S, Peng X, Jian X, Wang J. Development of 3D-printed basalt fiber reinforced thermoplastic honeycombs with enhanced compressive mechanical properties. Composites Part A: Applied Science and Manufacturing 2019;125:105518.

226. Wu X, Dzenis YA. Droplet on a fiber: geometrical shape and contact angle. Acta Mech 2006;185(3):215-225.

227. Chen P, Lu C, Yu Q, Gao Y, Li J, Li X. Influence of fiber wettability on the interfacial adhesion of continuous fiber-reinforced PPESK composite. J Appl Polym Sci 2006;102(3):2544-2551.

228. Matthews FL, Rawlings RD. Composite Materials: Engineering and Science. : Woodhead Publishing, 1999.

229. Singh B, Gupta M, Verma A. Influence of fiber surface treatment on the properties of sisal-polyester composites. Polymer Composites 1996;17(6):910-918.

230. Faruk O, Bledzki AK, Fink H, Sain M. Progress report on natural fiber reinforced composites. Macromolecular Materials and Engineering 2014;299(1):9-26.

231. Bledzki AK, Mamun AA, Jaszkiewicz A, Erdmann K. Polypropylene composites with enzyme modified abaca fibre. Composites Sci Technol 2010;70(5):854-860.

232. Kabir MM, Wang H, Lau KT, Cardona F. Chemical treatments on plant-based natural fibre reinforced polymer composites: An overview. Composites Part B: Engineering 2012;43(7):2883-2892.

233. Bera M, Alagirusamy R, Das A. A study on interfacial properties of jute-PP composites. J Reinf Plast Compos 2010;29(20):3155-3161.

234. Gassan J, Gutowski VS. Effects of corona discharge and UV treatment on the properties of jute-fibre epoxy composites. Composites Sci Technol 2000;60(15):2857-2863.

235. Seki Y, Sever K, Sarikanat M, Güleç HA, Tavman IH, The influence of oxygen plasma treatment of jute fibers on mechanical properties of jute fiber reinforced thermoplastic composites. In: Proceedings of the 5th International Advanced Technologies Symposium (IATS'09). , 2009.

236. Rong MZ, Zhang MQ, Liu Y, Yang GC, Zeng HM. The effect of fiber treatment on the mechanical properties of unidirectional sisal-reinforced epoxy composites. Composites Sci Technol 2001;61(10):1437-1447.

237. Huber T, Biedermann U, Müssig J. Enhancing the fibre matrix adhesion of natural fibre reinforced polypropylene by electron radiation analyzed with the single fibre fragmentation test. Composite Interfaces 2010;17(4):371-381.

238. Beg M, Pickering KL. Mechanical performance of Kraft fibre reinforced polypropylene composites: Influence of fibre length, fibre beating and hygrothermal ageing. Composites Part A: Applied Science and Manufacturing 2008;39(11):1748-1755.

239. Sanadi AR, Caulfield DF, Jacobson RE. Ago-fiber/thermoplastic composites. Paper and composites from agobased resources, RM Rowell, RA Young and JK Rowell, eds., Chapter 12, 377-402. 1997.

240. Norman DA, Robertson RE. The effect of fiber orientation on the toughening of short fiber-reinforced polymers. J Appl Polym Sci 2003;90(10):2740-2751.

241. Ben Amor I, Rekik H, Kaddami H, Raihane M, Arous M, Kallel A. Effect of palm tree fiber orientation on electrical properties of palm tree fiber-reinforced polyester composites. J Composite Mater 2010;44(13):1553-1568.

242. Carpenter JE, Miao MH, Brorens P, Deformation behaviour of composites reinforced with four different linen flax yarn structures. In: Advanced Materials Research. , 2007. p. 263-266.

243. Khalfallah M, Abbès B, Abbès F, Guo YQ, Marcel V, Duval A, Vanfleteren F, Rousseau F. Innovative flax tapes reinforced Acrodur biocomposites: A new alternative for automotive applications. Mater Des 2014;64:116-126.

244. Madsen B, Thygesen A, Lilholt H. Plant fibre composites–porosity and stiffness. Composites Sci Technol 2009;69(7-8):1057-1069.

245. Madsen B, Lilholt H. Physical and mechanical properties of unidirectional plant fibre composites—an evaluation of the influence of porosity. Composites Sci Technol 2003;63(9):1265-1272.

246. Habibi Y, Lucia LA, Rojas OJ. Cellulose nanocrystals: chemistry, self-assembly, and applications. Chem Rev 2010;110(6):3479-3500.

247. Moon RJ, Martini A, Nairn J, Simonsen J, Youngblood J. Cellulose nanomaterials review: structure, properties and nanocomposites. Chem Soc Rev 2011;40(7):3941-3994.

248. Oksman K, Aitomäki Y, Mathew AP, Siqueira G, Zhou Q, Butylina S, Tanpichai S, Zhou X, Hooshmand S. Review of the recent developments in cellulose nanocomposite processing. Composites Part A: Applied Science and Manufacturing 2016;83:2-18.

249. Wang Z, Xu J, Lu Y, Hu L, Fan Y, Ma J, Zhou X. Preparation of 3D printable micro/nanocellulose-polylactic acid (MNC/PLA) composite wire rods with high MNC constitution. Industrial crops and products 2017;109:889-896.

250. Dong J, Li M, Zhou L, Lee S, Mei C, Xu X, Wu Q. The influence of grafted cellulose nanofibers and postextrusion annealing treatment on selected properties of poly (lactic acid) filaments for 3D printing. Journal of Polymer Science Part B: Polymer Physics 2017;55(11):847-855.

251. Tebaldi ML, Maia ALC, Poletto F, de Andrade FV, Soares DCF. Poly (-3-hydroxybutyrate-co-3-hydroxyvalerate)(PHBV): Current advances in synthesis methodologies, antitumor applications and biocompatibility. Journal of Drug Delivery Science and Technology 2019;51:115-126.

252. Nair NR, Sekhar VC, Nampoothiri KM, Pandey A. 32 - Biodegradation of Biopolymers. In: Pandey A, Negi S, Soccol CR, editors. Current Developments in Biotechnology and Bioengineering. : Elsevier, 2017. p. 739-755.

253. Reshmy R, Philip E, Vaisakh PH, Sindhu R, Binod P, Madhavan A, Pandey A, Sirohi R, Tarafdar A. Chapter 14 - Biodegradable polymer composites. In: Binod P, Raveendran S, Pandey A, editors. Biomass, Biofuels, Biochemicals. : Elsevier, 2021. p. 393-412.

254. Niaounakis M. Chapter 1 - Introduction. In: Niaounakis M, editor. Biopolymers: Processing and Products. Oxford: William Andrew Publishing, 2015. p. 1-77.

255. Jiang L, Zhang J. 7 - Biodegradable and Biobased Polymers. In: Kutz M, editor. Applied Plastics Engineering Handbook (Second Edition). : William Andrew Publishing, 2017. p. 127-143.

256. Zarrintaj P, Saeb MR, Jafari SH, Mozafari M. Chapter 18 - Application of compatibilized polymer blends in biomedical fields. In: A.R. A, Thomas S, editors. Compatibilization of Polymer Blends. : Elsevier, 2020. p. 511-537.

257. Hu Y, Hu YS, Topolkaraev V, Hiltner A, Baer E. Crystallization and phase separation in blends of high stereoregular poly(lactide) with poly(ethylene glycol). Polymer 2003;44(19):5681-5689.

258. Jacobsen S, Fritz HG. Plasticizing polylactide - the effect of different plasticizers on the mechanical properties. Polym Eng Sci 1999;39(7):1303-1310.

259. Pillin I, Montrelay N, Bourmaud A, Grohens Y. Effect of thermo-mechanical cycles on the physico-chemical properties of poly(lactic acid). Polym Degrad Stab 2008;93(2):321-328.

260. Catoni SE, Trindade KN, Gomes CA, Schneider AL, Pezzin A, Soldi V. Influence of poly (ethylene grycol)-(PEG) on the properties of influence of poly (3-hydroxybutyrate-CO-3-hydroxyvalerate)-PHBV. Polímeros 2013;23(3):320-325.

261. Wang S, Winistorfer PM, Young TM, Helton C. Step-closing pressing of medium density fiberboard; Part 1. Influences on the vertical density profile. Holz als roh-und Werkstoff 2001;59(1-2):19-26.

262. Hunt JF, Leng W, Tajvidi M. Vertical density profile and internal bond strength of wet-formed particleboard bonded with cellulose nanofibrils. Wood and Fiber Science, 2017.49 (4): 1-11. 2017;49(4):1-11.

263. Hu Z. Chapter 6 - Characterization of Materials, Nanomaterials, and Thin Films by Nanoindentation. Microscopy Methods in Nanomaterials Characterization 2017:165-239.

264. VanLandingham MR, Villarrubia JS, Guthrie WF, Meyers GF. Nanoindentation of polymers: an overview. Macromol Symp 2001;167(1):15-44.

265. Byrn SR. Differential Scanning Calorimetry and Thermogravimetric Analysis. Hoboken, 6.

266. Golebiewski J, Galeski A. Thermal stability of nanoclay polypropylene composites by simultaneous DSC and TGA. Composites Sci Technol 2007;67(15):3442-3447.

267. Ebnesajjad S. 4 - Surface and Material Characterization Techniques. In: Ebnesajjad S, editor. Surface Treatment of Materials for Adhesion Bonding. Norwich, NY: William Andrew Publishing, 2006. p. 43-75.

268. Bellehumeur C, Li L, Sun Q, Gu P. Modeling of Bond Formation Between Polymer Filaments in the Fused Deposition Modeling Process. Journal of Manufacturing Processes 2004;6(2):170-178.

269. Sun Q, Rizvi GM, Bellehumeur CT, Gu P. Effect of processing conditions on the bonding quality of FDM polymer filaments. Rapid prototyping journal 2008.

270. Sun Q, Rizvi GM, Bellehumeur CT, Gu P, Experimental study of the cooling characteristics of polymer filaments in FDM and impact on the mesostructures and properties of prototypes. In: 2003 International Solid Freeform Fabrication Symposium. , 2003.

271. Huang T, Miura M, Nobukawa S, Yamaguchi M. Chain Packing and Its Anomalous Effect on Mechanical Toughness for Poly(lactic acid). Biomacromolecules 2015;16(5):1660-1666.

272. Srithep Y, Nealey P, Turng L. Effects of annealing time and temperature on the crystallinity and heat resistance behavior of injection-molded poly(lactic acid). Polym Eng Sci 2013;53(3):580-588.

273. Zou R, Xia Y, Liu S, Hu P, Hou W, Hu Q, Shan C. Isotropic and anisotropic elasticity and yielding of 3D printed material. Composites Part B: Engineering 2016;99:506-513.

274. Chacón JM, Caminero MA, García-Plaza E, Núnez PJ. Additive manufacturing of PLA structures using fused deposition modelling: Effect of process parameters on mechanical properties and their optimal selection. Mater Des 2017;124:143-157.

275. Tymrak BM, Kreiger M, Pearce JM. Mechanical properties of components fabricated with open-source 3-D printers under realistic environmental conditions. Mater Des 2014;58:242-246.

276. Bayraktar Ö, Uzun G, Çakiroğlu R, Guldas A. Experimental study on the 3D-printed plastic parts and predicting the mechanical properties using artificial neural networks. Polym Adv Technol 2017;28(8):1044-1051.

277. Yao T, Deng Z, Zhang K, Li S. A method to predict the ultimate tensile strength of 3D printing polylactic acid (PLA) materials with different printing orientations. Composites Part B: Engineering 2019;163:393-402.

278. Hsueh M, Lai C, Wang S, Zeng Y, Hsieh C, Pan C, Huang W. Effect of printing parameters on the thermal and mechanical properties of 3d-printed pla and petg, using fused deposition modeling. Polymers 2021;13(11):1758.

279. Young D, Wetmore N, Czabaj M. Interlayer fracture toughness of additively manufactured unreinforced and carbon-fiber-reinforced acrylonitrile butadiene styrene. Additive Manufacturing 2018;22:508-515.

280. Ferreira RTL, Amatte IC, Dutra TA, Bürger D. Experimental characterization and micrography of 3D printed PLA and PLA reinforced with short carbon fibers. Composites Part B: Engineering 2017;124:88-100.

281. Wach RA, Wolszczak P, Adamus-Wlodarczyk A. Enhancement of Mechanical Properties of FDM-PLA Parts via Thermal Annealing. Macromol Mater Eng 2018;303(9):1800169.

282. Oliver WC, Pharr GM. An improved technique for determining hardness and elastic modulus using load and displacement sensing indentation experiments. J Mater Res 1992;7(6):1564-1583.

283. Dickson AN, Barry JN, McDonnell KA, Dowling DP. Fabrication of continuous carbon, glass and Kevlar fibre reinforced polymer composites using additive manufacturing. Additive Manufacturing 2017;16:146-152.

284. Gradinaru S, Tabaras D, Gheorghe D, Gheorghita D, Zamfir R, Vasilescu M, Dobrescu M, Grigorescu G, Cristescu I. Analysis of the anisotropy for 3D printed pla parts usable in medicine. UPB Scientific Bulletin 2019;81.

285. Ausejo JG, Rydz J, Musioł M, Sikorska W, Janeczek H, Sobota M, Włodarczyk J, Szeluga U, Hercog A, Kowalczuk M. Three-dimensional printing of PLA and PLA/PHA dumbbell-shaped specimens of crisscross and transverse patterns as promising materials in emerging application areas: Prediction study. Polym Degrad Stab 2018;156:100-110.

286. Gonzalez Ausejo J, Rydz J, Musioł M, Sikorska W, Sobota M, Włodarczyk J, Adamus G, Janeczek H, Kwiecień I, Hercog A, Johnston B, Khan HR, Kannappan V, Jones KR, Morris MR, Jiang G, Radecka I, Kowalczuk M. A comparative study of three-dimensional printing directions: The degradation and toxicological profile of a PLA/PHA blend. Polym Degrad Stab 2018;152:191-207.

287. Vigil Fuentes MA, Thakur S, Wu F, Misra M, Gregori S, Mohanty AK. Study on the 3D printability of poly (3-hydroxybutyrate-co-3-hydroxyvalerate)/poly (lactic acid) blends with chain extender using fused filament fabrication. Scientific reports 2020;10(1):1-12.

288. Kantaros A, Karalekas D. Fiber Bragg grating based investigation of residual strains in ABS parts fabricated by fused deposition modeling process. Mater Des 2013;50:44-50.

289. Gerard T, Budtova T. Morphology and molten-state rheology of polylactide and polyhydroxyalkanoate blends. European Polymer Journal 2012;48(6):1110-1117.

290. Fortunati E, Puglia D, Iannoni A, Terenzi A, Kenny JM, Torre L. Processing conditions, thermal and mechanical responses of stretchable poly (lactic acid)/poly (butylene succinate) films. Materials 2017;10(7):809.

291. Imre B, Pukánszky B. Compatibilization in bio-based and biodegradable polymer blends. European Polymer Journal 2013;49(6):1215-1233.

292. Pivsa-Art W, Fujii K, Nomura K, Aso Y, Ohara H, Yamane H. The effect of poly (ethylene glycol) as plasticizer in blends of poly (lactic acid) and poly (butylene succinate). J Appl Polym Sci 2016;133(8).

293. Zhang K, Mohanty AK, Misra M. Fully Biodegradable and Biorenewable Ternary Blends from Polylactide, Poly(3-hydroxybutyrate-co-hydroxyvalerate) and Poly(butylene succinate) with Balanced Properties. ACS Appl Mater Interfaces 2012;4(6):3091-3101.

294. Douglas P, Kuhs M, Sajjia M, Khraisheh M, Walker G, Collins MN, Albadarin AB. Bioactive PCL matrices with a range of structural & rheological properties. React Funct Polym 2016;101:54-62.

295. Su S, Kopitzky R, Tolga S, Kabasci S. Polylactide (PLA) and its blends with poly (butylene succinate)(PBS): A brief review. Polymers 2019;11(7):1193.

296. Ruellan A, Guinault A, Sollogoub C, Ducruet V, Domenek S. Solubility factors as screening tools of biodegradable toughening agents of polylactide. J Appl Polym Sci 2015;132(48).

297. Zhou J, Wang X, Hua K, Duan C, Zhang W, Ji J, Yang X. Enhanced mechanical properties and degradability of poly (butylene succinate) and poly (lactic acid) blends. Iranian Polymer Journal 2013;22(4):267-275.

298. Bhatia A, Gupta R, Bhattacharya S, Choi H. Compatibility of biodegradable poly (lactic acid)(PLA) and poly (butylene succinate)(PBS) blends for packaging application. Korea-Australia rheology journal 2007;19(3):125-131.

299. Ou-Yang Q, Guo B, Xu J. Preparation and characterization of poly (butylene succinate)/polylactide blends for fused deposition modeling 3D printing. ACS omega 2018;3(10):14309-14317.

300. Qahtani M, Wu F, Misra M, Gregori S, Mielewski DF, Mohanty AK. Experimental design of sustainable 3D-printed poly (lactic acid)/biobased poly (butylene succinate) blends via fused deposition modeling. ACS Sustainable Chemistry & Engineering 2019;7(17):14460-14470.

301. Park JW, Im SS. Phase behavior and morphology in blends of poly (L-lactic acid) and poly (butylene succinate). J Appl Polym Sci 2002;86(3):647-655.

302. Wasti S, Triggs E, Farag R, Auad M, Adhikari S, Bajwa D, Li M, Ragauskas AJ. Influence of plasticizers on thermal and mechanical properties of biocomposite filaments made from lignin and polylactic acid for 3D printing. Composites Part B: Engineering 2021;205:108483.

303. Rosário F, Corradini E, Casarin SA, Agnelli JA. Effect of gamma radiation on the properties of poly (3-hydroxybutyrate-co-3-hydroxyvalerate)/poly (ε-caprolactone) blends. Journal of Polymers and the Environment 2013;21(3):789-794.

304. Ma P, Hristova-Bogaerds DG, Lemstra PJ, Zhang Y, Wang S. Toughening of phbv/pbs and phb/pbs blends via in situ compatibilization using dicumyl peroxide as a free-radical grafting initiator. Macromolecular Materials and Engineering 2012;297(5):402-410.

305. Peshne H, Satapathy BK. Comparative studies of structural, thermal, mechanical, rheological and dynamic mechanical response of melt mixed PHB/bio-PBS and PHBV/bio-PBS blends. Journal of Polymer Research 2022;29(12):1-22.

306. Zhang K, Mohanty AK, Misra M. Fully biodegradable and biorenewable ternary blends from polylactide, poly (3-hydroxybutyrate-co-hydroxyvalerate) and poly (butylene succinate) with balanced properties. ACS applied materials & interfaces 2012;4(6):3091-3101.

307. Qiu Z, Yang W, Ikehara T, Nishi T. Miscibility and crystallization behavior of biodegradable blends of two aliphatic polyesters. Poly(3-hydroxybutyrate-co-hydroxyvalerate) and poly(ε-caprolactone). Polymer 2005;46(25):11814-11819.

308. Laoutid F, Lenoir H, Molins Santaeularia A, Toncheva A, Schouw T, Dubois P. Impact-Resistant Poly (3-Hydroxybutyrate)/Poly (ε-Caprolactone)-Based Materials, through Reactive Melt Processing, for Compression-Molding and 3D-Printing Applications. Materials 2022;15(22):8233.

Appendix

Comparison of the nanoindentation results that on and off the grooves.

Indentation number	PLA/PHBV 70:30 wt%		PLA/PHBV 30:70 wt%	
	Hardness (GPa)	Modulus (GPa)	Hardness (GPa)	Modulus (GPa)
0	0.376	7.31	0.330	7.22
1	0.361	6.90	0.317	6.71
2	0.325	6.98	0.329	7.39
3	0.296	6.22	0.298	7.01
4	0.326	6.74	0.275	6.55
5	0.293	6.43	0.253	6.80
6	0.321	6.50	0.359	7.69
7	0.345	6.88	0.280	6.87
8	0.310	6.77	0.376	7.28

Journal publications

- Zhou, Y., Hui, D., **Wang, Y**. and Fan, M. (2021) 'Nanomechanical and Dynamic Mechanical Properties of Rubber-Wood-Plastic Composites', *Nanotechnology Reviews*, 11, pp. 167-175.

- **Wang, Y.**, Zhou, Y., Lin, L., Corker, J. and Fan, M. (2020) Overview of 3D additive manufacturing (AM) and corresponding AM composites, *Composites Part A: Applied Science and Manufacturing*, 139, pp. 106114.

- Madyan, O. A., **Wang, Y.**, Corker, J., Zhou, Y., Du, G. and Fan, M. (2020) Classification of wood fibre geometry and its behaviour in wood poly(lactic acid) composites, *Composites Part A: Applied Science and Manufacturing*, 133, pp. 105871.

- Sivanathan, A., Dou, Q., **Wang, Y.**, Li, Y., Corker, J., Zhou, Y. Fan, M. (2020) Phase change materials for building construction: An overview of nano-/micro-encapsulation, *Nanotechnology Reviews*, 9, pp. 896-921.

- Zhou, Y., **Wang Y.** and Fan, M. (2019) Incorporation of tyre rubber into wood plastic composites to develop novel multifunctional composites: Interface and bonding mechanisms, *Industrial Crops and Products*, 141, pp. 111788(1-10).